Design Analysis of 3D Lithium-ion Batteries with Computational Modeling

Chih-Hsuan Hung

A dissertation

submitted in partial fulfillment of the

requirements for the degree of

Doctor of Philosophy

University of Washington

2025

Reading Committee:

Corie L. Cobb, Chair

John C. Kramlich

Srikanth Allu

Program Authorized to Offer Degree:

Mechanical Engineering

University of Washington

Abstract

Design Analysis of 3D Lithium-ion Batteries with Computational Modeling

Chih-Hsuan Hung

Chair of the Supervisory Committee:

Corie L. Cobb

Mechanical Engineering

This dissertation reports on the investigation of micrometer-scale three-dimensional (3D) batteries on the transport, kinetic, and deposition mechanisms in Lithium-ion battery (LIB) cells using physics-based computational models. Conventional LIBs use planar electrodes composed of a randomly distributed solid particle network infused with liquid electrolyte. A planar electrode imposes a trade-off between energy density and power density in LIB cells, where a higher cell capacity requires more active materials in the electrodes, which inevitably increases the electrode thickness and introduces high transport impedances. 3D electrodes address this limitation by redistributing the solid electrode particles into non-planar configurations, providing additional transport and kinetic benefits and effectively loosening the trade-off.

Although various 3D LIBs have been modeled and fabricated over the last two decades, the relative performance advantages across different 3D electrode architectures and material systems remain unclear. This dissertation systematically analyzes these architectures, proposing frameworks to design, compare, and evaluate 3D LIB configurations for optimal energy and power density. The focus is on two categories of 3D LIBs: (1) the Interdigitated Electrodes (IDEs), which feature intertwined cathode and anode geometries that shorten the transport distance between the electrodes, and (2) the Structured Electrodes (SEs), which have macro-porosity integrated across the electrode thickness, acting as low tortuosity ionic transport pathways.

Physics-based 3D volume-average electrochemical models were generated in *VIBE-AMPERES*, a battery modeling software developed by Oak Ridge National Laboratory, to assess the impact of 3D electrode architectures and materials on the charge and discharge performance of both single-layer and multi-layer battery cells. Material systems studied include $Li_4Ti_5O_{12}$ (LTO) anode paired with $LiFePO_4$ (LPF) cathode, graphite anode with $LiNi_{0.5}Mn_{0.3}Co_{0.2}O_2$ (NMC-532) cathode, and graphite anode with $LiNi_{0.6}Mn_{0.2}Co_{0.2}O_2$ (NMC-622) cathode. Additionally, this dissertation presents a lithium plating model developed through the 3D volume-average method, which is employed to explore how SEs influence the onset and location of lithium plating in graphite|NMC-532 cells. By investigating how controlled electrode heterogeneity affects transport and kinetic processes through 3D physics-based, continuum-scale computational models, this work reveals critical insights into cell-level performance metrics such as charge and discharge capacity, energy density, power density, and lithium plating. The overarching objective is to advance 3D electrode design strategies by deepening the fundamental understanding of these mechanisms through analytical studies.

TABLE OF CONTENTS

LIST OF FIGURES

LIST OF TABLES

ACKOWLEDGEMENT

I would like to express my sincere gratitude to my advisor, *Prof. Corie L. Cobb*, for her guidance and support throughout my doctoral journey. Prof. Cobb has gone out of her way to help me build a research career, and I always be thankful for the opportunities she has opened for me.

My thanks also go to *Dr. Srikanth Allu* for his mentorship in scientific modeling and high-performance computing, and for his confidence in my ability to undertake new challenges. I am grateful to *Prof. John C. Kramlich* for his thoughtful engagement with my work – always asking thought-provoking questions in the most supportive and nonjudgmental way. I also appreciate *Prof. Daniel T. Schwartz* for his invaluable advice on battery science and electrochemistry.

I am thankful to *Wanwisa Kisalang*, the academic advisor in the Mechanical Engineering Department, for her warm support and encouragement throughout my time in the program.

I would also like to thank everyone in the Integrated Fabrication Laboratory, especially my fellow Ph.D. students — *Emilee, Michelle, Vinh, Zack,* and *Evan* — for their camaraderie. Additionally, I extend my gratitude to alumni master's students *Phong* and *Katrina* for their assistance in publishing a journal article, and to undergraduate students *Carlos* and *Elizabeth* for their contributions to Excel VBA programming.

My heartfelt appreciation goes to my partner, *Lezhi*, who has witnessed all the highs and lows of this process and remained a constant source of love, patience, and understanding.

A special thank you to my friends, *Joyce* and *Meredith*, for carrying me through difficult times and celebrating my successes. I will miss our Friday evening gatherings.

Finally, I am deeply grateful to my parents; my aunties, *Mary* and *Stephanie*; my sisters, *Jessie* and *Wendy*; my brother, *Ted*; and my nieces, *Anna* and *Sophia*, for constantly reminding me that I have a safe place to fall back on. I am very fortunate to have their unwavering support.

This work was partly funded by a Defense Advanced Research Projects Agency (DARPA) Young Faculty Award and Director's Fellowship under grant number D19AP00038. The views, opinions, and findings expressed in this work are those of the authors and should not be interpreted as representing the official views or policies of the Department of Defense or the U.S. Government, and no official endorsement should be inferred. This is approved for public release and distribution is unlimited.

This material is partly based upon work supported by the U.S. Department of Energy's Office of Energy Efficiency and Renewable Energy (EERE) under the Advanced Materials and Manufacturing Technologies Office, Award Number DE-EE0010226. This report was prepared as an account of work sponsored by an agency of the United States Government. Neither the United States Government nor any agency thereof, nor any of their employees, makes any warranty, express or implied, or assumes any legal liability or responsibility for the accuracy, completeness, or usefulness of any information, apparatus, product, or process disclosed, or represents that its use would not infringe privately owned rights. Reference herein to any specific commercial product, process, or service by trade name, trademark, manufacturer, or otherwise does not necessarily constitute or imply its endorsement, recommendation, or favoring by the United States Government or any agency thereof. The views and opinions of authors expressed herein do not necessarily state or reflect those of the United States Government or any agency thereof.

This work was partly carried out at Oak Ridge National Laboratory under Contract No. DE-AC05-00OR22725 with UT-Battelle, LLC. The US government retains and the publisher, by accepting the article for publication, acknowledges that the US government retains a nonexclusive, paid-up, irrevocable, worldwide license to publish or reproduce the published form of this manuscript, or allow others to do so, for US government purposes. DOE will provide public access

to these results of federally sponsored research in accordance with the DOE Public Access Plan (http://energy.gov/downloads/doe-public-access-plan).

This research was partly supported by an appointment to the Oak Ridge National Laboratory GRO Program, sponsored by the U.S. Department of Energy and administered by the Oak Ridge Institute for Science and Education.

This material is partly based upon work supported by the state of Washington through the University of Washington Clean Energy Institute.

DEDICATION

To my dear parents,

洪永裕 & 林智惠

Chapter 1. INTRODUCTION

*The content in sections 1.1 is adapted from Hung, C.-H.; Allu, S.; Cobb, C. L. "Modeling Current Density Non-Uniformities to Understand High-Rate Limitations in 3D Interdigitated Lithium-Ion Batteries." *J. Electrochem. Soc.* **2021** under CC BY 4.0 (https://creativecommons.org/ licenses/by/4.0/).[1] The content in section 1.2 is reprinted and adapted with permission from Hung, C.-H.; Huynh, P.; Teo, K.; Cobb, C. L. "Are Three-Dimensional Batteries Beneficial? Analyzing Historical Data to Elucidate Performance Advantages." *ACS Energy Lett.* **2022**, 296–305. Copyright 2023 American Chemical Society.[2]

1.1 CONVENTIONAL LITHIUM-ION BATTERIES (LIBS)

Lithium-ion batteries (LIBs) are rechargeable batteries widely utilized for applications ranging from portable electronics to vehicle electrification. Conventional LIBs are approaching their theoretical energy limits with today's commercialized materials and manufacturing processes. For example, commercialized LIBs have energy densities of 150 – 250 Wh/kg and 300 – 700 Wh/L,[3] but the United States Advanced Battery Consortium (USABC) has advised that advanced electric vehicle (EV) batteries should target useable energy densities of 350 Wh/kg and 750 Wh/L at the cell level and 235 Wh/kg and 500 Wh/L at the system level, both at a C/3 discharge rate.[4–6] In addition, portable electronics[7] and micro-robotics[8] also have a growing need for smaller and lighter weight form factors around 0.1 cm^3 in size while retaining the same, if not higher, energy and power performance. Broadly speaking, the advancement of battery technologies across all application scales requires smaller, lighter, and longer-life energy storage devices. Developing LIBs with concurrent high energy and power density has thus become an important goal for LIB researchers. Motivated by the same goal, this dissertation investigates the impact of 3D battery electrodes on improving energy and power density in LIBs.

1.1.1 *LIB Cell Components*

A single-layer battery cell is the basic building block of a LIB where the electrochemical reactions that convert chemical energy to electricity occur. There are five components in a single-layer cell: a positive current collector, a cathode, a separator, an anode, and a negative current collector, as illustrated in Figure 1.1(a). The cathode, anode, and separator are porous mediums that are soaked in liquid electrolyte, as shown in Figure 1.1(b). The cathode, anode, and the electrolyte are components that participate in electrochemical reactions and determine the charge and discharge capacity (Ah) of a LIB cell. The separator and the current collectors are considered inactive cell components that are critical for cell operation but do not drive a cell's capacity. The separator protects the battery from forming an internal short-circuit, which can lead to a series of safety hazards. Current collectors conduct electrons between the external circuit and the electrodes, ensuring a uniform current flow during charge and discharge. At scale, single-layer cells in Figure 1.1 (a) are stacked layer-by-layer to increase the total capacity (Ah) and energy (Wh). An example of a cell stack in a pouch cell format is illustrated in Figure 1.1 (c).

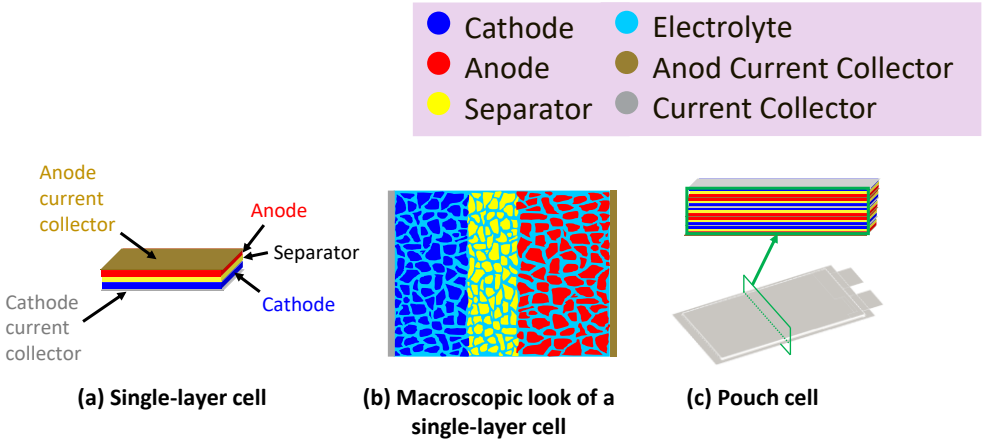

Figure 1.1. The different scales of LIBs: (a) a single-layer cell, (b) a single-layer cell with the porous structures displayed, and (c) a pouch cell with cross-section of a multi-layer cell stack shown.

Conventional LIB electrodes are porous and are typically manufactured with slot-die and doctor-blade coating. Electrode slurries are coated onto current collector substrates, [9] and the slurries consist of active material, conductive carbon, and polymer binder particles suspended in a solvent. The coating is then dried, forming a porous, solid particle network, which is then compressed by calendering to enhance contact between particles and the electrode film and the current collector. The anode and cathode are made in independent production lines, and the two electrodes are then assembled with a porous separator sandwiched in between to form a single-layer cell. The cells are stacked into a multi-layer stack, and liquid electrolyte is infiltrated into the stack to form an ionically conducting liquid-phase network in the pores of the anode, cathode, and separator.

1.1.2 *Energy and Power Trade-offs in LIBs*

Conventional LIB single-layer cells exhibit a performance trade-off between energy and power when the material chemistry and composition are fixed. Figure 1.2 illustrates two discharging single-layer LIB cells, one with thick electrodes and the other with thin electrodes. The amount of active material that facilitates the intercalation reaction is represented by the number of orange circles labeled “Li+,” and orange dash lines depict the Lithium-ion (Li-ion) transport distance. For simplicity, electron transport within the solid electrode is not shown, although electrons move in the opposite direction to Li-ions within the electrodes in actual operation. Compared to thick-electrode LIBs, thin-electrode planar LIBs have high power performance (W) due to a shorter transport length across the electrode thickness, allowing the Li-ions and electrons to travel more quickly between electrodes. In contrast, thick electrodes offer higher capacity (Ah) and energy (Wh), as they contain more active material and a greater number

of intercalation sites. However, the transport distances in thick electrodes are much longer, resulting in low power performance.

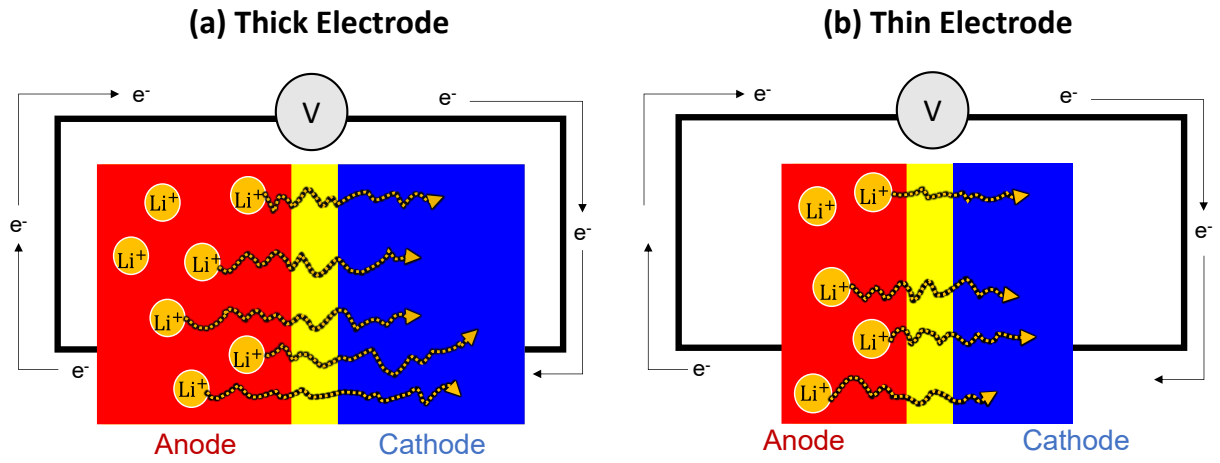

Figure 1.2. Comparison of thick and thin planar LIBs during discharge. The orange dashed arrows represent the Li-ion transport pathway and the number of orange circles (Li^+) represents the amount of active material in the cell.

In addition to the energy and power trade-offs associated with electrode thickness, a similar performance trade-off arises from electrode porosity. Increasing electrode porosity allows for a greater volume of liquid electrolyte within the cell, enhancing Li-ion transport in the liquid phase and, in certain situations, increasing the phase boundary surface area between the solid electrode and the liquid electrolyte that facilitates intercalation kinetics. However, a higher porosity reduces the quantity of active material in the single-layer cell, which in turn decreases the capacity (Ah) and energy (Wh) at scale. Conversely, a lower electrode porosity facilitates a denser packing of active material within the LIB, but it restricts transport and results in diminished power performance. It is also important to note that there is a practical limit to how porous an electrode can be; excessive porosity can hinder the formation of a conductive solid network, while a very low porosity creates a discontinuous liquid phase network.

A common question arises: can stacking multiple thin-electrode single-layer cells improve energy performance while maintaining fast transport? Individual cells are often stacked into larger cell formats such as the pouch cell illustrated in Figure 1.1 (b) to increase the total battery capacity (Ah) and energy (Wh). Although staking single-layer cells increases the overall capacity and energy, it does not improve capacity and energy on a per-weight or per-volume basis (Ah/kg, Ah/L, Wh/kg, Wh/L). As previously noted at the beginning of Chapter 1.1, the volumetric and gravimetric energy density are critical performance metrics for electric vehicles and micro-robotics. Research conducted by Cobb and Solberg illustrates that, compared to thick-electrode cells, thin-electrode cells necessitate a greater number of current collectors within a cell stack, which subsequently leads to a decrease in energy density performance.[10] Furthermore, as the number of stacked layers increases, the volume ratio of active materials, i.e. the electrodes and the electrolyte, to inactive materials, including the separators and the current collectors, within the multi-layer cell stack eventually plateaus, leading to diminished benefits with increases in electrode thickness. Ultimately, the energy and power density (Wh/kg, Wh/L, Wh/kg, and W/L) of a multi-layer cell stack are constrained by the transport and kinetics present in a single-layer cell.

1.1.3 *Modeling Electrochemical Processes in a LIB Cell*

To mitigate the energy and power trade-off, we must first understand the electrochemical mechanisms that govern the physics within a single-layer cell during charging and discharging. The Doyle-Fuller-Newman (DFN) electrochemical model is a set of nonlinear transient partial differential equations that describe the transport and kinetic physics in a single-layer cell.[11] The system modeled includes the volumes of the cathode, the anode, the separator, and the electrolyte. Current collectors are implemented as boundary conditions in the DFN model. The equations are

solved using the finite element method to find the local potential, concentration, and reaction current across a LIB cell. When an LIB cell is placed in an open circuit that has no current flow, the potential in each electrode is equal to the material's chemical potential versus Lithium metal. The is called the open-circuit potential, U_{OCP}, which is a function of the Li-ion concentration within the solid phase and is commonly measured in experiments using the galvanostatic intermittent titration technique (GITT). The solid-phase potential difference between the cathode and the anode creates a static potential gradient in the liquid electrolyte network, which is referred to as ϕ_e. When a charged LIB is connected to an external circuit, this potential gradient will drive electrochemical reactions.

In the DFN model, the local driving force for Li-ion intercalation and de-intercalation reactions at the phase boundary is the surface overpotential (η), which is a measure of the local potential difference between the solid and the liquid phases and is calculated independently for the cathode and the anode across their thicknesses. Equation 1.1 defines the surface overpotential in the unit of V as the difference between local potential drop across the solid and liquid phases, $\phi_s - \phi_e$ and the open-circuit potential of the solid phase (U_{OCP}). Film resistance, R_{film}, exists and adds to the overpotential if a solid-electrolyte interface (SEI) develops on the electrode active material particle surface due to side reactions between the electrode active material and the electrolyte.[11,12] In Equation 1.1, j^{Li} represents the pore-wall Li-ion flux across the liquid and solid phases. Equation 1.2 describes a_s, the specific surface area of the porous electrode in cm^{-1}, which is a function of the electrode volume fraction ε_s and active material particle radius R_s. The specific area represents the surface area of active materials that are in contact with the liquid electrolyte per volume of the porous electrode, and the calculation in Equation 1.2 assumes the active material particles are spherical. Note that at the beginning of discharge when the LIB is still in equilibrium

and there is no film resistance, ϕ_s is the same as U_{OCP}, and the liquid phase potential ϕ_e is the sole driver. Overtime, the solid-phase potential can shift away from the open-circuit potential due to influences from local concentration gradients.

$$\eta = \phi_s - \phi_e - U_{OCP} - \frac{j^{Li}}{a_s} R_{film} \quad (1.1)$$

$$a_s = \frac{3\varepsilon_s}{R_s} \quad (1.2)$$

The Butler-Volmer relationship in Equations 1.3 models the pore-wall Li-ion flux across phase boundary (j^{Li}) in the unit of A·cm^{-3} as a function of the surface overpotential. Note that when the surface overpotential is zero, there will be no reaction current and zero ionic flux. The rates of the (de-)intercalation reactions depend on local Li-ion concentrations in both phases. Therefore, in Equation 1.3, the exchange current density (i_o) in the unit of A·cm^{-2} is included to describe the (de-)intercalation reaction rate as a function of local Li-ion concentrations. In Equation 1.4, k is the reaction rate constant in A·mol$^{-1.5}$cm$^{2.5}$, c_e is the liquid-phase L-ion concentration in mol·cm^{-3}, c_s is the solid-phase L-ion concentration in molcm^{-3}, and $c_{s,max}$ is the maximum solid-phase Li-ion concentration in mol·cm^{-3}, as determined by the material chemistry. Additionally, in Equation 1.3, a_s is the specific surface area of the porous electrode in cm^{-1}, α_a and α_c are the unitless symmetric anodic and cathodic reaction transfer coefficients ($\alpha_a = \alpha_c = 0.5$), R is the universal gas constant (8.314 J·mol^{-1}K^{-1}), T is the temperature in K, F is Faraday's constant (96485 C·mol^{-1}).

$$\frac{j^{Li}}{a_s} = i_o\left(\exp\left(\frac{\alpha_a F}{RT}\eta\right) - \exp\left(-\frac{\alpha_c F}{RT}\eta\right)\right) \quad (1.3)$$

$$i_o = k(c_e)^{\alpha_{aj}}(c_{s,max} - c_s)^{\alpha_{aj}}(c_s)^{\alpha_{cj}} \quad (1.4)$$

Following the (de-)intercalation reactions, electrons and Li-ions are conducted in the porous network to ensure charge neutrality and mass conservation. The electrons are conducted between the solid particle network and the external circuit, and the Li-ions conduct or diffuse in the liquid electrolyte. The conduction in each phase is modeled using Ohm's law and the Nernst equation in Equations 1.5 and 1.6, where ε_e and ε_s are the volume fractions of liquid and solid, κ^{eff} is the effective Li-ion conductivity in the electrolyte, and σ^{eff} is the effective electronic conductivity in the solid phase.

$$\nabla \cdot (\varepsilon_e \kappa^{eff} \nabla \phi_e) + \nabla \cdot \left(\varepsilon_e \frac{2RT(t_+^0 - 1)}{F} \kappa^{eff} \nabla \ln c_e \right) = -j^{Li} \quad (1.5)$$

$$\nabla \cdot (\varepsilon_s \sigma^{eff} \nabla \phi_s) = j^{Li} \quad (1.6)$$

The second term on the lefthand side of Equation 1.5 is a variation of the Nernst equation, which describes the reaction current correlated to the Li-ion concentration gradient in the electrolyte. This term is not included in Equation 1.6 since electronic conduction in the solid phase is not affected by Li-ion concentration. Within the system defined by the DFN model, charge neutrality and mass conservation must be maintained. Therefore, when a battery is being charged or discharged at high current rates, the system will respond with fast reaction kinetics and conduction. If transport or kinetics fail to keep up with the set current rate, Li-ions will accumulate at the location where the highest resistance occurs, and a Li-ion concentration gradient will form over time. The concentration gradients drive the Li-ion to diffuse from high concentration to low concentration regions within each phase, and these diffusion physics are governed by Fick's law. In the DFN model, Li-ion diffusion in the liquid network is described by Equation 1.7, where D_e^{eff}

is the effective Li-ion diffusivity in electrolyte in the unit of cm^2s^{-1}, and t_+^0 is the transference number.

$$\frac{\partial(\varepsilon_e c_e)}{\partial t} - \nabla \cdot \left(\varepsilon_e D_e^{eff} \nabla c_e\right) = \frac{1-t_+^0}{F} j^{Li} \quad (1.7)$$

In the solid phase, the DFN model captures the diffusion of Li-ions at the length scale of the active material particles. A spherical coordinate system is used, with the origin of the coordinate system set at the center of the active material particle. Diffusion is governed by Fick's law and modeled along the radius of an active material particle, r, in Equation 1.8, where D_s^{eff} is the effective Li-ion diffusivity in the solid-phase. Equations 1.9 and 1.10 are the boundary conditions imposed at the center of the particle ($r = 0$) and particle surface ($r = R_s$) to ensure symmetry and mass conservation.

$$\frac{\partial c_s}{\partial t} = D_s^{eff}\left(\frac{\partial^2 c_s}{\partial r^2} + \frac{2}{r}\frac{\partial c_s}{\partial r}\right) \quad (1.8)$$

$$\frac{\partial c_s}{\partial t} = 0 \; at \; r = 0 \quad (1.9)$$

$$D_s^{eff}\left(\frac{\partial c_s}{\partial r}\right) = \frac{-j^{Li}}{F} at \; r = R_s \quad (1.10)$$

When Li-ions are conducted or diffused in the liquid electrolyte network, they need to maneuver around the solid particle network. As a result, the transport pathway is always longer than the ideal point-to-point distance. Likewise, the transport of electrons and Li-ions in the solid phase experience the same issue. Tortuosity, τ, is a measure of the length a Li-ion or electron has travelled normalized to the ideal point-to-point distance. The Bruggeman relationship describes the tortuosity of a porous medium having a volume fraction, ε, in Equation 1.11, where the

tortuosity increases exponentially with the volume fraction, and p is the Bruggeman constant that is dependent on the microstructure of the porous medium.[13,14] In the DFN mode, the impact of tortuosity is account for in the use of effective transport properties, including D_e^{eff}, D_s^{eff}, σ^{eff}, and κ^{eff} from Equations 1.5 – 1.10. These effective transport properties, denoted as A^{eff} in Equation 1.12, represent the true conductivity or diffusivity when the conducting medium has a volume fraction less than 1. In Equation 1.12, A represents diffusivity or conductivity measured in a non-porous medium, ε is the volume fraction associated with the phase in which the transport property is considered, and τ is the tortuosity described in Equation 1.11.

$$\tau = \varepsilon^{1-p} \quad (1.11)$$

$$A^{eff} = \frac{A\varepsilon}{\tau} \quad (1.12)$$

Equations 1.1 – 1.12 constitute a pseudo-two-dimensional (pseudo-2D, or P2D) physics-based electrochemical model. The conduction of Li-ions and electrons as well as Li-ion diffusion in the liquid phase are one-dimensional across the electrode thickness direction. The diffusion of Li-ions in the solid phase is also one dimensional but in the radial direction of the active material particles. This radial dimension is defined in a cylindrical coordinate system that is different from the Cartesian system used by the electrode thickness. Hence, the model is considered pseudo-2D instead of 2D. Extending their original P2D model development, Doyle et al.[11] categorized single-layer cell parameters into two types: system-specific parameters and design-adjustable parameters. The system-specific parameters relate to transport and thermodynamic properties that depend on the materials used, while the design-adjustable parameters are those that can be modified independently of the material system (see Table 1.1).

Once a material system and initial conditions have been established, the primary design-adjustable parameters at the cell level are electrode porosity, thickness, and particle size. In addition to the energy and power trade-offs associated with varying electrode thickness and porosity, several other factors complicate the design process. For example, increasing electrode thickness, reducing particle size, and increasing porosity can increase the reaction surface area and improve intercalation kinetics. However, the reaction rate is also correlated to the local solid-phase and liquid-phase Li-ion concentrations, which are dependent on ionic transport. Moreover, reducing particle size leads to shorter Li-ion transport distances within the solid particles, although this may also result in increased transport tortuosity at the scale of electrode thickness.[15]

Table 1.1. System specific and design adjustable parameters as defined by Doyle et al.[11] The system-specific parameters are intrinsic material properties, while design-adjustable parameters are design-driven and independent of the material system.

System specific Parameter	**Description**	**Unit**
D_s	Diffusion coefficient in the solid phase	$m^2 \cdot s^{-1}$
Σ	Electric conductivity	$S \cdot m^{-1}$
c_s^{max}	Maximum Li-ion concentration in the solid phase	$mol \cdot m^{-3}$
K	Reaction rate constant	$A \cdot cm^{2.5} mol^{-1.5}$
D_e	Diffusion coefficient in the liquid phase	$m^2 \cdot s^{-1}$
κ	Ionic conductivity	
Design adjustable Parameter	**Description**	**Unit**
c_e^0	Initial concentration in the liquid phase	$mol \cdot m^{-3}$
c_s^0	Initial concentration in the solid phase	$mol \cdot m^{-3}$
R_s	Particle radius	m
ε_e	Volume fraction of liquid	N/A
ε_s	Volume fraction of solid	N/A
δ	Electrode Thickness	m

In research experiments and conventional manufacturing, electrode thickness is controlled by the casting thickness, thermal drying conditions, slurry properties, and the calendering process. Particle size can be regulated through both synthesis conditions and post-synthesis grinding, while

porosity can be adjusted by changing the solvent content in the slurry or through calendering to compact the pore structure. Employing numerical simulations to assess the impact of electrode thickness, porosity, and particle size over a range of C-rates is a valuable approach before resources are invested in manufacturing when designing batteries with a new material system.[16–20] However, the inherent trade-off between power and energy density in LIBs cannot be solved with the current electrode design parameters in Table 1.1.

1.2 3D BATTERIES

As illustrated in Figure 1.3, 3D batteries have unique electrode geometries that set them apart from the conventional planar form factor. In 3D batteries, electrode materials are redistributed in controlled heterogeneous spatial arrangements to optimize Li-ion and electron transport without sacrificing total active material content in the cell.[10,21–23] Based on the electrode architecture, 3D LIBs can be generally categorized into two main groups: (1) "Interdigitated Electrodes (IDEs)" in Figure 1.3 (b), where the cathode and anode have micron-scale feature sizes and are intertwined, shortening the transport distance between electrodes, and (2) "Structured Electrodes (SEs)" in Figure 1.3 (c), where micron-scale channels filled with liquid electrolyte are patterned into the electrodes to provide Li-ions with transport "highways" in place of the tortuous pathways through the solid particle network.

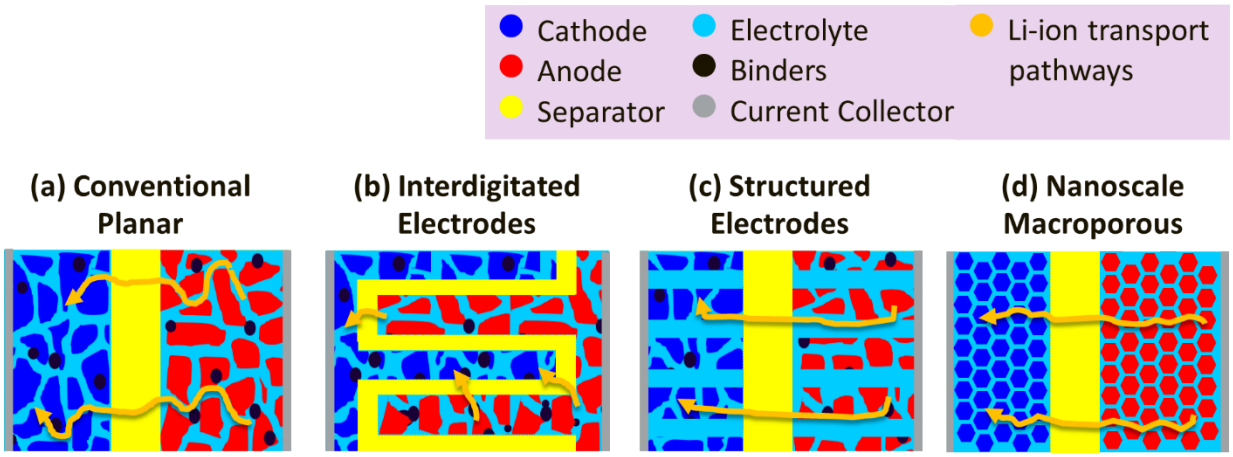

Figure 1.3. (a) Conventional planar LIBs have long and tortuous transport pathways (highlighted in orange) that prevent concurrent high-energy and high-power performance. 3D LIBs with (b) Interdigitated Electrodes (IDEs), (c) Structured Electrodes (SEs), and (d) Nanoscale Macroporous Electrodes enable concurrent high-energy and high-power by rearranging the electrode materials without reducing the total amount of electrode material in a fixed volume.

3D electrode architectures can also be engineered at the nanoscale, as shown in Figure 1.3 (d). These 3D LIBs have periodic or aperiodic electrode porosity controlled at the nanometer scale, which results in "sponge-like" electrodes.[24–26] Nanoscale electrode structuring such as nanowires,[27–30] nanosheets,[31,32] and 3D ordered porous electrodes[25,32–36] provides additional transport enhancements in the solid phase and higher kinetic activity over micron-scale 3D electrodes.[33,34,37,38] In some scenarios, nanoscale 3D electrodes can be combined with micrometer-scale 3D electrodes to form hierarchically ordered 3D electrodes. Nanoscale 3D electrodes face a different subset of challenges than micron-scale 3D electrodes, including extensive side reactions due to enlarged surface area[38,39] and electrolyte wetting issue due to the small feature sizes. The difference in scale can also be shown by looking at their respective fabrication methods. Micron-scale 3D electrodes can still leverage conventional slurry-based methods, while nanoscale 3D electrodes are directly synthesized or electro- and vapor- deposited onto pre-manufactured

substrates.[25,40–44] From the perspective of the electrochemical modeling approach used in this dissertation, nanoscale electrode architectures that engineer geometry and material on a scale below 500 nm are considered intrinsic material property changes. The evaluation of nanoscale 3D LIBs requires a different set of modeling tools than those used for micrometer-scale 3D LIBs. Therefore, this dissertation focuses on the micron-scale 3D LIBs in Figure 1.3 (a) and Figure 1.3 (b): the IDEs and the SEs. From here on, the term 3D LIBs will be used to refer to both IDEs and SEs.

1.2.1 *3D Interdigitated Electrodes (IDEs) Design Challenges and Opportunities*

IDEs were initially proposed to enhance the areal capacity of thin-film batteries in microelectrochemical systems (MEMS). These designs often feature arrays of cathode and anode plates or columns in various shapes – such as circles, squares, triangles, or crosses – assembled into a full cell. In some configurations, the cathode and anode adopt different geometries: one electrode consists of columns covered by a separator layer, while the other fills the remaining void space. The interpenetrating configuration maintains a short Li-ion transport between the anode and the cathode that is independent of the electrode length. As a result, a higher active material loading can be achieved by increasing the electrode length without adding to the transport distance.

Another significant advantage of IDEs is their enlarged surface area between the electrodes and the separator. In conventional planar LIB cells, intercalation reactions typically concentrate near the separator-cathode interface toward the end of discharge. This trend in reactivity results from slow ionic transport within the cathode, where reaction rates are greater at locations that have more Li-ion availability. This is primarily near the separator since Li-ions are released from the anode. IDEs provide more surface area for direct access to the high-concentration liquid electrolyte in the separator, enhancing capacity at high discharge rates.

Although the IDE approach in theory yields improved utilization of the active materials and leads to higher cell capacity, it has been shown to negatively impact areal, gravimetric, and volumetric energy density if the cell dimensions were not optimized. In 2007, Chamran et al. fabricated Li-ion 3D electrode column arrays with mesocarbon microbeads (MCMB) and silicone micromachining, demonstrating a ten-fold increase in areal capacity over planar electrodes.[45] However, no significant improvement was observed in specific capacity per electrode weight (mAh/g). Dokko et al. fabricated fully interdigitated electrodes with sol-gel methods using Lithium titanate ($Li_4Ti_5O_{12}$, LTO) and Lithium Manganese Oxide ($LiMn_2O_4$, LMO), but their micro-battery showed a lower areal capacity than its conventional planar counterpart.[46] Subsequently, Teixidor et al. fabricated circular and cross-shaped MCMB electrode arrays through epoxy resin pyrolysis, achieving ten times more areal capacity, but the cell exhibited less than half of the gravimetric capacity of the planar electrode.[47] Chamran et al., Dokko et al., and Teixidor et al. attributed the low gravimetric or areal capacity performance to suboptimal 3D electrode dimensions. More recently, Sun et al. employed 3D direct-ink writing to print interdigitated LTO and Lithium iron phosphate ($LiFeO_4$, LFP) electrodes. These electrodes demonstrated improved areal energy and power density compared to equivalent planar counterparts, although only moderate energy density improvements were realized.

Two factors may have contributed to the lower IDE performance noted above. First, compared to conventional electrodes, IDEs have a higher volume fraction of separator within a single-layer cell. Some authors also fabricated IDEs using a 3D current collector substrate coated by a thin layer of conformal electrode material;[41,43,48–52] in these cases, the volume fraction of current collectors is greater than that found in conventional cells. The increased volume fractions of inactive components within the IDE cell can lead to reduced energy and power density metrics

in Wh/kg, Wh/L, W/kg, and W/L, when evaluating performance in the context of a fully packaged cell, despite improvements in material utilization (mAh/cm^2 and mAh/g_{active}). Second, the effects of IDEs on cell performance are contingent upon the material system and cell configuration. For instance, prior modeling research has focused on non-porous IDE electrodes.[50,53–56] These non-porous IDEs tend to be kinetic-limited because charge transfer reactions only occur at the contact surface between the separator and the electrodes, and optimizing the electrode-separator contact surface area became a key design goal for these configurations. In comparison, porous IDEs with planar current collectors, as illustrated in Figure 1.3 (b), have intercalation reactions occur throughout the porous electrode network, and their performance can be limited by a mix of kinetic and transport processes within the cell. Depending on the intrinsic rate-limiting mechanisms of the material system, enhancements in reaction kinetics and reductions in physical distances between the electrodes may not significantly influence material utilization. The fundamental mechanisms by which porous IDEs contribute to performance improvements, the specific length scales at which these effects occur, and their correlation to both the material system and electrode architecture are not yet fully understood.

Beyond the aforementioned design challenges, IDEs possess unique geometric features that introduce complex and nonlinear performance characteristics. In the early 2000s, Hart et al. modeled the equipotential lines within IDE designs, demonstrating how IDE electrode geometries generate complex potential fields, in contrast to the uniform fields typical of planar electrodes. If these heterogeneities are not properly managed, they can lead to significant non-uniformities in potential and current distribution, ultimately resulting in diminished battery capacity. Experimental evidence has indicated material underutilization due to spatial inhomogeneities, as observed in the IDE LIB developed by Talin et al.[48] Computational studies by Zadin et al. have

further illustrated that IDEs with larger electrode thicknesses, sharper edges, and mismatched electrode conductivities exhibited less uniform current densities, subsequently lowering material utilization.[53–55,57] While it is widely recognized that non-uniformities in IDEs adversely impact cell performance, further investigation is needed to understand the scale at which these non-uniformities become significant and how they influence performance enhancements related to improved transport and kinetics.

1.2.2 *3D Structured Electrodes (SEs) Design Challenges and Opportunities*

SEs reduce the electrode tortuosity in the liquid-phase by engineering straight macro-porous channels as additional transport "highways" that contain only liquid electrolyte. While the Li-ion transport distance remains the same, the total path length travelled by the Li-ions can be greatly reduced. Similar to IDEs, the shape of the structured electrolyte channels can have various geometry patterns, with the most commonly used patterns being the line and grid patterns shown in Figure 1.4. Unlike IDEs, SE architectures are isolated to single electrodes. Therefore, SEs are more adaptable to large-scale battery integration for applications like EVs and grid storage. SEs have been fabricated using sol-gel phase-version, 3D printing, laser ablation, and acoustic focusing techniques,[21,58–62] and many computational studies have been conducted to optimize SE designs.

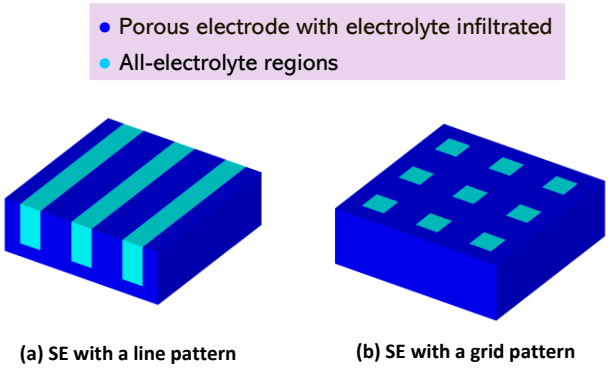

Figure 1.4. Structured electrodes with "all-electrolyte" regions in (a) a line pattern and (b) a grid pattern

SEs, by design, are not constrained by the percolation limits found in planar electrodes and can accommodate a larger electrolyte volume within the single-layer cell. This prompts a fundamental question of whether the performance benefits of SEs stem primarily from the additional electrolyte volume. If so, their advantages may be confined to systems where liquid-phase transport is the rate-limiting factor. Moreover, it is important to analyze the potential benefits of SEs in relation to existing design alternatives, such as increasing electrolyte formulation concentration or implementing porosity grading in planar electrodes by casting electrode slurries of different compositions layer-by-layer to reduce the transport tortuosity in electrode regions closer to the separator interface.[19,63,64] Incorporating SE designs also significantly alters the volume proportion of cathode, anode, electrolyte, and separator within a single-layer cell, which impacts the overall weight and volume of the multi-layer stack. The performance improvements offered by SEs, much like the IDEs, must justify the increased complexity of developing new manufacturing technologies.

Both experimental and modeling studies have also indicated that SEs can help mitigate lithium plating,[21,59,60,65,66] an undesirable Lithium metal deposition reaction that occurs on a graphite anode during the charging process. Modeling studies conducted by Habedank et al. and Chen et al. reported reduced concentration gradients across the electrode thickness in SEs.[21,67] While some attributed the improvements in lithium plating to this diminished concentration gradient, others have also highlighted the role of SEs in facilitating improved electrolyte wetting within the electrodes, leading to a more uniform reaction current density in the electrode and less lithium plating.[59,66] In a post-mortem analysis, Dunlap et al. found a plated lithium pattern that matched the geometry pattern of their SEs, indicating the SE geometry pattern can cause kinetic non-uniformity across the electrode surface.[59] This finding prompts an essential question: can SEs

be intentionally designed to regulate the location of lithium plating, thereby enhancing overall battery performance?

1.2.3 *Designing 3D LIBs with Computational Models*

As detailed in sections 1.2.1 and 1.2.2, 3D LIBs are designed with the goals of shortening Li-ion transport pathways and increasing reaction kinetics, but they also introduce new design complexities that can potentially lower battery performance. These complexities include spatial nonuniformity in the electrochemical processes and the changes in the volume proportions of cell components within the cell. The reasons 3D LIBs improve performance over planar cells are often multi-faceted, and it is important to identify the sources of these performance improvements and understand the fundamental contribution of 3D electrode architectures. To do so, comparative and systematic studies must be conducted to holistically evaluate the impact of 3D LIBs across multiple performance metrics. Physics-based computational modeling is an effective method to evaluate the performance of 3D LIBs made with a series of electrode architectures and materials and analyze the underlying physics. One major obstacle is the resource-intensive and time-consuming nature of full 3D computational models.[68] Consequently, reduced-order models are often employed, but these models fall short in capturing the spatial distribution of current density, potential, and concentration. This dissertation addresses these modeling gaps by leveraging *VIBE-AMPERES*, a battery modeling program developed and distributed by Oak Ridge National Laboratory, to enable 3D electrochemical modeling of 3D LIBs.

As discussed in section 1.1.3, the physics-based DFN model based on mass and charge conservation equations are used to model conventional single-layer cells with planar electrodes. Unlike conventional LIBs whose transport processes are predominantly one-dimensional (1D), 3D LIBs have spatial variations that must be considered in all dimensions. As shown in Figure 1.5, a

series of mathematical formulations have been developed over the years to aid in this effort, including two-dimensional (2D) axisymmetric,[48,49] pseudo-2D (P2D),[10,69] volume-average 3D models, [70,71] and 3D direct numerical simulation (DNS).[50,53,57,72] In Figure 1.5, models closer to the bottom of the pyramid have a higher computational efficiency, while models at the top of the pyramid have a higher model accuracy.

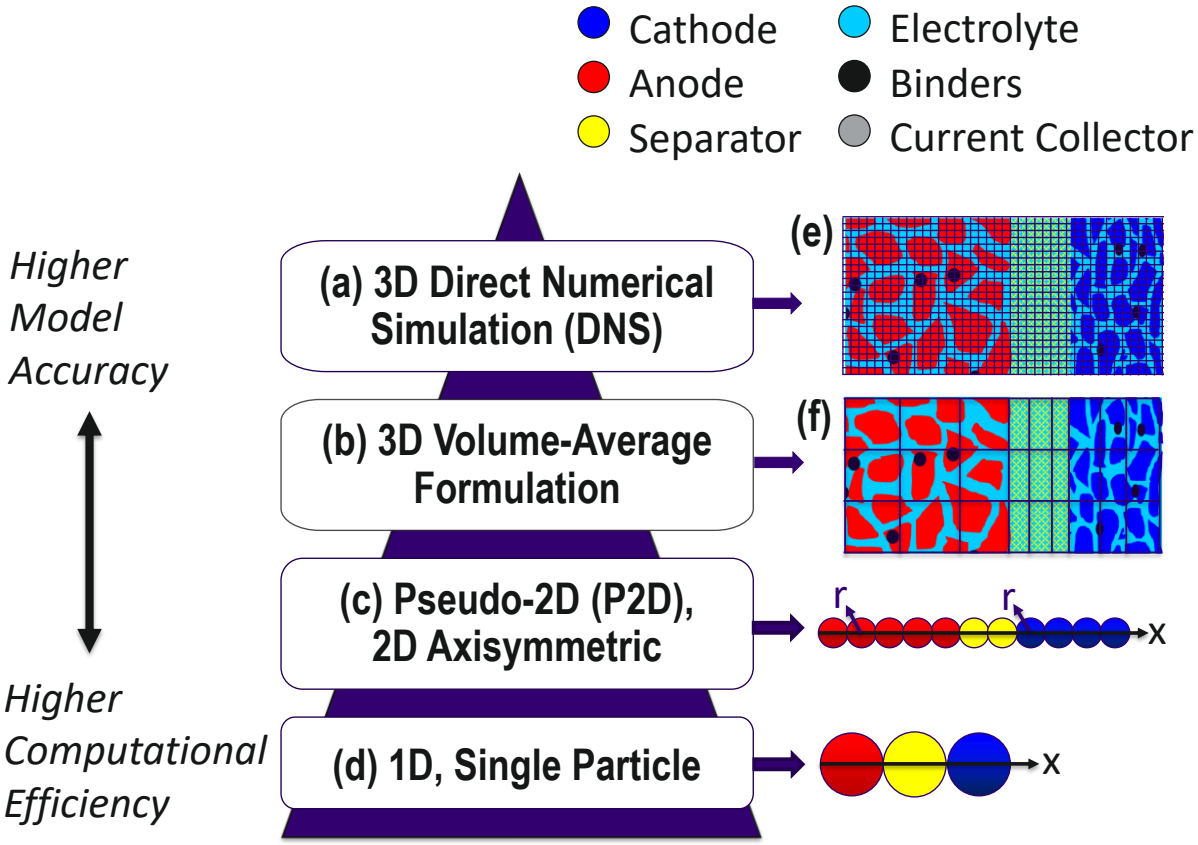

Figure 1.5. Physics-based computational models for a single-layer battery cell at different levels of resolution.

The 2D axisymmetric model in Figure 1.5 (c) is often used for concentric IDE designs with a geometry that is symmetric around a central axis. Due to this boundary setup, the 2D axisymmetric model does not capture transport in the angular direction around the central axis. The P2D model in Figure 1.5 (c) solves for Li-ion transport in the electrode thickness direction as

a 1D model and calculates the solid-phase Li-ion concentration in the particle radius direction based on Fick's second law of diffusion. The P2D model works well for planar electrode geometries, but due to its simplified view of electrode transport, this model does not enable multi-dimensional transport investigation for 3D LIBs, which is critical for modeling the impact of micrometer-scale 3D electrode geometry on Li-ion transport within the cell.

For higher resolution modeling, electrochemical equations can be solved in 3D on a particle-resolved scale with DNS in Figure 1.5 (a) or on the continuum scale with porous electrode theory using the volume-average formulation in Figure 1.5 (b). Fully-resolved 3D DNS models capture the spatial heterogeneity in 3D LIBs by finely discretizing the electrode microstructures at the solid-liquid interfaces. In DNS, mesh elements are smaller than the active material particles and pores as shown in Figure 1.5 (e). Each element is assumed to be filled with non-porous solid active material, binder, or electrolyte. The scale of this model allows for direct construction of microstructural morphology in a porous electrode and is capable of solving concentration gradients in the particles. Therefore, DNS is often used to analyze the effect of particle morphology and the microstructural tortuosity on transport properties.[73–76] However, using discretization smaller than the electrode active material particles is computationally expensive for modeling 3D LIBs.

To balance solution accuracy and computational efficiency, volume-average 3D models shown in Figure 1.5 (b) were created by researchers.[70,71] Volume-average 3D models discretize the battery cell on the scale of the electrode feature sizes as illustrated in Figure 1.5 (f), and they account for the proportion of solid and liquid phases in each discretization to approximate porosity and electrode spatial variation. The liquid and solid phases in the electrode are treated as superimposed continua in each mesh element, which is called the representative volume element (RVE) in the volume-average approach.[77,78] The RVEs are larger than the primary particles and

smaller than the electrode geometry features. Physical quantities such as concentration, potential, and current as well as their gradients are averaged over the RVE.[79,80]

This dissertation utilizes the *VIBE-AMPERES* software developed by Allu et al. to generate 3D volume-averaged models for 3D LIBs.[70,81] These models solve the 3D spatial gradients of current density, potentials, and concentrations at a resolution that effectively reflects the impact of micron-scale electrode architectures. According to the Allu et al.,[70] volume averages of the physical quantity ψ , represented by $< \psi >$, is calculated by the volume integral of the quantity scaled by a weight function $g(r)$, as expressed in Equation 1.13. By definition, the weight function must satisfy Equation 1.14 and monotonically decreases with increasing parameter *r*, where *r* is the radius of the RVE, such that the volume of the RVE is normalized across the model.

$$< \psi >= \int_V \psi g(r) dV \quad (1.13)$$

$$4\pi \int_0^\infty g(r) r^2 dr = 1 \quad (1.14)$$

Additionally, the transient and spatial gradient volume averages, assuming there is no convection within the cell, are defined in Equations 1.15 and 1.16.

$$< \frac{\partial \psi}{\partial t} >= \epsilon \frac{\partial < \psi >}{\partial t} \quad (1.15)$$

$$< \nabla \psi >= \epsilon \nabla < \psi > \quad (1.16)$$

In *VIBE-AMPERES*, the models for intercalation kinetics, conductions, and liquid-phase diffusion in Equations 1.1 – 1.7 are re-formulated and presented as Equations 1.17 – 1.22. In addition, the same Bruggeman relationship from Equation 1.12 is reused in *VIBE-AMPERES* to

capture transport tortuosity and effective transport properties. Equations 1.17 – 1.19 below represent the volume-average form of the intercalation kinetics from Equation 1.1 – 1.4. It is worth noting that the general equation structures remain the same between Equations 1.1 – 1.7 and Equations 1.17 – 1.22, except that the Li-ion flux, concentrations, and potentials are in 3D volume-average forms.

$$\frac{<j^{Li}>}{a_s} = i_o(\exp\left(\frac{\alpha_a F}{RT}\eta\right) - \exp\left(-\frac{\alpha_c F}{RT}\eta\right)) \quad (1.17)$$

$$i_o = k(< c_e >)^{\alpha_a}(c_{s,max} - c_s)^{\alpha_a}(c_s)^{\alpha_c} \quad (1.18)$$

$$\eta =< \varphi_s > -< \varphi_e > -U_{ocp} - \frac{<j^{Li}>}{a} R_{film} \quad (1.19)$$

Similarly, the electron and Li-ion conduction expressions from Equations 1.5 and 1.6, as well as the Li-ion diffusion model in Equation 1.7 become Equations 1.20 – 1.22. Notably, the gradients and divergences in these equations are now computed in the 3D Cartesian coordinate system.

$$\nabla \cdot (\varepsilon_e \kappa^{eff} \nabla < \varphi_e >) + \nabla \cdot \left(\varepsilon_e \frac{2RT(t_+^0 - 1)}{F} \kappa^{eff} \nabla < \ln c_e >\right) = - < j^{Li} > \quad (1.20)$$

$$\nabla \cdot (\varepsilon_s \sigma^{eff} \nabla < \varphi_s >) =< j^{Li} > \quad (1.21)$$

$$\frac{\partial(\varepsilon_e < c_e >)}{\partial t} - \nabla \cdot \left(\varepsilon_e D_e^{eff} \nabla < c_e >\right) = \frac{1 - t_+^0}{F} < j^{Li} > \quad (1.22)$$

Under the 3D volume-average formulation, the solid-phase concentration diffusion model in Equations 1.8 – 1.10, which are solved on the scale of electrode active material particles, are

replaced with Equations 1.23 – 1.24. Equation 1.24 correlates the volume-averaged solid-phase concentration at the particle surface, $< c_{s,avg} >$, to the solid-phase Li-ion concentration in the center of the particle, c_s, which is used then used in Equation 1.18 to more accurately capture the concentration-dependent reaction kinetics.

$$\frac{\partial(\varepsilon_s < c_{s,avg} >)}{\partial t} - \nabla \cdot \left(\varepsilon_s D_s^{eff} \nabla < c_{s,avg} >\right) = \frac{-< j^{Li} >}{F} \quad (1.23)$$

$$c_s = < c_{s,avg} > + \frac{< j^{Li} > R_s}{5 a_s F D_s} \quad (1.24)$$

1.3 Research Objectives and Dissertation Organization

Designing a 3D LIB to exceed conventional battery performance metrics such as capacity, energy density, and power density poses significant challenges. Achieving optimal 3D structures in each LIB material system requires a comprehensive understanding of how each 3D design fundamentally alters Li-ion transport and kinetics, creating a need for LIB design evaluation metrics and parameters. This dissertation investigates 3D LIBs through the lens of computational design and analysis. The research findings in this dissertation will systematically guide scientists and engineers on 3D LIB design. The scope of the research is framed by the following key questions:

Research Question 1a. What are the critical design parameters for 3D LIBs that impact the electrochemical performance of single-layer cells and multi-layer stacks?

Research Question 1b. How do IDE designs fundamentally improve transport and kinetic mechanisms at the single-layer cell level, and how does the material system impact IDE performance?

Research Question 1c. How do SE designs fundamentally improve transport and kinetic mechanisms at the single-layer cell level, and how does the material system impact SE performance?

Research Question 2a. How to quantify and evaluate the impact of current density non-uniformity on battery capacity in IDE designs?

Research Question 2b. How can SEs be designed to reduce and control the locations of lithium plating in a LIB cell?

1.3.1 *Dissertation Organization*

This dissertation is structured to address the research questions introduced in section 1.3 above. Chapter 2 addresses Research Question 1a through an empirical analysis of historical 3D LIB data, identifying performance patterns based on cell parameters across the existing 3D LIB design landscape. Published 3D LIB performance data from literature is systematically reviewed and quantitatively analyzed using an established empirical model.[82] This chapter uncovers trends in geometric design parameters and cell performance, providing a comprehensive overview and highlighting the distinct features of each 3D electrode category analyzed.

Chapter 3 focuses on Research Question 1a, 1b, and 2a by modeling four different 3D IDE architectures using a physics-based, 3D volume-averaged electrochemical model in *VIBE-AMPERES*. Two material systems, $Li_4Ti_5O_{12}|LiFePO_4$ and graphite$|LiNi_{0.5}Mn_{0.3}Co_{0.2}O_2$, are included to evaluate the impact of material selection. This comparative analysis examines the

effects of IDE architecture and materials on specific capacity, lithiation profile, energy density, and power density. Transport and kinetic behaviors in the cells are further analyzed through 3D Li-ion concentration plots. A mathematical expression is developed to quantify non-uniformities 3D LIBs, creating a uniformity index that correlates with performance metrics such as capacity and utilization.

In Chapter 4, a design analysis of 3D SE is performed to address Research Question 1a and 1c. This chapter investigates how SE cathodes can enhance discharge rate capability in ultra-thick electrodes (>100 μm), evaluated in terms of gravimetric and volumetric energy density (Wh/kg, Wh/L). A graphite|$LiNi_{0.6}Mn_{0.2}Co_{0.2}O_2$ material system is used for modeling. Parametrically designed SEs are modeled with a range of electrolyte volume fractions (EVFs) in the electrode while holding active material mass loading constant. The analysis compares SE design with two geometry patterns, a grid and a line as defined in Figure 1.4, against planar electrodes. Planar electrodes with two layers of porosity are also modeled to compare the effects of porosity grading versus electrode structuring in battery performance. This chapter assesses the impact of EVF as a 3D LIB design parameter and examines the impact of additional electrolyte volume and reduced transport tortuosity on battery rate capability in single-layer cells. A pouch cell analysis is also conducted to understand how single-layer cell capacity improvements translate to multi-layer cell energy density by considering the weight of all cell components.

Chapter 5 continues the investigation of Research Question 1a and 1c and focuses on a line pattern SE. A holistic design analysis that considers the charge and discharge performance of graphite| $LiNi_{0.6}Mn_{0.2}Co_{0.2}O_2$ SE cathodes paired with planar anodes, SE anodes paired with planar cathodes, and full cells with structuring in both electrodes is conducted. In contrast to Chapter 4, which investigates ultra-thick cathodes >100 μm, this chapter models full cells with electrode

thicknesses between 50 – 90 μm. SEs with a line geometry pattern are modeled. The effects of structuring the anode versus the cathode on charge and discharge capacity and Li-ion transport within a single-layer cell are examined. The chapter also explores how SEs influences overall mass density as well as volumetric and gravimetric active material mass loading in a multi-layer cell stack. Metrics including the discharge energy density (Wh/kg and Wh/L) and charge capacity (Ah/kg and Ah/L) per stack weight and volume were utilized to evaluate the advantages of structuring either or both electrodes in cell stacks. Additionally, the impact of the spatial alignment of SE line geometries in full cells with both electrodes structured on Li-ion concentration non-uniformity and cell capacity is analyzed.

Chapter 6 addresses Research Question 2b by developing a new 3D volume-averaged lithium plating model within the *VIBE-AMPERES* framework to analyze lithium deposition in 3D SEs. Simulations explore how electrode spatial heterogeneity caused by difference SE configurations affects lithium plating behavior in comparison to conventional planar cells. This study identifies the onset and locations of lithium plating and investigates the potential causes behind these effects through the lens of a computational model.

Chapter 2. 3D BATTERY DESIGN LANDSCAPE: EMPIRICAL ANALYSIS USING HISTORICAL DATA

*The content in Chapter 2 has been published in *ACS Energy Letters* and modified for this dissertation.[2] Reprinted and adapted with permission from Hung, C.-H.; Huynh, P.; Teo, K.; Cobb, C. L. "Are Three-Dimensional Batteries Beneficial? Analyzing Historical Data to Elucidate Performance Advantages." *ACS Energy Lett.* **2022**, 296–305. Copyright 2023 American Chemical Society. Master's student coauthors Phong Huynh and Katrina Teo collected and extracted all 3D LIB data. Phong Huynh created the plotting component of the curve-fitting Python code and made computer-aided design (CAD) images shown in Figure 2.1.

Chapter 2 motivates Research Question 1a from section 1.1.2. To understand the current design landscape of 3D LIBs to serve as a reference point for this dissertation, an explorative data analysis study was conducted using experimental 3D LIB cases published in the 2007 – 2020 timeframe. Due to the wealth of experimental research conducted so far, we have come to a point where it is possible to characterize and compare multiple 3D LIB designs using a quantitative approach based on historical data. In this chapter, 3D LIB cases were extracted from literature along with their geometric design parameters including electrode thickness, electrode surface area, and cell footprint area. The extracted 3D LIBs were then categorized based on their 3D electrode architectures. Using a previously developed empirical model,[82] we obtained parameters that quantify the rate capability performance and rate-limiting transport or kinetic mechanisms of 3D LIBs. The impact of electrode thickness, surface area, and architecture on the rate capacity and rate-limiting mechanism was analyzed. Finally, a discussion on the applicability of 3D LIBs at different application scales based on the cell footprint area was included.

2.1 METHODS

2.1.1 *3D LIB Taxonomy Deduced from Historical 3D LIBs*

To facilitate the data analysis, 3D LIB data were extracted from experimental publications. A taxonomy structure was defined in Figure 2.1. For each 3D LIB category, two images are shown for illustration purposes in Figure 2.1: (1) the battery cell fully assembled and (2) an exploded view where the battery cell is separated for a clearer view of the individual components, wherein the cathode is blue, the anode is red, the separator is yellow, and regions filled with only liquid, gel, or solid-state electrolyte are green. The current collector is emphasized with a black dashed outline, and the electrode thickness (L) is marked in pink.

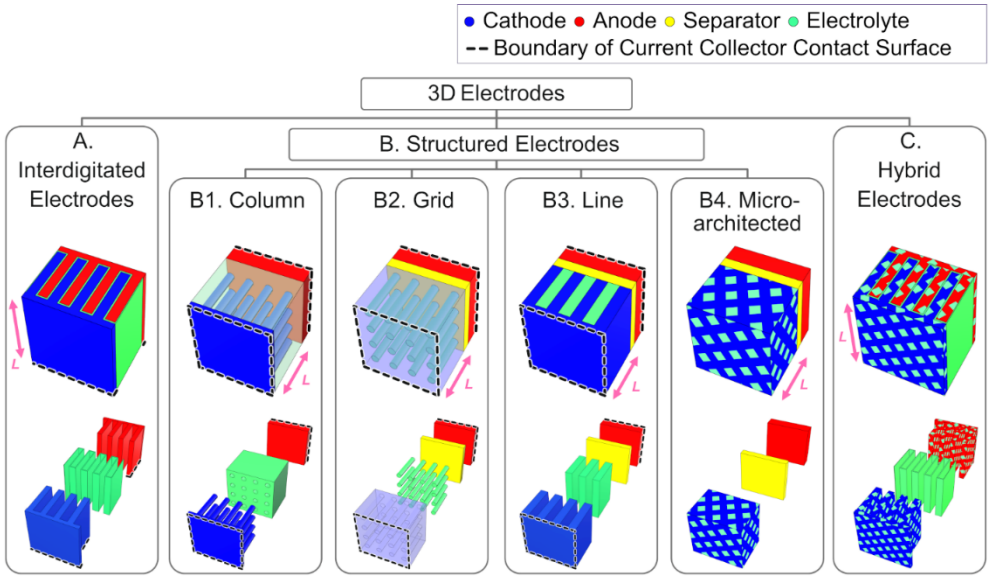

Figure 2.1. Taxonomy for 3D LIBs separated into three primary categories based on electrode design. Category A (Interdigitated Electrodes) has an interwoven cathode and anode. Category B (Structured Electrodes) has individually structured and non-interwoven electrodes and can be further divided into four subcategories based on the electrode geometry. Category C (Hybrid Electrodes) is a design that combines facets of Category A and Category B, wherein the electrodes are both interwoven and structured.

Three core categories of 3D LIBs (Categories A, B, and C) are shown in Figure 2.1. Category A represents 'Interdigitated Electrodes', and these 3D LIBs enable more efficient Li-ion transport by interweaving the cathode and the anode to shorten Li-ion and electron transport distances across the electrode thickness. These designs consist of alternating plates of cathode and anode material, commonly referred to as 'electrode fingers.' During fabrication, the region between the electrode fingers is left as void space and filled with liquid or polymer-based electrolyte.[22,83,46] It is important to note that for all categories in Figure 2.1, the red and blue electrode regions can have randomized porosity infiltrated with additional electrolyte, while the electrolyte regions (emphasized in green Figure 2.1) consist of pure electrolyte regions where no active material is present.

Category B denotes 'Structured Electrodes' and has controlled macro-pores inserted into the electrode for electrolyte to infiltrate and serve as additional transport 'highways' for Li-ions. In Category B, the 3D architecture is confined to the anode or cathode electrode, and unlike Category A (Interdigitated Electrodes), the anode and cathode are not interwoven with each other.[23,84,60,65,85–87,61,88] For illustration purposes, Figure 2.1 only shows 3D architecture in the cathode for Category B and its associated subcategories. Category B (Structured Electrodes) can be further broken down into four subcategories based on how electrode material is structured with electrolyte. The 'Column' design (Subcategory B1) has arrays of standing electrode pillars in its cathode,[23] while in the 'Grid' design (Subcategory B2), pillars of electrode material are removed and replaced with electrolyte.[60,65,84–86] The 'Line' design (Subcategory B3) has an electrode structure similar to the cathode of Category A (Interdigitated Electrode), but the void space between the cathode electrode fingers is filled with electrolyte instead of being interwoven with

the anode electrode fingers.[61,87] Subcategory B4, called 'Micro-architected,' has an ordered lattice-like electrode architecture with open volume that is flooded with electrolyte.[88]

Category C (Hybrid Electrodes) has micron-scale interdigitated electrode fingers like Category A (Interdigitated Electrodes) with additional porosity control via defined pore channels that are 330 – 500 nm wide in the electrodes.[89,42,41] Conceptually, Category C represents a hybrid approach of Categories A and B, since the ordered porosity in Category C resembles the transport 'highway' topology in Subcategory B4. However, this porosity is controlled at a much smaller length scale. Unlike Category C (Hybrid Electrodes), Category A (Interdigitated Electrodes) and Category B (Structured Electrodes) have randomized porosity that is dependent on the material and fabrication process.

Table 2.1 summarizes the specific 3D LIB cases extracted from literature, including their associated 3D LIB category from Figure 2.1, active electrode materials, separator type (if used and reported), and electrolyte composition. The cases identified in Table 2.1 must have sufficient battery and electrochemical information available to enable the data analysis procedure detailed section 2.2.2. Thus, it is important to acknowledge that the cases in Table 2.1 represent a selected list of 3D LIBs that have been fabricated from 2007 to 2020.

Table 2.1. 3D LIB cases analyzed in this chapter. Thirty-four 3D LIB cases were extracted from a total of fifteen experimental publications.[22,23,41,42,46,60,61,65,83–89] Each case is a unique 3D LIB design and is assigned a case number in the format of the category defined in Figure 2.1 followed by a numerical case number. For example, A:1 indicates the first case extracted from a publication and assigned to Category A. Each row in Table 2.1 groups cases by their unique publication source. A case-by-case table summarizing the materials and geometric properties can be found in Appendix A.

Case	# Of cases	Category	Cathode	Anode	Separator	Electrolyte	Reference
A:1	1	A	$LiFePO_4$	$Li_4Ti_5O_{12}$	Liquid electrolyte	1M $LiClO_4$ in 1v:1v EC:DMC	Sun et al.[22]
A:2	1	A	$LiCoO_2$	$Li_4Ti_5O_{12}$	PMMA gel electrolyte	1M $LiClO_4$ in 1v:1v EC:DEC	Yoshima et al.[83]
A:3	1	A	$LiMn_2O_4$	$Li_4Ti_5O_{12}$	PMMA gel electrolyte	1M $LiClO_4$ in 1v:1v EC:DEC	Dokko et al.[46]
B1:1	1	B1	$LiFePO_4$	Lithium Metal	Solid-state electrolyte	0.5M LiTFSI [BMIM] TFSI (ionogel)[90]	Ashby et al.[23]
B2:1 – B2:3	3	B2	$LiCoO_2$	Lithium Metal	Polypropylene films (two layers of Celgard 2500)	1.3M $LiPF_6$ in a blend of alkyl carbonates	Bae et al.[84]
B2:4[a]	1	B2	NMC111[b]	Graphite	Glass fiber film (Type 691, VWR)	1 M $LiPF_6$ in 3:7 EC:EMC (2% VC)	Habedank et al.[60]
B2:5[a] – B2:8[a]	4	B2	NMC111[b]	Graphite	Glass fiber film (Type 691, VWR)	1 M $LiPF_6$ in 3w:7w EC:EMC	Kraft et al.[65]
B2:9 – B2:10	2	B2	$LiCoO_2$	Lithium Metal	Polypropylene film (Celgard 2340)	1 M $LiPF_6$ in 1w:1w:1w EC:DMC:EMC	Lu et al.[85]
B2:11– B2:16	6	B2	$LiCoO_2$	Lithium Metal	Polypropylene film (two layers of Celgard 305)	1.3 M $LiPF_6$ in EC:DMC	Sander et al.[86]
B3:1	1	B3	$Li_4Ti_5O_{12}$	Lithium Metal	Polypropylene film (manufacturer not reported)	1 M $LiPF_6$ in 1v:1v EC:EMC	Izumi et al.[87]
B3:2 – B3:4	3	B3	$Li_4Ti_5O_{12}$	Lithium Metal	Film, material not reported	1M $LiPF_6$ in 1v:1v EC:DEC	Liu et al.[61]
B4:1 – B4:4	4	B4	Silver	Lithium Metal	PP/PE/PP film (Celgard, part number not reported)	1M $LiPF_6$ in 1:1:3 EC:PC:EMC	Saleh et al.[88]
C:1	1	C	$LiMnO_2$	NiSn	Liquid electrolyte	1M $LiClO_4$ in 1:1 EC:DMC	Pikul et al.[89]
C:2	1	C	$LiMnO_2$	NiSn	Liquid electrolyte	1M $LiClO_4$ in 1w:1w EC:DMC	Ning et al.[42]
C:3 – C:6	4	C	$LiMnO_2$	NiSn	Liquid electrolyte	1M $LiClO_4$ in 1:1 EC:DMC	Pikul et al.[41]

[a] 3D LIBs in Category B with 3D architecture in the anode rather than the cathode.
[b] For brevity, NMC111 is used for $LiNi_{0.33}Mn_{0.33}Co_{0.33}O_2$.

To further clarify the information presented in Table 2.1 and Figure 2.1, Figure 2.2 includes an example experimental image from literature for each category defined in Figure 2.1. We can see an example of Category A (Interdigitated Electrodes) in Figure 2.2 (a), which was created with 3D printing technology to generate electrode finger widths around 60 µm. Anodes and cathodes structured in the shapes of columns, grid, lines, and lattices, representing Subcategories B1 – B4, are shown in Figure 2.2 (b) – (e). These electrodes were manufactured via silicon mold infiltration in Figure 2.2 (b), laser structuring in Figure 2.2 (c), and 3D printing in Figure 2.2 (d) and Figure 2.2 (e), demonstrating electrolyte 'highways' that are 30 – 500 µm wide. Figure 2.2 (f) shows the interdigitated cathodes and anodes for Category C, along with their ordered porosity and features down to ~0.5 µm in the inset images. The 3D LIB in Figure 2.2 (f) is made by electrodepositing active materials onto 3D nickel current collectors.

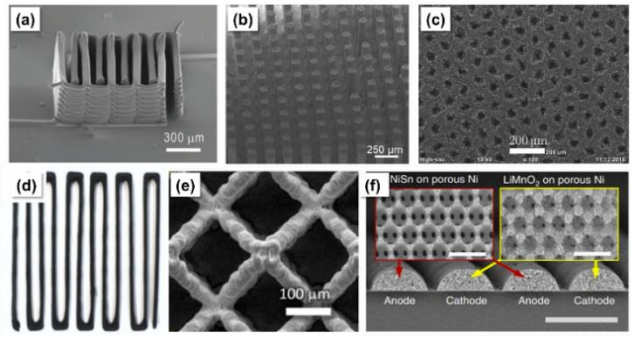

Figure 2.2. Example 3D LIB experimental images for each category in Figure 2.1. (a) Category A (Interdigitated Electrodes); reprinted with permission from ref [22]. © Copyright 2013 John Wiley and Sons. (b) Subcategory B1 (Column); reprinted with permission from ref [23]. © Copyright 2020 American Chemical Society. (c) Subcategory B2 (Grid); reprinted with permission from ref [65] under CC BY 4.0 (https://creativecommons.org/ licenses/by/4.0/). © Copyright 2019 Kraft et al. (d) Subcategory B3 (Line), where the average printed electrode finger width is 500 µm; reprinted with permission from ref [61], © Copyright 2019 Elsevier. (e) Subcategory B4 (Micro-architected); reprinted with permission from ref [88], © Copyright 2018 Elsevier. (f) Category C (Hybrid), where the scale bars are 50 µm in the main image and 1µm in the insets; reprinted with permission from ref [89], © Copyright 2013 Springer Nature.

2.1.2 *Empirical Model for Capacity-Rate Analysis*

Rate capability is a battery's ability to maintain its nominal capacity with increasing rates of charging and discharging, commonly referred to as the C-rate.[91] Battery engineers often evaluate a LIB's effectiveness in Li-ion and electron transport through the electrode thickness based on its rate capability. As the C-rate increases, LIBs inevitably lose capacity due to Li-ion concentration and ohmic polarization (see black markers in Figure 2.3). Therefore, rate capability can be gauged by how soon a LIB loses its capacity to increasing C-rates on a capacity-rate plot, where battery capacity (mAh, mAh/g_{active}, mAh/cm^2, or mAh/cm^3) is on the y-axis and C-rate (1/hour) is on the x-axis.

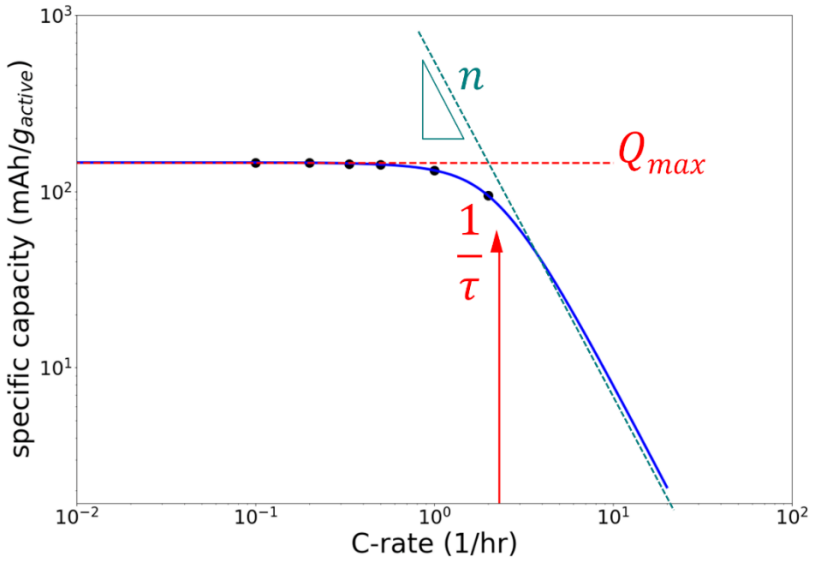

Figure 2.3. An example of a generalized capacity-rate plot where black markers represent data that may be extracted from literature by *WebPlotDigitizer*.[92] The blue curve shows the result of the curve fitting process, and the fitting parameters Q_{max}, τ, and n are annotated on the curve.

Conventional LIBs possess a trade-off between rate capability (better for thin electrodes) and capacity (better for thick electrodes) at the cell level due to the planar formfactor of their electrodes. Similar to the energy and power trade-off discussed in Chapter 1, conventional planar LIBs achieve higher capacity (mAh or mAh/cm^2) by increasing the electrode thickness to add more active material mass (g_{active}) to the cell. Nonetheless, thick electrodes also elongate Li-ion and electron transport pathways, which leads to underutilization of the active material at high C-rates and poor rate capability.

An empirical model previously developed by Tian et al.[82], displayed in Equation 2.1(2.1), is used to quantify the properties of capacity-rate plots for analyzing 3D LIB rate capability. Tian et al.'s approach was chosen for this analysis because it is applicable to electrodes spanning multiple compositions and material chemistries and provides a wholistic view. Following their approach, Equation 2.1 was fit to the extracted 3D LIB capacity-rate data from literature via a least-square regression method. The fitting method returns a best-fit curve, where the sum of squares for the deviation between the experimental data and the curve is minimized. This best-fit curve is defined by Equation 2.1, where any combination of fitting parameters Q_{max}, τ, and n returns a unique curve. An example of the best-fit curve is illustrated in blue in Figure 2.3.

$$Q = Q_{max}[1 - (R\tau)^n\left(1 - e^{-(R\tau)^{-n}}\right)] \quad (2.1)$$

In Equation 2.1, capacity and C-rate (denoted as Q and R, respectively) are input experimental data, while Q_{max}, n, and τ are output fitting parameters. Q_{max} represents the maximum reversible capacity of a LIB and matches the units of Q (mAh, mAh/g_{active}, mAh/cm^2, or mAh/cm^3), which is determined by the material chemistry and electrode active material loading. Exponent n regulates how quickly a LIB loses its capacity once it enters the high-rate regime (typically ≥ 1C).

In previous studies, it has been asserted that exponent n can be used to indicate the dominant rate-limiting transport mechanism in supercapacitors and planar batteries.[82,93,94] Characteristic time (τ) is in units of seconds, and it represents minimum time needed to charge or discharge a LIB to its full capacity, where smaller characteristic time values mean better rate capability. Planar LIBs have characteristic time (τ) values in the range of $5 - 10^4$ seconds as previously calculated by Tian et al.[82]

2.1.3 *Curve-Fitting Method Setup*

The curve-fitting results and output fitting parameters for all cases are shown in Appendix A. To find the best-fit curve, a trust region reflective optimization algorithm was used to minimize the sum of squares between blue model curve and the experimental data points.[95] Constrained by the nature of this curve-fitting approach, extracted cases from literature must have capacity-rate data with four or more data points at different C-rates. The 3D LIBs considered in this analysis had C-rates ranging from C/30 to 1000C. To ensure the data fitted captures both high-power and high-energy performance regimes, 3D LIB cases that are only tested at slow C-rates (< 1C) or cases did not show a capacity drop >10% with respect to their lowest-rate (≤ 1C) capacity were not considered in the analysis.

On a capacity-rate curve, Q_{max} controls the y-axis position as shown by the red dashed line in Figure 2.3. It is worth noting that τ and n are independent of Q_{max} and Q. In other words, Q_{max} only affects the position of the curve and does not control the shape of the curve. As a result, using total capacity (mAh) or a capacity metric that is a function of mass (mAh/g_{active}), area (mAh/cm^2), or volume (mAh/cm^3) for Q_{max} and Q does not impact τ and n. Thus, although the 3D LIB cases examined in this chapter may use different capacity units, this does not affect the conclusions drawn in this comparative analysis.

Fitting parameter Q_{max} generally represents the maximum practical capacity of a battery, which should never exceed the theoretical capacity of the material. Furthermore, Q_{max} must be as large as the maximum capacity value reported in the experimental capacity-rate data extracted from the publications. To ensure a realistic solution for Q_{max} was found in the curve-fitting scheme, an upper-bound and a lower-bound for Q_{max} are defined for each 3D LIB. That is, Q_{max} was upper-bounded by the maximum theoretical capacity reported by the authors or in additional literature[96] and lower-bounded the maximum capacity value reported by the authors in the experimental capacity-rate data for each case. In Appendix A, we report the upper-bound values defined for each 3D LIB case in our analysis and their reference sources. Note that for cases C:3 – C:6 and B2:11 – B2:16, the Q_{max} was left unbounded because their theoretical capacity was not reported by the authors and could not be found in literature. With these cases specifically, it is observed that the curve-fitting result of Q_{max} is not affected by the presence of an upper-bound.

Next, characteristic time (τ) marks the transition C-rate (R) where a capacity-rate curve begins to show a drastic loss in capacity. If 'transition C-rate', $R_{transisiton}$, is defined as the C-rate (R) where some percentage (x) of capacity loss from Q_{max} is observed, then the conversion between τ and $R_{transition}$ can be described by Equation 2.2.[82,94] As an example, the red arrow in Figure 2.3 points to a $R_{transition}$ at 10% capacity loss ($x = 0.1$) based on the characteristic time (τ) found by the least square method. Characteristic time (τ) must be greater than zero to provide meaningful results for the rate capability analysis, and therefore, τ is lower bounded by zero in this analysis.

$$R_{transition} = \frac{(x)^{\frac{1}{n}}}{\tau} \quad (2.2)$$

Finally, exponent n controls the slope of the capacity loss curve at higher rates, which is illustrated by the green triangle in Figure 2.3. When n increases, the best-fit curve becomes steeper at high rates and vice versa. For the purpose of this analysis, n is left unbounded.

2.1.4 *Data Extraction from Literature*

The extraction of capacity-rate data from literature was done in *WebPlotDigitizer,* an opensource software tool designed to reverse-engineer images and plots to numerical data.[92] In addition to capacity-rate data, this analysis also considered the geometric parameters of 3D electrodes, including electrode thickness (L), cell footprint area, electrode surface area (SA), and cathode volume (V). The cell footprint area is the rectangular footprint area that bounds the area occupied by the entire battery cell, with a surface normal vector pointing in the direction of the electrode thickness (L). The electrode surface area (SA) is the sum of the anode and cathode surface area that are directly in contact with the separator or the regions that only contain electrolyte. The cathode volume (V) is the volume of the bounding box that encloses the entire cathode. The cathode volume is used instead of the full 3D LIB cell volume because some papers did not report the anode thickness for their 3D LIBs, particularly those that used Lithium metal anodes. All feature sizes needed to calculate the aforementioned geometric parameters were either extracted from the text or measured from an experimental image in the associated references in Table 2.1.

2.2 Results and Discussion

2.2.1 *3D LIB Rate Capability Compared to Planar LIBs*

In Figure 2.4, the 3D LIBs from Table 2.1 are plotted with electrode thickness (L) on the x-axis and characteristic time (τ) on the y-axis; cases that map to Table 2.1 are labeled accordingly. The black diamond markers represent planar LIB data previously collected and analyzed by Tian et al.[82] and were used to facilitate a general comparison between planar LIBs and 3D LIBs. Planar LIBs have characteristic time (τ) values in the range of 5 – 10^4 seconds,[82] while 3D LIBs in this analysis have τ values ranging from 0.003 – 12 seconds. 3D LIBs share similar τ values across design categories, and there is no clear ranking in rate capability among Categories A – C. These τ values, however, are significantly lower than planar LIBs across all thicknesses, confirming that 3D LIBs, in general, have better rate capability. Although this performance advantage was expected of 3D LIBs based on prior work in the field,[21,97] this analysis provides a more systematic quantification of this benefit across materials and design variants of micron-scale 3D LIBs fabricated to date.

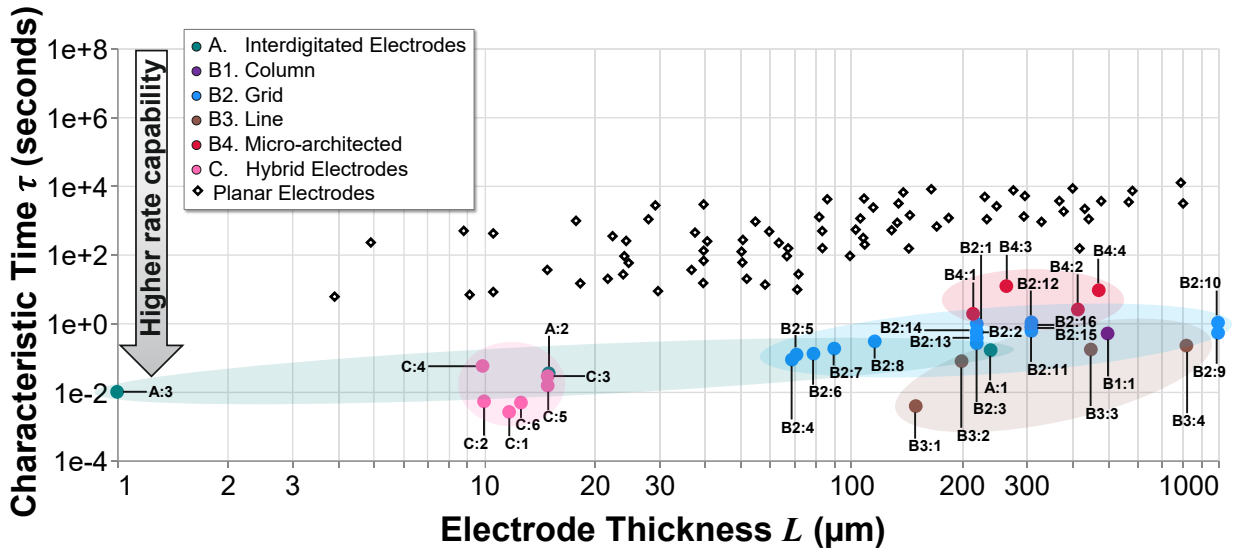

Figure 2.4. Characteristic time (τ) as a function of electrode thickness (marked as L in Figure 2.1) for 3D and planar LIBs. A smaller characteristic time value indicates better rate capability, and the data shows that in general, 3D LIBs outperform planar LIBs.

2.2.2 *Impact of Electrode Thickness on Rate Capability*

In Figure 2.4, both 3D and planar LIBs demonstrate a performance dependency based on electrode thickness (L), where increasing thickness leads to poorer high-rate performance. Thickness dependency is common in planar LIBs, where rate capability decays with increasing electrode thickness at high charge and discharge rates. This decay is attributed to slower Li-ion and electron transport behavior that occurs as distances between the anode and cathode are increased in thicker electrodes.[98–100] Thus, micron-scale 3D LIBs with electrode thicknesses between 1 – 1000 μm are still significantly affected by transport in the thickness direction.

It is observed that Category A (Interdigitated Electrodes) historically has the widest-spread electrode thickness, ranging from 1 – 250 μm. Category B has thicker electrodes from 70 – 1000 μm, indicating Category B have been mostly investigated for high-capacity cells. Category C, on the other hand, are limited to 10 – 20 μm thick. Note that the electrode thickness (L) of 3D LIBs

is defined according to current collector orientation as shown by the pink arrows in Figure 2.1. Category A (Interdigitated Electrodes) and Subcategories B1 – B3 (Column, Grid, and Line) have current collectors that are planar relative to the electrodes. For these 3D LIBs, electrode thickness (L) was the thickness normal to the planar current collectors. Subcategory B4 (Micro-architected) and Category C (Hybrid Electrodes) have 3D current collectors integrated into the electrode volume, but their L is defined by the same high-level definition used for the other categories to help facilitate a consistent analysis.

2.2.3 *Electrode Surface Area*

Another geometric metric used for evaluating 3D LIBs is the surface area (SA) to volume (V) ratio defined as SA/V.[72,88] In physical terms, SA is the apparent electrode surface area in contact with the separator or the regions that only contain electrolyte. SA does not capture the interfacial pore boundaries for porous electrodes infiltrated with electrolyte, regardless of whether the porosity is randomized or controlled. SA is used to quantify the increased reaction phase boundary for the Li-ion insertion process between different 3D LIBs. Trembacki et al. explain that the increased reaction phase boundary is favorable to LIB performance because a larger SA contributes to a smaller current density gradient in the electrode, which facilitates more uniform reactions and in turn higher capacity.[72] Since large SA values can lead to a larger cell foot print area and cell volume by design (and in turn lower power and energy densities), SA was further divided by the cathode volume (V) to normalize the cell size for more consistent comparisons between Categories A-C in this analysis.

In Figure 2.5, characteristic time (τ) is plotted versus SA/V for 3D LIBs. In theory, a higher SA/V value should lead to better rate capability and thus lower characteristic time (τ). However, this trend is not observed in Figure 2.5, and no cross-category relationships can be seen based on

the data presented. Nonetheless, it is observed that 3D LIBs from the same publication exhibit a somewhat linear relationship between *SA/V* and characteristic time (τ) when 3D LIB cases are isolated by publication, as shown by the three 3D LIB groups boxed and shaded in Figure 2.5. These results suggest that *SA/V* may only be useful for local design comparisons when confined to the same 3D LIB architecture with the same material composition and porosity. The limitation of *SA/V* as a comparative metric for 3D LIBs can be partially explained by comparing Category C (Hybrid) to Category A (Interdigitated Electrodes). Both categories have a similar 3D LIB architecture on the micron-scale, which results in similar *SA/V* values. However, *SA/V* by design does not capture the highly ordered sub-micron porosity in Category C (Hybrid); thus *SA/V* does not accurately reflect any performance benefits in this scenario.

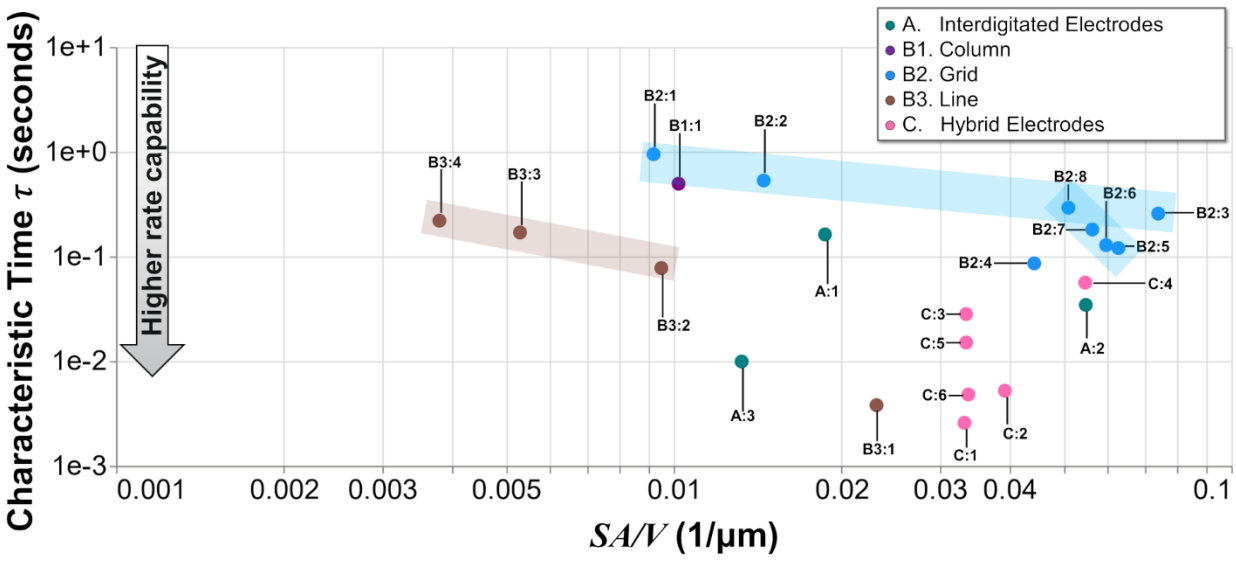

Figure 2.5. Characteristic time (τ) versus *SA/V* for 3D LIBs. Planar cases are not included as their *SA/V* information was not reported by Tian et al.[82] 3D LIB cases B2:9 – B2:16 and B4:1 – B4:4 were not plotted because their *SA/V* values cannot be calculated with the information available in the associated literature.

2.2.4 *Cell footprint Area*

Cell footprint area is defined as the smallest rectangular footprint that contains the entire battery cell, with a surface normal vector pointing in the direction of the electrode thickness (L) as shown in Figure 2.1. Cell footprint area drives the areal and volumetric capacity metrics of 3D LIBs and defines potential end applications. In Table 2.2, the demonstrated footprint area range for each 3D LIB category from Figure 2.1 is summarized and color coded with personal viewpoints on potential manufacturability and application scale. Focusing on large scale applications such as EVs, Subcategories B2 (Grid) and B3 (Line) are the most promising 3D LIBs as they have the largest reduced-to-practice footprint on a cm^2 scale with low characteristic time values of 0.004 – 1 s to facilitate good rate capability. While functional cells have been tested over a cm^2 area, Chen et al.[21] recently demonstrated the ability to scale these types of 3D LIBs to even larger areas with laser patterning techniques.

For 3D LIBs with electrodes thicker than 100 μm in Table 2.2, similar rate capabilities between Categories A and B are observed based on their characteristic time values. However, the thick electrode case in Category A (case A:1)[22] was fabricated with low-voltage materials that have low transport properties. Conversely, most cases in Category B used higher-voltage cathode materials combined with more conductive $LiPF_6$-based liquid electrolytes.[101] Although thick electrode data in Category A is limited, Category A might have the potential to outperform Category B if high-conductivity electrolyte and high-voltage electrode materials are used.[102] It is important to note that the intricate architecture of Category A has been mainly fabricated by micro-scale 3D printing[22] and semiconductor processing.[46] These manufacturing processes are adaptable to microbatteries but are not compatible with the larger meter-scale areas needed for EV-type

applications. Thus, outside of higher capacity material systems, rapid large-area manufacturing techniques and more robust assembly processes for Category A must be concurrently developed.

Taking a closer look at Category B, Subcategory B4 (Micro-architected) stands out from the rest of the subcategories with its high characteristic time (τ) values of 2 – 12 s, which translates to poorer rate performance. Given these high values, Subcategory B4 (Micro-architected) is not recommended for high-power applications. The lower rate capability of Subcategory B4 relative to B1 – B3 is likely a result of the use of high-capacity alloy materials which experience high volume expansion during charge and discharge due to their lack of intercalation sites.[96] However, the layout of Subcategory B4 contains a large amount of volume occupied by electrolyte and current collectors, and this design currently still requires the use high-capacity alloy materials to achieve comparable volumetric and gravimetric energy density relative to other 3D LIBs.

The volume expansion issue in Subcategory B4 is better controlled by Category C (Hybrid Electrodes) through its additional sub-micron ordered porosity control. Category C used alloy materials with 3D current collectors and demonstrates the best rate performance over all 3D LIBs. In particular, cases C:1 – C:6 have been discharged at 200C – 1000C without immediate cell failure,[41,42,89] showing promise for applications that require ultra-high-power rate capability. Category C is recommended for high power microbatteries over μm^2 – mm^2 footprint areas. In comparison, 3D LIBs in Category A, with a μm^2 footprint scale, maintained 63% (case A:2) and 78% (case A:3) of their maximum capacity when discharged at 20C, showing good rate capability although not as strong as Category C.

Despite excellent rate capability at smaller scales, Category C is expected to exhibit no significant benefit over Categories A and B at larger scales given the thickness dependency trend observed Figure 2.4. Based on publicly available research literature, 3D LIBs in Category C have

not yet been fabricated at electrode thicknesses greater than 20 μm, limiting what can currently be concluded about its potential for large-area applications and future manufacturing scale-up. At larger footprint scales, the selection and optimization of designs between Categories A, B and C will be determined by the efficiency and reliability of the manufacturing process required for the end application.

Table 2.2. Summary of demonstrated cell footprint areas and characteristic time (τ) for the 3D LIBs defined in Figure 2.1 based on the data from cases in Table 2.1. Black circles represent cell footprint areas reduced to practice based on the publications shown in Table 2.1. Red and green color coding represents the design recommendations in this study; green indicates high potential for applications at the given area scale, and red indicates limitations to the area scale given the demonstrated footprint area and fabrication process.

	3D LIB Categories					
Cell footprint area scale	**A**	**B1**	**B2**	**B3**	**B4**	**C**
μm^2	•					
mm^2	•	•	•	•	•	•
cm^2			•	•		
m^2						
τ (seconds)	0.01 – 0.03	0.5	0.09 – 1	0.004 – 0.2	2 – 12	0.003 – 0.06

2.2.5 *Rate-limiting Mechanisms*

Moving back to Equation 2.1, the relevance of exponent *n* on 3D LIBs and their rate-limiting mechanisms is explored. Exponent *n* was first developed by Higgins et al.[93] as an indicator for rate-limiting mechanisms in supercapacitors and later used by Tian et al.[82] on planar LIBs. Unlike the original *n* metric that focused on the distinction of diffusion and conduction limitations, a modified *n* value range is proposed for studying the relative divergence between solid-phase diffusion and liquid-phase diffusion in 3D LIBs (see Table 2.3). Based on observations, as *n* approaches 3, 3D LIBs are more limited by solid-phase diffusion because higher *n* values lead to

more rapid capacity loss with increasing C-rates, and it is believed this reflects short transport lengths and time scales in the active material particles. In contrast, a liquid-phase diffusion limitation arises as n goes to 0.5. This limitation arises when a non-uniform Li-ion concentration build up occurs across the separator and electrode thickness, which is orders of magnitude larger than the active material particle size. Additionally, the proposed n range aligns with Tian et al.'s and states a conduction dominant 3D LIB has $n = 1$. The transitional region ($0.5 < n < 3$) in Table 2.3 represents a continuum among all rate-limiting mechanisms, making it difficult to isolate and distinguish the impact of conduction versus diffusion.

Table 2.3. Summary of the n metric developed by Tian et al.[82] and the proposed n range for 3D LIBs to better define the transition between liquid-phase and solid-phase diffusion limitations.

Rate-limiting Mechanism	**From Tian et al.**[82]	**Proposed 3D LIB Range**
Undefined *n* region	$n > 1$ and $n < 0.5$	$n > 3$ and $n < 0.5$
Conduction	$n = 1$	$n = 1$
Diffusion	$n = 0.5$ (no distinction between liquid and solid phases)	$n = 0.5$ (liquid) $n = 3$ (solid)
Transition region	$0.5 < n < 1$	$0.5 < n < 3$

In Figure 2.6, characteristic time (τ) is plotted on the x-axis and exponent n on the y-axis to evaluate diffusion trends. No correlation between rate capability and rate-limiting mechanism is found in Figure 2.6. The majority of Category A (Interdigitated Electrodes) and Category B (Structured Electrodes) exhibit large n values, indicating a dominant solid-phase diffusion mechanism due to significantly improved liquid-phase diffusion over planar LIBs. This trend agrees with the earlier observation – Categories A and B perform well at larger thicknesses and footprint areas relative to the other categories because their rate capability is limited by active material particle size. In contrast, Category C (Hybrid Electrodes) is mainly limited by liquid-

phase diffusion. This means increasing electrode thickness will likely lead to rapid deterioration of rate capability. From a practical design perspective, *n* values can help battery engineers decide which design parameters to adjust for better rate performance. Specifically, 3D LIBs with high *n* values will benefit from a smaller active material particle size or a material with higher bulk diffusivity values,[103] while designs with low *n* values can be improved with additional topology optimization or smaller feature sizes.[69]

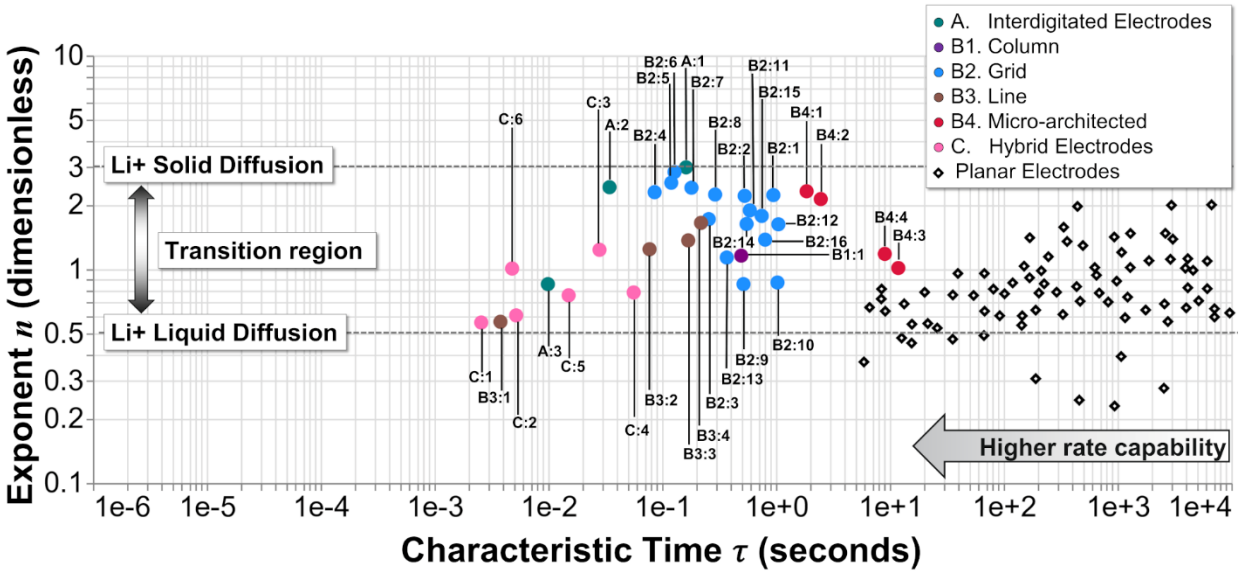

Figure 2.6. Exponent *n* versus characteristic time (τ) for 3D and planar LIBs. The proposed 3D LIB *n* value range from Table 2.3 is annotated to define Li-ion (Li^+) solid-phase and liquid-phase diffusion transition regimes for 3D LIBs.

2.3 CONCLUSIONS

This data analysis demonstrated that 3D LIBs in general have better rate capability than planar LIBs with the same electrode thicknesses. It was found that while 3D LIBs have improved rate capability over planar LIBs, they experience the same thickness dependency observed in planar LIBs, where rate capability decreases with increasing electrode thickness, regardless of the 3D electrode architecture. The results quantitatively showed that the *SA/V* ratio serves as a good rate capability performance indicator when parametrically designing 3D LIBs using fixed materials, porosity, and electrode architecture, reaffirming the heuristic used in literature. However, *SA/V* cannot be used across 3D LIBs made with different materials or electrode architectures. Whether or not *SA/V* is a good performance indicator for 3D LIBs with fixed materials and porosity and varying electrode architectures remains inconclusive.

This study also showed that within the same 3D LIB category, the rate-limiting mechanism can swing between solid-phase diffusion, liquid-phase diffusion, and conduction. This indicates the rate-limiting mechanism is not dominated by the 3D electrode architecture but likely impacted by several other factors including the materials and feature sizes. In theory, the correlation between 3D LIB rate capability and their geometric design parameters will change based on the rate-limiting mechanism of the cell. For example, if a 3D LIB is rate-limited by liquid-phase diffusion, it is more likely to benefit from reducing electrode thickness than from increasing the *SA/V*. The interplay between 3D architecture, materials, electrochemistry, and manufacturing is complex, and more fundamental studies on these interactions are needed to enable a more efficient and integrated design and manufacturing workflow for 3D LIBs.

Lastly, the end application scale was summarized for each 3D LIB category in a cell footprint area analysis. It was found that 3D interdigitated electrodes (Category A) and 3D

structured electrodes (Category B) are equally effective in enabling fast transport in millimeter-scale to meter-scale batteries, with the ‘Line’ and ‘Grid’ designs displaying the most promise for large-scale applications like EVs if associated manufacturing and materials challenges can be addressed. Microbatteries with a size scale below a centimeter and above a millimeter demonstrated good high-rate capability in all 3D LIB categories except for the ‘Micro-architected’ design (Subcategory B4). 3D LIBs using a hybrid approach (Category C), with micrometer-scale interdigitated electrodes and sub-micron ordered porosity, are greatly beneficial for high-power microbatteries down to a micron scale. However, this design scenario has manufacturing limitations that require further investigation at footprint scales larger than 1 cm^2.

Chapter 3. INTERDIGITATED ELECTRODES: MODELING HIGH-RATE SPECIFIC CAPACITY AND NON-UNIFORMITIES

This chapter investigates how IDE architectures and materials influence high-rate discharge performance, addressing Research Questions 1a and 1b from Chapter 1. As noted in section 1.2, prior research has primarily focused on the dimensional optimization of predetermined IDE architectures, leaving unanswered questions around the impact of varying the spatial arrangement of LIB active materials. Physics-based electrochemical models were developed for four 3D IDE designs across two distinct material systems: $Li_4Ti_5O_{12}$ (LTO)|$LiFePO_4$ (LFP) and graphite|$LiNi_{0.5}Mn_{0.3}Co_{0.2}O_2$ (NMC-532). In this study, we modeled four unique IDE architectures with controlled active material loading (mg_{active}/cm^2) and a fixed distance between current collectors. Building on the analysis in section 2.2.3, the relationship between the electrode surface area to cell volume ratio (*SA/V* ratio) and the cell's specific capacity at a high C-rate was evaluated. Furthermore, we investigated the effects of both material system and IDE architecture by comparing the solid-phase Li-ion concentration at both the beginning and the end of the discharge. In response to Research Question 2a, we developed a uniformity index to quantify the non-uniformity of current density within the IDE models. The uniformity index served as a metric to evaluate the non-uniformity of the intercalation reaction caused by different active material spatial arrangements. The correlation between discharge specific capacity and the uniformity index was

analyzed. To further explore current density non-uniformity within an IDE architecture, we visualized the Li-ion transport pathways within the porous electrodes using current density streamlines, plotted using the modeling data generated by *VIBE-AMPERES*.

3.1 METHODS

3.1.1 *3D IDE Architecture and Design Parameterization*

To investigate the impact of 3D electrode architecture and material selection, four 3D IDE LIB designs were modeled as part of a comparative computational analysis. The selected designs and their respective cross-sections are shown in the first and second columns of Figure 3.1. Each IDE design can be modeled as a representative model unit, as shown in the third column of Figure 3.1, by taking advantage of symmetry and repeating geometrical patterns. This reduces the computational runtime of the models and more efficiently screens IDE designs for the purpose of this analysis. In the second column in Figure 3.1, boundaries perpendicular to the isopotential lines are outlined with solid green lines. Isopotential lines in 3D LIBs were first modeled by Hart et al.[104] to represent regions that share the same liquid-phase potential. Since current moves perpendicular to the isopotential lines, Li-ions move along but never across the outlined green boundaries. Thus, these green boundaries are assigned a zero-flux boundary condition, and the models are implemented such that model unit geometry follows these green boundaries. For Design 2, an additional symmetry condition is added and represented by the green dashed line in the second column of Figure 3.1 to further decrease computational runtime. This symmetry condition has been validated previously by a study conducted by Zadin et al.,[55] where a similar interdigitated battery design is modeled. The dimensions of all IDE designs are labeled in the third and fourth column of Figure 3.1, and their values are reported in Table 3.1.

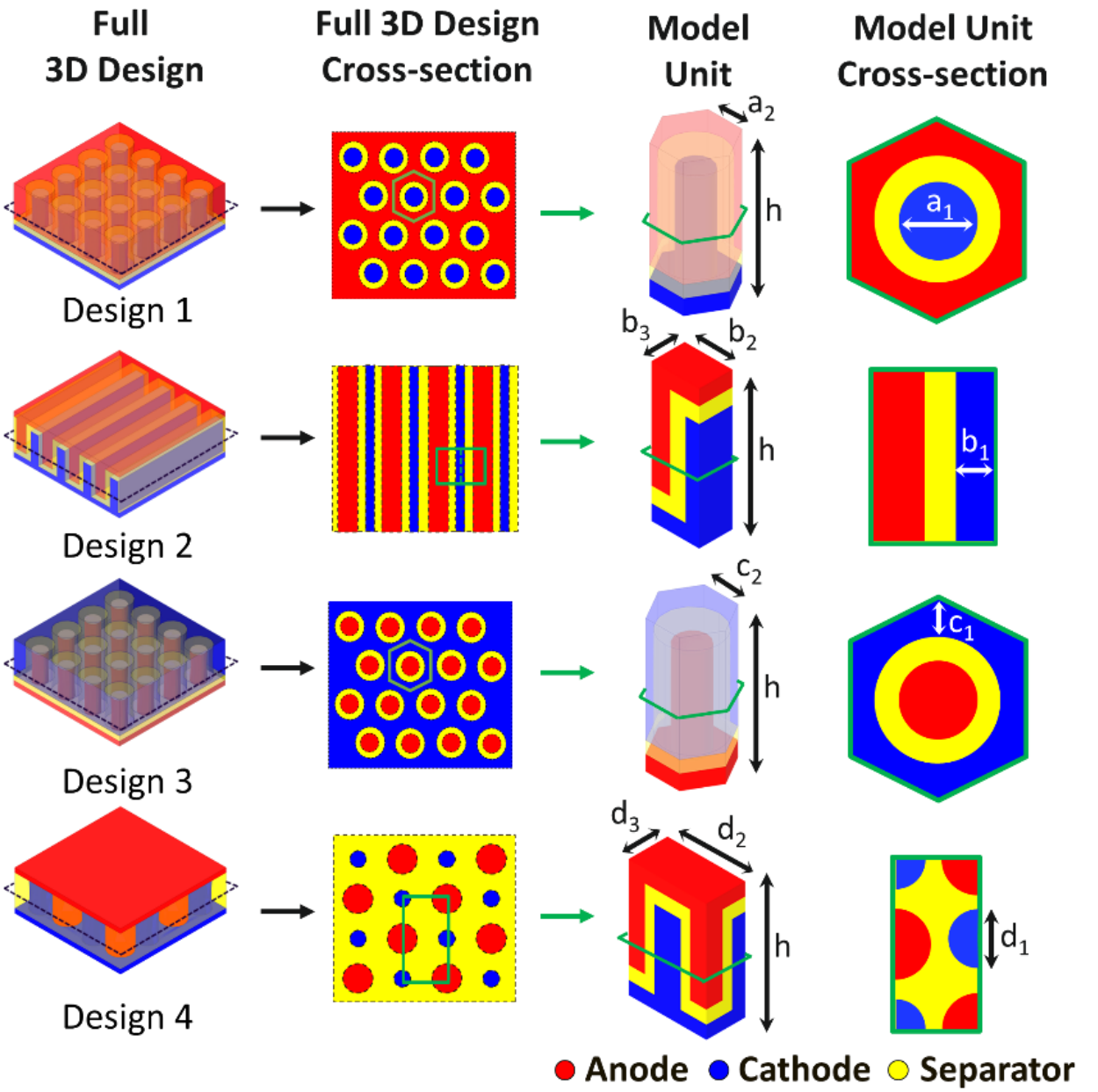

Figure 3.1. Four 3D IDE designs are modeled as shown. The total mass of the cathode electrode is conserved across all designs. The volume varies as needed in each design to ensure the total mass of cathode material is constant.

Design 1 is a concentric column design consisting of multiple arrays of cathode columns coated by a layer of separator. The separator is conformal to the cathode columns, and the remaining space is then filled with anode material. Prior experimental demonstrations of Design 1

have employed 3D current collectors.[44,48] Since manufacturing concentric designs requires the columnar electrodes to serve as the mold for the counter electrode, the fabrication process usually involves silicon micromachining and vacuum infiltration.[23,48,58,105] If 3D columnar current collectors are used as substrates, the deposition thickness of electrode materials can be 40 nm – 300 nm.[44,48] To enable a fair comparison to Designs 2 – 4, a planar current collector design is employed in the analysis for Design 1 to obviate any unfair advantages due to current collector geometry when comparing the impact of electrode architecture across all design cases.

Design 2 is an interdigitated plate design with an alternating cathode and anode plate geometry and is one of the most studied IDE designs using computational modeling.[54–57,70,72,89] Experimental research for fabrication of Design 2 has focused on polymer casting[83] and 3D printing approaches.[22,46,106] Design 3 has the same geometry as Design 1, but the anode and cathode orientations are inverted such that the anode forms the columnar geometry, and the cathode fills in the remaining space. Most recently, Design 3 was fabricated using silicon anode materials with a column diameter of 100 μm, and the cathode region was vacuum-infiltrated with $LiNi_{0.8}Co_{0.15}Al_{0.05}O_2$.[105] Design 3 is included to understand its relative performance to Design 1. Lastly, Design 4 is an interdigitated column design where both electrodes are circular in cross-section, and they are placed in a checkerboard-style arrangement. Design 4 has been fabricated previously by Kotobuki et al. where a $LiCoO_2$ cathode and a $Li_4Mn_5O_{12}$ anode are sol-gel materials molded into a honeycomb spatial arrangement.[107]

Table 3.1. Dimensions for IDE designs shown in Figure 3.1

	LTO|LFP (μm)	Graphite|NMC-532 (μm)
a_1	50	50
a_2	65	63
b_1	22	23
b_2	78	75
b_3	54	54
c_1	11	11
c_2	67	65
d_1	50	50
d_2	148	142
d_3	74	71
h	225	180

3.1.2 *Full Cell Model Constraints and Considerations*

This study investigates the distribution of a fixed amount of electrode mass in space while holding the distance between current collectors fixed and considering practical manufacturing limitations. To explore the impact of electrode design and the overall spatial arrangement of anode, cathode, and separator material, the total cathode mass and associated composition of cathode active material, binder, and carbon black is fixed across all model units. The anode and cathode mass are then matched such that the anode to cathode capacity ratio, referred to as the N/P ratio, is between 1.00 – 1.10. In most Li-ion cells, a N/P ratio of 1.0 – 1.2 is ideal to ensure safety and effective material lithiation.[108] Moreover, to ensure a reasonable mesh quality, dimensional changes of electrode features are restricted to increments of 1 μm for the purposes of achieving a N/P ratio of at least 1.0 or more for each battery design. Due to this approach, there are minor 0.0 – 3.0% fluctuations in active material mass (g_{active}) across the four IDE designs. These small fluctuations in mass are within the allowable error tolerance of the models and allow for fair

comparisons across Designs 1 – 4 for the purposes of examining cell capacity and overall lithiation profile.

In addition to electrode design, the impact of material selection on IDE design is examined. To support this, Designs 1 – 4 are each modeled with the two different material models mentioned previously – LTO|LFP and graphite|NMC-532. LTO|LFP is chosen because it has previously been used to print Design 2.[22] LTO|LFP is a low voltage material system but is often used to prototype IDE s due to its lack of volume expansion and solid-electrolyte interface (SEI) formation.[14109,110] Thus, it is a good initial material system to examine for a relative comparison to IDEs fabricated previously in literature. graphite|NMC-532 is a high voltage material system that is being investigated heavily for EV applications.[108,111–114] graphite|NMC-532 is used as a secondary material case study to help provide additional insight into IDE behavior with the goal of understanding how material selection from a computational standpoint impacts the relative performance of the LIB designs studied.

A minimum electrode feature size of 20 μm is imposed as a manufacturing constraint in this analysis. This constraint is based on a battery 3D printed by Sun et al.,[22] which has an identical electrode architecture to Design 2 in Figure 3.1. This electrode feature size restriction is enforced when matching mass and N/P ratios across the IDE designs to ensure all batteries presented in this study have the potential to be fabricated with 3D printing or similar additive manufacturing techniques. As shown in Figure 3.1, the total height (h) of all 3D IDE designs is kept constant for each material system. LTO|LFP models has fixed h at 225 μm based on previous work[115] since this is the electrode thickness range where a significant capacity degradation begins to occur at high discharge rates.

For the LTO|LFP material model, the diameter of the cathode column, a_1, in Design 1 is set to 50 μm as this is the electrode thickness where LTO|LFP conventional planar cells start to show 20% or greater capacity fade at high discharge rates based on prior experimental results.[22,115] The dimensions for Designs 2 – 4 are adjusted such that the cathode active material mass for the model units is fixed at 1.02 – 1.05 μg_{active}, which corresponds to a volumetric cathode loading of 0.33 – 0.47 g_{active}/cm^3. As mentioned previously, Design 2 has an additional symmetry condition, thus the total mass in the model unit for this design is half of that observed for Designs 1, 3 and 4. This does not affect the consistency of the model predictions based on the boundary and symmetry conditions selected for the model. Similarly, for the graphite|NMC-532 cases, feature a_1 is set to 50 μm and the cell height is 180 μm based on a previous dimensional analysis done by Cobb and Solberg.[10] Using these values results in a cathode active material mass of 1.24 – 1.26 μg_{active} for the model units and a volumetric cathode loading of 0.52 – 0.71 g_{active}/cm^3.

The separator thickness and porosity in the IDE designs are assumed to be the same as a monolayer Celgard 2400 separator for LTO|LFP and a monolayer Celgard 2325 for Graphiate|NMC.[116,117] It is important to acknowledge that existing commercial grade separators cannot be placed in IDEs, and a new separator or polymer electrolyte material formulation must be developed to help facilitate these designs experimentally.[118] However, for the purposes of this computational analysis, the separator properties outlined in Table 3.3 are assumed as a starting point to help facilitate a more fundamental understanding around how the selected IDE design cases perform relative to a conventional planar battery LIB. The separators in Designs 1 – 3 are conformal layers, and their thickness is held constant at 25 μm. For Design 4, the separator thickness is not uniform by the nature of its design, so the average separator thickness around the

cathode is calculated and set to 25 μm. Keeping these parameters in mind, the material selection and dimensions will allow us to properly evaluate the relative performance of Designs 1 – 4.

In addition to the IDEs, planar LIBs for both material systems were modeled and analyzed to give a reference baseline for comparison purposes. As previously discussed in section 1.1.2, conventional planar cells can only be designed for high power (thin electrodes) or high energy (thick electrodes). IDEs enable concurrent high power and high energy performance relative to conventional planar cells. Typical electrode thicknesses reported for high-power applications are around 34 – 57 μm[20,119,120] for LTO|LFP and 23 – 69 μm[108,121] for graphite|NMC-532. Based on this, the LTO|LFP planar reference cell is modeled with a 53 μm thick cathode and 66 μm thick anode, and the graphite|NMC-532 planar reference cell is modeled with a 47 μm thick cathode and a 51 μm thick anode. These high-power planar reference cells have similar loadings to their respective IDE counterparts, enabling us to understand how 3D architecture truly impacts LIB performance at high discharge rates.

The goal of this modeling study is to analyze the impact of 3D electrode spatial arrangement and materials on IDE lithiation profiles and specific capacity. As discussed previously in section 1.2.3, the 3D volume-average battery modeling software *VIBE-AMPERES*[70,81] was used to model the IDEs. The boundary conditions used for the 3D models are shown in Figure 3.2 (a) and Figure 3.2 (b) using Design 2's model unit as an example to illustrate the model's boundary surfaces. The surfaces in contact with the current collectors are assigned as current collector boundary conditions, while all other boundary surfaces are herein referred to as the model unit boundary conditions. The Li-ion flux is assumed zero at both types of boundary conditions as shown in Equations 3.1 and 3.2, where $\vec{n}$ is the normal vector of boundary surfaces. Additionally, the voltage at the anode current collector boundary is kept constant at the plateau voltage of the

anode open circuit potential, U_{ref}. A constant current density, I_{app}, is applied to the cathode current collector boundary to enable a galvanostatic discharge cycle.

$$\vec{n} \cdot \nabla c_s = 0 \quad (3.1)$$

$$\vec{n} \cdot \nabla c_e = 0 \quad (3.2)$$

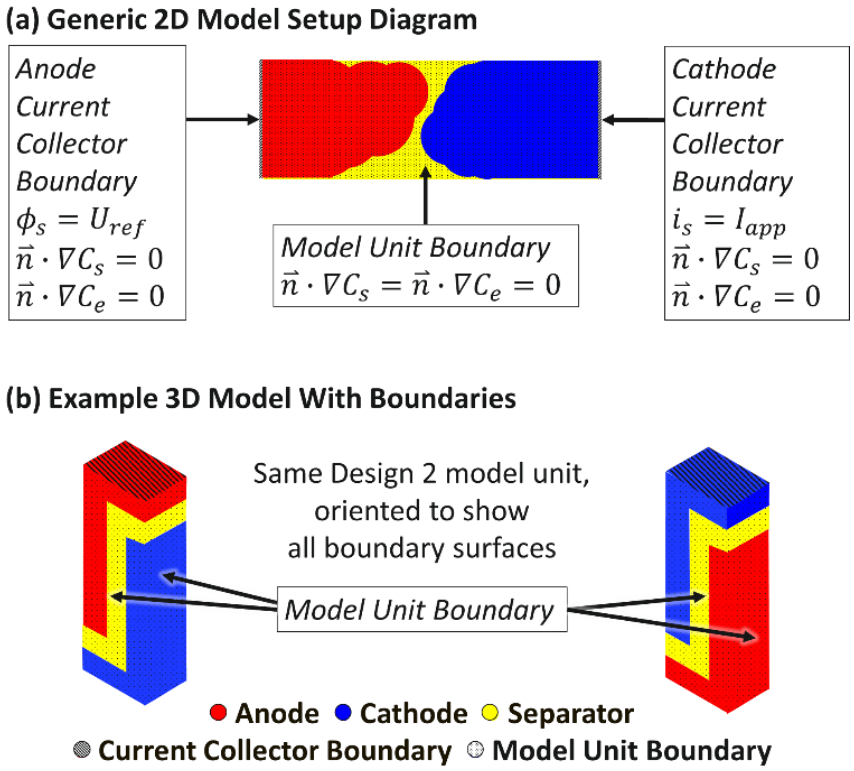

Figure 3.2. Model setup and boundary conditions used in *VIBE-AMPERES*.

3.1.3 *Material Models*

Transport properties for the LTO|LFP and graphite|NMC-532 material models were extracted from literature and validated against published experimental data. The LTO|LFP material model is a lower voltage system with a specific capacity of 150 mAh/g_{active}. The LTO|LFP system follows an 80:12:8 weight ratio composition of active material:carbon:binder based on the work

done by Jaiswal et al.[115] The open-circuit potentials for LTO (U_{LTO}) and LFP (U_{LFP}) at each state of charge, x, are taken from literature[122,123] and shown in Equations 3.3 and 3.4.

$$U_{LFP} = 3.382 + 0.0047x + 1.627e^{-81.163x^{1.0138}} + 7.6445 \times 10^{-8}e^{25.36x^{2.469}} - 8.441 \times 10^{-8}e^{25.262x^{2.478}} \quad (3.3)$$

$$U_{LTO} = 2.73577 - 2.55862x + 0.773926e^{-24.5394x} + (1.15846 - 1.53876x)tanh\big(26.4455(x - 1.00134)\big) \quad (3.4)$$

All other material properties are summarized in Table 3.2 and Table 3.3. As shown in Table 3.3, a 1M $LiPF_6$ in 10:27:63 PC:EC:DMC electrolyte is used based on its prior use in literature for LTO|LFP cells[115] and the availability of its properties for modeling.[124] The concentration-dependent ionic conductivity of the electrolyte is shown in Equation 3.5, where the temperature T is assumed to be fixed at 300K for the purposes of the model.

$$\kappa(c_e, T) = \left(\frac{c_e}{1000}\right)(-10.5 + 0.0740T - 6.96 * 10^{-5}T^2 + 0.668c_e - 0.0178c_eT + 2.8 * 10^{-5}c_eT^2 + 0.494{c_e}^2 - 8.86 * 10^{-4}{c_e}^2T)^2 \quad (3.5)$$

The graphite|NMC-532 material model has a higher capacity due to its larger operating voltage window relative to LTO|LFP. This material system is considered one of the most promising for EVs and has a theoretical specific capacity near 177 mAh/g_{active}.[108,114] Standard weight ratio compositions of 90:5:5 (active:carbon:binder) for the NMC cathode and 92:2:6 (active:carbon:binder) for the graphite anode are employed. 2M $LiPF_6$ in 3:7 EC:EMC[111,112,125,126] electrolyte is used, and its conductivity is defined with Equation 3.6.

$$\kappa(c_e) = \left(\frac{1}{100}\right)(2.184c_e - 1.559{c_e}^2 + 0.3869{c_e}^3 - 0.0333{c_e}^4) \quad (3.6)$$

Because prior research has shown that 3D LIBs demonstrate performance improvements over conventional planar cells at high rates,[10,22,72,89] each material system in this analysis is examined at a discharge rate that typically has a 20% – 50% capacity fade in conventional planar cells. This corresponds to 10C for LTO|LFP and 4C for graphite|NMC-532.[111,115] Based on this information, the applied current for each material system at their respective discharge rate is calculated based on the cathode active material mass which is constrained by the defined N/P ratios, total height, separator thickness, electrode composition and manufacturing constraints. The applied current for the LTO|LFP designs at 10C is 0.002 mA and for the graphite|NMC-532 designs at 4C is 0.001 mA. For the model implementation, the current value is halved for Design 2 because of the additional symmetry boundary condition discussed earlier. Table 3.3 shows the porosity and additional parameters used for each electrode.

Table 3.2. Model parameters for the electrode materials

Parameter	Description	Unit	LFP	NMC-532	LTO	Graphite
D_s	Diffusion coefficient	m^2/s	$8\cdot10^{-18}$ [109]	$3\cdot10^{-15}$ [127]	$3.25\cdot10^{-17}$ [110]	$5\cdot10^{-14}$ [113]
σ	Electric conductivity	S/m	0.591[128]	0.04[127]	1[110]	100
c_s^{max}	Maximum concentration	mol/m^3	20950[109]	49500[113]	22852[110]	30000[113]
c_s^0	Initial concentration	mol/m^3	419[119]	17820[129]	21700[110]	29670[129]
α_a	Anodic transfer coefficient	N/A	0.5[123]	0.5	0.5[110]	0.5
α_c	Cathodic transfer coefficient	N/A	0.5[123]	0.5	0.5[110]	0.5
k	Reaction rate constant	$A\cdot cm^{2.5}/mol^{1.5}$	0.01127[130]	0.23327	0.482[110]	0.4854
t_+^0	Transference number	N/A	0.363	0.462[112]	0.363	0.462[112]
R_{film}	Film resistance	$\Omega\cdot m^2$	0[109]	0.014[112]	0[110]	0.025[112]
ε_e	Volume fraction of liquid	N/A	0.263	0.331	0.383	0.351
ε_s	Volume fraction of solid	N/A	0.500	0.560	0.421	0.521
ε_f	Volume fraction of filler	N/A	0.237	0.108	0.196	0.128
R_s	Particle radius	m	$5\cdot10^{-7}$	$1\cdot10^{-6}$ [114]	$5\cdot10^{-7}$	$2.5\cdot10^{-6}$ [114]
p	Bruggeman constant	N/A	2.7	2.0[113]	2.7	2.7[113]

Table 3.3. Material parameters the electrolyte and separator

Parameter	Description	Unit	LTO|LFP	Graphite|NMC-532
N/A	Electrolyte	*N/A*	1M $LiPF_6$ in 10:27:63 PC:EC:DMC	2M $LiPF_6$ in 3:7 EC:EMC
D_e	Diffusion coefficient	m^2/s	$3 \cdot 10^{-10}$ (124)	$1 \cdot 10^{-10}$ (112)
c_e^0	Initial concentration	mol/m^3	1000 (109)	2000 (125)
t_+^0	Transference number	*N/A*	0.363	0.462(112)
ε_e	Separator volume fraction of liquid	*N/A*	0.41	0.39
ε_s	Separator volume fraction of solid	*N/A*	0.59	0.61
p	Bruggeman constant	*N/A*	2.8(131)	2.0(112)

3.1.4 *Uniformity Index, Model Cross-sections, and Column Shapes*

3D LIBs are heterogeneous by design, and it is critical to better quantify and understand how heterogeneities impact the performance of a 3D LIB. A uniformity index (*UI*) was created in this study to leverage work developed by Grazioli et al.,[56] where a 2D interdigitated battery geometry is modeled using non-porous electrodes to investigate the current density uniformity at the electrode-electrolyte interface. Grazioli et al.'s equation is shown in Equation 3.7, where $\bar{J}$ is the mean current density transferred through the electrode-electrolyte interface, $\bar{S}$ is the area of the electrode-electrolyte interface, and j_{el} is the local current density along the profile of the electrode-electrolyte interface.

$$UI = \frac{\sqrt{\frac{\int_{\bar{S}} j_{el}^2 dS}{\bar{S}} - \bar{J}^2}}{\bar{J}} \quad (3.7)$$

Equation 3.7 captures the variability of current density for an electrode-electrolyte interface in 2D. Due to the nature of IDEs, it is critical to examine and visualize current density variation in

all dimensions to gain better insight into possible designs flaws that may lead to premature failure during battery operation. For the 3D models, Equation 3.8 was used to capture current density at each finite element node across any surface or volume. For a galvanostatic discharge cycle, *VIBE-AMPERES* outputs the local current densities in the electrode regions in Designs 1 – 4 at each model time step. Leveraging this data, the numerator in Equation 3.8 was generalized with the standard deviation of current density across any number of nodes, n, in the mesh to quantify current density variability among any designated group of finite element nodes. Equation 3.8 is the generalized UI_{3D} equation for 3D analysis where j_k is the scalar current density at node k, n is the number of nodes, and $\bar{j}$ is the mean of the current density.

$$UI_{3D} = \frac{\sqrt{\frac{\sum_k (j_k - \bar{j})^2 - \frac{(\sum_k (j_k - \bar{j}))^2}{n}}{n-1}}}{\bar{j}} \quad (3.8)$$

As opposed to Grazioli et al.'s work where the electrodes are non-porous and solid, *VIBE-AMPERES* accounts for electrode porosity, and interfacial current densities are calculated at all finite element nodes in the porous electrode volume. These modeled current densities are negative in the cathode and positive in the anode to represent the direction of the Li-ion intercalation reaction during a discharge cycle. UI_{3D} is calculated in the cathode region during discharge to ensure the opposite signs of the current density in the anode and cathode do not result in negligible magnitude values for UI_{3D}.

Cross-sections A and B in Figure 3.3 are analyzed to examine the impact of current density uniformity across both the length and width of the cathode. Additionally, the rate of change in UI_{3D} with respect to specific capacity (Q), denoted by dUI_{3D}/dQ, is investigated as another metric for evaluating IDEs based on the designs shown in Figure 3.1. As shown in Figure 3.3 (a), cross-

section A is the projection of a horizontal slice in the middle of the IDE model unit, and cross-section B is formed from a vertical slice at the center of the IDE model unit. An additional analysis on the impact of IDE feature geometry was conducted by changing the column shape of Design 1, as shown in Figure 3.3 (b). All models were run on a Linux server with eight Intel(R) Xeon(R) E5-2698 v3 central processing units with up to 32GB RAM and took anywhere from one to thirty hours to complete.

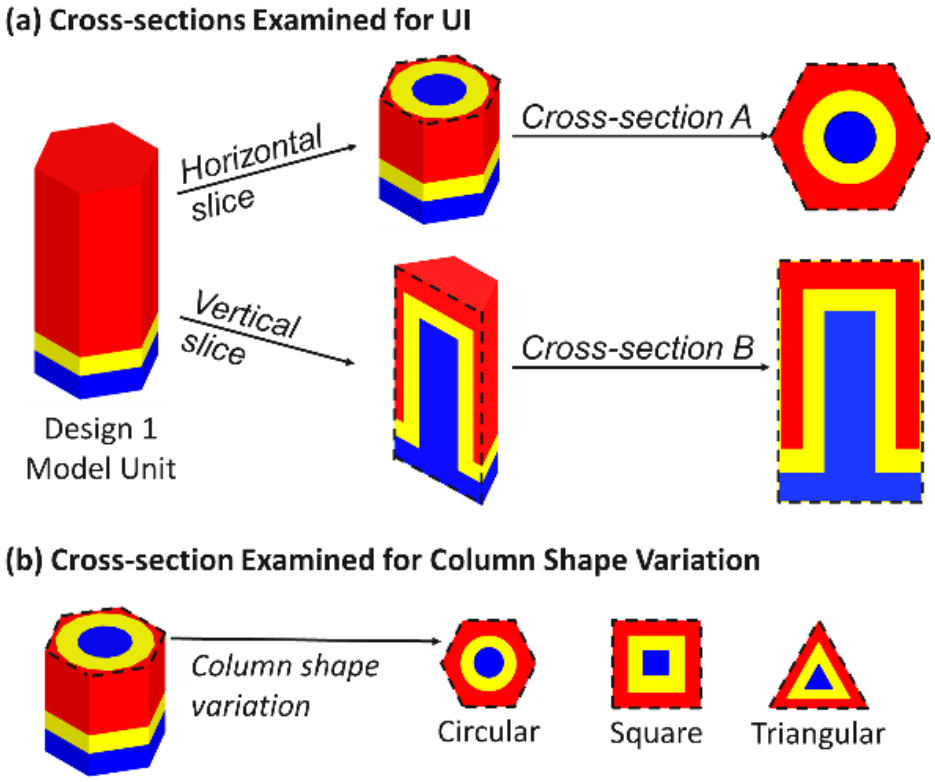

Figure 3.3. Cross-sections examined for current density uniformity and column shape variation.

3.2 Results and Discussion

3.2.1 *Discharge Specific Capacity*

Table 3.4 shows the discharge specific capacity of the IDEs and planar reference cells. For LTO|LFP, the planar reference cell yields a 10C capacity of 45 mAh/g_{active}. LTO|LFP Designs 1 – 4 have a capacity of 96, 63, 109, and 89 mAh/g_{active}, respectively. These values all demonstrate a 113%, 40%, 141%, and 98% improvement relative to the planar reference cell for Designs 1 – 4, respectively. Among the LTO|LFP IDEs, Design 2 has a lower specific capacity than the other designs with equal mass and similar dimensions. The graphite|NMC-532 planar reference cell has a 4C discharge specific capacity of 120 mAh/g_{active}. In comparison, the capacities for graphite|NMC-532 Designs 1 – 4 are 122, 78, 132, and 99 mAh/g_{active}, which corresponds to a 2%, -34%, 10%, and -17% deviation from the planar reference cell. With the graphite|NMC-532 material model, Designs 2 and 4 have a lower capacity than the planar reference cell relative to the results observed with LTO|LFP.

Table 3.4. Summary of specific capacity performance for the IDEs and planar reference cells. For the LTO|LFP cells, the discharge specific capacity at 10C was modeled. For the graphite|NMC-532 cells, the discharge specific capacity at 4C was modeled.

	LTO | LFP	**Graphite | NMC-532**
Design	**Specific Capacity ($\frac{mAh}{g_{active}}$)**	**Specific Capacity ($\frac{mAh}{g_{active}}$)**
planar	**45**	**120**
1	96	122
2	63	78
3	109	132
4	89	99

Based on the modeling results, all LTO|LFP IDEs show improvements in specific capacity over the planar reference cell. On the other hand, among the graphite|NMC-532 designs, only

Designs 1 and 3 have improved specific capacity over the planar reference cell. Despite this difference, in both material systems the specific capacity ranking among Designs 1 – 4 follows the same high to low order; Design 3 is the best performing design and Design 1, Design 4, and Design 2 subsequently experience a degradation in specific capacity performance relative to Design 3 with Design 2 being the worst performing design in each scenario. The analysis shows that IDEs share the same relative specific capacity performance gains across different material systems, but their absolute performance gains relative to a conventional planar cell change with each material system.

3.2.1.1 Electrode Surface Area in IDEs

Figure 3.4 demonstrates the impact of electrode surface area on the specific capacity performance of 3D IDEs. The *SA/V* ratio was defined as the ratio between the electrode surface area that interface with the separator in both electrodes to the full-cell volume, which included the volumes of the cathode, the anode, the separator, and the electrolyte. As shown in Figure 3.4, the specific capacity results for the LTO|LFP IDE models and the graphite|NMC-532 IDE models both exhibit a positive correlation to the *SA/V* ratio. The data analysis conducted in section 2.2.3 of Chapter 2 showed that increasing the *SA/V* ratio leads to a higher rate capability for 3D IDEs made with the same material and same architecture, but whether or not the *SA/V* ratio can be used as a performance indicator across different electrode architectures was inconclusive. Here, for the four IDE designs examined, it is found that the *SA/V* ratio serves as a good performance indicator across different architectures made with the same material system.

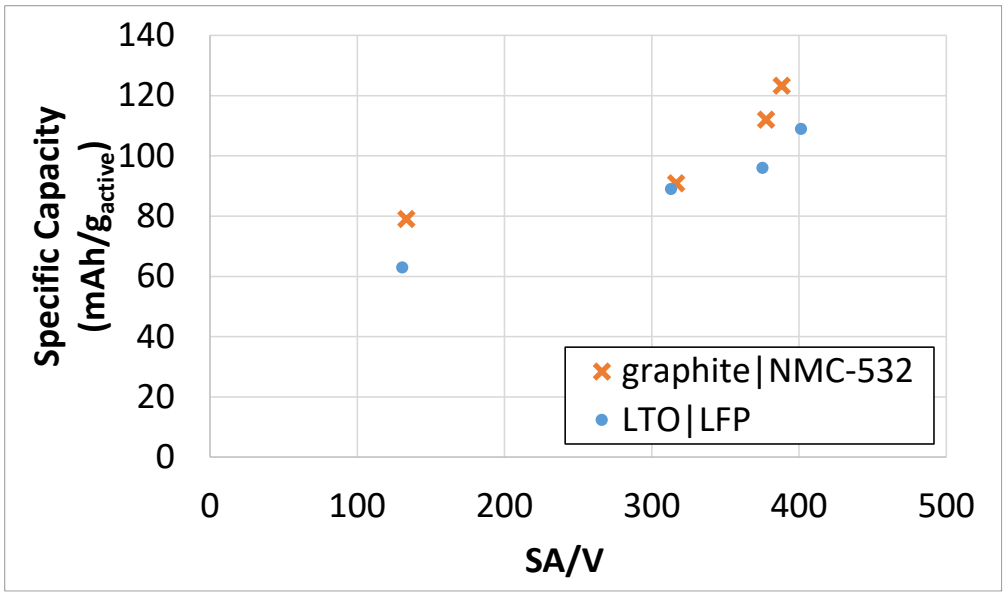

Figure 3.4. Specific capacity of 3D IDEs as a function of the *SA/V* ratio, defined as the ratio of separator surface area in contact with the anode and the cathode to the cell volume. For LTO|LFP IDEs, the discharge specific capacity at 10C was modeled. For graphite|NMC-532 IDEs, the discharge specific capacity at 4C was modeled.

3.2.2 *Lithiation Profile*

Here the lithiation profile and progression in each material system is analyzed. Figure 3.5 and Figure 3.6 show the solid-phase Li-ion concentration profiles in all IDE designs and the planar reference cells. The depth of discharge (DoD) is calculated as the specific capacity (mAh/g_{active}) delivered by a LIB at a given time divided by the maximum theoretical specific capacity defined in the cathode material model. DoD at 10% and 50% is examined for the behavior at the beginning and toward the end of discharge. For the planar reference cell and Design 2, the end of discharge does not reach 50% of the total discharge capacity, and therefore the maximum DoD is used. A LIB reaches 100% DoD when the active material in the cell is fully utilized. In these contour plots blue and red signify the minimum and maximum Li-ion concentration for the electrode materials as reported in Table 3.2. In the LTO|LFP models, the initial colors of the cathode and the anode

are dark blue and orange, respectively. Over the discharge cycle, the electrode colors change following the color bar in Figure 3.5 and Figure 3.6, indicating the amount lithiation progression in each design. Figure 3.3 (a) shows the 3D model units sliced at cross-section A, and Figure 3.3 (b) shows the model units sliced at cross-section B. All planar reference cells in Figure 3.5 and Figure 3.6 are unsliced so the concentration profiles can be more easily seen.

At 10% DoD in Figure 3.5 (a), the dark blue cathode regions in Designs 1 – 4 transition to light blue around the cathode surfaces facing the anode. This phenomenon is most pronounced in Designs 2 and 4 where we can see light blue outlines tracing the profile of the cathode region. Looking closer at Designs 1 – 4 at 10% DoD in Figure 3.5 (b), the initial lithiation profile is uniform along the length of the cathode column, with slightly more solid-phase Li-ion concentration on the top of the cathode columns. At 50% DoD, all designs in Figure 3.5 show only a partially red cathode, which indicates underutilization of the Li-ion cathode material. At the same time, the anodes in the IDE designs are uniformly green, which means uniform extraction of Li-ions from the anode. In contrast, the anode in the planar reference cell shows disparate green, yellow, and orange regions, signifying more non-uniform material utilization in the anode region at high discharge rates.

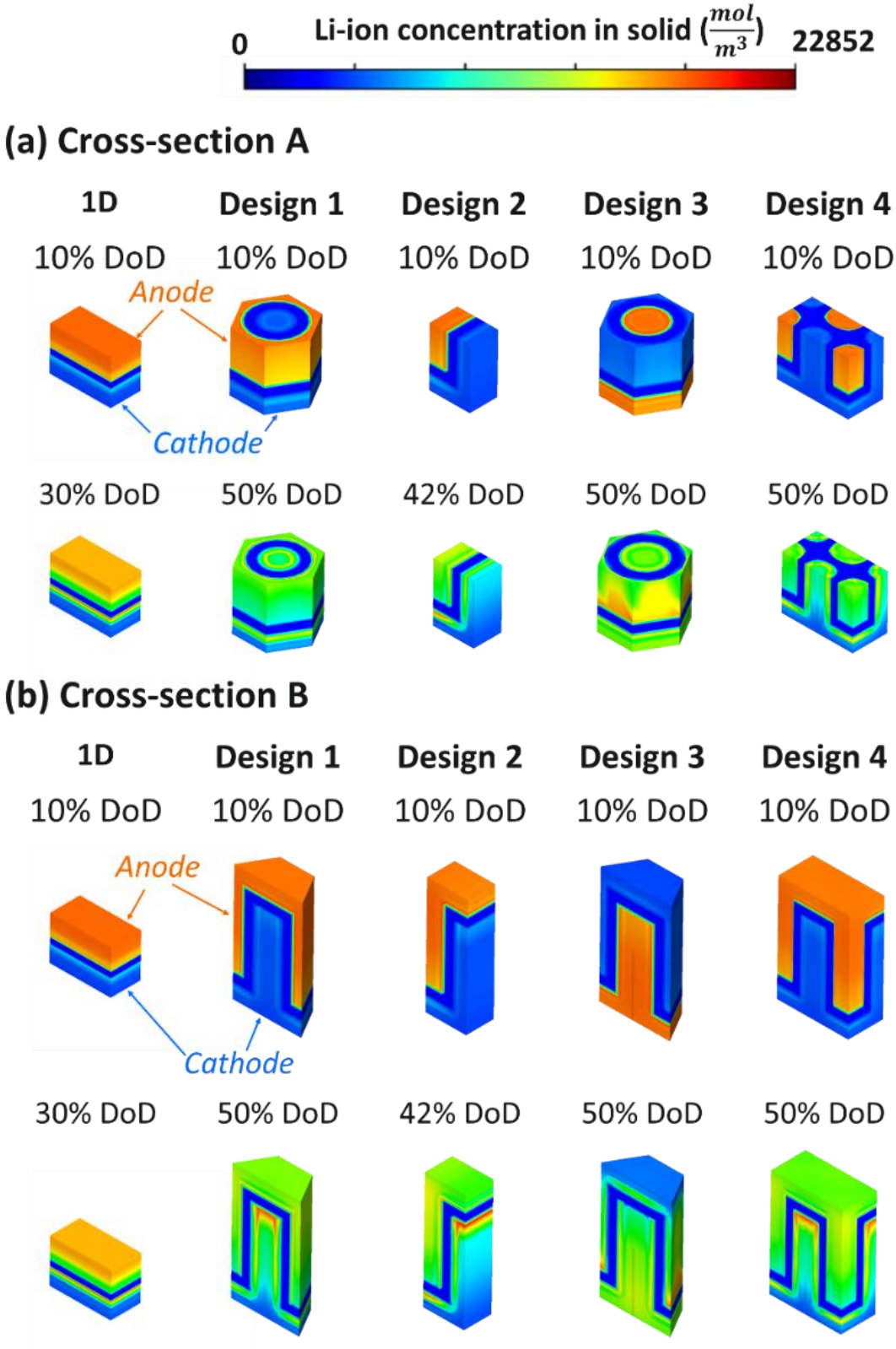

Figure 3.5. LTO|LFP solid-phase concentration plots at cross-section A and cross-section B based on Figure 3.3.

The Li-ion material utilization in each design can be observed in the concentration profiles at 50% DoD. At 50% DoD in Figure 3.5 (a), Design 1 shows a uniform yellow region of high Li-ion concentration around 15,000 mol/m^3 in the cathode in cross-section A. However, in Design 4 there are segmented clusters of high Li-ion concentration in the cathode. At 50% DoD in Figure 3.5 (b), red regions which represent zones of high Li-ion concentration can be seen on the top of the cathode column, indicating full lithiation of the cathode material. For Designs 1, 3, and 4, the lithiation front progresses from the top of the cathode to the bottom of the cathode near the current collectors. Looking at Design 1 in Figure 3.5 (b), a high Li-ion concentration profile (shown in yellow and red) is located at the top and outer perimeter of the cathode column. Design 2 is the only IDE design that does not reach 50% DoD at the end of discharge. Comparing Design 2 to other the other cases in Figure 3.5 (b), an additional high concentration region at the bottom of the cathode facing the top of the anode column is seen. Design 4 demonstrates similar behavior, but less pronounced, at 50% DoD.

Figure 3.6 shows the concentration plots for the graphite|NMC-532 material system. Since graphite|NMC-532 has a different initial concentration from LTO|LFP, the initial cathode and anode colors in the contour plots are dark blue (17,820 mol/m^3) and light green (30,000 mol/m^3). In Figure 3.6 (a), unlike the LTO|LFP models, there is no concentration regions on cross-section A in the graphite|NMC-532 models, indicating a more uniform current density distribution on cross-section A. In Figure 3.6 (b), a concentration gradient in the IDEs along the vertical direction is seen. Lithiation in the graphite|NMC-532 models starts from the bottom of the cathode electrodes near the current collectors and moves to the top of the cathode columns. Designs 2 and 4 both have high localized Li-ion concentration at 50% DoD, which explains their low specific capacity values relative to Designs 1 and 3 in Figure 3.6.

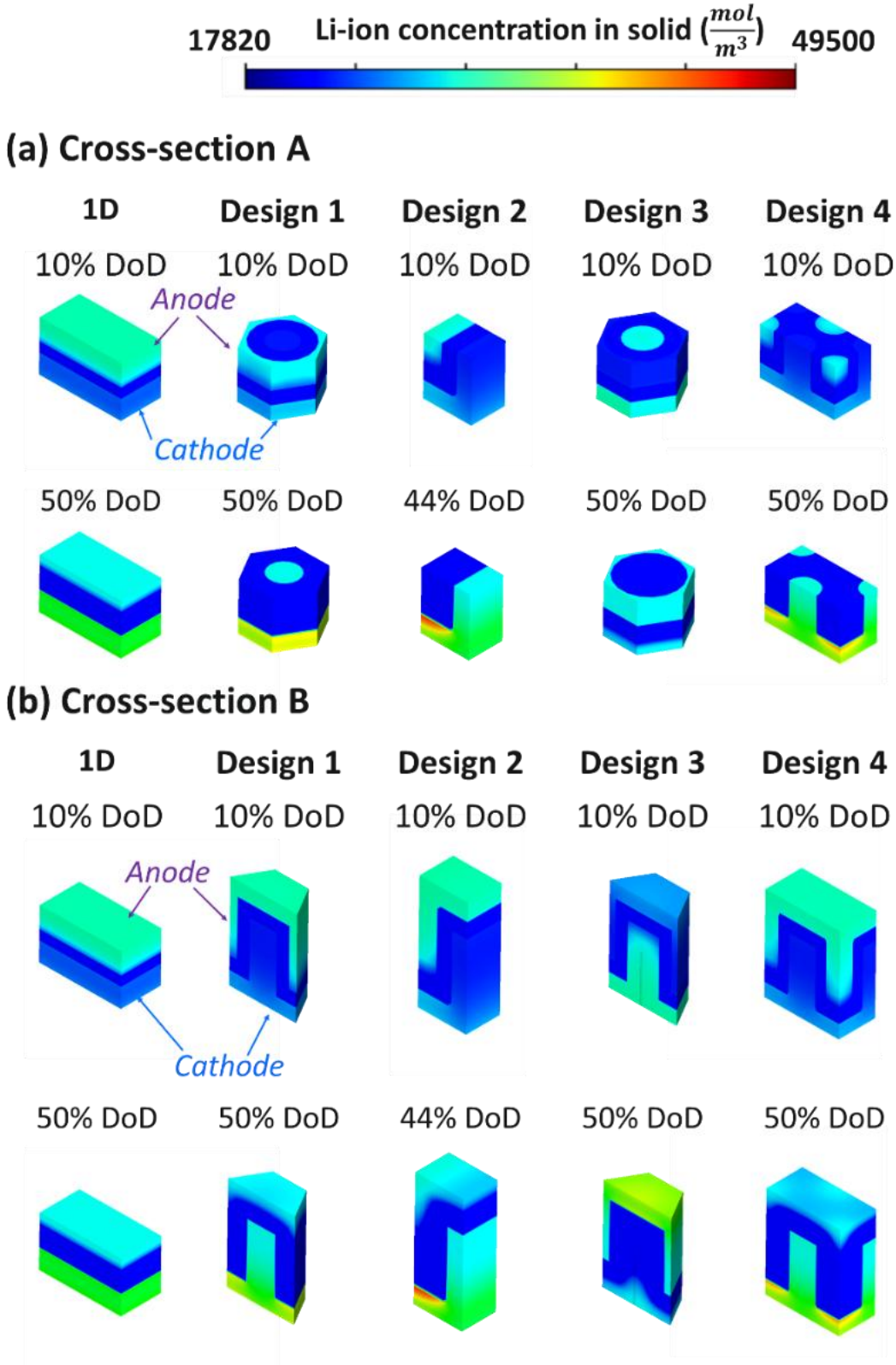

Figure 3.6. Graphite|NMC-532 solid-phase concentration plots at cross-section A and cross-section B based on Figure 3.3.

3.2.2.1 Impact of Material Selection and IDE Architecture on Lithiation Profile

Material selection has a significant impact on the lithiation profile in IDEs. From the solid-phase concentration plots in Figure 3.5 and Figure 3.6, different lithiation processes in the LTO|LFP and graphite|NMC-532 models are observed. The concentration gradient seen in cross-section A in Figure 3.5 (a) for LTO|LFP is not observed in the graphite|NMC-532 designs in Figure 3.6 (a). Comparing the plots at 10% DoD on cross-section B in Figure 3.5 (b) to Figure 3.6 (b), we see in LTO|LFP IDEs have a uniform lithiation profile, shown in light blue which corresponds to a constant 500 mol/m^3, while in the graphite|NMC-532 IDEs, the lithiation starts unevenly at the bottom of the cathode.

We can explain these lithiation profiles using a basic resistance analysis. At the beginning of discharge – before significant concentration gradients have developed, there is little diffusion, and transport within the cell is predominantly driven by conduction. Equation 3.9 defines the electric and ionic transport resistances, which are inversely proportional to the material conductivity, σ, and increase with a longer transport distance, L, and a smaller transport pathway cross-sectional area, A. In a porous medium, the resistance scales with the volume fraction of the conducting phase, ε.

$$R = \varepsilon \frac{L}{A\sigma} \ [\Omega\,] \quad (3.9)$$

Three resistances correlated to three conduction mechanisms within an LIB can be calculated using Equation 3.9: (1) the ohmic resistance in the cathode, $R_{Ohm,c}$, (2) the ionic resistance in the electrolyte, R_{Ionic}, and (3) the ohmic resistance in the anode, $R_{Ohm,a}$. Furthermore, the lithiation profile is impacted by the speed of intercalation kinetics at the phase boundary

between the active materials and the liquid electrolyte. These effects can be evaluated as charge transfer resistances in the cathode and the anode, $R_{CT,c}$ and $R_{CT,a.}$ using Equation 3.10, which is a linearized form of the Butler-Volmer relationship defined by Equations 1.3 and 1.4 from Chapter 1. In Equation 3.10, $V_{electrode}$, represents the volume of the electrode.

$$R_{CT}[\Omega] = \frac{RT}{F} * \frac{1}{i_0 * a_s * V_{electrode}} \quad (3.10)$$

The calculated resistances are summarized in Table 3.5. It is found that for the LTO|LFP models, the largest resistance resides in charge transfer in the cathode. While there are active phase boundaries throughout the porous cathode, the reaction rate is the highest at the cathode surface directly in contact with the separator due to Li-ions conducted from the separator interface. As a result, the initial lithiation profile in LTO|LFP models traced the outline of the IDE cathodes, as shown by the red regions on cross-section B in Figure 3.5 (b). For the graphite|NMC-532 models, the highest resistance is the ohmic conduction in the cathode, indicating electronic transport in the cathode thickness is the rate-limiting mechanism. As a result, in Figure 3.6 (b), lithiation started at the bottom of the NMC cathode because it is thermodynamically more favorable for the electrons entering into the cell via the positive current collector to participate in the charge transfer reaction at the porous phase boundary close to the current collector than to conduct to the top of the cathode.

Table 3.5. Summary of resistances in the electrodes, electrolyte, and at the phase boundary in IDE models.

LTO|LFP	**$R_{Ohm,c}$ (Ω)**	**$R_{Ohm,c}$ (Ω)**	**R_{Ionic} (Ω)**	**$R_{CT,c}$ (Ω)**	**$R_{CT,a}$ (Ω)**
Design A	1.11E+05	3.45E+04	6.53E+03	1.44E+06	1.79E+04
Design B	2.08E+04	8.28E+03	1.22E+03	1.45E+06	1.89E+04
Design C	7.23E+04	5.96E+04	4.24E+03	1.30E+06	1.99E+04
Design D	1.16E+05	3.72E+04	6.53E+03	1.41E+06	1.78E+04
Graphite|NMC-532	**$R_{Ohm,c}$ (Ω)**	**$R_{Ohm,c}$ (Ω)**	**R_{Ionic} (Ω)**	**$R_{CT,c}$ (Ω)**	**$R_{CT,a}$ (Ω)**
Design A	1.11E+06	3.43E+02	6.53E+03	1.33E+04	1.17E+05
Design B	2.53E+05	8.96E+01	1.49E+03	1.33E+04	1.19E+05
Design C	8.23E+05	4.65E+02	4.85E+03	1.20E+04	1.21E+05
Design D	1.28E+05	3.97E+01	6.53E+03	1.31E+04	1.15E+05

Electrode architecture has a smaller and more localized impact on the lithiation profile in the cell compared to the choice of material system. Comparing Design 1 to Design 4 in Figure 3.5 (a), we can see that although both designs have cathodes with the same diameter, the lithiation front is uniformly distributed on cross-section A in Design 1 but more clustered in Design 4. According to past model predictions by Hart et al.,[104] the highest current density in the cathode region of Design 4 will be located at the point closest to the anode. Instead, the results in Figure 3.5 (a) show that the Li-ion concentration in Design 4's cathode gathers at an angle between the two adjacent anodes. In Design 1, where the cathode is uniformly surrounded by anode material, the Li-ion concentration does not accumulate at any particular angle. Therefore, the Li-ion concentration clusters in Design 4 are likely the result of counteracting potentials from the adjacent anode electrodes and are primarily driven by physical distance between the anode and cathode.

3.2.3 *Energy Density and Power Density*

Beyond specific capacity, the gravimetric, volumetric, and areal energy and power densities for a single-layer cell are calculated and summarized in Table 3.6 to give further insight into overall battery performance. The volume and weight of the electrodes (active, binder, carbon),

separator, electrolyte, and current collectors are included in all calculations. A 20 μm thick aluminum current collector with a density of 2.70 g/cm^3 on the cathode and a 15 μm thick copper current collector with a density of 8.96 g/cm^3 on the anode are assumed for the purposes of this analysis. The density of the separator is assumed to be 0.90 g/cm^3 and the density of the liquid electrolyte is set to 1.23 g/cm^3.

Table 3.6. Summary of energy and power densities for the IDEs. All weight (active, binder, carbon) and volume of the electrodes, separator, electrolyte, and current collectors are included. IDE results that show improvements over the planar reference cell are highlighted in green.

Design	Gravimetric Energy Density ($\frac{mWh}{g}$)	Gravimetric Power Density ($\frac{mW}{g}$)	Volumetric Energy Density ($\frac{mWh}{cm^3}$)	Volumetric Power Density ($\frac{mW}{cm^3}$)	Areal Energy Density ($\frac{mWh}{cm^2}$)	Areal Power Density ($\frac{mW}{cm^2}$)
LTO | LFP						
planar	11	362	32	1019	0.57	18
1	19	290	43	657	1.12	17
2	15	340	37	828	0.97	22
3	20	277	43	615	1.13	16
4	18	295	40	670	1.05	17
Graphite | NMC						
planar	118	684	340	1970	5.38	31
1	101	579	241	1382	5.17	30
2	78	692	199	1771	4.28	38
3	103	551	242	1301	5.21	28
4	84	579	204	1397	4.38	30

Examining the LTO|LFP designs in Table 3.6, the gravimetric energy densities of Designs 1 – 4 are 19, 15, 20, and 18 mWh/g and the areal energy densities are 1.12, 0.97, 1.13, and 1.05 mWh/cm^2, respectively. Based on this, Design 3 has the highest energy density, and Design 2 has the lowest energy density. The volumetric energy density follows a slightly different trend with Designs 1 and 3 both having the highest volumetric energy density at 43 mWh/cm^3. Looking at gravimetric, volumetric, and areal power densities, Design 2 has the highest power densities at 340

mW/g, 828 mW/cm^3, and 22 mW/cm^2 while Design 3 has the lowest power densities at 277 mW/g, 615 mW/cm^3, and 16 mW/cm^2. Overall, the LTO|LFP IDE designs have 36 – 73% higher gravimetric, 18 – 36 % higher volumetric, and 71 – 98% higher areal energy densities than the selected planar reference cell. Lower power densities relative to the planar reference cell are observed in all the designs with the exception of Design 2's areal power density which is 18% greater than the planar reference cell in Table 3.6.

The graphite|NMC-532 IDE designs also have the same high-to-low rank order of energy densities as the high-to-low rank order of their specific capacity values. Design 3 has the highest energy densities (103 mWh/g, 242 mWh/cm^3, and 5.21 mWh/cm^2), while Design 2 has the lowest energy densities (78 mWh/g, 199 mWh/cm^3, and 4.28 mWh/cm^2). With respect to power densities, Design 2 has the highest power densities (692 mW/g, 1771 mW/cm^3, and 38 mW/cm^2) while Design 3 has the lowest power densities (551 mW/g, 1301 mW/cm^3, and 28 mW/cm^2). For graphite|NMC-532, the planar reference cell outperforms all IDE designs except for Design 2 which has a 1% improvement in gravimetric power density and a 22% improvement in areal power density over the planar reference cell in Table 3.6.

It is worth noting that the power density here was calculated simplistically by dividing the energy density by the total discharge time. As a result, models that have a lower specific capacity and a shorter discharge time will have a higher power density. However, their low capacities mean that these models do not have good rate capability. As a result, the power density presented in Table 3.6 is only meaningful when comparing two cells with similar a discharge capacity. Thus, the higher power densities of Design 2 are not significant improvements.

Looking at specific capacity again, Design 3 is the best performing design followed by Design 1, Design 4, and Design 2. This same trend is observed in the gravimetric and areal energy

densities for the LTO|LFP designs and all energy density values for the graphite|NMC-532 designs. This suggests that the four IDE architectures have similar volume ratios of cathode, anode, separator, and electrolyte. Although a multi-layer battery stack analysis is required to understand the true energy and power impact with reduced inactive components,[10] the energy and power values for the single-layer 3D IDE designs provide insight into the relative energy and power gains that may be observed at larger scales.

While the LTO|LFP IDEs all demonstrated improvements in energy densities over the planar reference cell, the graphite|NMC-532 designs demonstrated reduced energy densities despite exhibiting improvements in specific capacity. These results emphasize that IDE architectures can change the overall mass density of the battery cell, and depending on the material system, the effects can be detrimental to energy density. Therefore, it is imperative to consider the overall mass density of IDEs and the weight and volume percentage of active materials in the cell at early design stage to ensure high energy and power densities.

3.2.4 *Impact of IDE Column Geometry*

Design 1 in LTO|LFP was modeled under different geometric conditions, where the cathode columns are a circle, square or triangular shape in cross-section as shown in Figure 3.3 (b) to better understand the impact of electrode column shape on IDE design. The cathode mass is fixed across the three designs, and the N/P ratios are between 1.05 – 1.06. The fluctuation in IDE volume is shown in Table 3.7 and is the result of varying separator volumes, which by design must vary based on the geometry of the electrodes to keep the average separator thicknesses constant at 25 μm. All designs were run at a 10C (0.002 mA) discharge current. The specific capacity for each column shape is reported in Table 3.7. The original Design 1 with circular columns and has a discharge capacity of 96 mAh/g_{active}. Changing the column shape from circular to square

demonstrates a 95 mAh/g_{active} specific capacity. The triangular column Design 1 has a specific capacity of 90 mAh/g_{active}, corresponding to a 5% drop in specific capacity relative to the circular columns. The specific capacity does not deviate substantially among the different column shapes at high discharge rates. Examining the volume of each design, it is found that by the nature of the geometry, the square and triangular columns take up 6% and 13% more volume than the original circular column shape, indicating the choice of column shape can have a negative impact on performance.

Table 3.7. Specific capacities at 10C for Design 1 with different column shapes as shown in Figure 3.3 (b)

Column Shape	**Specific Capacity** ($\frac{mAh}{g_{active}}$)	**Model Unit Volume** (mm^3)
Square	95	$2.62 \cdot 10^{-3}$
Circular	96	$2.47 \cdot 10^{-3}$
Triangular	90	$2.81 \cdot 10^{-3}$

The column shape analysis gives insight into the impact of feature geometry in IDEs. As seen in Table 3.7, Design 1 was modeled with three shapes: a circle, square, and triangle. All results demonstrated less than a 5% deviation in specific capacity with the volume-averaged modeling approach. This number is within precision of the modeling setup, and these three designs can be deemed nearly identical from a specific capacity standpoint in the models. In practicality, fabricating electrodes with sharp corners presents other issues such as stress concentration points or sharp heterogeneities that can lead to electrode cracking or adverse lithium plating effects. These are critical issues to consider when fabricating a 3D LIB but are beyond the scope of what the models in this study can predict.

3.2.5 *Uniformity Index UI_{3D}*

To investigate the relationship between specific capacity and the UI_{3D} metric, the evolution of UI_{3D} over the full discharge cycle for the LTO|LFP designs on cross-sections A and B are plotted in Figure 3.7 and Figure 3.8. On the horizontal cross-section A, the UI_{3D} of the planar reference cell is close to zero at all time steps. The end of discharge in the planar reference cell is not a continuous line (see black line in Figure 3.7) because the average current density is zero, which leads to division by zero in Equation 3.8. On the other hand, the IDEs have a much higher average UI_{3D}, ranging approximately between 1 – 3, and higher UI_{3D} variability over the course of the discharge cycle. Design 4 has the highest UI_{3D} on cross-section A, and this high UI_{3D} value appears to not necessarily be correlated to low specific capacity performance.

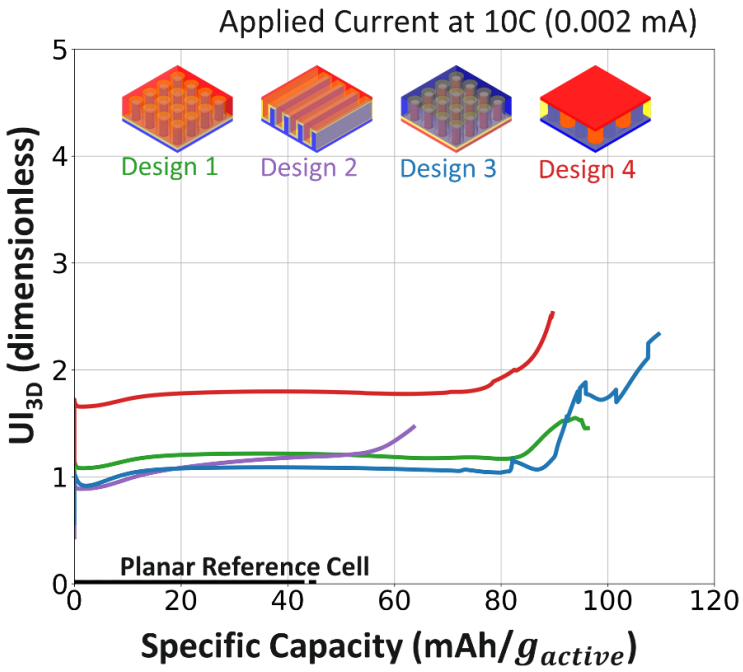

Figure 3.7. UI_{3D} on cross-section A in Figure 3.3 compared to specific capacity for the LTO|LFP designs. The applied current used in all cases is 0.002 mA which is equivalent to a 10C rate.

The profile of the UI_{3D} curves in Figure 3.7 shows that all IDEs experience an initial drop in UI_{3D} followed by a quick rise before 10% DoD or 15 mAh/g_{active}. In Designs 1, 3, 4, the UI_{3D} plateaus after 10% DoD, but in Design 2, the UI_{3D} continues to increase after 10% DoD. Design 2 eventually reaches its end of discharge at 63 mAh/g_{active}, which is 35 – 57% less than the other IDE design cases. In contrast, Designs 1, 3, and 4 sustain a longer discharge cycle after the UI_{3D} stabilizes. Near the end of discharge, all IDEs undergo a significant increase in UI_{3D}, which eventually leads to cell failure.

Similarly, in Figure 3.8 the evolution of UI_{3D} over time is examined on the vertical cross-section B. Compared to Figure 3.7, UI_{3D} on cross-section B in Figure 3.8 has shorter plateau regions, and the planar reference cell has a UI_{3D} that is on the same order of magnitude as the IDEs. Focusing on the data between 0 – 20 mAh/g_{active}, it is seen that the planar reference cell and Design 2 have the highest UI_{3D} line slopes, and Design 3 has the lowest UI_{3D} slope among all designs. Coincidentally, the designs with higher slopes have much lower specific capacities in the range of 45 – 70 mAh/$g_{active,}$ while Design 3 (with the lowest slope) has the highest specific capacity. Comparing UI_{3D} in the specific capacity range of 40 – 60 mAh/g_{active}, it is seen that the LTO|LFP designs with higher plateau UI_{3D} values on cross-section B also have lower specific capacities.

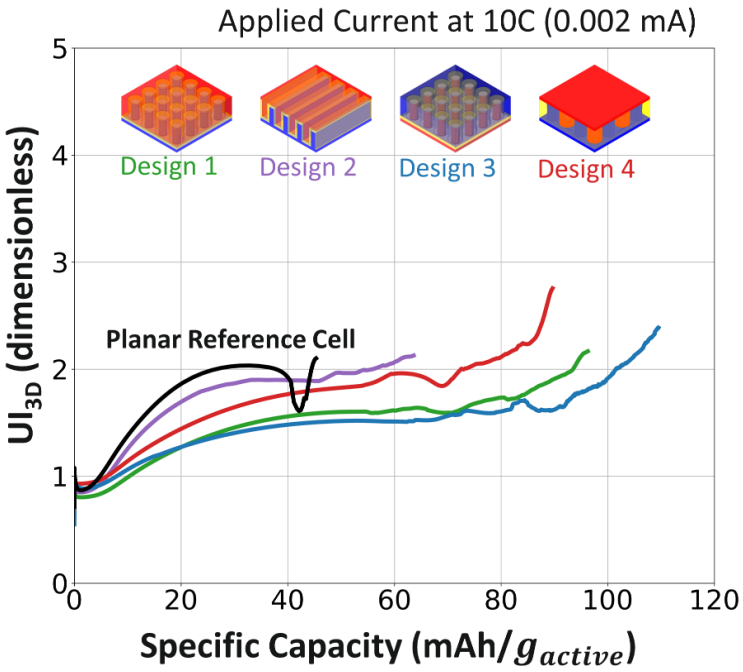

Figure 3.8. UI_{3D} for cross-section B in Figure 3.3 compared to specific capacity for LTO|LFP designs. The applied current used in all cases is 0.002 mA which is equivalent to a 10C rate.

In Figure 3.9 and Figure 3.10, UI_{3D} versus specific capacity is plotted for the graphite|NMC-532 designs on the same cross-sections used for LTO|LFP. In Figure 3.9, UI_{3D} remains mostly flat during discharge in cross-section A. In addition, a relatively high UI_{3D} value is observed in Design 4, similar to the LTO|LFP designs in Figure 3.7. In Figure 3.10, on the vertical cross-section B, the UI_{3D} demonstrates a different trend from that seen for LTO|LFP in Figure 3.8. The UI_{3D} starts at a high value at the beginning of the discharge, quickly drops until a temporary plateau is reached and then rises again at the end of discharge.

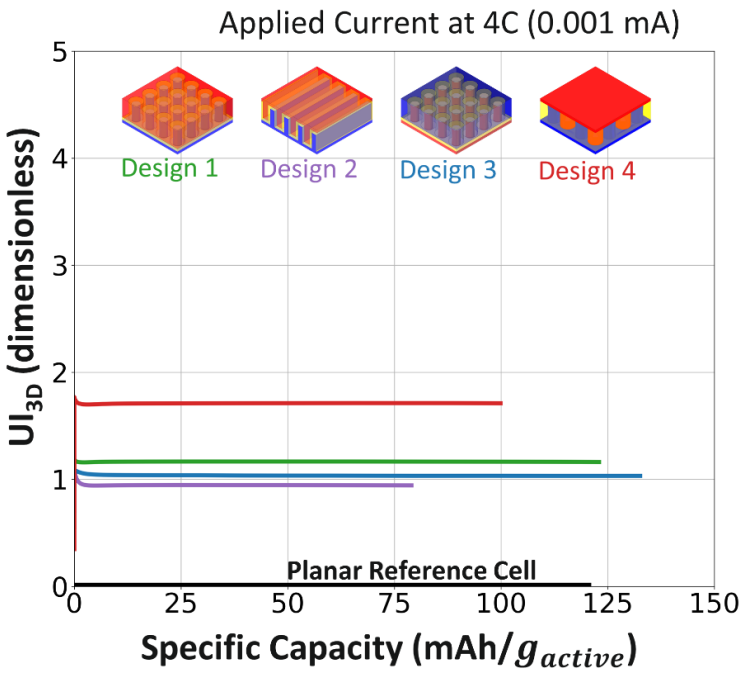

Figure 3.9. UI_{3D} for cross-section A in Figure 3.3 compared to specific capacity for graphite|NMC-532 designs. The applied current used in all cases is 0.001 mA which is equivalent to a 4C rate.

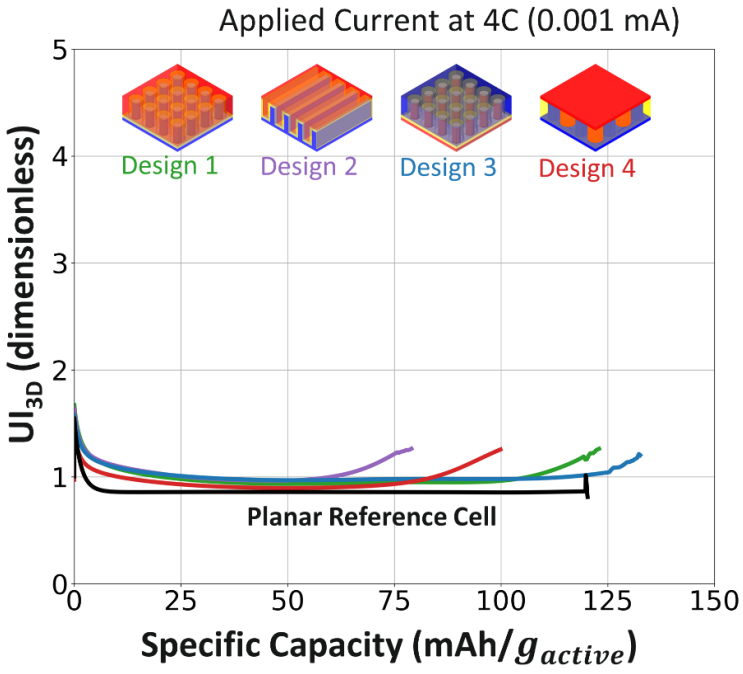

Figure 3.10. UI_{3D} for cross-section B in Figure 3.3 compared to specific capacity for graphite|NMC-532 designs. The applied current used in all cases is 0.001 mA which is equivalent to a 4C rate.

Based on the analysis in Figure 3.7 – Figure 3.10, the slopes of the UI_{3D} versus specific capacity plots around 10% DoD show an interesting trend that can give better insight into IDE performance instead of the absolute value of UI_{3D}. As a result, the slopes of UI_{3D} versus specific capacity were calculated and denoted as dUI_{3D}/dQ. Table 3.8 summarizes dUI_{3D}/dQ at 10% DoD for all IDE designs and the planar reference cells on cross-sections A and B along with the specific capacity values. For the planar reference cells, cross-section A is the horizontal slice which is the cross-sectional surface parallel to the current collectors. On cross-section A, dUI_{3D}/dQ is zero for both LTO|LFP and graphite|NMC-532 planar reference cells. Cross-section B for the planar reference cells is the vertical slice that runs perpendicular to the current collectors. On cross-section B, dUI_{3D}/dQ for the planar reference cells is higher at 0.04755 for LTO|LFP and 0.00011 for graphite|NMC-532.

Table 3.8. Summary of dUI_{3D}/dQ and specific capacity performance for IDEs.

		LTO | LFP		**Graphite | NMC-532**	
Slice Orientation	**Design**	dUI_{3D}/dQ **at 10% DoD**	**Specific Capacity** $(\frac{mAh}{g_{active}})$	dUI_{3D}/dQ **at 10% DoD**	**Specific Capacity** $(\frac{mAh}{g_{active}})$
Cross-section A	**planar**	**0.00000**	**45**	**0.00000**	**120**
	1	0.00473	96	0.00008	122
	2	0.00987	63	0.00001	78
	3	0.00426	109	-0.00009	132
	4	0.00476	89	0.00013	99
Cross-section B	**planar**	**0.04755**	**45**	**0.00011**	**120**
	1	0.02798	96	-0.00624	122
	2	0.04219	63	-0.00335	78
	3	0.01843	109	-0.00471	132
	4	0.02977	89	-0.00440	99

Among the LTO|LFP IDEs, Design 2 has the lowest specific capacity at 63 mAh/g_{active}, but Design 2 still shows a 40% improvement in specific capacity over the planar reference cell.

Designs 1, 3, and 4 show higher discharge capacities that are 98% – 142% more than the planar reference cell. The dUI_{3D}/dQ of Design 2 on cross-section A is 0.00987, which is two times greater than the dUI_{3D}/dQ values of Designs 1, 3, and 4. Although not as prominent, the same pattern is observed on cross-section B. The dUI_{3D}/dQ of Design 2 on cross-section B is 0.04219, which is slightly larger than the dUI_{3D}/dQ for other designs which range between 0.01843 – 0.02977.

For graphite|NMC-532, Designs 2 and 4 have a 34% and 17% lower specific capacity than the planar reference cell. In contrast, Designs 1 and 3 have specific capacities of 122 mAh/g_{active} and 132 mAh/g_{active}, which are 2% and 10% greater than the planar reference cell, respectively. As shown in Table 3.8, dUI_{3D}/dQ on cross-section A for all of the designs results in very small numerical values with zeros down to the third decimal place. These results align with Figure 3.9 where the UI_{3D} of the graphite|NMC-532 designs is flat and constant throughout the discharge cycle. On cross-section B, the dUI_{3D}/dQ values have larger magnitude. Unlike the LTO|LFP designs, which all have positive dUI_{3D}/dQ values, the graphite|NMC-532 designs have negative dUI_{3D}/dQ values, which can be explained by the profiles observed in Figure 3.10. The results show that on cross-section B, Designs 2 and 4 have the least negative dUI_{3D}/dQ at -0.00335 and -0.00440, respectively. Although not in proportion to the loss in specific capacity, these values are 7 – 49% less than the magnitude of dUI_{3D}/dQ in Designs 1 and 3 at -0.00624 and -0.00471, respectively.

3.2.6 *Uniformity Index as Performance Indicators*

The analysis of UI_{3D} versus specific capacity in Figure 3.7 – Figure 3.10 reveals the variations in current density uniformity at each stage of the discharge cycle. The data affirms that after the first 10 – 15% DoD, most IDEs reach an eventual plateau UI_{3D} value, and all IDEs have a drastic rise in UI_{3D} near the end of discharge. Figure 3.8 illustrates UI_{3D} for LTO|LFP on cross-

section B and is the only result that captures a direct correlation between specific capacity and UI_{3D}. More specifically, the plateau UI_{3D} values in Figure 3.8 at 30 mAh/g_{active} and onwards demonstrate a trend where IDEs with an overall higher UI_{3D} have a lower discharge specific capacity.

A limitation of the UI_{3D} metric is that it does not account for the relative locations of local current density values. Therefore, effective usage of UI_{3D} depends on careful selection of the cross-sections. In addition, as shown in Figure 3.5 and Figure 3.6, the lithiation profile in the IDEs is highly dependent on the implemented material models. Therefore, it is challenging to determine the cross-section that will show evident trends as in Figure 3.8 for each material system without a more automated implementation to locate areas of interest in each model.

As an alternative to UI_{3D}, the slope of UI_{3D} (dUI_{3D}/dQ) at 10% DoD is examined to help gain further insight into the behavior of IDEs. With LTO|LFP, a high dUI_{3D}/dQ is observed in Design 2, indicating a rapid change in current density uniformity (see Table 3.8). This result demonstrates the applicability of dUI_{3D}/dQ as an early model screening metric for LTO|LFP to understand which designs may not reach a high specific capacity value by the end of discharge. With the graphite|NMC-532 designs, dUI_{3D}/dQ is less conclusive on cross-section A. This coincides with the concentration plots in Figure 3.6 (a) where no gradients are seen on cross-section A at any point during the discharge cycle. On cross-section B, dUI_{3D}/dQ values are negative in the graphite|NMC-532 IDEs, suggesting a reduction in current non-uniformity caused by a rate-limiting mechanism that is different from LTO|LFP. In this case, we can identify the lower-performing Designs 2 and 4 by their lower dUI_{3D}/dQ (flatter negative slope), which are 7 – 49% less than the dUI_{3D}/dQ of Designs 1 and 3.

The distinction between dUI_{3D}/dQ as a screening metric for LTO|LFP versus graphite|NMC-532 is likely a result of their different rate-limiting mechanisms, which is captured by the UI_{3D} versus capacity evolution curves in Figure 3.8 and Figure 3.10. For the LTO|LFP designs, the UI_{3D} increases right at the beginning of the discharge cycle. A higher slope (dUI_{3D}/dQ) leads to an early plateau of UI_{3D}, which is quickly followed by the final rise in UI_{3D} that signifies the termination of the discharge cycle (see Design 2 in Figure 3.8). On the other hand, the graphite|NMC-532 designs have a decreasing UI_{3D} value at the start of discharge, and instead of higher slopes, as observed in LTO|LFP, lower slopes in graphite|NMC-532 cause the UI_{3D} to plateau and terminate early (see Designs 2 and 4 in Figure 3.10). Based on this data, if we know the UI_{3D} evolution profile for a given material system, we can leverage dUI_{3D}/dQ at 10% DoD as an early model screening metric to identify IDEs that will yield a relatively lower specific capacity value by the end of a model discharge cycle.

The lithiation profiles yield interesting UI_{3D} behavior in Figure 3.7 – Figure 3.10. The UI_{3D} in Figure 3.10 starts high and quickly decreases until 25 mAh/g_{active}, which is likely due to the faster solid-phase transport in graphite|NMC-532 models, while the continual rise in UI_{3D} in Figure 3.8 for LTO|LFP materials represents opposite behavior. The impact of material selection is further demonstrated by Design 4. With LTO|LFP, Design 4 yields a 98% improvement in specific capacity over the planar reference cell and with graphite|NMC-532, Design 4 suffers a 17% capacity loss. As discussed previously, Design 4, which has a higher separator volume by design, is more adversely impacted by the low liquid-phase transport in the graphite|NMC-532 model. Thus, Design 4 with graphite|NMC-532 has a lower cathode material utilization and in turn a lower specific capacity than what can be achieved with LTO|LFP. This indicates that Design 4 favors materials with high liquid-phase transport.

3.2.7 *Impact of Non-uniformity on Transport Pathways*

In Figure 3.11 and Figure 3.12, the Li-ion transport pathways in the solid electrode are visualized following the approach developed by Zadin et al. [55] where current density streamlines are calculated with the gradients of local current densities and plotted to visualize the transport pathways. This approach is based on the assumption that Li-ions flow from low to high current density regions, and the intercalation activity is the highest in the cathode. Cross-section A in Figure 3.3 for LTO|LFP IDE Designs 1 and 4 at the beginning and end of discharge are examined. Blue and red in the contour plots represent the maximum (5 A/cm^2) and minimum current density (-20 A/cm^2). The region of interest is marked by the black boxes on the model unit cross-sectional diagrams. Within the region of interest, the cathode is outlined with white lines. Figure 3.11 and Figure 3.12 compare Li-ion transport pathways in Designs 1 and 4 at 10% DoD and 50% DoD respectively for the purposes of a comparative discussion to give further insight into the model results.

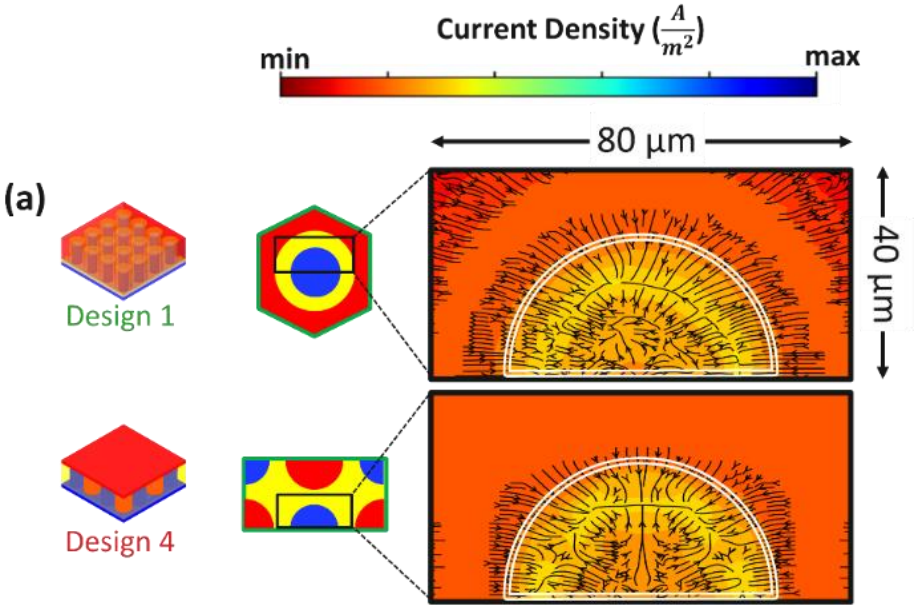

Figure 3.11. Transport pathways plotted on cross-section A (top-down view) in two LTO|LFP designs at the beginning of discharge.

At 10% DoD in Figure 3.11, the ion-transport pathways are more clustered and tortuous in Design 4 than in Design 1, indicating less effective transport caused by the non-uniform current density. At 50% DoD in Figure 3.12, there is a more severe current density gradient than at 10% DoD in Design 1. Since this gradient is consistent along the circumference of cathode, the ion-transport paths stay relatively unchanged in the radial direction. This result indicates that if the location of localized non-uniformity is well-balanced, the negative impact of non-uniformity on ion-transport pathways can be minimized. To reiterate this insight, Design 4 demonstrates a high current density at the top left and right corners of cathode, resulting in a highly non-uniform and unbalanced current density distribution. Therefore, the ion-transport pathways are much longer and more tortuous in Design 4 than in Design 1 as shown in Figure 3.12. The spatial non-uniformity and lengthened ion-transport pathways in Design 4 in Figure 3.11 and Figure 3.12 corresponds to its high UI_{3D} value of approximately 1.8 in Figure 3.7, which is much higher than Design 1's UI_{3D} value of 1.1.

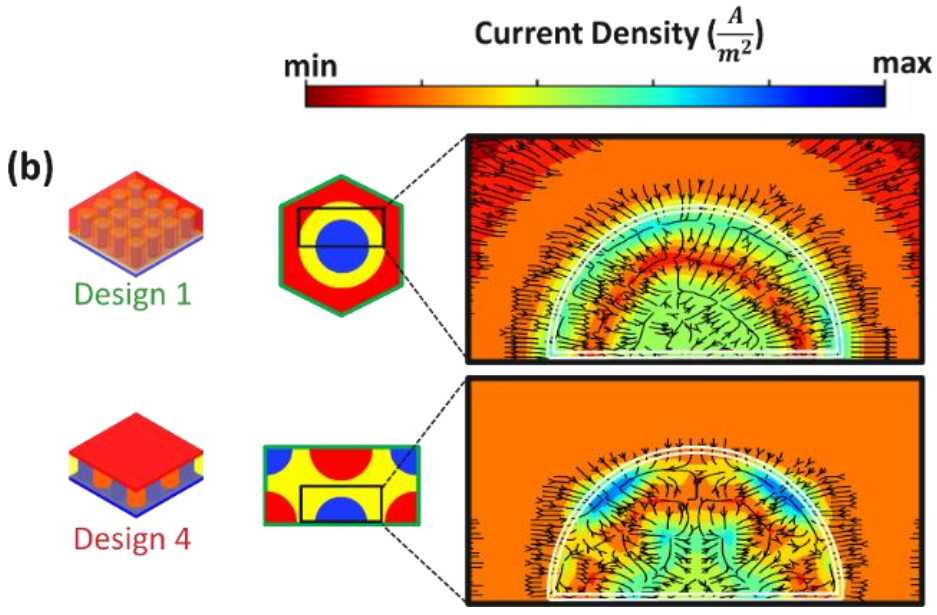

Figure 3.12. Transport pathways plotted on cross-section A (top-down view) in two LTO|LFP designs at the end of discharge.

3.3 CONCLUSIONS

Four IDE LIB designs were modeled with two different material systems with a consistent cathode mass to evaluate the impact of IDE electrode architecture on single-layer cell performance. The findings indicated that the relative rank order of high-rate specific discharge capacity performance among the IDE designs is primarily driven by electrode architecture. Within the same material system, it was confirmed that a higher electrode surface area leads to a higher specific capacity, demonstrating the feasibility of utilizing *SA/V* as a performance indicator across different IDE electrode architectures.

Design 3, featuring a circular column-shaped anode, a conformally coated separator, and a cathode occupying the remaining space, exhibited the most significant improvements in specific capacity, driven by its high *SA/V* ratio. Design 1, with an inverted anode and cathode structure relative to Design 3, demonstrated the second-highest performance improvements. Design 4, characterized by an interdigitated checkerboard arrangement of anode and cathode columns, ranked third in performance. Design 2, with its interdigitated plate electrode structure, showed the lowest *SA/V* ratio and corresponding specific capacity.

The energy density performance closely followed the ranking of specific capacity, suggesting that the volume proportions of electrodes, separator, and current collectors within the single-layer cell remained relatively constant across the different IDE architectures. It was found that the shape of electrode columns has a minimal impact on specific capacity in IDEs. However, changing the column shape from a circle to a triangle with fixed cathode mass can lead to a 13% cell volume increase. All LTO|LFP IDEs demonstrated improvements in discharge specific capacity and energy density over the planar reference cell. In contrast, three graphite|NMC-532 IDEs showed capacity gains but no improvements in energy density, indicating that IDEs may

negatively influence the overall weight, volume, and active material loading relative to single-layer cells made with graphite|NMC-532 materials.

The uniformity and distribution of current density in IDEs is highly dependent on both the electrode architecture as well as the material model. The general direction of lithiation across the electrode thickness and the rate-limiting mechanism are material-dependent. However, 3D electrode architecture contributes to local non-uniformities within smaller regions of the electrodes. Thus, good capacity performance at high discharge rates requires a delicate balance between electrode architecture and material selection. The current density uniformity analysis indicates that IDEs that reached their plateau UI_{3D} value early in a discharge cycle are more likely to demonstrate poor specific capacity performance in a given material system. By knowing the evolution of UI_{3D} in a given material system and the dUI_{3D}/dQ early in a discharge cycle, we can more rapidly screen, with computational tools, promising IDE designs for eventual fabrication. Furthermore, the Li-ion transport analysis shows that non-uniformity within the battery cell is influenced by the spatial arrangement of cathode and anode and that higher non-uniformity leads to longer transport lengths. The transport plots and the UI_{3D} results provide new means to systematically identify and quantify transport limitations due to current density non-uniformities.

Chapter 4. STRUCTURED ELECTRODES PART 1: MODELING THE IMPACT OF CATHODE STRUCTURING ON DISCHARGE RATE CAPABILITY IN ULTRA-THICK GRAPHITE|NMC-622 BATTERIES

*The content in Chapter 4 is adapted from Hung, C.-H.; Allu, S.; Cobb, C. L. "Modeling Structured Electrodes and Graded Porosity for Improving Discharge Rate Capability in Ultra-Thick Graphite|$LiNi_{0.6}Mn_{0.2}Co_{0.2}O_2$ Batteries." *J. Electrochem. Soc.* **2025**, *172* (1), 010513. under CC BY 4.0 (https://creativecommons.org/ licenses/by/4.0/).[132]

4.1 INTRODUCTION

In this chapter, physics-based electrochemical models were developed to quantify the impact of SEs on the discharge rate capability of ultra-thick, high-energy density LIBs and to analyze the underlying mechanisms that may facilitate performance enhancements. A $LiNi_{0.6}Mn_{0.2}Co_{0.2}O_2$ (NMC-622) cathode and a graphite anode were used as the model material system due to their relevance for EVs and the availability of validated model parameters in literature. For NMC, there is a move towards lower cobalt containing compositions, which has shifted industry and academic research focus from $LiNi_{0.3}Mn_{0.3}Co_{0.3}O_2$ (NMC-111) and $LiNi_{0.5}Mn_{0.3}Co_{0.2}O_2$ (NMC-532) to NMC-622 and $LiNi_{0.8}Mn_{0.1}Co_{0.1}O_2$ (NMC-811). As illustrated in Figure 4.1 (a), conventional NMC-622 planar electrodes have uniformly distributed electrode materials at a macroscopic level, and they are referred to as UEs in this chapter. UEs experience a capacity loss exceeding 50% at 4C and higher charge/discharge rates when the electrode thickness is greater than 100 μm. As discussed in the section 1.1.2, the poor rate capability is a result of the energy and power trade-off, where a thicker electrode has a higher Li-ion transport tortuosity.

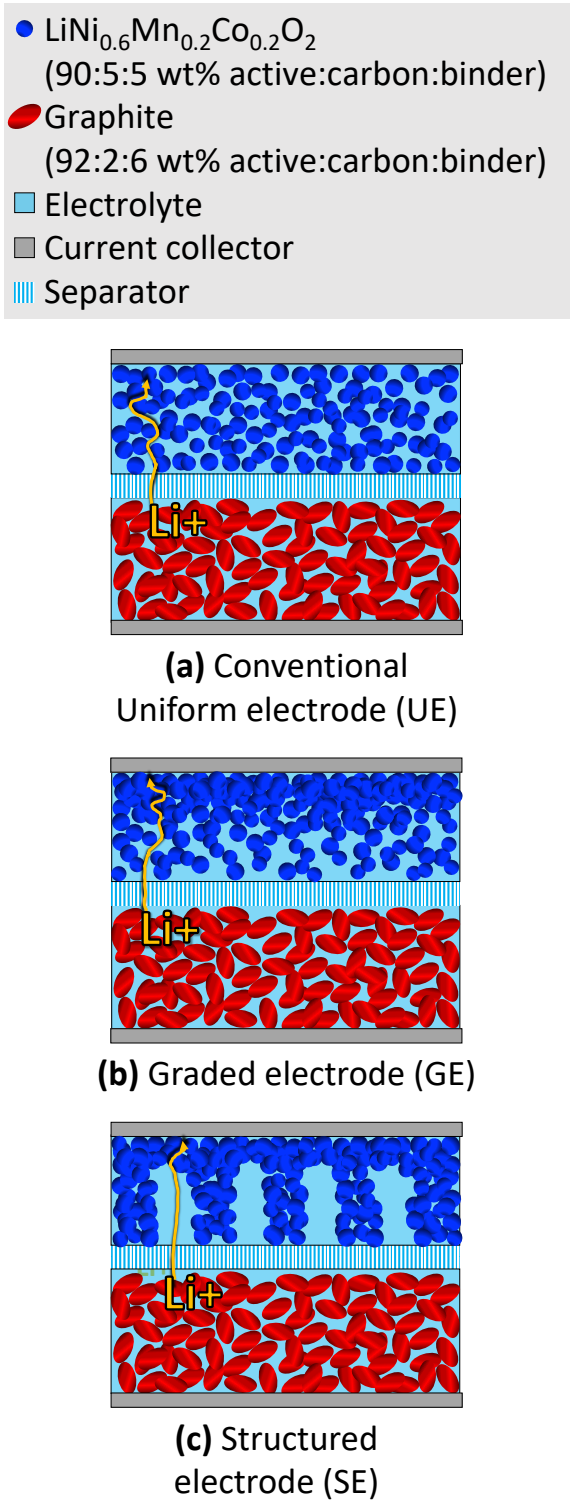

Figure 4.1. Schematic of (a) a conventional uniform electrode (UE), (b) a graded electrode (GE), and (c) a structured electrode (SE). All structuring conducted in this study is for the cathode only. The graphite anode maintains a conventional UE structure.

SEs have engineered micron-scale porosity referred to as “all electrolyte” regions that are free of active materials, binder, and carbon, as depicted in Figure 4.1 (c). The patterned “all electrolyte” regions are typically in the shape of “grid” or “line” patterns in literature, and these regions serve as low tortuosity pathways that enhance Li-ion transport in the liquid electrolyte. Compared to UEs, these “all-electrolyte” regions lead to a larger volume content of electrolyte in SEs and more “mobile” Li-ions in the liquid phase, which can have a significant effect on the performance observed for SEs in experiments. However, the impact of these additional Li-ions has not been analyzed in literature. A question that arises is whether performance improvements seen in SEs can be realized in UEs with similar electrolyte volumes.

As illustrated in Figure 4.1 (b), porosity-graded electrodes (GEs) have a more porous electrode layer in contact with the separator, which facilitates faster ionic transport at high C-rates. Towards the electrode-current collector interface, the electrode porosity decreases and has a denser active material packing, with the goal of adding capacity back to the overall electrode that was sacrificed for the porous “high-power” layer near the separator. Here GEs were modeled as a counterpart to SEs, as the GE designs also allow for reduced tortuosity and increased electrolyte volume. While several studies have reported performance improvements attributed to GEs, two notable single-objective optimization studies conducted by Dai and Srinivasan and Qi et al. have ultimately concluded that GEs offer little to no advantage over UEs when the electrode porosity and thickness are not constrained. In essence, any performance benefits observed in a GE design can be replicated in a UE through the appropriate selection of electrode porosity and thickness.

Compared to GEs, SEs offer several design advantages. First, the “all-electrolyte” regions in SEs are expected to significantly reduce transport tortuosity, more so than merely adjusting the porosity in GEs. Nevertheless, the extent to which this reduction in tortuosity influences discharge

specific capacity and energy density is still not fully understood. Second, both UEs and GEs have a percolation limit; beyond a certain porosity range, the electrode no longer form an effective conducting matrix for electrons.[133,134] For NMC electrodes, practical porosity ranges for functional cells fall in a range of 20% – 50% based on literature.[100,135–137] SEs do not have issues with this percolation threshold, allowing for an overall electrolyte volume ratio that is greater than what is permissible in UEs ad GEs.

In this chapter, single-layer cell models were developed for UEs, GEs, and SEs with systematically varied electrolyte volumes in the cathode. The objective is to separately study the effects of reduced tortuosity from those of increased electrolyte volume on material utilization. Furthermore, the energy and power density (Wh/L, Wh/kg, W/L, and W/kg) was calculated assuming the single-layer cells were assembled into a multi-layer stack, where the volume and weight of cathodes, anodes, separators, current collectors, and electrolyte were taken into account. The chapter aims to address Research Question 1a and 1c from section 1.3 on how SEs fundamentally improve transport and kinetic mechanisms at the cell level.

4.2 METHODS

4.2.1 *Material Model and Uniform Electrode (UE) Reference Cell Definition*

All models have material properties obtained from literature that correlate to the behavior of an NMC-622 cathode, a graphite anode, a Celgard 2325 separator, and a 1.2M $LiPF_6$ in 3:7 EC:EMC electrolyte. All UE, SE, and GE cells were modeled with the aforementioned properties, which are summarized in Table 4.1 and Table 4.2. The NMC-622 electrodes have a 90/5/5 weight percent (wt%) ratio of active material, carbon additive, and polyvinylidene fluoride (PVDF) binder, respectively. The graphite electrodes have a 92/2/6 wt% ratio of graphite, carbon additive, and PVDF binder. The assumed specific capacity is 187 mAh/g_{active} for NMC-622 and 370 mAh/g_{active} for graphite. Based on each electrode composition, the cathode and anode areal capacities were calculated, and the electrodes were designed to have a 1.0 negative (anode) to positive (cathode) electrode capacity ratio (N/P ratio). The applied current density for running a discharge cycle was calculated based on the cathode capacity, and the discharge models were run at C/10, C/5, C/2, 1C 2C, 4C, and 6C current rates.

In experimental literature, NMC-111, NMC-532, and NMC-622 electrodes have been made with a porosity range between 20% – 50% and a thickness range of 30 – 320 μm. [15,65,100,108,121,127,135,136,138–140] Electrodes >100 μm in thickness have been fabricated with slot-die coating[15,136] and doctor blade coating. [65,135,138,140] A recent tear-down study of the Volkswagen ID.3 pouch cells reported an 87.3 μm thick NMC cathode with a loading of 27.9 mg/cm^2,[141] which highlights how automakers are moving to thicker and more highly loaded electrodes. In a study conducted by Kraft et al.,[65] full cells were made with NMC-111 cathodes and grid-pattern SE graphite anodes of equal thicknesses between 71 μm – 116 μm. Their results showed that SE full

cells demonstrated a significant capacity improvement over UE full cells at 1C – 6C discharge rates when the electrode thicknesses were 116 μm. Moreover, a modeling study conducted by Azami-Ghadkolai et al. found SEs with a 30 mg/cm^2 loading can deliver the same areal capacity as its UE counterpart but at a rate which is three times faster.[142]

Leveraging these findings in literature, we created a baseline UE cell that has a cathode that is 116 μm thick with 35% porosity, which results in a cathode active material loading of approximately 30.6 mg_{active}/cm^2. Additional UEs were modeled with cathode porosities ranging from 20% to 50% and thicknesses between 94 μm and 151 μm. In the UE models, the cathode active material loading had small variances between 30.5 – 30.8 mg_{active}/cm^2 due to concurrent changes in electrode thickness and porosity, but these small variances do not affect our ability to systematically compare cells designs. Starting from the lowest porosity (UE-1) and ending with the highest porosity (UE-7), the UE models were labeled sequentially from UE-1 to UE-7 as noted in Appendix B. All graphite anodes have a 35.1% porosity and have a matching capacity to each cathode to ensure an N/P ratio of 1.0 is maintained. To examine the feasibility of meeting the USABC cell-level energy density goals of 300 Wh/kg and 750 Wh/L at a C/3 discharge rate,[143] two extremely thick UEs with a cathode active material loading of 65.0 mg_{active}/cm^2 were modeled as additional comparison points. Design parameters for all UE models are reported in Table B-I and Table B-II in Appendix B.

Table 4.1. Model parameters used for kinetics and transport in the solid phase.

Parameter	Description	Units	NMC-622	Graphite
D_s	Diffusion coefficient	m^2/s	$8.91 \cdot 10^{-13}$ (138)	$5 \cdot 10^{-14}$ (113)
σ	Electric conductivity	S/m	2 (138)	100
c_s^{max}	Maximum concentration	mol/m^3	49520 (113)	30000 (113)
c_s^0	Initial concentration	mol/m^3	14856 (129)	29670 (129)
α_a	Anodic transfer coefficient	N/A	0.5	0.5
α_c	Cathodic transfer coefficient	N/A	0.5	0.5
k	Reaction rate constant	$A \cdot cm^{2.5} / mol^{1.5}$	0.23327 (1)	0.4854 (1)
t_+^0	Transference number	N/A	0.462 (112)	0.462 (112)
R_{film}	Film resistance	$\Omega \cdot m^2$	0.014 (112)	0.025 (112)
ε_e	Volume fraction of liquid	N/A	0.35	0.351
ε_s	Volume fraction of solid	N/A	0.55	0.521
ε_f	Volume fraction of filler	N/A	0.1	0.128
R_s	Particle radius	m	$7.5 \cdot 10^{-6}$	$5.5 \cdot 10^{-6}$
p	Bruggeman constant	N/A	4.0 (138)	1.75 (112)

Table 4.2. Electrolyte and separator model parameters. N/A means not applicable.

Parameter	Description	Units	Electrolyte
D_e	Diffusion coefficient	m^2/s	$1 \cdot 10^{-9}$ [138]
c_e^0	Initial concentration	mol/m^3	1200 [113]
κ	Ionic conductivity	$\frac{S}{m}$	$\kappa(c_e) = (2.184c_e - 1.559{c_e}^2 + 0.3869{c_e}^3 - 0.0333{c_e}^4)$ [112]
Parameter	**Description**	**Units**	**Separator**
ε_e	Volume fraction of liquid	*N/A*	0.39
ε_s	Volume fraction of solid	*N/A*	0.61
p	Bruggeman constant	*N/A*	2.5 [112]

4.2.2 *Comparing Graded versus Structured Electrode Design*

The GE and SE cathodes paired with a conventional UE anode were designed as illustrated in Figure 4.2. Gallagher et al.[100] and Parikh et al.[136] both noted that thick-electrode graphite|NMC-622 cells are limited by Li-ion mass transport in the thickness direction, and mass transport is predominantly facilitated by the liquid electrolyte phase. This means additional electrolyte volume in thick electrodes has the potential to improve a battery's practical capacity. Nonetheless, if the electrode becomes too porous, it can introduce issues with low active material loading and limited particle percolation. This chapter focused on UE, GE, and SE cathodes with different electrolyte volumes to examine the impact of increasing the liquid phase volume fraction on cell performance. To ensure all cell models fall within practical regimes, the SE and GE models in this study were parameterized to have similar loadings as the UE models while allowing other SE and GE parameters such as feature dimensions and porosity to change.

This study further aims to separate transport behavior due to the increased electrolyte volume from other physics modalities caused by the SE and GE structures. To comparatively examine UEs, SEs, and GEs, it is important to independently quantify and examine the impact of additional electrolyte volume introduced into each system. For our analysis, we have defined an evaluation metric called the "electrolyte volume fraction" (EVF), which is the ratio of the electrolyte volume in the cathode to the apparent volume of the cathode. The apparent volume of the cathode encompasses all liquid and solid phases in the cathode, assuming there is no additional void space in the cathode. By comparing SEs and GEs to UEs with the same controlled EVF value, we can attribute the differences in their specific discharge capacity results to the SE or GE structure. In a conventional UE, the EVF is equal to the cathode porosity, as there is only one uniform electrode region, which we herein refer to as the "porous electrode + electrolyte" region.

A series of bilayer GE designs with a "first layer" interfacing the current collector and a "second layer" interfacing the separator were modeled as shown in Figure 4.2 (a). All GE designs were set up to have a less porous first layer and a more porous second layer. Within each layer, the porosity value is held constant, where t_1 is the thickness of the first layer with a porosity of ε_1 and t_2 is the thickness of the second layer with a porosity of ε_2. In each GE cathode, there were two "porous electrode + electrolyte" regions (one for each layer), and the EVF accounted for the electrolyte volume in both regions. The thickness and porosity of each GE layer were adjusted to ensure GE designs had a 35% – 55% EVF while maintaining a fixed cathode active material loading of approximately 31 mg_{active}/cm^2. Due to concurrent changes in the electrode porosity and thickness, all GE designs had an actual active material loading ranging from 30.6 – 30.7 mg_{active}/cm^2. Similar to the UE designs, these small fluctuations in active material loading do not

affect our ability to systematically compare all designs. The GE designs modeled in this study are further summarized in Table B-III and Table B-IV in Appendix B.

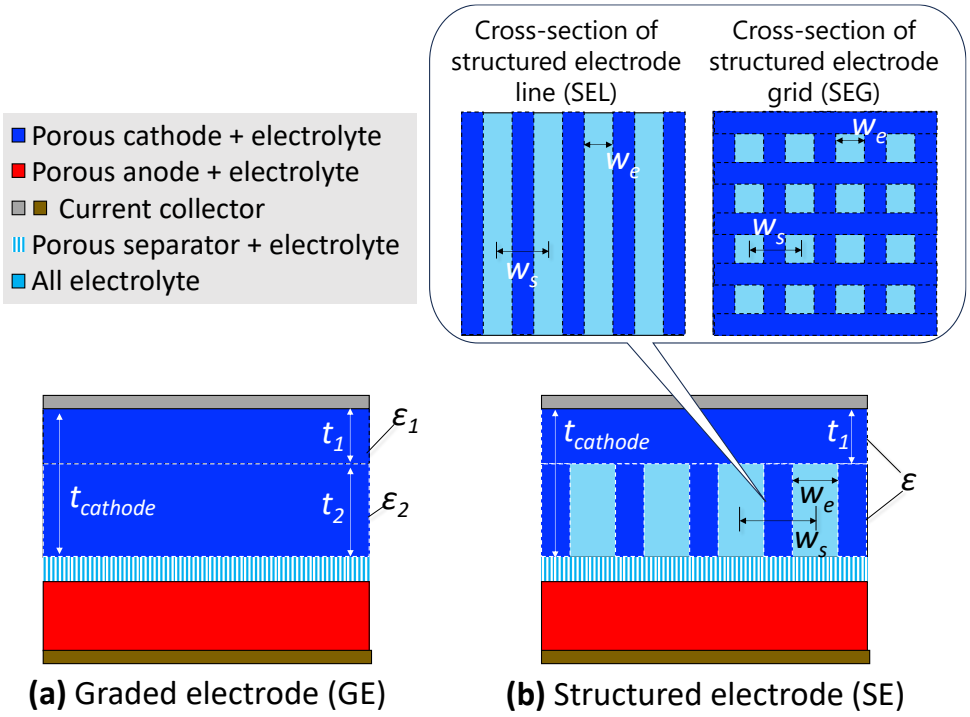

Figure 4.2. Illustrations of a (a) graded electrode (GE) and (b) structured electrode (SE) with design parameters labeled. The SE and GE design parameters include the dimensions and porosities of the "porous cathode + electrolyte" regions.

SEs with grid and line patterns were designed as illustrated in Figure 4.2 (b). As noted previously, these are the two most widely studied SE geometries in literature.[10,21,65] SEs with a grid pattern are referred to as SEGs, and SEs with a line pattern are referred to as SELs. An SE design is fully defined by its cathode thickness, $t_{cathode}$, first layer thickness, t_1, electrolyte channel width, w_e, electrolyte channel spacing, w_s, and porosity ε in the "porous cathode + electrolyte" region as labeled in Figure 4.2 (b). We refer to the SEs regions that are filled with only electrolyte as the "all electrolyte" regions, and the local porosity in the "all electrolyte region" is set to 100% in our models. The EVF calculation for SEs accounts for both the electrolyte volume in the "all

electrolyte" region as well as the "porous electrode + electrolyte" region. The SEGs and SELs modeled in this study are summarized in Table B-V – Table B-VIII and are further explained in Appendix B. All SE models have a 35% porosity value in the "porous cathode + electrolyte" region, as shown in Figure 4.2(b). An additional design configuration that has both structuring and grading in the cathode, which we refer to as SE+GE, was also modeled. The SE+GE design parameters, modeling results, and a short discussion can be found in Appendix B. This design configuration did not yield a performance improvement over UEs, GEs, or SEs, and as a result, SE+GE designs were not pursued further in our analysis.

9 UE, 9 GE, 10 SEG, 12 SEL, and 3 SE+GE design cases were modeled at C/10 – 6C discharge rates, resulting in 43 design cases and 230 discrete models for analysis. Each model generated discharge voltage versus time data for each C-rate, and during post-processing operations, specific discharge capacity (mAh/g_{active}) and energy (Wh) for the cell are calculated. This data was subsequently used to estimate Wh/kg and Wh/L performance in a hypothetical multi-layer EV pouch cell stack to examine if the additional EVF introduced by SEs and GEs impacts performance. Gravimetric and volumetric energy and power densities were calculated for a hypothetical multi-layer EV pouch cell stack assuming a total stack height of 0.98 – 1.03 cm, which corresponds to a 68 – 100 Ah pouch cell depending on the UE, SE, or GE design employed in the analysis. The weight and volume of the electrodes, electrolyte, separators, and current collectors were all taken into account in our calculations. The cell stack area was modeled based on the 2017 second generation Nissan LEAF® pouch cell form factor assuming a 10% cell seam.[144] We assumed the electrodes, separators, and current collectors all had the same area as the cell stack area. Additional details on our pouch cell stack assumptions and dimensions can be found in Appendix B.

4.3 Results and Discussion

4.3.1 *Electrolyte Volume Fraction (EVF) Trends*

Figure 4.3 demonstrates the impact of SEs and GEs on graphite|NMC-622 Li-ion utilization and discharge rate capability. By controlling the total EVF in UEs, GEs, and SEs, we examined whether the specific discharge capacity is driven by the electrolyte volume in the cathode, or if the electrode geometry is the dominating factor that affects cell performance. 2C, 4C, and 6C specific discharge capacity results for UEs, GEs, and SEs with "line" and "grid" patterns are plotted in Figure 4.3. The x-axis represents the total EVF as defined in section 4.2. All design cases in Figure 4.3 have a cathode active material loading of approximately 31 mg_{active}/cm^2 to study the impact of GEs and SEs on ultra-thick electrodes (>100 μm) with high loading. Due to percolation limits, UE and GE designs cannot exceed a 50% EVF. The SEs and GEs modeled do not have an EVF less than 35% due to the porosity constraints imposed as explained previously in section 4.2. For each design type, the model case numbers are ordered from low to high EVF, corresponding to UE-1 – UE-7, GE-1 – GE-7, SEL-1 – SEL-12, and SEG-1 – SEG-9. The details of the design parameters that compose each cell are summarized in Tables B-I – B-VIII in Appendix B. C/2 and 1C specific discharge capacity results (see Figure B5 in Appendix B) show that SEs and GEs exhibit negligible benefits at low C-rates, which is expected behavior based on previously published research results.[65] Thus, we focus our analysis on 2C, 4C, and 6C discharge rates to understand electrode design impacts at higher power rates.

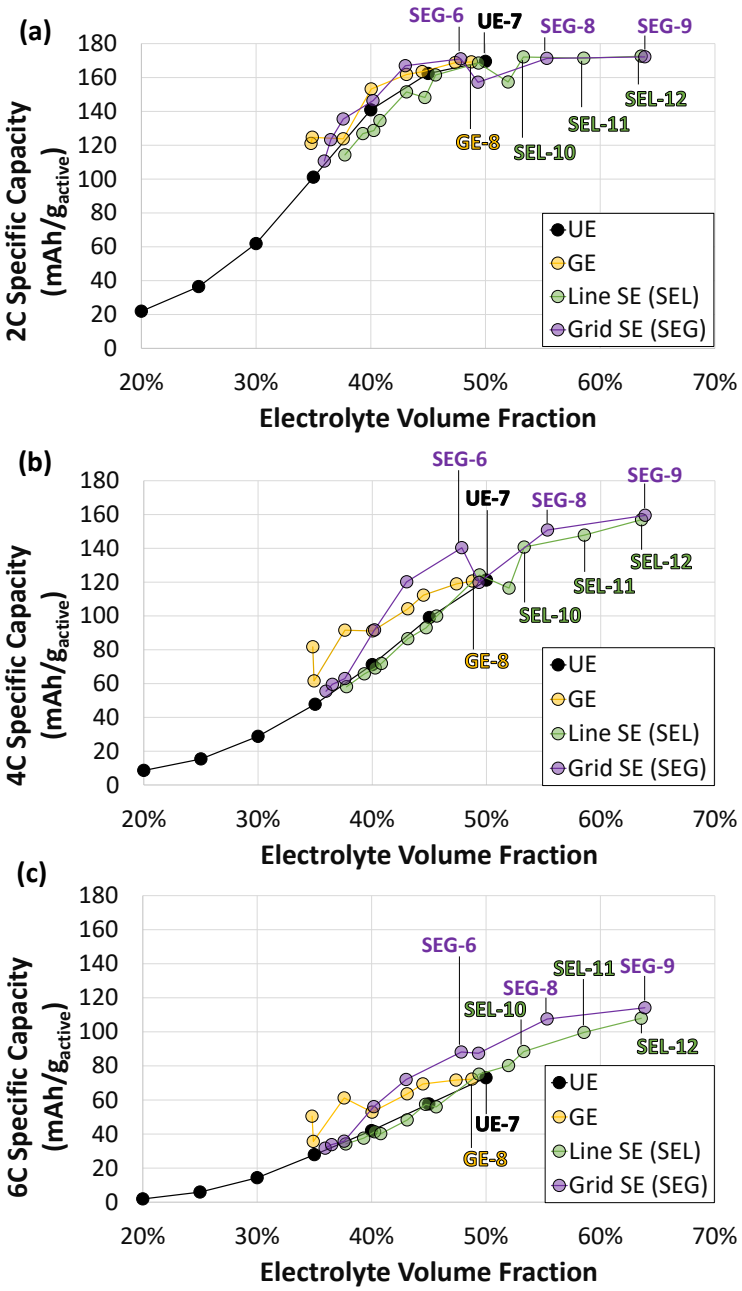

Figure 4.3. Specific discharge capacity at (a) 2C, (b) 4C, and (c) 6C discharge rates is plotted against the electrolyte volume fraction (EVF) for uniform electrode (UE), graded electrode (GE), "line" structured electrode (SEL), and "grid" structured electrode (SEG) models with electrolyte volume fractions between 20% and 64%.

Looking at Figure 4.3, the increasing EVF in the cathode leads to higher specific discharge capacity values across all designs. This result is expected as NMC materials are known to be predominantly liquid-phase transport limited.[100] At EVFs of 40% and higher, SEGs demonstrated the highest capacity values among all design types when compared at a fixed EVF value. At EVFs of 40% and lower, GEs had the highest specific discharge capacity values. We believe this result is due to the fact that at low EVFs, it is increasingly difficult for Li-ions to intercalate into the "porous electrode + electrolyte" regions in UEs and SEs, which in both design types have a 35% porosity. In contrast, GEs had a more porous second layer interfacing the separator with porosity values between 39% – 50%, which allowed the GEs to achieve higher lithiation and in turn realize higher capacity. Looking at all plots in Figure 4.3 holistically, the EVF has the greatest impact on cell performance regardless of the electrode design. This general observation supports our hypothesis that controlling the EVF is integral to enabling high Li-ion active material utilization in thick, highly loaded graphite|NMC-622 cells at high discharge rates. However, the variance in specific discharge capacity results among UEs, GEs, SELs, and SEGs at a fixed EVF value also indicates that the contribution of electrode design cannot be overlooked.

4.3.2 *Discharge Rate Capability Improvements with SEs*

Focusing on the 2C specific discharge capacity in Figure 4.3 (a), a plateau in SE capacity values is observed as the EVFs increase beyond 50%. Multiple SE cases, including SEG-6, SEG-8, SEG-9, SEL-10, SEL-11, and SEL-12, reached a specific discharge capacity of 170 mAh/$g_{active,}$ which is approaching the practical capacity limit of graphite|NMC-622 full cells. UE-7 and GE-7, with a 50% and 49% EVF respectively, also achieved 170 mAh/g_{active}. Thus, across the UE, GE, and SE design types, a high enough EVF value enables all cell designs to realize close to the practical capacity limit of graphite|NMC-622. As a reminder, all designs modeled in Figure 4.3

have a cathode active material loading of approximately 31 mg_{active}/cm^2. SE and GE designs exhibit no substantial benefit over UEs at a discharge rate of 2C, and a similar trend is also observed at 1C and C/2 discharge rates (see Figure B5 in Appendix B). This finding affirms that understanding the design benefits of SEs and GEs relative to UEs requires examining higher discharge rates.

Discharge rate capability is defined as a battery's ability to hold its capacity at increasing discharge rates. We now analyze the 4C and 6C specific discharge capacity results in Figure 4.3 for the cases that exhibited close to their practical capacity limit at 2C to see if better rate capability can be achieved. UE-7 and GE-7 both have specific discharge capacities between 119 – 121 mAh/g_{active} at 4C and between 72 – 73 mAh/g_{active} at 6C, indicating the best GE design modeled in this study showed no improvement in rate capability over a UE. In contrast, SEs demonstrated a specific discharge capacity of 140 – 160 mAh/g_{active} at 4C and 88 – 114 mAh/g_{active} at 6C. These values correspond to specific discharge capacity improvements of 17% – 33% at 4C and 17% – 52% at 6C over UE-7, demonstrating the ability of SEs to improve the rate capability of thick, highly-loaded graphite|NMC-622 cells relative to equivalent UE designs. Figure 4.4 shows the solid-phase and liquid-phase Li-ion concentrations at the beginning and end of discharge (EOD) at 6C. Cases that demonstrated the highest rate capability in each design category were plotted, which include UE-7, GE-8, SEL-12, and SEG-9. The models are arranged in Figure 4.4 such that the anode is the top electrode, and the cathode is the base electrode, with a 25 μm thick separator sandwiched in between the electrodes.

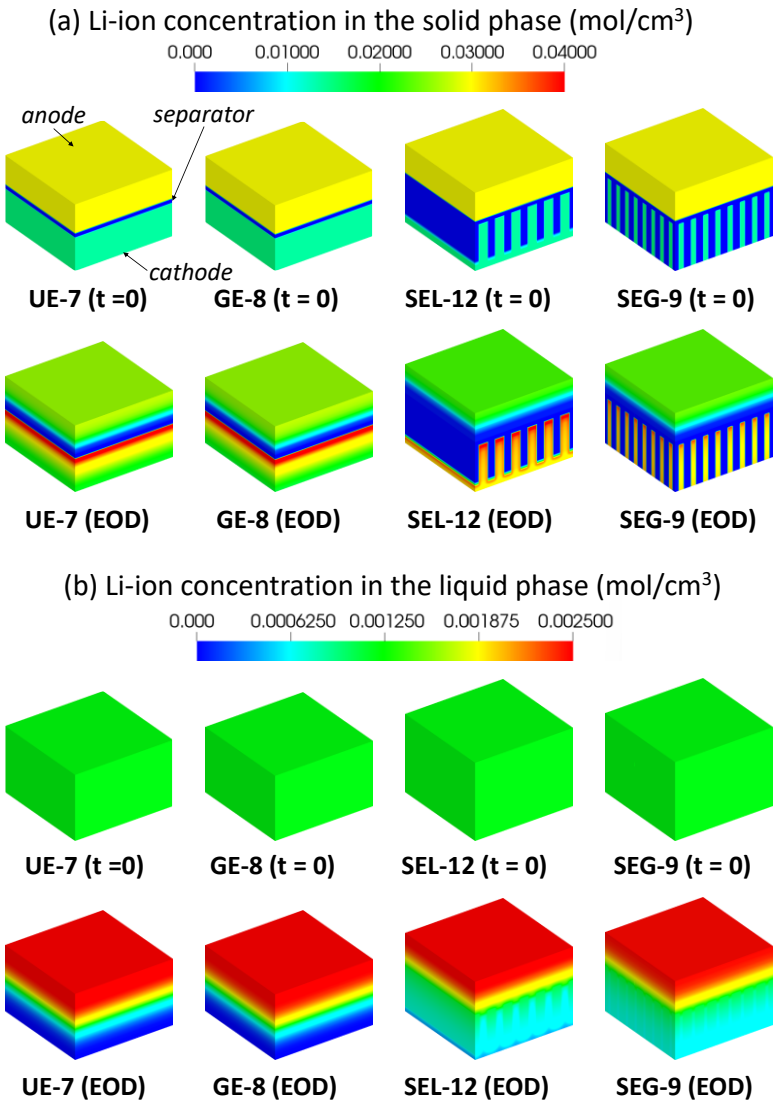

Figure 4.4. Comparison of Li-ion concentration gradients in selected uniform electrode (UE), graded electrode (GE), line structured electrode (SEL), and grid structured electrode (SEG) models. From left to right, each selected model case demonstrates the highest rate capability in its design category. Li-ion concentration in the (a) solid phase and (b) liquid phase at the beginning of 6C discharge (time, $t = 0$) and end of discharge (EOD) are plotted.

At $t = 0$, the graphite anodes had an initial solid-phase concentration of 0.029670 mol/cm^3 (displayed in yellow in Figure 4.4 (a)), and the NMC-622 cathodes had an initial solid-phase concentration of 0.014856 mol/cm^3 (displayed in the blue-green color Figure 4.4 (a)). At the EOD, the red regions in the cathode, displayed in Figure 4.4 (a), indicate electrode areas that had close to full lithiation. UE-7 and GE-8 had similar EOD solid-phase concentration gradients, where high lithiation was concentrated at the separator-cathode interface, but more than half of the cathode volume had minimal lithiation. In SEL-12 and SEG-9, high lithiation across the electrode thickness is reached as indicated by the red, orange, and yellow color gradients. Examining the liquid phase in Figure 4.4 (b), at $t = 0$, all models started out with a uniform liquid-phase Li-ion concentration of 0.0012 mol/cm^3, as noted in green. Once the EOD was reached, a high concentration gradient is observed in UE-7 and GE-8, and the dark blue color at the base of the cathodes indicates the electrolyte was close to being depleted in these models. Conversely, SEL-12 and SEG-9 had a more uniform liquid-phase concentration gradient at the EOD, likely due to the "all electrolyte" regions in the SE designs that facilitated transport more rapidly through the cathode thickness. In SEL-12 at the EOD, a slight columnar concentration gradient of non-uniformity tracing the geometry of the line pattern and dark blue regions (representing electrolyte depletion) is seen at the cathode base in Figure 4.4 (b). In comparison, SEG-9 did not have columnar concentration gradient and showed no sign of electrolyte depletion at the EOD. In summary, with a similar EVF value of 64%, SEG-9 facilitated better Li-ion transport than SEL-12, which explains its slightly higher 6C specific discharge capacity over SEL-12 and indicates an SE grid pattern can yield improved rate performance over an SE line pattern.

4.3.3 *Analyzing Reduced Tortuosity and Increased Li-ion Content*

We further analyze the SE cases that showed improvements in discharge rate capability to understand the underlying mechanism that led to these improvements. Prior research has noted that SEs help reduce the concentration gradient across the electrode thickness relative to UEs; This is often attributed to a reduction in electrode tortuosity, but little focus has been placed on the impact of the additional Li-ions due to higher EVFs.[21,65,145] This raises a question of whether or not increasing electrode porosity in UEs or GEs would yield similar performance improvements. Here we look at how additional Li-ions in the electrolyte phase versus reduced tortuosity impact SE rate capability improvements.

Six SEs demonstrated improved 4C and 6C rate capability over UEs: SEG-6, SEG-8, SEG-9, SEL-10, SEL-11, and SEL-12, as labeled in Figure 4.3. Among these cases, SEG-6 had a lower EVF (48%) than UE-7 (50%) but showed an improved specific discharge capacity. The specific discharge capacity improvements in SEG-6 over UE-7 were 15.8% (+19.1 mAh/g_{active}) at 4C and 20.8% (+15.1 mAh/g_{active}) at 6C. With a lower EVF value, these improvements are likely attributed to the SE architecture that reduced transport tortuosity. This illustrates how electrode structuring can have a larger impact than EVF, introducing specific discharge capacity improvements at higher discharge rates despite lower EVF values. Now we consider SEG-9, which had the highest EVF value (64%) in this study and contained the largest Li-ion content. Assuming the specific discharge capacity gains over UE-7 due to reduced tortuosity remain consistent across SEG-6 and SEG-9, we can attribute the remaining portion of specific discharge capacity improvements in SEG-9 to the increased Li-ion content. Based on this assumption, we can presume the specific discharge capacity improvement at 4C, due to a lower tortuosity, is +19.1 mAh/g_{active}, while the specific discharge capacity improvement resulting from an increase in Li-ions is +19.2 mAh/g_{active}. This

yields an approximate 1:1 ratio of specific discharge capacity between these two scenarios. At 6C, the specific discharge capacity ratio increases to 1:1.72 for the same analysis. Within the EVF range evaluated in this study, reduced tortuosity accounts for at least one-third of the rate capability improvements observed for SEs relative to UEs, and this performance improvement cannot otherwise be achieved by increasing the porosity in UEs.

From a design perspective, SEs can offer battery engineers more design options, and increasing the EVF, while effective, is not the only route available to improve rate capability. If we consider potential system-level impacts, an analysis published by Schmuch et al.[146] discussed how the electrodes form most of the cost of batteries made with carbon-based anodes and NMC cathodes. The carbonate-based electrolyte also has a much lighter mass density (~1.23 g/cm^3) than typical NMC materials (~4.7 g/cm^3). While a more detailed techno-economic analysis is needed, we believe these rough estimates indicate that potentially increasing the EVF in SEs can lead to a lower-cost and lighter-weight battery. Despite these benefits, we caution that the overall mass density of the cell may need to be re-balanced to maintain the necessary energy density targets depending on the end application. SEs provide additional design variables that can improve high-rate performance, but manufacturing these batteries at scale requires carefully balancing the additional design freedom SEs offer for electrode engineering.

4.3.4 *SE Nonlinear Design Trends and Performance Impacts*

Here the SE design trends shown in Figure 4.3 were investigated in more detail, focusing on the grid and line patterned cathode geometries and their relative performance against UEs. For UEs, the specific discharge capacity increases monotonically with increasing EVF, while for GEs and SEs, the data trends in a non-monotonic manner wherein some design cases have a lower specific discharge capacity despite increasing EVF values. Below we focus on the SE design

trends, and specifically on the SEG cases since they were the best overall performing designs as discussed in the previous section. Further details on the design trends observed with GEs can be found in Figure B2 in Appendix B.

From a design perspective, SEs exhibit nonlinear trends if we examine the response of the specific discharge capacity results to changing SE dimensions. The EVF in SEs was determined by systematically varying the first layer thickness (t_1) and electrolyte channel spacing (w_s), noted previously in Figure 4.2. Going in order from SEG-1 to SEG-9, every three designs had the same electrolyte channel spacing (see Table B-V and Table B-VI in Appendix B). Figure 4.5 shows the 4C end of discharge (EOD) Li-ion concentration in both the solid and liquid phases for SEG-1 – SEG-9. For the electrolyte channel spacing, SEG-1 – SEG-3 had a 200 µm spacing, SEG-4 – SEG-6 had a 90 µm spacing, and SEG-7 – SEG-9 had a 60 µm spacing. Within each row of SEGs in Figure 4.5 (a), the first layer thickness was decreased from 75 µm, to 50 µm, and to 0 µm. The SEL-1 – SEL-12 cases were designed using the same procedure, and their dimensions can be found in Table B-VII and Table B-VIII in Appendix B.

The specific discharge capacity results in Figure 4.3 shows that when SEs have a fixed electrolyte channel spacing (w_s), specific discharge capacity only increased when the first layer thickness (t_1) was reduced. What is interesting to observe is that in this scenario a nonlinear trend in specific discharge capacity improvement is observed. We first focus on the 4C discharge data in Figure 4.3 (b) for SEG-1 – SEG-3, where each design case has a w_s of 200 µm. Going from SEG-1 to SEG-2, reducing t_1 by 25 µm led to a +4.1 mAh/g_{active} improvement; Going from SEG-2 to SEG-3, reducing t_1 by 50 µm resulted in a +3.4 mAh/g_{active} improvement. Reducing t_1 in the same manner between SEG-4 to SEG-5 and SEG-5 to SEG-6 (w_s = 90 µm for these cases) resulted in larger specific discharge capacity improvements of +28.5 mAh/g_{active} and +20.2 mAh/$g_{active,}$

respectively. From SEG-7 to SEG-9 (w_s= 60 μm), the specific discharge capacity improvements displayed a nonlinear trend, showing a +31.0 mAh/g_{active} improvement from SEG-7 to SEG-8 and a smaller +8.7 mAh/g_{active} improvement from SEG-8 to SEG-9. These results demonstrate an interaction effect between two independent SE design parameters (w_s and t_1) on specific discharge capacity. Thus, it is important to examine both parameters concurrently when looking to improve the specific discharge capacity and discharge rate capability of SEs.

4.3.5 *Design Trend Analysis with 3D Li-ion Concentration Plots*

We now examine the specific discharge capacity results in Figure 4.3 (b) using the 4C EOD solid-phase and liquid-phase Li-ion concentration plots shown in Figure 4.5. In Figure 4.5 (a), having the widest 200 μm electrolyte channel spacing, SEG-1 – SEG-3 exhibited a lithiation front that yielded close to full lithiation (red) near the cathode-separator interface. Moderate but less lithiation (yellow) is observed around the electrode walls that bound the "all electrolyte" regions in the design. We believe this is because there is a stronger electrochemical driving force in the z-direction if we examine the liquid-phase concentration gradient in the blue-green regions in SEG-1 – SEG-3 in Figure 4.5 (b). This drives more Li-ions into the porous cathode in the z-direction. In comparison, the liquid-phase concentration gradient in the x- and y- directions was much lower within the "all electrolyte" regions.

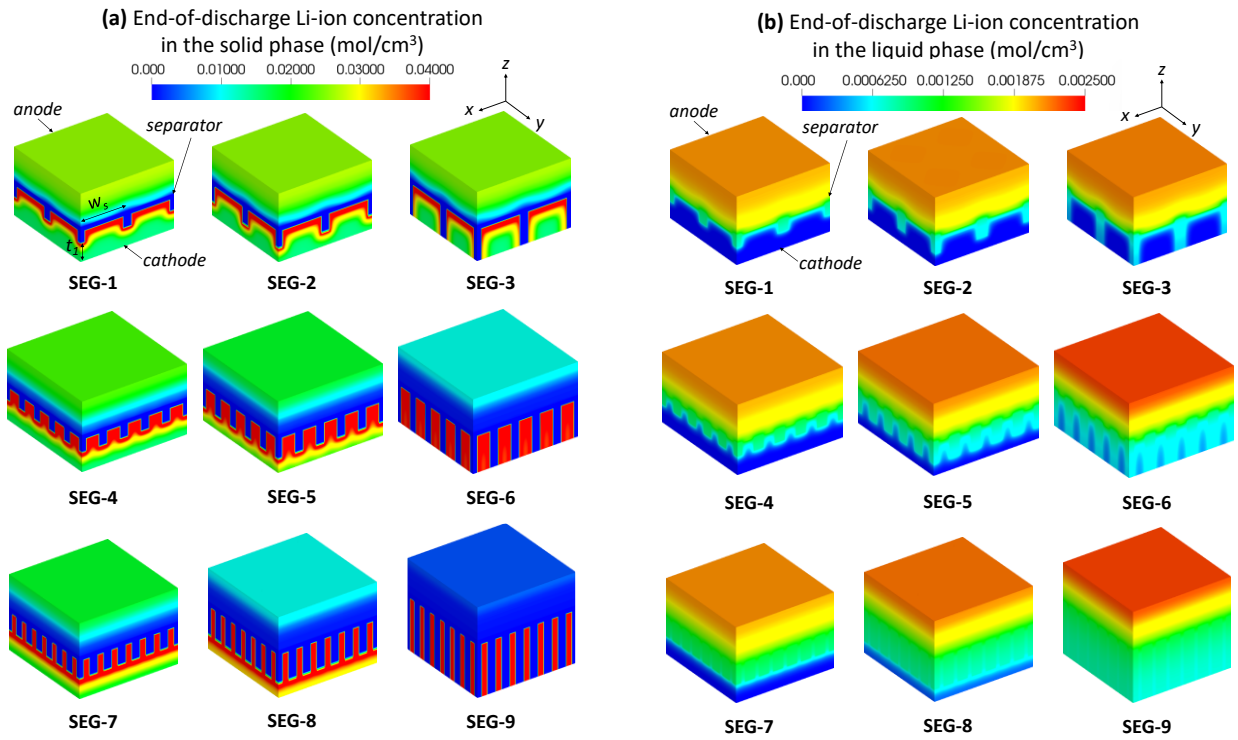

Figure 4.5. 4C end-of-discharge Li-ion concentration in the (a) solid phase and (b) liquid phase for grid structured electrodes (SEG) with increasing electrolyte volume fraction (EVF) displayed starting with the lowest porosity design SEG-1 and ending with the highest porosity design SEG-9. The electrolyte channel spacing (w_s) decreases from the first row (starting with SEG-1 – SEG-3) to the third row. In addition, the first layer thickness (t_1), starting with the SEG-1, SEG-4, SEG-7 column, goes in increments of t_1= 75 µm, 50 µm, and 0 µm, from left to right.

In Figure 4.5 (b), the porous cathode region is dark blue for SEG-1 – SEG-3, indicating Li-ion depletion has occurred and mass transport in the electrolyte region within the porous cathode was the rate limiting mechanism. The electrolyte channels in SEG-3, which extend through the entire cathode thickness in the z-direction, enabled Li-ions to travel further through the electrode thickness. We believe this behavior delayed the onset of electrolyte depletion and allowed more Li-ions to intercalate in the cathode. However, with a first layer thickness (t_1) of zero, SEG-3 exhibits less lithiation in the z-direction compared to SEG-1 and SEG-2. This offsets the benefit of delayed electrolyte depletion in SEG-3, which is why there was less capacity improvement

between SEG-2 and SEG-3 compared to the capacity improvement observed between SEG-1 and SEG-2. Moving on to SEG-4, SEG-5, and SEG-6, which had a smaller electrolyte channel spacing of w_s = 90 μm, we see the lithiation front progresses through the entire electrolyte channel at 4C EOD and stopped at the top of the first layer thickness in SEG-4 and SEG-5, as shown by the red regions in Figure 4.5 (a). Without a first layer thickness, SEG-6 demonstrated uniform lithiation throughout the cathode thickness. SEG-6 was more effective in resisting electrolyte depletion and exhibited fewer dark blue regions when compared to SEG-3, which still had a substantial amount of dark blue in the porous cathode in Figure 4.5 (b). As a result, higher specific discharge capacity improvements are seen in SEG-6 relative to SEG-5 versus the improvement seen from SEG-2 to SEG-3.

Comparing SEG-6 to SEG-7 in Figure 4.3 (b), SEG-6 has a higher specific discharge capacity despite its lower EVF value, showcasing another example where structuring the electrode has a larger impact than the EVF. SEG-7 had a 149 μm thick cathode and one of the smallest electrolyte channel spacings (w_s) to maintain a cathode active material loading of approximately 31 mg_{active}/cm^2. At this cathode thickness, the impact of the first layer thickness became more significant. In the liquid phase concentration plots Figure 4.5 (b), it is evident that the first layer in SEG-7 created a higher concentration gradient and, in turn, faster electrolyte depletion than SEG-5 and SEG-6. Reducing the first layer thickness from SEG-7 to SEG-8 improves the specific discharge capacity results. However, going from SEG-8 to SEG-9, a small improvement in specific discharge capacity is seen. In Figure 4.5 (a), the cathode of SEG-9 was almost entirely red, and the anode was nearly fully de-lithiated. The highest gradient in SEG-9 resided in the liquid phase of anode. We believe the rate-limiting step gradually transitioned from liquid-phase transport in cathode to that in anode between SEG-8 and SEG-9. At this point, increasing the cathode EVF did

not lead to a significant specific discharge capacity improvement because transport in the cathode no longer dominated the cell performance.

4.3.6 *Impact of SE Geometry*

Across the EVF values modeled, SEGs with grid pattern geometries had higher specific discharge capacity values, on average, when compared with SELs which had line pattern geometries. SE geometry type does affect specific discharge capacity, as exhibited by the non-linear trends in Figure 4.3 and the performance differences observed between the SEG and SEL cases modeled. However, compared to SEG-9, SEL-12 demonstrated very similar specific capacity results. SEL-12 only had a 2.6 mAh/g_{active} lower 6C specific capacity relative to SEG-9. These two cases had the highest EVF and rate capability in their respective design categories. As demonstrated in Figure 4.3, the green and purple lines converge with increasing EVF values. This tells us that while SE geometry is important, the impact of SE geometry becomes less significant with increasing EVF values, which coincides with our findings that the impact of reduced tortuosity decreases with a higher EVF. Based on the higher overall performance exhibited by the SEG cases modeled, relative to the SELs, we focused on the SEG category of SEs for a more in-depth comparative analysis of UEs, GEs, and SEs at larger scales in the next section.

4.3.7 *GE and SEG Energy Density Analysis for EV Pouch Cell Scales*

We analyze GE and SEG performance based on gravimetric and volumetric energy density, which are common metrics for EV applications. In a previous study conducted by Hung et al,[1] the authors note that the weight and volume of all cell components should be taken into account early in the design cycle in order to gain a true estimation of performance impact at scale. Thus, the energy density of SEGs and GEs were calculated assuming a hypothetical pouch cell electrode

stack based on a Nissan LEAF® form factor with a thickness in the range of 0.98 – 1.03 cm. The weight and volume of all electrodes, separators, current collectors, and electrolyte were included. A complete explanation of the energy density calculation used in this study can be found in Appendix B. In Figure 4.6, the gravimetric and volumetric energy density of GE-1 – GE-9 and SEG-1 – SEG-9 are plotted against the EVF. An additional GE case, GE-9, was modeled and plotted in Figure 4.6. GE-9 had a second layer porosity of 64% and was modeled to examine the design trend of a two-layer GE that exhibited an EVF greater than 50% as a comparison point to the SEs modeled in this study. The practical GE design range of 20% – 50 % porosity, discussed previously in section 4.2, is marked by the pink region in Figure 4.6.

Looking at the pouch cell analysis against the EVF in Figure 4.6, we see that as the EVF increases, the energy density initially rises and reaches a maximum value and then begins to drop. The data shows that too high of an EVF can negatively impact C/2 and 1C pouch cell performance; as seen in Figure 4.6, a decline of around 30 Wh/kg and 200 Wh/L is observed between EVFs of 35% to 65% in SEGs. This result is due to the increasing electrolyte content in the cell design and the relatively low mass density of the electrolyte (~1.23 g/cm^3). In Figure 4.6, we can find an EVF value range that led to the highest energy density result at each C-rate, and this EVF value range increases with an increasing C-rate. In Figure 4.6 **(**a), SEGs showed C/2 and 1C gravimetric energy density peaks at 38% – 40 % EVF, 2C gravimetric energy density peaks at 45 – 50% EVF, and 4C and 6C gravimetric energy density peaks at 55% – 65% EVF. Furthermore, the volumetric energy density results in Figure 4.6 (b) peaked at EVF value ranges that were about 5% less than the aforementioned EVF value ranges found for gravimetric energy density in Figure 4.6 (a). In practical design scenarios, it is important to choose an EVF target that yields the best balance between simultaneously improving both gravimetric and volumetric energy density. For an

application that requires high rate capability, our results show that the optimal SEG design will likely fall somewhere between 48% – 55% EVF.

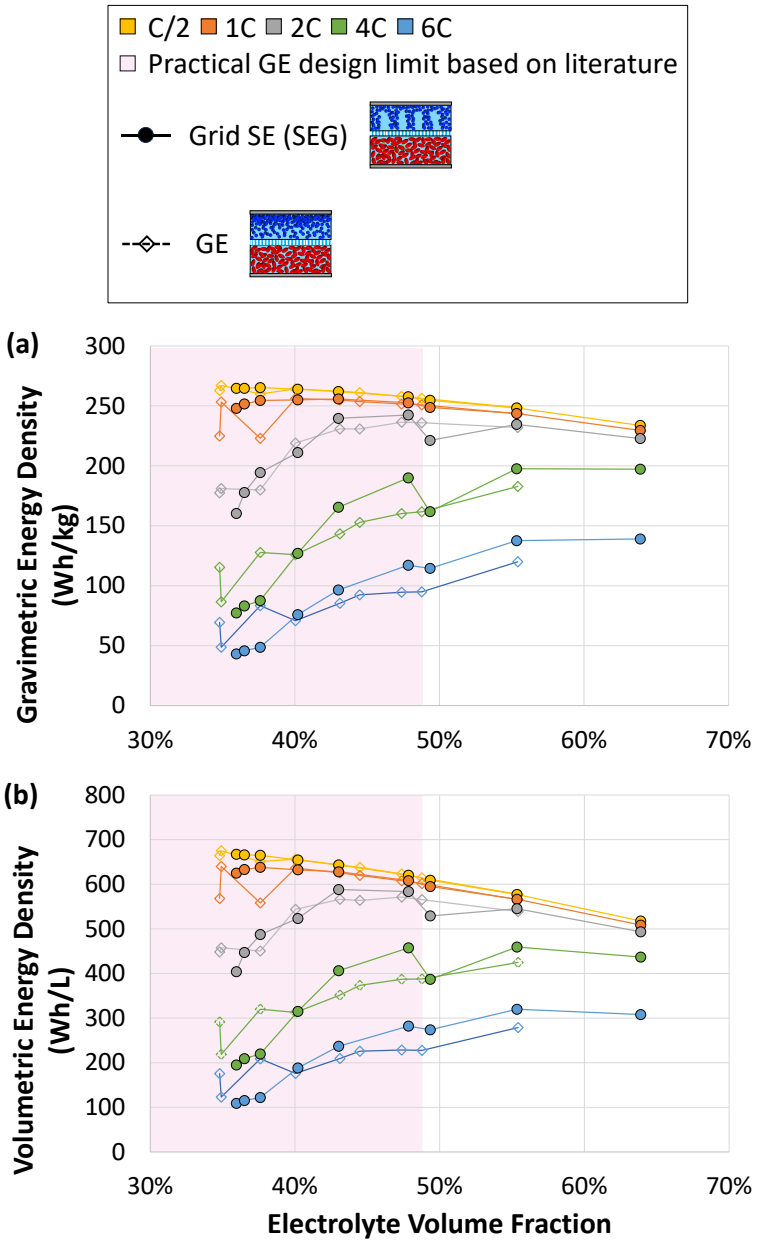

Figure 4.6. (a) Gravimetric energy density and (b) volumetric energy density for graded electrode (GE, empty diamond markers) and "grid" structured electrode (SEG, solid round markers) models with electrolyte volume fraction (EVF) values between 35% and 64%.

Similar to the specific discharge capacity results presented in Figure 4.3, GEs demonstrated no energy density improvement when compared to SEGs unless less than 40% EVF was employed. Our analysis found that SEGs and GEs with the same EVF have a similar cathode thickness (see Table B-III and Table B-V in Appendix B). Since electrode thickness has a high impact on the pouch cell weight calculation, there exists no significant difference in packaging efficiency to increase Wh/kg and Wh/L between these designs. The energy density performance differences between SEs and GEs were thus due to better transport in SEs enabled by the additional all electrolyte regions.

4.3.8 *UE, GE, and SEG Energy and Power Density*

Ragone plots for UEs, GEs, and SEGs with energy density on the vertical axis and power density on the horizontal axis are shown in Figure 4.7. Energy density was modeled and analyzed at C/2, 1C, 2C, 4C, and 6C discharge rates. Modeling results for all design cases presented in this study can be found in Table B-XII in Appendix B. Based on the modeling results, the maximum achievable C/2 energy density values are 266 Wh/kg (UE-4 and UE-5) and 672 Wh/L (UE-4) for UEs, 267 Wh/kg (GE-2) and 675 Wh/L (GE-2) for GEs, 265 Wh/kg (SEG-1 – SEG-3) and 667 Wh/L (SEG-1) for SEGs. In Figure 4.7, the design range for UEs, GEs, and SEs are upper bounded on the y-axis by cases that demonstrated the highest energy density values at 4C and 6C discharge rates. The lower bounds of the design ranges were determined by selected cases that demonstrated within a 3% loss in C/2 energy density but maintained the highest rate capability in its given design category. The same bounding cases are included in both gravimetric and volumetric Ragone plots. The design range for SEGs is shaded in purple, and the design range for GEs is shaded in yellow.

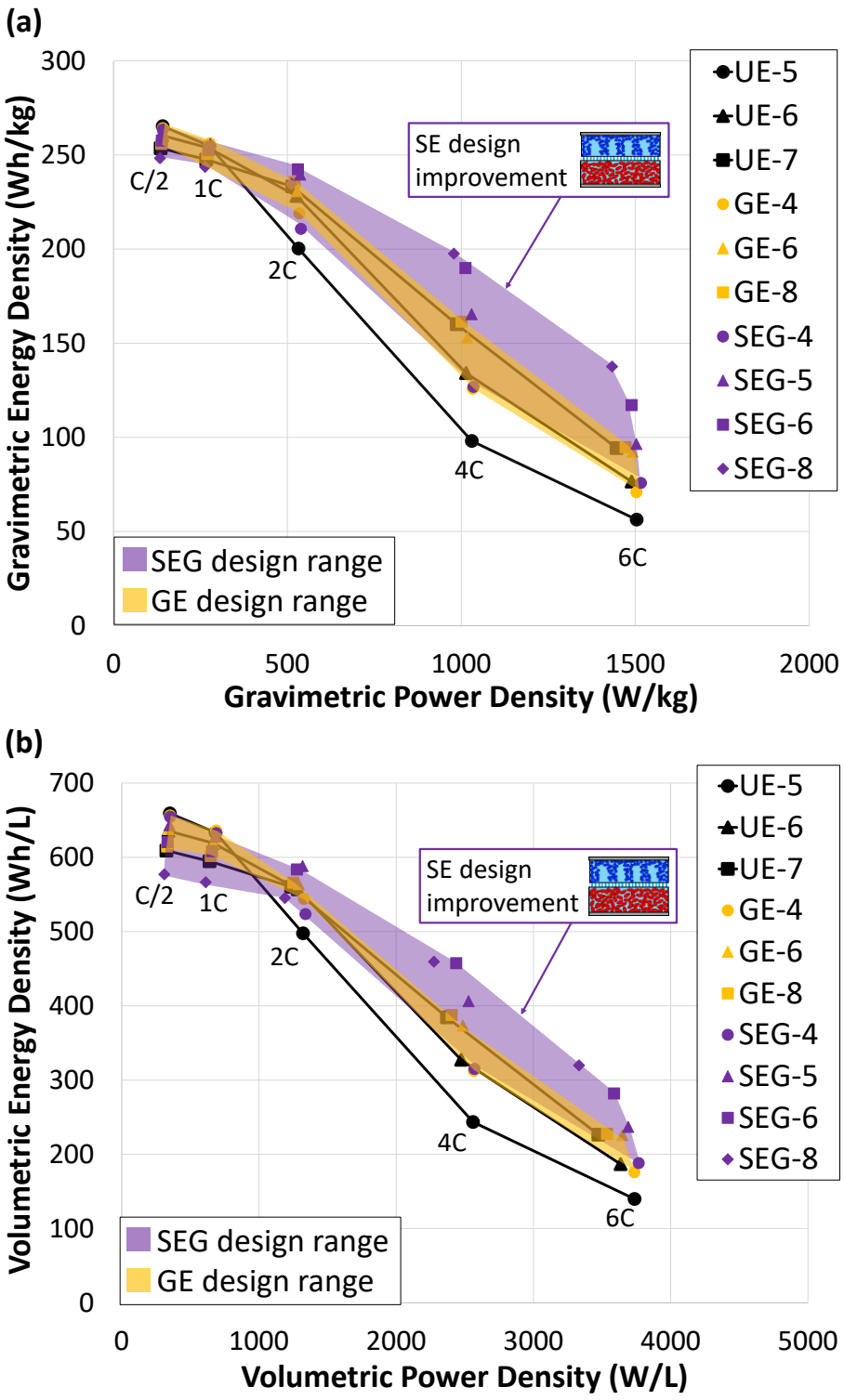

Figure 4.7. (a) Gravimetric and (b) volumetric energy and power density at C/2, 1C, 2C, 4C, and 6C discharge rates are plotted for the uniform electrode (UE), graded electrode (GE), and grid structured electrode (SEG) models. Design bounds for GEs are highlighted with a yellow shaded outline while the purple shaded outline annotates the SEG design bounds.

The design benefit of SEGs over GEs and UEs is demonstrated in the rate capability results shown in Figure 4.7 with the shaded purple region that extends above the other two design categories at 4C and 6C discharge rates. In Figure 4.7 (a), all design categories demonstrated similar C/2 gravimetric energy density value ranges, and SEGs as a design category showed up to a 40 Wh/kg increase in energy density between 2C and 6C discharge rates. Comparing one of the SEG upper-bounding cases, SEG-6 (purple square markers), to the upper-bounding UE case, UE-7 (black square markers), we observe a +0.8%, +1.1%, +3.0%, +17.7%, and +23.2% Wh/kg improvement over UEs at C/2, 1C, 2C, 4C, and 6C discharge rates, respectively. These improvements at higher-discharge rates highlight the benefit of SEGs for improving rate capability and energy density in thick electrodes. If we compare the other upper-bounding case SEG-8 (purple diamond markers) to UE-7 (black square markers), the results show a slightly different trend. Relative to UE-7, SEG-8 showed a -2.9%, -2.4%, -0.3%, +22.4%, and +44.7% Wh/kg performance difference at C/2, 1C, 2C, 4C, and 6C discharge rates, respectively. While a more substantial improvement is observed at 6C for SEG-8 than SEG-6, a slight loss at C/2 – 2C discharge rates is incurred with the SEG-8 design. Additional rate capability improvements of SEGs relative to UEs can also be seen in the volumetric energy density plot in Figure 4.7 (b), where the improvement trends for Wh/L were similar to those observed for Wh/kg. Relative to UE-7, SEG-6 demonstrated a +1.7%, +2.1%, +4.0%, +18.8%, and +24.3% improvement in Wh/L at C/2, 1C, 2C, 4C, and 6C discharge rates, respectively. The results showcase how an SE can enable energy density improvements up to 24% at all discharge rates between C/2 – 6C. Similar to its Wh/kg results, SEG-8 showed a -5.4%, -4.9%, -2.8%, +19.3%, and +41.0% Wh/L performance difference, relative to UE-7, at C/2, 1C, 2C, 4C, and 6C discharge rates, respectively. The results illustrate that

substantial improvements at high-power current rates will require some compromises in slow-rate performance.

The potential design improvement of GEs over UEs is also shown in Figure 4.7 where a shaded yellow region represents the GE design range. Relative to SEGs, GEs demonstrated less significant performance improvements over UEs, and the GE design overlapped more with the UE design range in Figure 4.7. By examining the upper-bounding cases, GE-8 (yellow square markers) showed a +0.2%, +0.5%, +0.3%, +0.2%, and -0.3% difference in Wh/kg relative to UE-7 (black square markers) at C/2, 1C, 2C, 4C, and 6C discharge rates, respectively. For volumetric energy density, when compared to UE-7, GE-8 demonstrated an improvement of +0.8%, +1.0%, +0.8%, +0.7%, and +0.4% at C/2, 1C, 2C, 4C, and 6C discharge rates, respectively. Our findings reaffirm that GEs can offer marginal benefits over UEs with thick electrodes, which align with results from previous modeling studies by Dai and Srinivasan and Qi et al.[19,63]

Based on the SEG and GE results, we also modeled a case where we combined the benefits of structured electrodes with electrode grading (called SE+GE) to examine whether concurrent grading and structuring of the electrodes will provide additional improvements in energy density at 2C and higher discharge rates over UEs. With the same EVF values, the analysis showed that SE+GEs demonstrated only modest specific discharge capacity improvements over GEs and no improvement over SEs. For example, compared to GE-5, the best-performing SE+GE case (SE+GE-3) demonstrated a specific discharge capacity (mAh/g_{active}) improvement of +0.1%, +0.3%, +3.0%, +12.6%, and +12.3% at C/5, 1C, 2C, 4C, and 6C discharge rates, respectively. Relative to SEG-5, SE+GE-3 showed a specific capacity performance difference of +0.1%, +0.5%, -0.2%, -2.4%, and -0.8% at C/5, 1C, 2C, 4C, and 6C discharge rates, respectively. For both gravimetric and volumetric energy density, SE+GEs demonstrated no performance advantage over

SEs and GEs, and further details on the results of this analysis can be found in Figure B4 and Table B-IX – Table B-XII in Appendix B.

4.3.9 *UEs and SEs with Extreme Cathode Active Material Loading (65 mg_{active}/cm^2)*

Modeling results from the previous sections showed that battery cells with a cathode active material loading target of 31 mg_{active}/cm^2 demonstrated a maximum gravimetric energy density of 267 Wh/kg (for GE-2) and a volumetric energy density of 672 Wh/L (for UE-4) at a C/2 discharge rate. To investigate the limits of NMC-622 cathodes, we modeled extremely thick electrodes with a cathode active material loading of 65 mg_{active}/cm^2 while maintaining a N/P ratio of 1.0 across C/10 – 6C discharge rates. We acknowledge a cathode active material loading of 65 mg_{active}/cm^2 cannot be readily manufactured today with conventional blade casting and slot die coating due to challenges with cracking and delamination that occur at these high loadings.[147] However, the purpose of this analysis is to explore the leading edge and push the bounds of experiments. We believe modeling this scenario provides meaningful insight into whether material and processing development for higher loading electrodes is worth further investment.

Figure 4.8 shows the Ragone plots for three extreme loading cases: UE-8, UE-9, and SEG-10. UE-8 has a porosity of 35% with a cathode thickness of 246 µm (solid black markers) and UE-9 has a porosity of 50% with a cathode thickness of 320 µm (empty black markers). SEG-10 has a porosity of 35% in the "porous cathode + electrolyte region" defined in Figure 4.2 and has an EVF of 48%. Two cases (UE-7 and SEG-6), which were some of the best performing cases from Figure 4.7**,** are re-included in Figure 4.8 for comparison purposes against the 31 mg_{active}/cm^2 cathode active material loading scenario. Modeling results for all models run in this study can a found in Table B-XII in Appendix B. Looking at Figure 4.8, one can see that increasing the SE cathode active loading from 31 mg_{active}/cm^2 to 65 mg_{active}/cm^2 improved the C/10 energy density

to 285 Wh/kg and 678 Wh/L (SEG-10). With more than double the amount of cathode active material loading, this energy density improvement demonstrates the limits of electrode thickness and cathode active material loading with our chosen graphite|NMC-622 model. We found the 65 mg_{active}/cm^2 SE (SEG-10) had a +51.8% to +408.6% energy density improvement at 4C and 6C discharge rates over its planar UE counterparts (UE-8 and UE-9). These values are much higher than the +17.7% to +24.3% improvement observed for the 31 mg_{active}/cm^2 SE (SEG-6) relative to its planar reference (UE-7) at 4C and 6C discharge rates. This is because electrodes with higher loading are more limited by mass transport. Thus, SEs, due to their inherent design that has engineered electrolyte channels through the electrode thickness, are a pathway to more substantial performance improvements at higher electrode loadings and thicknesses. However, we acknowledge that the design of SEs must be carefully balanced with the EVF to ensure a continuous porous network is formed in the electrode and the incorporation of additional electrolyte at the cell level does not come at the expense of larger-scale performance due to the removal of cathode active material. Ultimately, the design of an SE and its engineered porosity must be aligned with the limits of the material chemistry used in its manufacture to meet the energy and power needs of next-generation EV batteries.

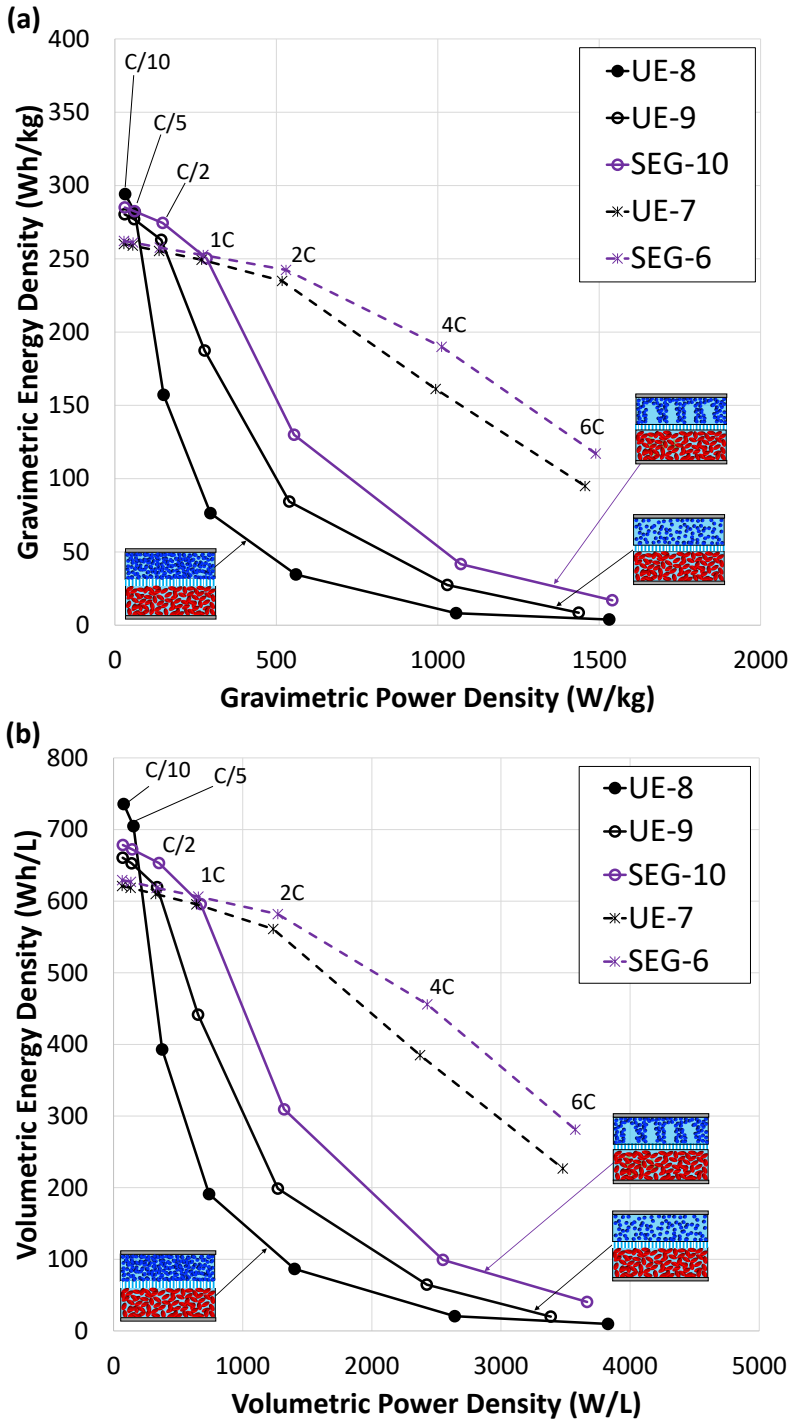

Figure 4.8. Comparison of "extreme loading" uniform electrodes (UEs) and grid structured electrodes (SEGs) on a (a) gravimetric and (b) volumetric energy and power density basis. Solid line models (UE-8, UE-9, and SEG-10) have a cathode active material loading of 65 mg_{active}/cm^2. UE-7 and SEG-6 have a cathode active material loading of 31 mg_{active}/cm^2 are plotted in dashed lines as a comparison point to elucidate the impact of increasing active material loading.

4.4 CONCLUSION

In this chapter, we have presented one of the first comparative, large-scale 3D computational analysis of UE, GE, and SE NMC-622 cathodes paired with graphite anodes to understand if porosity grading and structuring in ultra-thick, highly loaded cathodes can yield improved rate capability based on mAh/g_{active}, Wh/kg, and Wh/L performance metrics. A total of 43 design cases and 230 continuum-scale 3D electrochemical models were simulated using *VIBE-AMPERES* and analyzed assuming a hypothetical pouch cell stack with dimensions based on an EV pouch cell from a Nissan LEAF® vehicle.

Our study found that graphite|NMC-622 SEs with a line or grid pattern with an EVF >48% yielded the greatest performance improvement over UEs and GEs. The controlled electrolyte integration in SEs helps facilitate faster and more uniform Li-ion transport in ultra-thick electrodes. The SEG-6 design case was one of the best performing SEs, showing a rate capability improvement over UEs across all C/2 – 6C discharge rates based on mAh/g_{active}, Wh/kg, and Wh/L metrics. A 1% – 2% improvement at C/2 was observed, and the performance improvement increased to 23 – 24% at a 6C discharge rate. Our results also showed that in order to realize up to a 45% improvement in Wh/kg and Wh/L at 4C – 6C, an approximately 5% sacrifice in Wh/kg and Wh/L must be made at C/2 and slower C-rates due to the need to incorporate more electrolyte and remove cathode active material from the cells to facilitate faster ion transport and in turn better performance at high C-rates. In other words, NMC-622 cathode SEs can be designed to have energy density improvements across all C-rates, but improvements ≥25% at high C-rates requires compromising on the total cell energy density at slower C-rates.

Our analysis also demonstrated that GEs and UEs cannot achieve the same high rate capability performance observed in SEs. This is due to the inherent design of SEs that enables

electrolyte to be incorporated into thick electrodes in a more controlled manner than UEs and GEs. By design, SEs have a lower effective tortuosity than their equivalent GE and UE counterparts. In the EVF range assessed in this study, the reduction in tortuosity contributes to at least one-third of the observed enhancements in rate capability for SEs. Notably, this performance improvement cannot be attained in UEs by increasing the porosity. In addition, SEs allow for higher EVF values beyond the percolation thresholds that exist in UEs and GEs. However, when implementing these electrode designs into practical cells at larger application scales, such as EVs, the incorporation of additional electrolyte must be balanced at the pouch cell level to not sacrifice energy density or safety. We also found that dimensional changes to both an SE's channel spacing and first layer thickness exhibited a non-linear trend on capacity improvements. This non-linear trend is due to how lithiation progressed through the electrodes in our 3D models, and we found that the rate-limiting transport mechanism changed as the electrode thickness and electrolyte feature dimensions were altered.

For the GEs, the analysis did not yield a significant mAh/g_{active}, Wh/kg, or Wh/L performance improvement over the UEs, which was consistent with previous published computational results.[19,63] Analysis of the 3D Li-ion concentration data showed that the controlled SE architecture enables more Li-ions to move across the entire cathode thickness in the models. Conversely, although GEs have a higher porosity electrode layer interfacing the separator that facilitated fast Li-ion transport, the overall GE performance will inevitably be rate limited by the less porous electrode layer. Within the limit of the nine GE cases we examined, any benefit gained by the highly porous high-power layer in GEs was offset by the dense and low-power layer attached to the current collector. These results align with a previous modeling study published by

Dai and Srinivasan,[19] who modeled GEs with up to ten graded porosity layers and consequently found little performance improvements over UEs.

It is important to acknowledge that reliable and consistent scale up of SEs to scales meaningful for EV applications requires the development of new manufacturing systems and processes. Conventional slurry formulations used to make current graphite and NMC electrodes may also require changes to enable the thick, high loading electrodes modeled in this study. Our results show that when the cathode active material loading increases, an SE yields a higher energy density improvement over their UE counterpart with a similar cathode active material loading. In addition, our pouch cell stack analysis assumed an idealized packaging scenario which did not consider oversized separators, excess electrolyte, and N/P ratios greater than 1.0. If prismatic and cylindrical cells were to be considered, excess volume in the cell due to winding of the electrodes or the natural curvature of the packaging will require further analysis. We acknowledge that the energy density values may decrease as other packaging components are included, to eventually build up to a full system design, but the relative SE performance improvements over UEs and GEs should remain and scale accordingly.

Lastly, we believe SEs show strong potential for increasing battery pouch cell performance, but this warrants further experimental and modeling investigations into new electrode structures and material formulations. Focusing on materials, the results presented in this study are highly dependent on the rate-limiting mechanism in a battery cell. We believe the benefits of SEs modeled in this study are applicable to material systems that are predominantly limited by mass transport in the electrode thickness direction, which includes most ultra-thick NMC electrodes.

Chapter 5. STRUCTURED ELECTRODES PART 2: MODELING THE IMPACT OF ANODE AND CATHODE STRUCTURING ON CHARGE AND DISCHARGE PERFORMANCE IN GRAPHITE|NMC-622 BATTERIES

*The content in Chapter 5 is under review for publication in a journal.

5.1 INTRODUCTION

To address Research Question 1a and 1c, this chapter presents a holistic study using 3D computational models to investigate the isolated effects of structuring either the anode or the cathode, and the combined effects of structuring both electrodes on the charge and discharge capacity of single-layer cells at high rates. Figure 5.1 illustrates four types of battery cells. Figure 5.1 a contains a UE, as defined in Chapter 4. Figure 5.1 (b) contains a SE anode paired with a uniform, planar cathode, and we refer to this configuration as SEA. Next, Figure 5.1 (c) has a SE cathode paired with a uniform, planar anode, which we call SEC. Lastly, Figure 5.1 (d) shows a fully structured cell where a SE anode is paired with a SE cathode, and this design configuration for simplicity is referred to as SEA-SEC. The SEA has "all-electrolyte" regions in the graphite anode, while the SEC has "all-electrolyte" regions in the NMC-622 cathode. In both the SEA and SEC configurations, ionic transport and kinetics are expected to improve cell performance relative to a UE cell configuration due to the reduced tortuosity and the increased amount of electrolyte in the SEs. In material systems where the ionic transport resistance of one electrode is much higher than that of the other electrode, a SEA or SEC can enhance cell performance by targeting and structuring the electrode that has a higher resistance. In graphite|NMC cells, both electrodes can

often experience high ionic transport resistances at high charge and discharge rates.[65,100,136,148] Thus, employing a SEA-SEC configuration, in theory, can potentially reduce transport resistances even further and facilitate more rapid ionic transport across the entire cell. If properly designed, this behavior can improve LIB rate capability relative to a conventional UE cell.

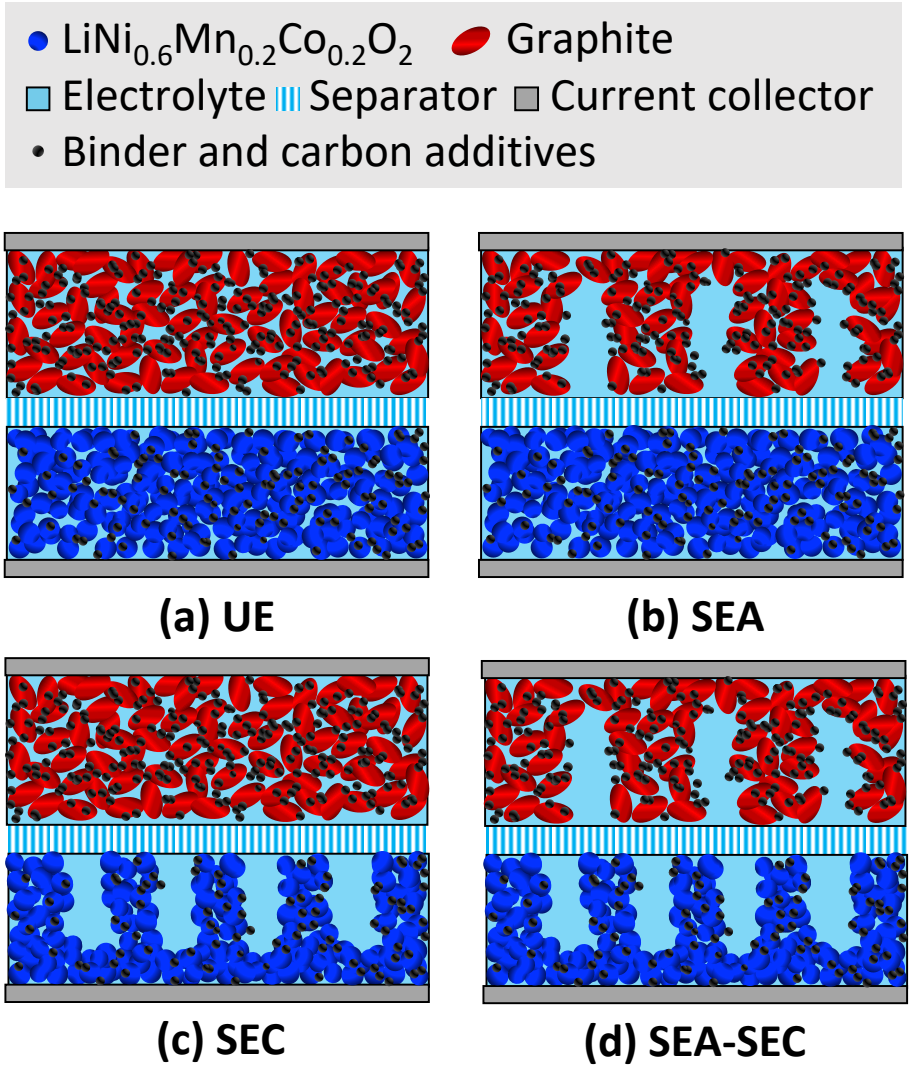

Figure 5.1 Illustrations of the cell configurations analyzed in this study: (a) conventional uniform electrodes (UEs), (b) a structured electrode anode paired with a UE cathode, referred to as a SEA in this chapter, (c) a structured cathode paired with a UE anode, referred to as a SEC in this chapter, and (d) a structured anode paired with a structured cathode, referred to as a SEA-SEC in this

chapter. Images (a) and (c) are adapted from Hung et al.[132] under CC BY 4.0 (https://creativecommons.org/ licenses/by/4.0/).

Existing research literature on graphite and NMC SEs has primarily focused on evaluating discharge rate capability, with results showing improved discharge capacity with SEA, SEC, and SEA-SEC configurations.[10,60,66,132,148,149] Recent work by Hung et al.,[132] also captured in Chapter 4 of this dissertation, with a graphite|NMC-622 material model demonstrated that when controlling the electrolyte volume fraction in a SE cathode to approximately 48%, energy density improvements up to 24% can be achieved across a discharge C-rate range of C/2 – 6C. Based on publicly available research literature, no systematic investigations have been conducted to date to show how SECs or SEA-SECs affect LIB charge performance. How SEAs impact LIB charge performance has been explored with a focus on lithium plating and cyclability in both experimental and modeling studies.[21,59,60,65] SEAs with a graphite|NMC-532 material system fabricated by Chen et al. exhibited improved C/2 discharge capacity retention over 500 cycles at charge rates of 4C and 6C.[21] However, their initial cycling data indicated SEAs have negligible improvements in charge capacity (Ah) when compared to equivalent UE configurations across C/2 – 6C. In contrast to Chen et al.'s findings, SEA modeling results from Kraft et al. suggested that charge capacity can be improved at 1C – 3C rates for graphite|$LiNi_{0.3}Mn_{0.3}Co_{0.3}O_2$ (NMC-111).[65] The authors found that the transport and kinetic overpotentials in the graphite anode can be reduced with electrode structuring.

Whether or not SEA, SEC, or SEA-SEC configurations can improve charge and discharge capacity (mAh/g_{active}) in a single-layer cell depends on the ionic transport and kinetic resistances in each individual electrode. If an electrode has a significantly high transport or kinetic mechanism that results in a higher overpotential relative to the other electrode, the high resistance electrode becomes the rate-limiting electrode in a LIB cell. In this scenario, structuring the rate-limiting

electrode is more critical to improving performance. Transport and kinetic resistances can vary in electrodes and typically depend on the particle size, particle morphology, electrode porosity, and weight percent composition of active material, binder, and carbon additives in the initial electrode slurry and final dried electrodes. Moreover, these resistances and their relative impact on charge and discharge overpotential are dependent on C-rate currents and charge versus discharge cycles. Both experimental and modeling studies on SEAs have revealed a restricted C-rate window where improvements in discharge capacity are possible, and the range of this C-rate window depends on the active material loading.[65,148] SEA configurations did not yield performance improvements outside of this C-rate window because the ionic transport and kinetic resistances in the graphite anode no longer dominated the cell performance.[65,148] This phenomenon is supported by Hille et al.'s experimental comparative analysis between a SEA, a SEC, and a SEA-SEC.[148] The authors found a SEA and a SEA-SEC yielded the largest improvements in discharge capacity at 2C and 3C, while a SEC showed the highest discharge capacity at 5C. These results indicate the rate-limiting electrode in a UE switched from the anode to the cathode when the discharge rate was increased to 5C.

The electrode exhibiting the highest ionic transport and kinetic resistances in a UE configuration often displays a large one-dimensional (1D) concentration and current density gradient through the electrode thickness direction. SEA and SEC configurations, by design, have three-dimensional (3D) geometry variations in the anode or cathode, which can lead to larger non-uniformities relative to UE configurations. In addition, depending on the physical orientation of the SE anode and SE cathode geometries, SEA-SEC configurations can potentially result in even larger concentration gradients if not carefully designed. Since electrochemical non-uniformities in a LIB cell have been shown to lead to premature electrolyte depletion and reduced cell capacity,[1]

it is critical to examine how concentration gradients and nonuniformities in UE, SEC, SEA, and SEA-SEC configurations affect electrochemical performance.

Despite the potential performance benefits in charge and discharge specific capacity offered by SEs in single-layer cells, it is important to consider a few electrode design caveats when examining them. When single-layer cells are stacked to form larger capacity multi-layer pouch cells, the integration of SEs increases the volume fraction of electrolyte while reducing the portion of active materials, separators, and current collectors. While reducing the number of current collectors and separators in a multi-layer stack can theoretically increase the energy density of a pouch cell,[10] the decrease in active material loading per volume and weight of the pouch cell stack (g_{active}/L_{stack} and g_{active}/kg_{stack}) can lead to lower energy density (Wh/L_{stack} and Wh/kg_{stack}) and reduced capacity (Ah/L_{stack} and Ah/kg_{stack}) if the SE electrolyte volume is not carefully balanced with the active material loading. Thus, it is important to consider multiple design facets of SEs in parallel to navigate this complex, multi-objective electrode design space. While prior experimental and modeling studies have demonstrated improvements in charge and discharge specific capacity (mAh/g_{active}) through the use of SEA, SEC, and SEA-SEC configurations,[21,59,60,65,67,145,148] it remains unclear whether these performance improvements extend to larger-scale discharge energy density metrics (Wh/L_{stack} and Wh/kg_{stack}) and charge capacity (Ah/L_{stack} and Ah/kg_{stack}) metrics for a multi-layer pouch cell stack. Moreover, the energy required to charge a battery's volumetric and gravimetric capacity (Wh per Ah/L_{stack} and Wh per Ah/kg_{stack}) must also be explored for a true holistic analysis of charge and discharge performance.

Based on available research literature, no consistent comparative analysis has been conducted that simultaneously examines the charge and discharge rate capabilities of SEA, SEC, and SEA-SEC configurations, while factoring in the total weight and volume associated with the

"all-electrolyte" regions in SE electrodes and considering the weight and volume of the separators and current collectors in a pouch cell stack. This analysis is critical but presents a significant experimental and monetary investment for any battery manufacturer. Thus, this is an opportunity where computational modeling and analysis can be leveraged to better guide battery manufacturers on the benefits and limitations of SE configurations for EV-scale applications before significant investment is made in experiments and future manufacturing technologies. A comprehensive analysis in this area requires that data be collected in a consistent manner using the same material system and computational model to obviate any comparison issues between UE, SEA, SEC and SEA-SEC configurations. To address this need, this study investigates the impact of UE, SEA, SEC, and SEA-SEC configurations, across a range of electrolyte volume fractions, on both the charge and discharge performance in a single-layer cell. The specific capacity (mAh/g_{active}) results for each cell configuration are then analyzed in terms of discharge energy density (Wh/L_{stack} and Wh/kg_{stack}) and charge capacity (Ah/L_{stack} and Ah/kg_{stack}) to understand performance impacts on a hypothetical multi-layer pouch cell stack that may be used in an EV. Finally for SEA-SECs, the physical orientation of the SE electrodes in space is analyzed to understand how relative alignment of the "all-electrolyte" regions impacts liquid phase concentration non-uniformities. The impact of SEA-SEC alignment on overall cell performance and future cell manufacturing is discussed.

5.2 METHODS

5.2.1 *Material Model and Reference UE Cells*

A model based on a UE configuration was developed. Table 5.1 and Table 5.2 summarize the model parameters used in this study, which were within ranges reported in literature and adjusted for best fit to the graphite|NMC-622 experimental charge and discharge voltage profiles from Wu et al.[150] More information on the model parameterization and validation can be found in Appendix C. Based on experimental data from Wu et al.,[150] the anode and cathode both have a porosity of 30%, an active material load of 13.1 mg_{active}/cm^2 for the NMC-622 cathode, and an active material loading of 7.5 mg_{active}/cm^2 for the graphite anode. Assuming theoretical capacities of 170 mAh/g_{active} for NMC-622 and 350 mAh/g_{active} for graphite, the negative to positive electrode capacity ratio (N/P ratio) was calculated to be 1.14. Herein, we refer to the UE model based on these cell parameters as UE-13 to reflect a configuration with a 13.1 mg_{active}/cm^2 cathode active material loading. For brevity in labeling UE model cases, only the first two digits for the cathode active material loading are added to the UE model name. To understand the limits of higher loading, an additional UE configuration was modeled with a cathode active material loading of 18.4 mg_{active}/cm^2 and an anode active material loading of 10.5 mg_{active}/cm^2. This UE model is referred to as UE-18 and has the same porosity and N/P ratio as UE-13. The SE electrodes modeled in this study have a cathode active material loading of 13.1 mg_{active}/cm^2 to match UE-13 or a cathode active material loading of 18.4 – 18.5 mg_{active}/cm^2 to match UE-18 for comparison purposes during analysis. The active material loading for the graphite anode is either 7.5 mg_{active}/cm^2 or between 10.5 – 10.6 mg_{active}/cm^2 to maintain a N/P ratio of 1.14.

Table 5.1. Model parameters used for kinetics and transport in the solid phase.

Parameter	Description	Units	NMC-622	Graphite
D_s	Diffusion coefficient	m^2/s	Equation [a,b,112,113]	$1 \cdot 10^{-11}$ [a,151]
σ	Electric conductivity	S/m	12 [152]	100 [109]
c_s^{max}	Maximum concentration	mol/m^3	49520 [113]	30000 [113]
c_s^0	Initial concentration	mol/m^3	19940 (discharge) [a] 49200 (charge) [a]	29451 (discharge) [a] 1774 (charge) [a]
k	Reaction rate constant	$A \cdot cm^{2.5}/mol^{1.5}$	1.5 [a,153]	3.2 [a,153]
t_+^0	Transference number	N/A	0.462 [112]	0.462 [112]
R_{film}	Film resistance	$\Omega \cdot m^2$	0 (discharge) [a] 0 (charge) [a]	0 (discharge) [a] 0.017 (charge) [a]
ε_e	Volume fraction of liquid	N/A	0.3 [150]	0.3 [150]
ε_s	Volume fraction of solid	N/A	0.545 [150]	0.648 [150]
R_s	Particle radius	m	$1.8 \cdot 10^{-6}$ [113]	$5.15 \cdot 10^{-6}$ [113]
p	Bruggeman constant	N/A	4.4 [a,112,113,138,148]	2.5 [a,112,113,138,148]

[a] Fitted to Wu et al.[150] experimental data

[b] $D_s = 5 * 10^4\left(10^{-2319x^{10}+6642x^9-5269x^8-3318x^7+10038x^6-9806x^5+5817x^4-2286x^3+575.3x^2-83.16x-9.292}\right)$ where $x = \frac{c_s}{c_{s,max}}$

Table 5.2. Electrolyte and separator model parameters.

Parameter	Description	Units	Electrolyte
D_e	Diffusion coefficient	m^2/s	$D_e = 10^{\left(-4.5227 - \frac{0.5382}{56.81-6.86*c_e} - 0.1976*c_e\right)}$ [112,113,124]
c_e^0	Initial concentration	mol/m^3	1200 [113]
κ	Ionic conductivity	$\frac{S}{m}$	$\kappa(c_e) = (2.184c_e - 1.559{c_e}^2 + 0.3869{c_e}^3 - 0.0333{c_e}^4)$ [112]
Parameter	**Description**	**Units**	**Separator**
ε_e	Volume fraction of liquid	N/A	0.39
p	Bruggeman constant	N/A	2.5 [112,113]

5.2.2 *SE Designs*

In the first part of this chapter, twenty SEA and SEC design configurations were modeled. Each configuration focused on "line" pattern geometries with "all-electrolyte" regions in the anode or cathode. This is one of the most studied SEs in literature and can be manufactured with co-extrusion,[69] laser patterning,[59] 3D printing,[61] and other manufacturing approaches. In Chapter 4,[132] we examined how the EVF in SEC configurations impacts discharge rate capability for LIBs. EVF is defined in Equation 1 as the ratio of liquid electrolyte volume within an SE to the volume of all materials within an SE, assuming there are no void spaces. It was found that EVF is an important design parameter for understanding and analyzing thick SE cathodes, and the impact of specific SE geometries on discharge rate capability plays a secondary role to EVF when EVF values are ≥ 64%.[132]

$$EVF = \frac{\epsilon_e V_{porous-electrode} + V_{all-electrolyte}}{V_{porous-electrode} + V_{all-electrolyte}} \quad (5.1)$$

In Equation 5.1, ϵ_e is the volume fraction of the liquid electrolyte within the porous electrode regions, $V_{porous-electrode}$ is the volume of the porous electrode regions, and $V_{all-electrolyte}$ is the volume of the "all-electrolyte" regions within a given SE. The sum of the porous electrode regions and the "all-electrolyte" regions is the total of volume of the SE.

The SEC configurations modeled in this study have an EVF value between 40% – 60%. Based on our prior modeling study on SECs in Chapter 4, this is the EVF range that demonstrated optimal SEC performance improvements in energy density over a UE counterpart for a multi-layer stack. Similarly, the SEAs were modeled across an EVF range between 35% – 60%. Since we were designing the SEAs and SECs to have specific EVF values for the purposes of analysis, the SE

dimensions were adjusted by increments of 1 µm appropriately with no electrode feature being smaller than 25 µm to ensure realistic manufacturing constraints. Based on prior line-patterned SE demonstrations,[59,132] all SEs have 40 µm wide "all-electrolyte" regions, as labeled in Figure 5.2 (a) and (b). The spacing between these "all-electrolyte" lines was then varied to enable different EVF values for analysis. The "all-electrolyte" regions represent areas that have 100% porosity in the SE for electrolyte to infiltrate. All electrode material regions in the SEs hold a 30% porosity to match the UE configurations to facilitate evaluating the impact of electrode structuring on cell performance. All dimensions and associated EVF values are summarized in Tables C-I and C-II in Appendix C.

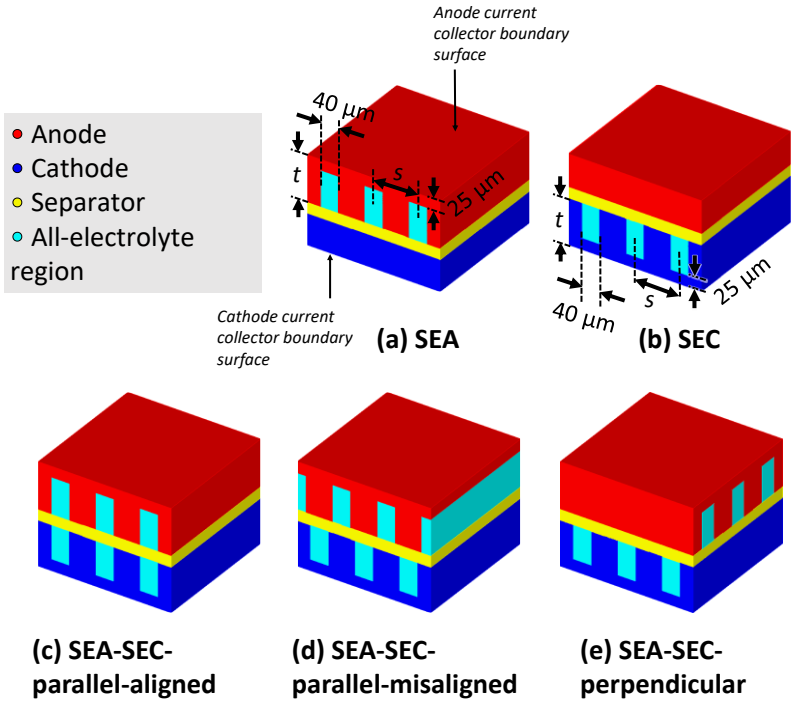

Figure 5.2. Representative illustrations of the following structured electrode (SE) full cell configurations examined in this study: (a) a SEA, (b) a SEC, (c) a SEA-SEC-180°-ee, (d) a SEA-SEC-180°-es, and (e) a SEA-SEC-90° design. All SEs have 40 µm wide "all-electrolyte" regions and 25 µm thick electrode layers interfacing the current collectors. The electrode thickness, *t*, and center-to-center line spacing, *s*, were varied in SEAs and SECs to create a range of electrolyte volume fractions (EVFs).

To enable a comparative analysis, nine SEA and SEC models were defined to have a cathode active material loading of 13.1 mg_{active}/cm^2 and an anode active material loading of 10.5 mg_{active}/cm^2 to match the loading of UE-13. The remaining eleven models have a cathode active material loading of 18.4 – 18.5 mg_{active}/cm^2 and an anode active material loading of 10.5 – 10.6 mg_{active}/cm^2 to match the cell loading of UE-18. All SE thicknesses were adjusted as needed to maintain a fixed cathode active material loading that aligned with UE-13 or UE-18 for a consistent comparative analysis for SEA and SEC configurations. In addition to controlling loading, all SE anodes and SE cathodes have a uniform layer of electrode material that is 25 μm thick and attached to the current collectors to ensure sufficient electronic conduction (see Figure 5.2 (a) and (b)). Following the labeling scheme used for the UE configurations, the SEA and SEC configurations are hyphenated with the cathode active material loading, and this is followed by the EVF value used in the cathode. For example, a SEA with a cathode active material loading of 18.4 mg_{active}/cm^2 and a SE anode EVF of 40% is labeled as SEA-18-40% for that model instance.

Once SECs and SEAs were analyzed, in the second part of this chapter, three SEA-SEC design configurations were modeled to investigate the impact of SE geometry alignment on rate capability when both electrodes are structured. The intent here is to understand how different configurations of SEA-SECs impact non-uniformities at the cell level. All SEA-SECs have a cathode active material loading of 18.4 mg_{active}/cm^2 and an anode active material loading of 10.5 mg_{active}/cm^2. Each SE anode and SE cathode has an EVF of 51% and a uniform electrode layer that is 25 μm thick attached to the current collectors. As illustrated in Figure 5.2 (c) – (e), the difference between the three SEA-SEC design configurations is the relative alignment of the "all-electrolyte" regions between the SE anode and the SE cathode. Figure 5.2 (c) and (d) show two SEA-SEC design configurations that have their line-patterned regions oriented in the same parallel direction.

The configuration in Figure 5.2 (c) has the "all-electrolyte" regions in the SE cathode directly opposing the "all-electrolyte" regions in the SE anode. This case is labeled as SEA-SEC-18-51%-parallel-aligned to indicate the following four cell attributes: (1) the cell has a cathode active material loading of 18.4 mg_{active}/cm^2, (2) the EVF in both electrodes is 51%, (3) the line-patterned regions in the anode and cathode run parallel to each other, and (4) the "all-electrolyte" regions in the SE anode align directly with those in the SE cathode in the cell thickness direction. In Figure 5.2 (d), the alignment of the "all-electrolyte regions" in the SEA-SEC design is the only cell attribute that differs from the SEA-SEC design case presented in Figure 5.2 (c); Here, the "all-electrolyte" regions in the SE anode and SE cathode do not align in the cell thickness direction and are shifted such that the "all electrolyte" regions in the SE cathode now oppose the electrode material regions in the SE anode. The case in Figure 5.2 (d) is referred to as SEA-SEC-18-51%-parallel-misaligned. The last SEA-SEC design configuration is shown in Figure 5.2 (e). Relative to Figure 5.2 (c), this configuration has the SE anode rotated 90 degrees relative to the SE cathode such that the "all-electrolyte" regions are now perpendicular to each other. This configuration is labeled as SEA-SEC-18-51%-perpendicular and maintains the same loading and EVF values as the design presented in Figure 5.2 (c). For the purposes of computational accuracy, a finer time resolution was implemented for the SEA-SEC models to better capture the impact of electrochemical non-uniformities on cell performance. The method for evaluating specific capacity for these models can be found in Figure C4 in the Appendix C.

For the SEA, SEC, and SEA-SEC configurations modeled in this chapter, the smallest possible model unit needed to capture the necessary electrochemical results was used assuming symmetry boundary conditions.[1,104] The current collectors were implemented as boundary conditions in the single-layer cell models. Galvanostatic charge and discharge cycles were

modeled using a constant voltage boundary at the anode-current collector interface and a constant current density boundary at the cathode-current collector interface. The discharge models had a lower cut-off voltage of 2.8 V, and the charge models had an upper cut-off voltage of 4.2 V. No constant-voltage cycle was modeled after charging the model cells to the cut-off voltage. Details regarding the finite element mesh generation, boundary conditions, and computing resources used can be found in Appendix C.

All 3D electrochemical models in this chapter were single-layer cells, each comprising one cathode, one anode, and one separator with the current collectors implemented as boundary conditions. To provide guidance on how UE, SEA, SEC, and SEA-SEC configurations impact larger scale batteries, irrespective of the end application, we report our multi-layer pouch cell stack metrics on a per weight and per volume basis. Specifically, charge capacity (Ah/L_{stack} and Ah/kg_{stack}) and discharge energy density (Wh/L_{stack} and Wh/kg_{stack}) metrics were evaluated across all cell configurations. All single-layer 3D electrochemical models were assembled into a hypothetical multilayer pouch cell stack wherein the total stack height is fixed at 1 cm. Based on this constraint, the total number of single-layer cells within the stack is between 40 – 69 for all models, as reported in Tables C-III and C-IV in Appendix C. The multilayer pouch cell stack calculations include the weight and volume of all electrodes, separators, current collectors, and the electrolyte. Further details on the calculation methodology for the multilayer pouch cell stack can be found in our previous publication.[132]

5.3 Results and Discussion

5.3.1 *Impact of SEA and SEC on Discharge Specific Capacity (mAh/g_{active}) in a Single-layer Cell*

The discharge specific capacity of SEAs and SECs at 4C and 6C rates is first examined as part of our analysis. Figure 5.3 shows the charge and discharge results, displaying the voltage profiles at 6C as a function of specific capacity for models with an 18.4 – 18.5 mg_{active}/cm^2 cathode active material loading. The model results for the 4C and 6C charge and discharge specific capacities for all models conducted in this chapter are in Table C-III and Table C-IV in Appendix C. Compared to the SEAs in Figure 5.3 (a), the SECs in Figure 5.3 (b) demonstrate significant improvements in discharge specific capacity relative to UE-18. Since the models had a 1.14 N/P ratio, their theoretical discharge capacities are fundamentally limited by the number of intercalation sites in the cathode if the anode and cathode experience similar transport and kinetic overpotentials. The improvements in SECs over UE-18 in Figure 5.3 (b) show that the cathode continued to drive cell discharge capacity. This indicates that the SE cathode has similar or greater transport and kinetic resistances than the anode at 6C.

Figure 5.4 provides additional insight into the data presented in Figure 5.3. Figure 5.4 shows the end of discharge (EOD) and end of charge (EOC) Li-ion concentrations in the liquid and solid phases for UE-18, SEA-18-50%, and SEC-18-50% at 6C rates. Both UE-18 and SEA-18-50% exhibited a large EOD concentration gradient in the planar cathode, as shown in Figure 5.4 (b). This gradient in the solid electrode phase led to a decrease in the cell voltage, causing it to drop below the cut-off voltage before achieving complete lithiation of the cathode. The SECs facilitated efficient liquid-phase transport behavior within the cathode relative to UE-18, as

evidenced from the uniform electrolyte concentration throughout the cathode thickness of SEC-18-50% in Figure 5.4 (a). Due to improved electrolyte transport, SEC-18-50% achieved uniform lithiation across the cathode thickness in Figure 5.4 (b), resulting in a longer discharge time and, in turn, an improved specific capacity.

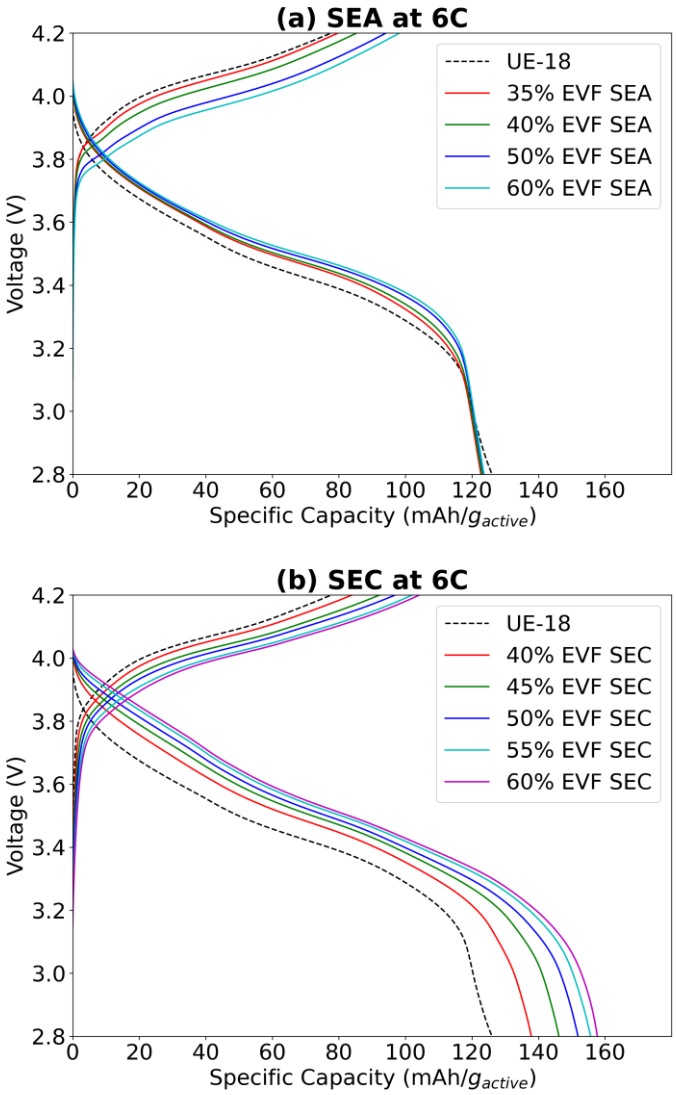

Figure 5.3 Charge and discharge voltage versus specific capacity at a 6C rate for graphite|NMC-622 single-layer models. (a) shows results for four SEAs with an electrolyte volume fraction (EVF) between 35% – 60%. (b) shows results for SECs with an EVF between 40% – 60%. A conventional reference single-layer UE cell, UE-18, is shown in black in each plot. All models shown here have a cathode active material loading of 18.4 – 18.5 mg_{active}/cm^2.

In Figure 5.3 (a), the SEAs exhibited a higher discharge plateau voltage compared to UE-18; however, the specific capacities of the SEAs were slightly lower than that of UE-18. Comparing SEA-18-50% to UE-18 at the EOD in Figure 5.4 (a), the electrolyte in the SE anode region in the SEA is orange and yellow, while for UE-18 it is mostly red. The color difference in the results indicates that SEA-18-50% better facilitated electrolyte transport within the anode. However, this improvement in transport does not necessarily correspond to enhanced Li-ion intercalation in the cathode, since the EOD solid-phase concentrations for SEA-18-50% and UE-18 are comparable as shown in Figure 5.4 (b). Conversely, Li-ions de-intercalated from the anode moved quickly through the "all-electrolyte" regions in the SE anode and accumulated at the surface of the cathode due to poor transport in the cathode. This sudden increase in local concentration led to rapid reaction kinetics at the cathode surface, creating a more pronounced concentration gradient and a near-depletion region, as shown in dark blue, in EOD SEA-18-50% in Figure 5.4 (a). The near-depletion region and the surrounding high concentration gradients likely resulted in a rapid cell voltage drop at the EOD, leading to reduced discharge specific capacity results for SEAs compared to UE-18 in Figure 5.3 (a). These results show that careful consideration must be given to the design of SEs. If the rate of transport and kinetics in the anode and cathode are not balanced, SEs can lead to increases in non-uniform reaction rates and concentration gradients, which can lower the specific capacity.

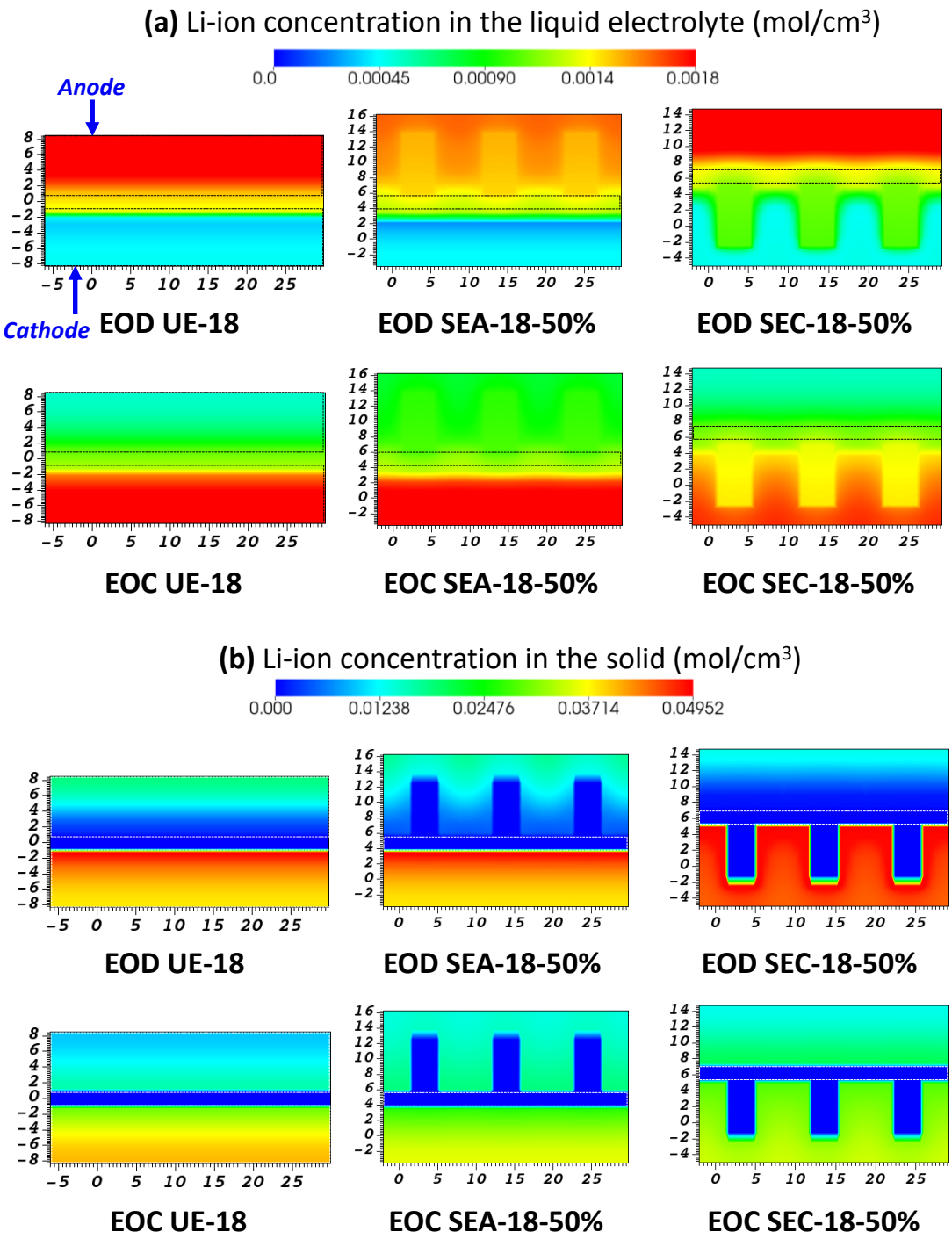

Figure 5.4 Li-ion concentration in (a) the liquid electrolyte and (b) the solid phase at 6C end of charge (EOC) and 6C end of discharge (EOD). All axes are units of 10^1 µm with the tallest single-layer cell being 198 µm. The SE model cases are labeled using the type of cell configuration, the cathode active material loading, and the electrolyte volume fraction (EVF). For instance, SEA-18-50% represents a SEA with an 18.4 mg_{active}/cm^2 loading and 50% EVF.

5.3.2 *Impact of SEA and SEC on Charge Specific Capacity (mAh/g_{active}) in a Single-layer Cell*

The SEAs and the SECs exhibited similar improvements in charge specific capacity relative to UE-18, as shown in Figure 5.3. As shown in Figure 5.4 (a), at the EOC, SEA-18-50% had a more uniform distribution of electrolyte concentration in the anode compared to UE-18. The reduction in concentration gradient within the SE anode enabled significant improvements in charge overpotential in Figure 5.3 (a) and prevented the cell from prematurely reaching the upper cut-off voltage. In Figure 5.4 (b), the solid-phase concentration plot of EOC SEA-18-50% shows more uniform gradients in both the cathode and the anode due to improved transport in the SE anode. Similarly, the SECs enhanced the charge specific capacity by improving the liquid-phase transport in the SE cathode. In the EOC electrolyte concentration plot in Figure 5.4 (a)**,** SEC-18-50% showed a lower concentration in the cathode region compared to UE-18 and SEA-18-50%, indicating improved Li-ion transport with SE cathodes.

In Figure 5.3**,** the SECs had a more significant impact on the charge specific capacity than the SEAs, which was also attributed to the N/P ratio being greater than unity. Upon closer examination, the SEAs exhibited a more substantial reduction in charge overpotential compared to the SECs, contributing to better charge energy conservation. An explanation for this can be interpreted from Figure 5.4. In the SE cathode of SEC-18-50% at EOC in Figure 5.4 (a), the "all electrolyte" regions (yellow) had a lower electrolyte concentration than the solid cathode regions shown in red. This observation suggests that the rate of ionic transport within the SE cathode of SEC-18-50% was lower than the rate of Li-ion de-intercalation. If the transport in the SE cathode is further improved, the charge overpotential can be further reduced. In comparison, the SE anode of SEA-18-50% did not have a distinct difference in electrolyte concentration between the "all

electrolyte" regions and the solid electrode regions, indicating the rate of Li-ion electrolyte transport in the SE anode was on par with the rate of the Li-ion intercalation reactions. With the same EVF value, the SEA configuration is more effective in improving the anode transport than SEC in improving the cathode transport. As shown in Figure 5.3, increasing the EVF in the SEC from 50% to 60% resulted in a substantial improvement in charge specific capacity, while increasing the EVF for SEAs from 50% to 60% yielded a much smaller improvement.

5.3.3 *Analyzing SEA and SEC Discharge Energy Density (Wh/L_{stack} and Wh/kg_{stack}) and Charge Capacity (Ah/L_{stack} and Ah/kg_{stack}) in a Multi-layer Pouch Cell Stack*

Figure 5.5 presents the charge and discharge performance of SEAs and SECs in a multi-layer cell stack in comparison to UEs. The discharge performance metrics used for this evaluation include volumetric and gravimetric energy density, evaluated in Wh/L_{stack} and Wh/kg_{stack}, respectively. For the charge models, volumetric and gravimetric capacity (Ah/L_{stack} and Ah/kg_{stack}) are employed, as these metrics reflect the quantity of Li-ions stored in the anode after charging. Ah is a unit for a battery's electron storage capacity while Wh is a measure of how much energy can be delivered. Capacity (Ah) was used instead of energy (Wh) because while the charge voltage affects charge energy utilization, it does not influence the subsequent discharge cycle once charging is complete. The discharge energy and charge capacity were further normalized by the total weight and volume of the multi-layer stack to enable a consistent data comparison and allow for an analysis that can be extrapolated to different large-scale stack configurations. The weight and volume of all models were calculated using the method described in section 5.2 and Appendix B. In Figure 5.5, the models that have an active cathode material loading of 18.4 – 18.5 mg_{active}/cm^2 are represented by solid lines, while those with a 13.1 mg_{active}/cm^2 cathode active material loading

are depicted with dashed lines.

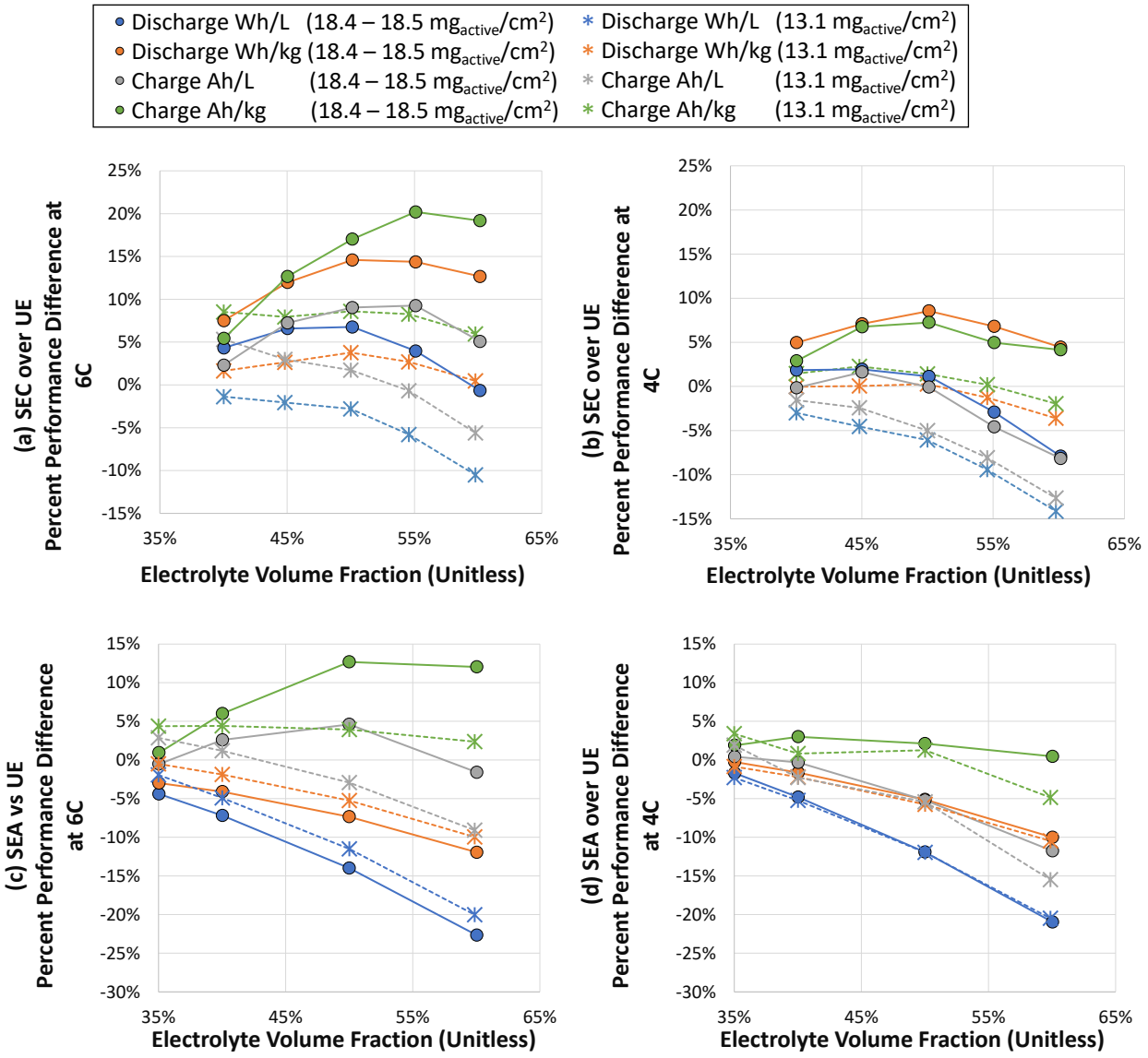

Figure 5.5 Performance difference in discharge energy density (Wh/kg$_{stack}$ and Wh/L$_{stack}$) and charge capacity (Ah/kg$_{stack}$ and Ah/L$_{stack}$) for (a) SEC models run at 6C, (b) SEC models run at 4C, (c) SEA models run at 6C, and (d) SEA models run at 4C. The performance difference in each metric is defined as the performance of the SEA or SEC subtracted by the performance of the UE (with the same cathode active material loading) and normalized to the performance of the UE. Models with a cathode active material loading of 18.4 – 18.5 mg$_{active}$/cm^2 are plotted with solid lines, and models with a cathode active material loading of 13.1 mg$_{active}$/cm^2 are plotted with dashed lines.

Figure 5.5 (a) and (b) present the 4C and 6C performance data for SECs compared to UEs, while Figure 5.5 (c) and (d) present the performance data for SEAs compared to UEs. As previously noted, Figure 5.3 indicated both SEAs and SECs can consistently improve the charge and discharge performance in a single-layer cell. Figure 5.5 shows the performance evaluation for a multi-layer stack. The solid lines in Figure 5.5 (a) demonstrate that SECs within the EVF range of 40% – 55% exhibited performance improvements over UE-18 across all charge and discharge metrics for a multi-layer stack. More specifically, an EVF range of 50% – 55% for SECs enables the highest overall 6C performance across all metrics evaluated (Wh/L_{stack}, Wh/kg_{stack}, Ah/kg_{stack}, and Ah/L_{stack}). SEC-18-55% and SEC-18-50% exhibited improvements of 9% in charge Ah/L_{stack}, 17% – 20% in charge Ah/kg_{stack}, 14% – 15% in discharge Wh/kg_{stack} and 4% –7% in discharge Wh/L_{stack}. While these results are promising, it is important to note that at an EVF of 60% in Figure 5.5 (a), SECs begin to negatively impact the multi-layer pouch cell stack performance, and SE dimensions must be carefully considered here.

The solid lines in Figure 5.5 (c) indicate that in a multi-layer cell stack, the 18.4 – 18.5 mg_{active}/cm^2 SEAs exhibited charge performance improvements over UE-18; however, with the graphite|NMC-622 material model examined in this chapter, the SEAs presented no performance improvements in discharge Wh/L_{stack} and Wh/kg_{stack} at 6C across the 35% – 60% EVF range. When the EVF is set to 50%, SEA-18-50% displayed the highest improvements of 5% in charge Ah/L_{stack} and 13% in charge Ah/kg_{stack}, despite experiencing a -7% decrease in discharge Wh/kg_{stack} and -14% decrease in discharge Wh/L_{stack} relative to UE-18. The lower discharge energy density values stemmed from (1) the small improvements in overpotential garnered in the SEA voltage profiles and (2) the reduced active material loading (g_{active}/L_{stack} and g_{active}/kg_{stack}) in the cell stack, as shown in Table 5.3. These results underscore the importance of considering all relevant charge and

discharge metrics as well as larger-scale pouch cell properties when designing SEs and optimizing their associated features.

Table 5.3. Stack properties, model specific capacity at 6C, and the resulting stack volumetric and gravimetric discharge energy density and charge capacity at 6C for selected models. All model results can be found in Tables C-III and C-IV in Appendix C. In stack properties, g_{active}/kg_{stack} and g_{active}/L_{stack} represent the cathode active material loading in a multi-layer cell stack.

	Stack Properties			**Discharge Model Results**			**Charge Model Results**		
Design	number of single-layer cells	g_{active}/kg_{stack}	g_{active}/L_{stack}	mAh/g_{active}	Wh/kg_{stack}	Wh/L_{stack}	mAh/g_{active}	Ah/kg_{stack}	Ah/L_{stack}
UE-18	53	414	1096	126	162	430	78	29	77
SEC-18-40%	50	402	1033	138	174	448	85	31	79
SEC-18-50%	46	387	955	152	186	459	98	34	84
SEC-18-60%	41	365	853	158	183	427	105	35	81
SEA-18-40%	50	400	1024	123	156	399	86	31	79
SEA-18-50%	46	384	943	124	150	369	95	33	81
SEA-18-60%	41	363	845	124	143	332	99	33	76
UE-13	69	377	1005	146	175	467	107	36	97
SEC-13-40%	65	366	946	151	178	461	120	40	102
SEC-13-50%	60	354	883	159	182	454	124	40	99
SEC-13-60%	55	337	800	161	176	418	127	39	92
SEA-13-40%	65	372	978	146	172	444	115	38	98
SEA-13-50%	60	366	946	146	166	414	119	38	94
SEA-13-60%	54	353	878	147	158	374	124	37	88

The incorporation of SEs into a multi-layer stack, while fixing the active material loading, inevitably increases electrode thicknesses and reduces the number of cells that can fit into a fixed stack volume. Although SEs enhanced the charge and discharge material utilization (mAh/g_{active}) in a single-layer cell, their advantage in mAh/g_{active} and Wh/g_{active} can be hindered by the decrease in the total active material (g_{active}) packed into the multi-layer cell stack. This analysis highlights that there are critical design caveats to SEs that must be carefully considered, and SEs do not always lead to unilateral improvements in all performance metrics simultaneously. Table 5.3

summarizes the stack properties and modeling results for selected UE, SEA, and SEC cases. The information for all model cases is available in Table C-III and Table C-IV in Appendix C.

5.3.4 *Analyzing C-rate and Active Material Loading Effects on SEA and SEC Performance in Single-layer Cells and Multi-layer Pouch Cell Stacks*

For both SEAs and SECs, regardless of the active material loading and C-rate, the most significant performance improvements in Figure 5.5 are observed in charge Ah/kg$_{stack}$, and the lowest performance improvements are seen in discharge Wh/L$_{stack}$. It is important to note that this phenomenon is material dependent and multifaceted. One contributing factor is that the baseline UE cell (UE-13), modeled after the work of Wu et al.,[150] exhibited a greater discharge rate capability compared to the charge rate capability. Experimental studies in literature have reported similar hysteresis in charge and discharge rate capability for graphite|NMC cells.[121,136] Furthermore, the mass densities of the NMC-622 (4.80 g/cm^3), graphite (2.27 g/cm^3), binder (1.77 g/cm^3), carbon additive (2.00 g/cm^3), separator (0.90 g/cm^3), electrolyte (1.23 g/cm^3), copper current collector (8.96 g/cm^3), and aluminum current collector (2.70 g/cm^3) also played a role. Incorporation of SEs into batteries increases the volume ratio of electrolyte within the single-layer cell and reduces the overall mass density of the cell stack. Consequently, incorporating SEs negatively affects the volumetric active material loading (g$_{active}$/L$_{stack}$) to a greater extent than the gravimetric active material loading (g$_{active}$/kg$_{stack}$). As a result, volumetric charge and discharge metrics (Ah/L$_{stack}$ and Wh/L$_{stack}$) were more adversely impacted by these stack properties than the gravimetric metrics (Ah/kg$_{stack}$ and Wh/kg$_{stack}$).

The EVF values that enabled the highest performance improvements at 4C are lower than the EVF values that yielded the best performance results at 6C. For SEAs, an EVF of 35% – 40% was found to positively impact the 4C charge capacity (Ah/L$_{stack}$ and Ah/kg$_{stack}$), while the SECs

required an EVF between 40% – 50% to demonstrate performance improvements across all metrics at 4C. A decrease in SE performance improvements (relative to UEs) across all charge and discharge metrics is observed when the C-rate is reduced from 6C to 4C, as seen by comparing Figure 5.5 (a) and (c) with Figure 5.5 (b) and (d). This reduction in performance improvements is attributed to lower transport resistances in UE-18 at 4C compared to 6C. The SEs, thus, yielded less improvements at the lower C-rates. This observation aligns with the findings of Habedank et al.,[67] which highlighted that SEAs exhibited a restricted C-rate window that facilitated improvements in discharge capacity (mAh/cm^2) over a conventional UE configuration.

Next, in Figure 5.5, we investigated the effect of active material loading by comparing the lower active material loading, 13.1 mg_{active}/cm^2 cases (represented by dashed lines) to the higher active material loading, 18.4 – 18.5 mg_{active}/cm^2 cases (drawn in solid lines). Compared to the higher loading SE cases, the 13.1 mg_{active}/cm^2 SEAs and SECs maintained a higher percentage of the volumetric and gravimetric cathode active material loading (g_{active}/L_{stack} and g_{active}/kg_{stack}) over the UE case. This is an advantage of the lower-loading cases, and it led to a higher 6C discharge energy density in Figure 5.5 (c), where the blue and orange dashed lines are positioned above their solid line counterparts. In all other conditions examined, the 13.1 mg_{active}/cm^2 SEs generally demonstrated less performance improvements than the 18.4 – 18.5 mg_{active}/cm^2 SEs. Since UE-13 had a specific capacity closer to the NMC-622 theoretical capacity at 4C, the potential for improvements using an SE was more constrained (see Table 5.3). Similar to the higher-loading cases, the 13.1 mg_{active}/cm^2 cases exhibited more performance improvements at 6C compared to 4C, although the difference is less pronounced, indicating the impact of C-rate decreases with lower active material loading.

For the 13.1 mg_{active}/cm^2 active material loading scenario at 4C and 6C, there was no SEA

or SEC case where improvements were observed across all four metrics (charge Ah/L_{stack}, charge Ah/kg_{stack}, discharge Wh/L_{stack}, and discharge Wh/kg_{stack}) evaluated in this study. The most favorable outcomes were achieved with SECs that had a 40% – 50% EVF range at 6C rates. This yielded improvements of approximately 8% in charge Ah/kg_{stack}, 2% – 5% in charge Ah/L_{stack}, and 2% – 4% in discharge Wh/kg_{stack}. However, there was a decrease in discharge Wh/L_{stack} of -3% – -1%. Based on these results, it is concluded that the integration of SEs into full cells with cathode active material loadings below 13.1 mg_{active}/cm^2 will likely offer no performance benefit in discharge energy density or charge capacity at rates slower than 4C. This C-rate and active material loading result is consistent with prior research outcomes in existing literature. [65,100]

5.3.5 *Impact of SEA-SEC on Discharge Energy Density (Wh/L_{stack} and Wh/kg_{stack}), Charge Capacity (Ah/L_{stack} and Ah/kg_{stack}), and Charge Energy Usage (Wh spent per Ah/L_{stack} stored and Wh spent per Ah/kg_{stack} stored)*

SEA-SECs, which contain SE anodes paired with SE cathodes, were modeled to investigate the combined effects of electrode structuring on the charge and discharge performance in a multi-layer pouch cell stack. Based on the analysis for SEA and SEC multi-layer stacks, the best performance improvements found for each charge and discharge metric evaluated in this study requires a slightly different EVF value. However, the EVF values for the best cases fell within a narrow range of 50% – 55%; thus, a 51% EVF was chosen as it offers the best balance in performance between all the charge and discharge metrics evaluated in the prior sections. To facilitate a SEA-SEC analysis, two additional SEC and SEA models were established to serve as comparison points for analysis: SEC-18-51% and SEA-18-51%. Both cases have a cathode active material loading of 18.4 mg_{active}/cm^2 and an anode active material loading of 10.5 mg_{active}/cm^2. The SEA-SEC models incorporated SE cathodes and SE anodes with electrode thicknesses and line

spacings matching those of the SE cathode in SEC-18-51% and the SE anode in SEA-18-51%. As described in section 5.2.2, three different SEA-SEC configurations were modeled based on their relative anode and cathode alignment: SEA-SEC-51%-parallel-aligned, SEA-SEC-51%-parallel-misaligned, and SEA-SEC-51%-perpendicular. All SEA-SEC configurations have an EVF value of 51% in the anode and an EVF value of 51% in the cathode.

Figure 5.6 (a) presents the volumetric versus gravimetric discharge energy density for UE-18, SEA-18-51%, SEC-18-51%, and all three SEA-SEC cases. Performance at a discharge rate of 4C is indicated with diamond markers, while performance at a discharge rate of 6C is represented by the round markers. The results in Figure 5.6 (a) reveal that the SEC configuration provided the most performance improvements, demonstrating discharge energy density gains over UE-18 of 6% in 6C Wh/L_{stack}, 15% in 6C Wh/kg_{stack}, 0.3% at 4C Wh/L_{stack}, and 22% in 4C Wh/kg_{stack}. In contrast, while the SEA-SEC configurations resulted in 10% – 15% improvements in gravimetric energy density (Wh/kg_{stack}) at 4C and 6C rates, the SEA-SECs led to a decrease of -12% – -4% in volumetric energy density (Wh/L_{stack}) compared to UE-18. Among all the configurations, the SEA exhibited the lowest discharge energy density, exhibiting a decline of -15% – -13% in Wh/L_{stack} at both C-rates and -7% Wh/kg_{stack} at 6C, despite a 7% improvement in Wh/kg_{stack} at 4C over the UE.

The EOD lithiation in the cathode at 6C, illustrated in Figure 5.7 (b), suggests that the SEA-SEC configurations exhibited similar active material utilization to the SEC configuration. As presented in Table 5.4 and the discharge profiles in Figure C3 in Appendix C, the SECs and the SEA-SECs demonstrated a specific discharge capacity close to 160 mAh/g_{active} at 4C and 6C, indicating nearly full active material utilization. Structuring both electrodes (SEA-SEC) maintained a higher discharge plateau voltage and slightly enhanced discharge specific energy (Wh/g_{active}). We believe these results demonstrate the limit of SEA-SECs on improving the

discharge voltage profiles for the graphite|NMC-622 material system studied. Structuring both electrodes resulted in increased cell thickness and additional overpotential. This is important to acknowledge because electrode thickness has been found to impact the rate capability of SEs.[2] Therefore, it is not unexpected that the SEC provided the best overall performance in discharge energy density, given the modest improvement in discharge specific capacity achieved by the SEA-SECs over the SEC and the corresponding reduction in g_{active}/kg_{stack} and g_{active}/L_{stack} associated with structuring both electrodes (see Table 5.4).

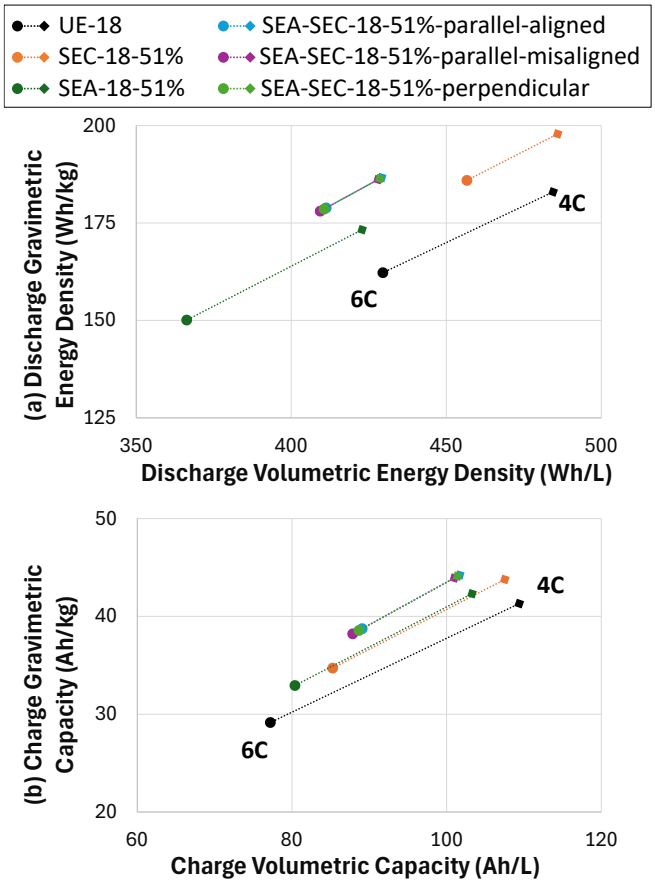

Figure 5.6 (a) Discharge gravimetric and volumetric energy density and (b) charge volumetric and gravimetric capacity results for UE-18, SEA-18-51%, SEC-18-51%, and three SEA-SEC cases (SEA-SEC-18-51%-parallel-aligned, SEA-SEC-18-51%-parallel-misaligned, and SEA-SEC-18-51%-perpendicular as illustrated in Figure 5.2). All cases have a cathode active material loading of 18.4 mg_{active}/cm^2.

Regarding charge performance, as depicted in Figure 5.6 (b), the SEA-SEC configurations exhibited the highest charge capacity (Ah/kg_{stack} and Ah/L_{stack}) at 6C compared to all other designs, demonstrating improvements of 14% – 33% over the UE. At a 4C charge rate, although the SEA-SEC cases maintained a 6% – 7% advantage in gravimetric charge capacity (Ah/kg_{stack}), their volumetric charge capacity (Ah/L_{stack}) was -8% – -7% lower than that of UE-18. Compared to the SEA-SECs, the SEC exhibited less charge performance improvements; however, the improvements were still noteworthy, with an increase of 10% in Ah/L_{stack} at 6C, 19% in Ah/kg_{stack} at 6C, a decrease of -2% in Ah/L_{stack} at 4C, and an increase of 6% in Ah/kg_{stack} at 4C. None of the structured configurations outperformed the UE configurations in terms of volumetric charge capacity at a 4C charge rate, highlighting the limitation of SEs at slower C-rates. This is not surprising given at lower C-rates, an electrode often realizes close to its theoretical capacity. At this point, the weight and volume of the entire multi-layer stack, which includes the current collectors and separators, begins to have a more dominant effect on the stack performance.

The SEA-SECs exhibited improvements in both charge overpotential and specific capacity over UE-18 in a single-layer cell, as shown in Figure C3 in Appendix C, due to improved Li-ion transport in both SE cathode and SE anode. As shown in the EOC concentration plots in Figure 5.7 (a), the SEA-SECs demonstrated improved electrolyte concentration gradients in the SE anode compared to SEC-18-51%, which had a planar anode. The resulting solid-phase concentration at EOC, shown in Figure 5.7 (b), indicates that the SE anodes in the SEA-SEC configurations exhibited higher lithiation, as represented by the dark green color. Likewise, the SE cathodes in the SEA-SECs showed lower Li-ion concentration and a smaller gradient compared to the planar cathode in SEA-18-51%, suggesting more effective ionic transport and de-lithiation. However, the SEA-SECs experienced a -25% reduction in g_{active}/L_{stack} and a -14% in g_{active}/kg_{stack} reduction

compared to UE-18 (see Table 5.4), diminishing the benefits of improved lithiation when calculating the overall volumetric and gravimetric charge capacity in a multi-layer pouch cell stack.

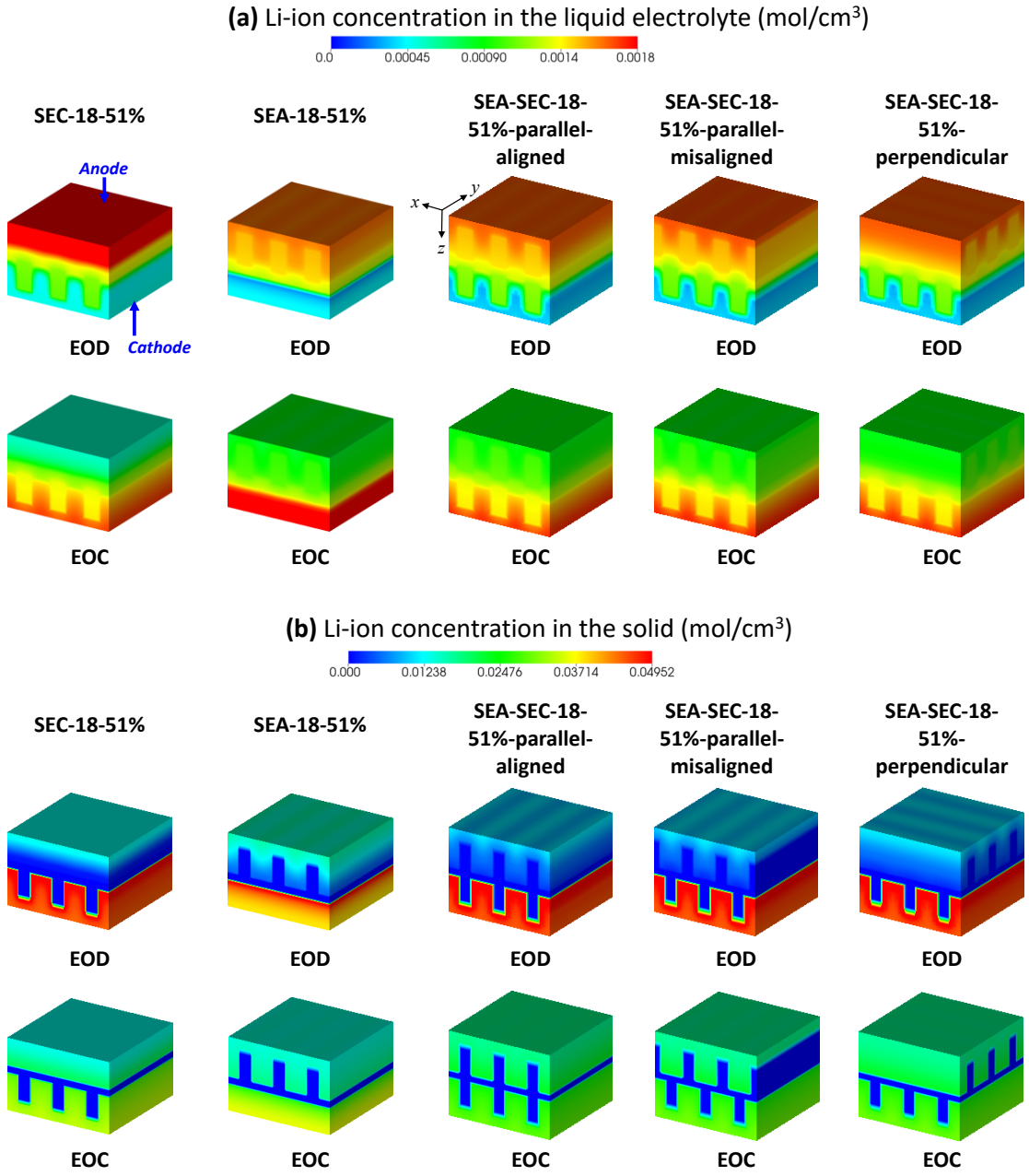

Figure 5.7. Li-ion concentration in the (a) liquid electrolyte and (b) solid phase at the end of charge (EOC) and the end of discharge (EOD) at 6C for SEA-18-51%, SEC-18-51%, and three SEA-SECs (SEA-SEC-18-51%-parallel-aligned, SEA-SEC-18-51%-parallel-misaligned, and SEA-SEC-18-51%-perpendicular, as illustrated in Figure 5.2). All cases have a cathode active material loading of 18.4 mg_{active}/cm^2.

The SEA-SECs exhibited improvements in both charge overpotential and specific capacity over UE-18 in a single-layer cell, as shown in Figure C3 in Appendix C, due to improved Li-ion transport in both SE cathode and SE anode. As shown in the EOC concentration plots in Figure 5.7 (a), the SEA-SECs demonstrated improved electrolyte concentration gradients in the SE anode compared to SEC-18-51%, which had a planar anode. The resulting solid-phase concentration at EOC, shown in Figure 5.7 (b), indicates that the SE anodes in the SEA-SEC configurations exhibited higher lithiation, as represented by the dark green color. Likewise, the SE cathodes in the SEA-SECs showed lower Li-ion concentration and a smaller gradient compared to the planar cathode in SEA-18-51%, suggesting more effective ionic transport and de-lithiation. However, the SEA-SECs experienced a -25% reduction in g_{active}/L_{stack} and a -14% in g_{active}/kg_{stack} reduction compared to UE-18 (see Table 5.4), diminishing the benefits of improved lithiation when calculating the overall volumetric and gravimetric charge capacity in a multi-layer pouch cell stack.

The alignment of SE cathode and SE anode geometries in the SEA-SECs, shown in Figure 5.2 (d) – (f), resulted in minimal performance variations, with result differences ranging from 0.3% to 1.4% in the discharge energy density and charge capacity. Since all SEA-SECs had the same g_{active}/kg_{stack} and g_{active}/L_{stack}, performance trends observed will be the same at the single-layer cell level and multi-layer stack level. Although these performance differences are minor, a trend was observed across all metrics, where SEA-SEC-18-51%-parallel-aligned consistently outperformed other configurations. SEA-SEC-18-51%-parallel-misaligned showed the lowest performance with an increase of approximately 10 mV overpotential across the charge and discharge voltage profiles, as shown in Figure C4 in Appendix C. These results present an interesting insight for battery manufacturers and researchers investigating experimental implementations of SEs. When employing SEA-SEC design configurations, if one cannot position the micrometer-scale SE

cathode and SE anode "all electrolyte" regions to have perfect parallel alignment, then positioning the SE electrodes in a perpendicular manner as shown in Figure 5.2 (e) offers almost the same performance benefits but more manufacturing flexibility during cell assembly. Thus, aligning the SE line geometries in a perpendicular manner may be the most feasible approach going forward for battery manufacturers, as it helps mitigate the risk of creating significant gradients in the electrode thickness (*z*) direction due to misalignment.

Table 5.4. Cathode active material loading in a multi-layer cell stack (g_{active}/kg_{stack} and g_{active}/L_{stack}), model charge and discharge specific capacity (mAh/g_{active}) at 4C and 6C, and the charge energy usage per specific capacity stored (Wh per Ah/kg_{stack} and Wh per Ah/L_{stack}) for UE-18, SEA-18-51%, SEC-18-51%, and all SEA-SEC models.

Design Case	g_{active}/kg_{stack}	g_{active}/L_{stack}	6C discharge mAh/g_{active}	6C charge mAh/g_{active}	6C charge Wh used per Ah/kg_{stack} stored	6C charge Wh used per Ah/L_{stack} stored
UE-18	414	1096	126	78	5.64E-05	1.49E-04
SEC-18-51%	384	943	153	100	5.66E-05	1.39E-04
SEA-18-51%	383	935	124	95	5.57E-05	1.36E-04
SEA-SEC-18-51%-parallel-aligned	357	822	156	120	5.62E-05	1.29E-04
SEA-SEC-18-51%-parallel-misaligned	357	822	156	118	5.63E-05	1.29E-04
SEA-SEC-18-51%-perpendicular	357	822	156	119	5.63E-05	1.29E-04
Design Case	g_{active}/kg_{stack}	g_{active}/L_{stack}	4C discharge mAh/g_{active}	4C charge mAh/g_{active}	4C charge Wh used per Ah/kg_{stack} stored	4C charge Wh used per Ah/L_{stack} stored
UE-18	414	1096	138	110	5.55E-05	1.47E-04
SEC-18-51%	384	943	160	126	5.49E-05	1.35E-04
SEA-18-51%	383	935	141	122	5.38E-05	1.31E-04
SEA-SEC-18-51%-parallel-aligned	357	822	160	137	5.53E-05	1.27E-04
SEA-SEC-18-51%-parallel-misaligned	357	822	160	136	5.53E-05	1.27E-04
SEA-SEC-18-51%-perpendicular	357	822	160	137	5.53E-05	1.27E-04

The impact of SE alignment on SEA-SEC cell performance can be further seen in the concentration plots. As illustrated in the yellow regions in Figure 5.7 (a), at the EOD, wave-like concentration gradient patterns developed in the *x*-*y* plane within the separator regions of the SEA-SECs. The SEA-SEC aligned in parallel exhibited a 1D gradient that was uniform in the *y*-direction. Conversely the perpendicular alignment for SEA-SEC-18-51%-perpendicular displayed a 2D gradient in the *x*-*y* plane. SEA-SEC-18-51%-parallel-misaligned resulted in the most substantial fluctuations in the *z*-direction gradient, which led to lower specific capacity (mAh/g_{active}) and increased overpotential as mentioned previously. In comparison, the gradients in the *z* direction for SEA-SEC-18-51%-parallel-aligned and SEA-SEC-18-51%-perpendicular were less pronounced. It is worth noting that the SE anode and SE cathode in these SEA-SECs had the same "all-electrolyte" region width and spacing (*s* in Figure 5.2). If the SE cathode and SE anode have mismatched feature sizes, or if they have larger feature sizes, the concentration gradient resulting from SE geometry alignment will likely increase, thereby impacting the overall cell performance more.

In Table 5.4, we report additional metrics to evaluate the charge energy consumption (Wh) per specific capacity stored (Ah/kg_{stack} and Ah/L_{stack}) at 4C and 6C. These metrics evaluate how efficient energy is utilized to charge a battery and account for the effects of the charge voltage trajectory. If a battery requires a higher average voltage to charge, it indicates a lower efficiency in utilizing the charge energy. In Table 5.4, the "charge Wh used per Ah/kg_{stack} stored" column shows that all SEs enhanced gravimetric charge efficiency by 7% – 14%. In comparison, the "charge Wh used per Ah/L_{stack} stored" column in Table 5.4 indicates that all SEs maintained a similar volumetric charge efficiency within a 3.2% variation to the UE. The SEA-SECs demonstrated the best improvements in charge efficiency, with a reduction of -14% – -13% in

charge energy expenditure per Wh/kg_{stack} of stored capacity over UE-18. In comparison, SEA-18-51% showed a reduction of -11% – -9% energy used to charge per Ah/kg_{stack}, and SEC-18-51% required -8% – -7% less energy to charge per Ah/kg_{stack}. Overall, the SEA-SECs demonstrated the most advantages in charge energy utilization and charge capacity (Ah/L_{stack} and Ah/kg_{stack}) for a multi-layer pouch stack, while the SECs provided more improvements in discharge energy density (Wh/L_{stack} and Wh/kg_{stack}).

5.4 CONCLUSION

This Chapter presented a holistic computational study analyzing the isolated and combined effects of electrode structuring in the anode and the cathode of a Li-ion battery made from graphite|$LiNi_{0.6}Mn_{0.6}Co_{0.2}O_2$. Three types of electrode configurations were analyzed: SEAs, SECs, and SEA-SECs. For the purposes of analysis, to understand the impact of EVF and electrode structuring on charge and discharge performance, all SEs had a line-patterned electrode geometry. For all cell configurations, charge and discharge specific capacity (mAh/g_{active}), discharge energy density (Wh/L_{stack} and Wh/kg_{stack}), and charge volumetric and gravimetric capacity (Ah/L_{stack} and Ah/kg_{stack}) were modeled and comparatively examined. Single-layer cells were modeled in 3D using *VIBE-AMPERES* and a multi-layer pouch cell stack analysis was conducted thereafter to understand performance impacts at larger scales relevant to EVs. The graphite|NMC-622 material model was based on experimental data from literature,[150] and our results confirm that a UE cathode exhibits higher but still comparable ionic transport and kinetic resistances to a UE anode for this particular material model. In the single-layer cells, SEAs and SECs improved ionic transport in the electrolyte phase, leading to reduced overpotential in the charge and discharge voltage profiles for these cell configurations. With increasing EVFs, SEAs and SECs demonstrated less charge and discharge overpotential. Our results show that SECs enhanced both charge and discharge specific capacity of a cell relative to the UE counterpart. In comparison, SEAs only showed improvements in charge specific capacity but exhibited a lower discharge specific capacity over the UE. This is because SEAs facilitated an imbalance in anode and cathode ionic transport resistances during discharge, which led to deterioration of the reaction and concentration gradients within the cathode. This resulted in lower specific capacity results for the SEAs when compared to the UEs.

When a multi-layer pouch cell stack was analyzed, the SECs exhibited improvements

across all performance metrics, including 6C discharge energy density (Wh/L_{stack} and Wh/kg_{stack}) as well as charge capacity (Ah/L_{stack} and Ah/kg_{stack}). Within the 40% – 60% EVF range studied, the SECs with a 50% – 55% EVF value showed performance improvements over the UEs of 9% in charge Ah/L_{stack}, 17% – 20% in charge Ah/kg_{stack}, 14% – 15% in discharge Wh/kg_{stack}, and 4% – 7% in discharge $Wh/L_{stack,}$ all at 6C rates. In contrast, the SEAs demonstrated an increase in charge capacity but a reduction in discharge energy density relative to the UE. For the SEAs, a 50% EVF yielded the largest gain in charge performance, achieving improvements of 5% in charge Ah/L and 13% in charge Ah/kg_{stack}. It is important to note that these improvements were accompanied by a decrease in discharge Wh/kg_{stack} of -7% and a decrease in discharge Wh/L_{stack} of -14%. This is due to the lower active material loading (g_{active}/L_{stack} and g_{active}/kg_{stack}) within the multi-layer stack with SEs. At the 4C rate, SEAs and SECs demonstrated performance improvements, but on a smaller scale relative to the 6C rate results, confirming that electrode structuring and higher EVFs benefit cell performance at higher rates. SEAs and SECs with a cathode active material loading less than 13.1 mg_{active}/cm^2 will likely not yield performance benefits in discharge energy density and charge capacity at 4C and slower rates, confirming the benefit of SEs will be observed at higher material loadings.

The SEA-SEC design configurations improved material utilization at 4C and 6C more significantly than the SEA and SEC configurations. However, the lower stack active material loading (g_{active}/L_{stack} and g_{active}/kg_{stack}) of the SEA-SEC configurations diminished these improvements in a multi-layer pouch cell stack. When focusing solely on gravimetric metrics, the SEA-SECs, with a cathode active material loading of 18.4 – 18.5 mg_{active}/cm^2 in the single-layer cell, demonstrated improvements of 10% – 15% in discharge Wh/kg_{stack} and 6% – 33% in charge Ah/kg_{stack} relative to the UE counterpart. Furthermore, the analysis of charge energy used per

capacity stored indicated that SEA-SECs charge more efficiently than UEs, with improvements of 0.1% – 0.4% charge Wh usage per Ah/L_{stack} and a notable 13% – 14% improvement in charge Wh consumed per Ah/kg_{stack} stored. Nevertheless, these performance enhancements were accompanied by performance decreases of -12% – -4% in discharge Wh/L_{stack} at both C-rates and -8% – -7% in charge Ah/L_{stack} at 4C. In contrast, the SEC configuration exhibited the best overall performance, with improvements of 0.3% – 22% across all metrics, although there was a slight reduction of 2% in charge Ah/L_{stack} at 4C and a 0.3% decrease in energy efficiency per Ah/L_{stack} charged at 6C.

Lastly, the alignment of the SE line geometry on SEA-SEC performance appeared to have a small but consistent impact on performance based on the cases analyzed in this chapter; its impact may become more significant with different SE feature sizes. The concentration gradient created in the electrode thickness direction negatively impacts specific capacity at the cell level. Based on these results, we recommend aligning the "all-electrolyte" regions in the anode and cathode as shown in Figure 5.2 (c**)** to minimize concentration gradients that may negatively impact electrochemical performance. If perfect alignment of the μm-scale features is not achievable, aligning the SE line structures in a perpendicular manner as shown in Figure 5.2 (e) may, from a manufacturing perspective, facilitate assembly benefits over the orientation shown in Figure 5.2 (d).

Chapter 6. MODELING AND ANALYSIS OF LITHIUM PLATING

6.1 INTRODUCTION

This chapter addresses Research Question 2b from Chapter 1 and investigates the impact of 3D electrode architecture on lithium plating behavior. Lithium plating is a phenomenon that occurs during charging, where Li-ions deposit as metallic lithium on the anode surface instead of intercalating into the anode material.[154,155] Once lithium plating occurs, it can severely degrade the performance of a LIB cell by causing irreversible capacity losses and reductions in rate capability. This phenomenon also raises safety concerns for cell manufacturers as plated lithium can form dendrites and eventually puncture through the separator layer, short-circuiting a cell and causing thermal runaway.[156,157] Lithium plating is an anode-centric issue that occurs when the local potential in the anode drops below 0 V (versus lithium). Graphite anodes paired with the following cathode materials have all exhibited lithium plating phenomena: LFP, Lithium Manganese Oxide (LMO), Lithium Cobalt Oxide (LCO), Lithium Nickel Cobalt Aluminum Oxide (NCA), NMC-111, NMC-532, NMC-622, and NMC-811.[154]

It is important to note that Lithium plating is more likely to occur under fast charge conditions (above a 1C rate) and at temperature lower than 0°C, where electrochemical non-uniformities in Li-ion concentration are more substantial and may locally lower the potential of graphite below 0 V.[60] Previous research studies have observed a reduction in lithium plating caused by structuring the anode using a computational voltage relaxation analysis [60] and experimental post-mortem imaging.[21,59] Each study has concluded that a SEA configuration, as defined in Chapter 5, leads to improved cycle life performance. The authors attributed this performance improvement to a reduced concentration gradient in the structured anode compared to the planar

counterpart. While experimental operando investigations have been conducted to understand the conditions and scenarios that trigger the onset of lithium plating,[158–160] modeling can provide another means to examine this phenomenon early on in the cell design process. In this chapter, a 3D lithium plating model, coupled with the electrochemical model described in section 1.2.3, is developed using the 3D volume-average formulation. The model is implemented in *VIBE-AMPERES* to capture the onset time and location of lithium plating in the UE, SEA, and SEA-SEC configurations defined in Chapter 5.

6.2 METHODS

6.2.1 *3D Volume-averaged Model for Lithium Plating*

To investigate the impact of SEs on lithium plating, the 3D electrochemical model in *VIBE-AMPERES* must be modified to include physical equations that describe lithium plating mechanisms. A physics-based lithium plating model, initially developed by Aurora et al.[161] and later expanded by Ge et al.,[162] estimates the occurrence of lithium plating by calculating the plating overpotential η_{pla} in Volts. In Equation 6.1, ϕ_s is the potential in the solid phase, ϕ_e is the potential in the liquid phase, and $U_{Li\ metal}$ is the open-circuit potential of lithium metal. Using lithium as a reference point to evaluate potential, $U_{Li\ metal}$ is commonly assumed to be zero. $\Delta\phi_{film}$ represents the potential drop caused by any existing plated lithium metal on the active material particles.

$$\eta_{pla} = \phi_s - \phi_e - U_{Li\ metal} - \Delta\phi_{film} \quad (6.1)$$

If the plating overpotential η_{pla} is less than zero, there exists a plating current (in units of $A \cdot cm^{-3}$), j_{pla}. In Equation 6.2, a is the specific area in units of cm^{-1} as defined in Equation 1.2, $i_{0,pla}$ is the exchange current density for lithium plating reaction in units of $A \cdot cm^{-2}$, and T is the cell temperature in units of K. F is the Faraday's constant in units of $C \cdot mol^{-1}$ and R is the ideal gas constant in units of $J \cdot K^{-1} mol^{-1}$.

$$j_{pla} = min\left\{0,\ ai_{0,pla}\left[exp\left(\frac{0.3F}{RT}\eta_{pla}\right) - exp\left(-\frac{0.7F}{RT}\right)\eta_{pla}\right]\right\} \quad (6.2)$$

The potential drop across the plated film, $\Delta\phi_{film}$, can be calculated with Equation 6.3, where δ_{film} is the thickness of the deposited film and κ_{film} is the electric conductivity of the film. The thickness of the plated film will grow as time proceeds and is modeled with Equation 6.4, where M_{Li} is the molar mass of lithium in $g \cdot mol^{-1}$, a is the specific area of the particle size as defined in Equation 1.2, and ρ_{Li} is the mass density of lithium metal in $g \cdot cm^{-3}$. Note that in Equation 6.4, the plating current j_{pla} in $A \cdot cm^{-3}$ denotes the volumetric current density at the solid-liquid phase boundary. Dividing the plating current by Faraday's constant returns the moles of electrons transferred per second per electrode volume, as presented by units of $mol \cdot s^{-1} \cdot cm^{-3}$. Since lithium plating is a single-electron transfer reaction, the moles of electrons transferred is equal to the moles of Li-ions plated. Further multiplying this expression by the molar mass, M_{Li}, and dividing it by the specific area, a, yields the mass of lithium plated per second per electrode surface area, represented by units of $g \cdot s^{-1} \cdot cm^{-2}$. The rate of change in lithium plating thickness is then calculated by dividing this term by the mass density, ρ_{Li}, assuming lithium deposits uniformly on all electrode surface area within the finite element volume. With this assumption, the variability

in the lithium plating thickness can only be captured at a length scale that is larger than the size of a single finite element used in the mesh discretization.

$$\Delta\phi_{film} = j_{pla}\frac{\delta_{film}}{\kappa_{film}} \quad (6.3)$$

$$\frac{d\delta_{film}}{dt} = -\frac{j_{pla}M_{Li}}{a\rho_{Li}F} \quad (6.4)$$

In conventional planar LIBs, engineers attempt to set an upper cut-off voltage, an operating charge current range, and a temperature range that will mitigate or avoid the occurrence of lithium plating. Prior modeling research has focused on capturing the onset time of lithium plating in response to C-rates and temperature gradients in the electrode thickness direction. Based on publicly available research literature, prior lithium plating models have been primarily formulated into pseudo-2D (P2D) implementations.[161–164] Vishnugopi et al. modeled lithium plating in planar graphite|NMC-111 cells using a P2D formulation and identified ranges of electrode porosity and C-rates that can avoid lithium plating at temperatures of -10°C, 0°C, and 25°C.[164] Carelli and Bessler combined a 1D thermal model and a P2D plating model for a LIB pouch cell made with a graphite anode and a NCA and LCO composite cathode.[163] Their P2D models examined lithium plating at different locations along the electrode thickness and across the anode particle radius. In this chapter, the lithium plating model in Equations 6.1 – 6.4 was formulated using the 3D volume-average method and coupled with the existing 3D electrochemical models in Equations 1.17 – 1.24 to allow for an investigation of the 3D spatial distribution of lithium plating in SEs. The resulting 3D volume-average lithium plating model is presented in Equations 6.5 – 6.17 and implemented in *VIBE-AMEPRES*.

Equations 6.5 and 6.6 model the conservation of mass within the system and were adapted from Equations 1.22 and 1.23. Equation 6.5 describes the transient behavior of Li-ion concentration within the electrolyte phase as a function of the diffusion, the intercalation reaction, and the plating reaction. Since lithium plating does not directly interact with the solid phase of the porous electrode, the equation used to model the solid-phase Li-ion concentration in the coupled electrochemical-plating model, Equation 6.6, is identical to Equation 1.23 used in the electrochemical model.

$$\frac{\partial \varepsilon_e <c_e>}{\partial t} = \nabla \cdot \left(\varepsilon_e D_{e,eff} \nabla < c_e >\right) + \frac{\left(1-t_+^0\right)}{F}(< j_{int} > + < j_{pla} >) \quad (6.5)$$

$$\frac{\partial \varepsilon_s <c_{s,ave}>}{\partial t} = \nabla \cdot \left(\varepsilon_s D_{s,eff} \nabla < c_{s,ave} >\right) - \frac{<j_{int}>}{F} \quad (6.6)$$

Equation 6.7 introduces an additional physical quantity that does not exist in the electrochemical model, which is the 3D volume-averaged concentration of plated lithium metal in the representative volume element (RVE), $< c_{Li\ metal} >$, in mol·cm^{-3}. Due to the static nature of our finite element mesh setup, our model does not create a new domain for the plated lithium phase. Instead, $< c_{Li\ metal} >$ is developed as an artificial concept to capture the mole of Li-ions that are converted into lithium metal. Using Equation 6.8, the average concentration of lithium metal within the representative volume can be used to calculate the average thickness of the plated lithium on the surface of the spherical anode active material particles.

$$\frac{\partial <c_{Li\ metal}>}{\partial t} = -\frac{j_{pla}}{F} \quad (6.7)$$

$$\delta_{pla} = \frac{M}{a\rho} < c_{Li\,metal} > \quad (6.8)$$

The electrochemical potential in the solid and liquid phases are governed by Equations 6.9 and 6.10 following the general form of Ohm's law. In a coupled electrochemical-plating model, the local potential gradients are correlated to the local intercalation reactions and plating reactions.

$$\nabla \cdot \left(\varepsilon_e \kappa_{eff} \nabla < \phi_e > + \varepsilon_e \kappa \frac{2RT}{F}(t_+^0 - 1)\left(1 + \frac{dlnf}{dlnc_e}\right)\nabla < lnc_e >\right) = -(< j_{int} > + < j_{pla} >)$$

(6.9)

$$\nabla \cdot \left(\varepsilon_s \sigma_{eff} \nabla < \phi_s >\right) = (< j_{int} > + < j_{pla} >) \quad (6.10)$$

Two sets of kinetic equations are used in the coupled electrochemical-plating model. Equations 6.11 – 6.13 model the intercalation reaction current based on Butler-Volmer relationship, and they are identical to Equations 1.17 – 1.19 in the electrochemical model from Chapter 1. In this implementation, lithium plating is considered to be the only source of film resistance. Therefore, Equation 6.14 describes film resistance as the thickness of the plated lithium metal divided by its conductivity.

$$< j_{int} > = a i_{0,int}[e^{\frac{\alpha_{a,int}F}{RT}(\eta_{int})} - e^{-\frac{\alpha_{c,int}F}{RT}\eta_{int}}] \quad (6.11)$$

$$i_{0,int} = k_{int} < c_e^{\alpha_{a,int}} > (c_{s,max} - < c_s >)^{\alpha_{a,int}} < c_s^{\alpha_{c,int}} > \quad (6.12)$$

$$\eta_{int} = < \phi_s > - < \phi_e > - U_{OCP} - \frac{< j_{int} >}{a} R_{film} \quad (6.13)$$

$$R_{film} = \frac{\delta_{pla}}{\kappa_{Li\ metal}} \quad (6.14)$$

Equations 6.15 – 6.17 describe the plating reaction kinetics. A Butler-Volmer relationship is used, and an asymmetric forward and backward reaction kinetic for lithium plating is assumed with a ratio of 0.3:0.7 in Equation 6.15. These kinetic constants indicate that the forward reaction that results in lithium deposition has a higher probability of occurring than the backward reaction, where the plated lithium metal dissolves into ionic form in the electrolyte.

$$< j_{pla} >= min\ (0, ai_{0,pla}[e^{\frac{0.3F}{RT}\eta_{pla}} - e^{-\frac{0.7F}{RT}\eta_{pla}}]) \quad (6.15)$$

$$i_{0,pla} = ak_{pla} < c_e^{\alpha_{a,pla}} > \quad (6.16)$$

$$\eta_{pla} = < \phi_s > - < \phi_e > - \frac{< j_{pla} >}{a} R_{film} \quad (6.17)$$

6.2.2 SE and Conventional Pouch Cell Parameterization

As illustrated in Figure 6.1, one UE, two SEA, and two SEA-SEC configurations were modeled. These are the same cell configurations defined in Chapter 5, where a UE consists of a uniform anode and a uniform cathode, a SEA has a structured anode paired with a planar cathode, and a SEA-SEC has both electrodes structured. The models in this chapter use a labeling convention where their cell configuration name (UE, SEA, or SEA-SEC) is noted first and is then followed by the anode thickness and the cathode thickness. All SEs modeled in this chapter have a grid patterned electrode geometry. A reference UE configuration is shown in Figure 6.1 (a). This

case is labeled as UE-68-60, where the anode is 68 µm thick and the cathode is 60 µm thick, yielding an N/P ratio of 1.17. UE-68-60 was designed to match the graphite|NMC-532 cell fabricated by Chen et al.[21] The cell parameters from Chen et al.'s are summarized in Table 6.1 and Table 6.2; The associated transport and kinetic properties from Table 4.1 and Table 4.2 in Chapter 4 were reused for the models in this chapter. Initial solid-phase concentrations, also reported in Table 6.1, were selected such that the NMC-532 material modeled has an SOC close to one in the beginning of charge, while the graphite has an SOC close to zero.

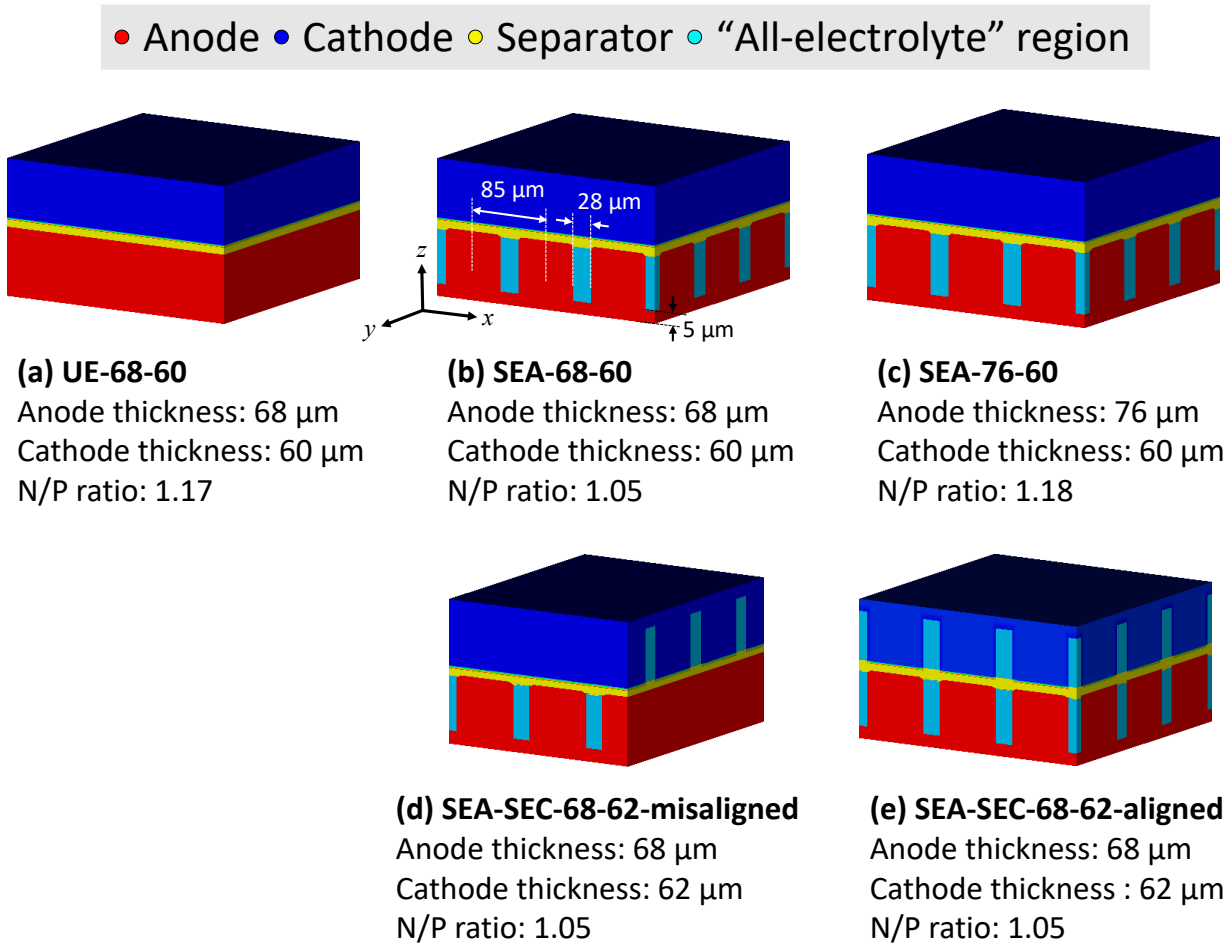

Figure 6.1 Illustrations of (a) UE-68-60, (b) SEA-68-60, (c) SEA-76-69, (d) SEA-SEC-68-62-misaligned, and (e) SEA-SEC-68-62-aligned. The x-y-z coordinates can be found near (b). These are the five cases modeled in this chapter. All models had a fixed cathode active material loading of 17.5 mg_{active}/cm^2.

The SEA-68-60 configuration shown in Figure 6.1 (b) has the same electrode thicknesses as UE-68-60.[21] Modeled after Chen et al's SEA design, the base layer thickness of the SE anode is 5 μm, and the spacing between the "all-electrolyte" regions is 85 μm for SEA-68-60, as labeled in Figure 6.1 (b). In Chen et al.'s study, the SE anode grid patterns were manufactured using laser ablation, resulting in circular, cone-shaped "all-electrolyte" regions with a smaller width closer to the anode-current collector interface. To reduce the impact on computational resources, the SE anodes and SE cathodes modeled in this chapter have square columnar shape "all-electrolyte" regions with a uniform width. In addition, Chen et al.'s SEA cell had a ~10% less anode mass than their UE cell. To match this information, the "all-electrolyte" region width for the SE anode in SEA-60-68 was calculated to be 28 μm, as labeled in Figure 6.1 (b). All SE anodes and SE cathodes in this chapter utilize the same "all-electrolyte" region width, base layer thickness, and spacing between the "all-electrolyte" regions to help facilitate a comparative analysis between models. All models had a fixed cathode active material loading of 17.5 mg_{active}/cm^2 and are described further below.

Due to the 10% reduction in anode mass, SEA-68-60 had a lower N/P ratio of 1.05 compared to UE-68-60. The N/P ratio has a strong correlation to lithium plating, where a higher N/P ratio lowers the chances of lithium plating occurrence.[161,165,166] Chen et al. found their SEA, having a lower N/P ratio relative to the UE configuration, still demonstrated a reduction in lithium plating.[21] To understand the impact of electrode architecture versus the effects of N/P ratio on lithium plating, a SEA with a 76 μm thick anode, a 60 μm thick cathode, and a N/P ratio of 1.18, was modeled as shown in Figure 6.1 (c) and labeled as SEA-76-60. The base layer thickness, the width, and the spacing of the "all-electrolyte" regions in SEA-76-60 are the same as SEA-68-60. Since the geometric resolution for the models is set to 1 μm, adjustments to the cell configurations

were made in increments of 1 μm. As a result, the N/P ratio of SEA-76-60 is 1.18 and will not be 1.17 to exactly match UE-68-60. Finally, two SEA-SEC models were created with the same active material mass loading and N/P ratio as SEA-60-68. One SEA-SEC model has the "all-electrolyte" regions misaligned and labeled as SEA-SEC-68-62-misaligned in Figure 6.1 (d), while the other has the "all-electrolyte" regions perfectly aligned and labeled as SEA-SEC-68-62-aligned in Figure 6.1 (e).

Table 6.1. Model parameters used for the single-layer cell analysis

Parameter	Description	Units	NMC-532	Graphite
c_s^0	Initial concentration	mol/m^3	49272	15
ε_e	Volume fraction of liquid	*N/A*	0.3411 [21]	0.3132 [21]
ε_s	Volume fraction of solid	*N/A*	0.6062 [21]	0.6456 [21]
ε_f	Volume fraction of filler	*N/A*	0.053 [21]	0.041 [21]
R_s	Particle radius	*m*	$2.65 \cdot 10^{-6}$ [21]	$4.06 \cdot 10^{-6}$ [21]

Table 6.2. Electrolyte and separator model parameters. N/A means not applicable.

Parameter	Description	Units	Electrolyte
c_e^0	Initial concentration	mol/m^3	1000 [21]
Parameter	**Description**	**Units**	**Separator**
t_{sep}	Separator thickness	*M*	0.0012 [21]
ε_e	Volume fraction of liquid	*N/A*	0.47 [21]

6.3 Results and Discussion

6.3.1 *Charge Capacity and Lithium Plating Onset*

The charge voltage versus specific capacity results at a 6C rate are presented in Figure 6.2, and the onset of lithium plating is marked with a star. The onset of lithium plating is defined by the first occurrence of a non-zero plating current in the model. In Equation 6.15, the plating current is non-zero when the plating overpotential, as defined by Equation 6.13, is less than zero. This is a necessary condition to trigger lithium plating because the plating overpotential is a thermodynamic driving force for the lithium plating reaction. Modeling results in Figure 6.2 predicted that lithium plating occurred in UE-68-60, SEA-68-60, SEA-SEC-68-62-misaligned, and SEA-SEC-68-62-aligned. Comparing UE-68-60 to SEA-68-60, the charge voltage profile and end of charge (EOC) capacity are similar, with SEA-68-60 having a slightly higher charge capacity and lower charge overpotential. Lithium plating was detected in both models, and the onset of the plating current density occurred approximately 30 seconds earlier in UE-68-60 than in SEA-68-60. These results qualitatively align with Chen et al's finding that reducing the anode mass by 10% with the use of the "all-electrolyte" regions in the SEA can reduce lithium plating. However, it is important to acknowledge in the context of this model that a 30 second time difference requires further investigation to understand broader design impacts.

Modeling results for SEA-76-60 exhibited no lithium plating current density, which implies this design case, as shown in Figure 6.2, had no lithium plating. In SEA-76-70, the plating overpotential, as defined in Equation 6.13, did not drop below zero during the charge cycle; thus, no lithium plating reactions occurred in the model. Additional improvements in charge capacity and overpotential were seen in SEA-76-60 relative to SEA-68-60 in Figure 6.2. Examining the solid and liquid phase Li-ion concentration profiles in Figure 6.3 and Figure 6.4, one can see that

these improvements are likely due to the increased volume fraction of electrolyte in SEA-76-60 relative to SEA-68-60. While SEA-76-60 and SEA-68-60 had similar concentration gradients in the solid phase in Figure 6.3, SEA-76-60 exhibits fewer dark blue regions in the contour plot and a more uniform Li-ion concentration gradient in Figure 6.4, leading to an improved concentration overpotential.

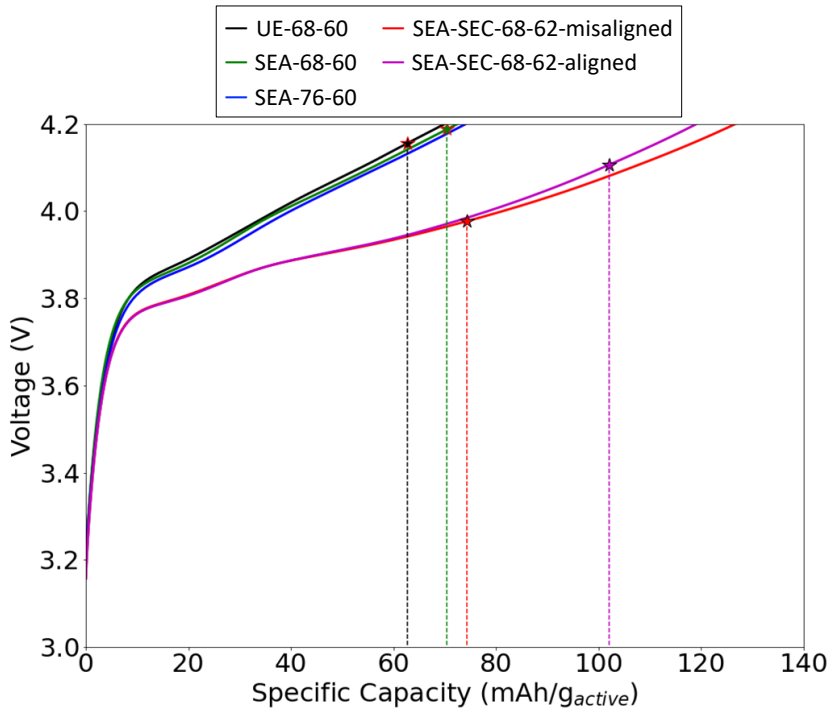

Figure 6.2 6C Charge voltage over specific capacity for UE-68-60, SEA-68-60, SEA-76-60, SEA-SEC-68-62-misaligned, and SEA-SEC-68-62-aligned. Lithium plating occurred in UE-68-60, SEA-68-60, SEA-SEC-68-62-misaligned, and SEA-SEC-68-62-aligned. The onset of lithium plating in these cells are marked by the star annotations. Plating did not occur in SEA-76-60. The specific capacity is normalized to the weight of the cathode active material.

In Figure 6.2, the SEA-SEC configurations demonstrated improved charge over potential and charge capacity. As shown in Figure 6.4, the planar cathodes in UE-68-60, SEA-68-60, and SEA-76-60 exhibited a high liquid-phase Li-ion concentration in the electrolyte at EOC. This indicates the de-intercalated Li-ions have accumulated in the cathodes due to poor liquid-phase

transport during the charge cycle. As a result, fewer Li-ions are transported to the anode, and the anodes in UE-68-60, SEA-68-60, and SEA-76-60 have begun to develop dark blue regions, where the electrolyte is nearly depleted at EOC. In contrast, the SE cathodes in the SEA-SECs in Figure 6.2 exhibited a lower electrolyte concentration gradient in the *z*-direction at EOC and lower charge overpotential during the charge cycle, indicating better Li-ion transport from the cathode to the anode.

A higher active material utilization, as shown in Figure 6.3, and a higher charge capacity, as shown in Figure 6.2, are observed at the EOC in the SEA-SEC configurations relative to the UE and SEA configurations modeled. Comparing SEA-SEC-68-62-aligned to SEA-SEC-68-62-misaligned, it was found that not aligning the "all-electrolyte" regions, resulted in a higher charge capacity. However, lithium plating started earlier in SEA-SEC-68-62-misaligned than SEA-SEC-68-62-aligned, as seen in Figure 6.2. Concentration plots in Figure 6.3 and Figure 6.4 do not reveal significant differences between the concentration profiles in the electrode thickness (*z*-direction) between the two SEA-SEC configurations modeled, indicating the specific capacity difference between SEA-SEC-68-62-misaligned and SEA-SEC-68-62-aligned is likely influenced more by electrochemical non-uniformities in the *x*-*y* plane. However, further investigation into additional geometrical variants of SEA-SEC configurations is needed to understand this trend.

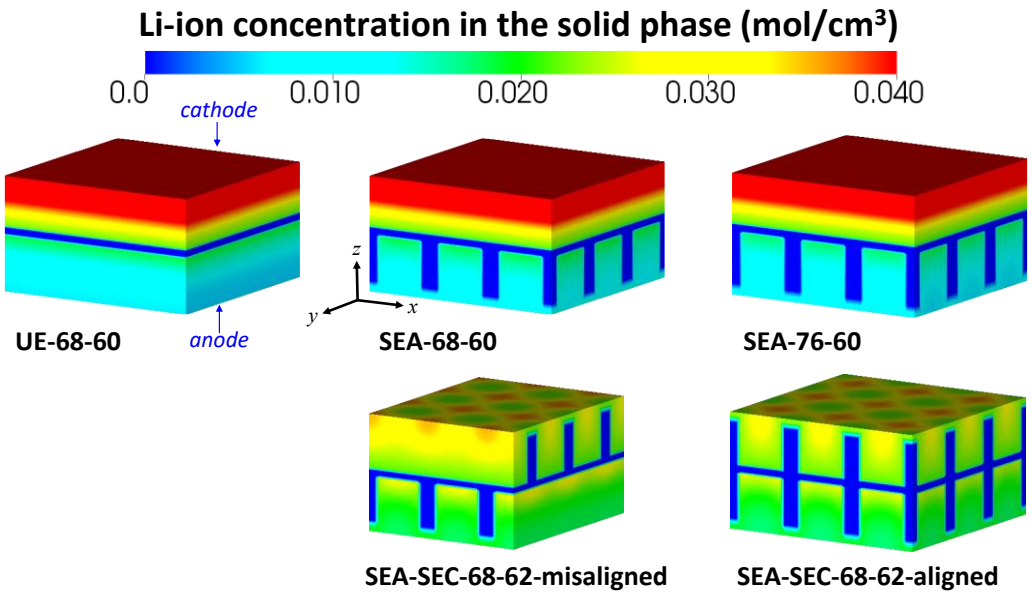

Figure 6.3 Solid-phase Li-ion concentration plots at the end of charge (EOC) for UE-68-60, SEA-68-60, SEA-76-60, SEA-SEC-68-62-misaligned, and SEA-SEC-68-62-aligned. For visualization of the internal structure, the illustration for SEA-SEC-68-62-misaligned is partially sliced, revealing the grid structures in the cathode.

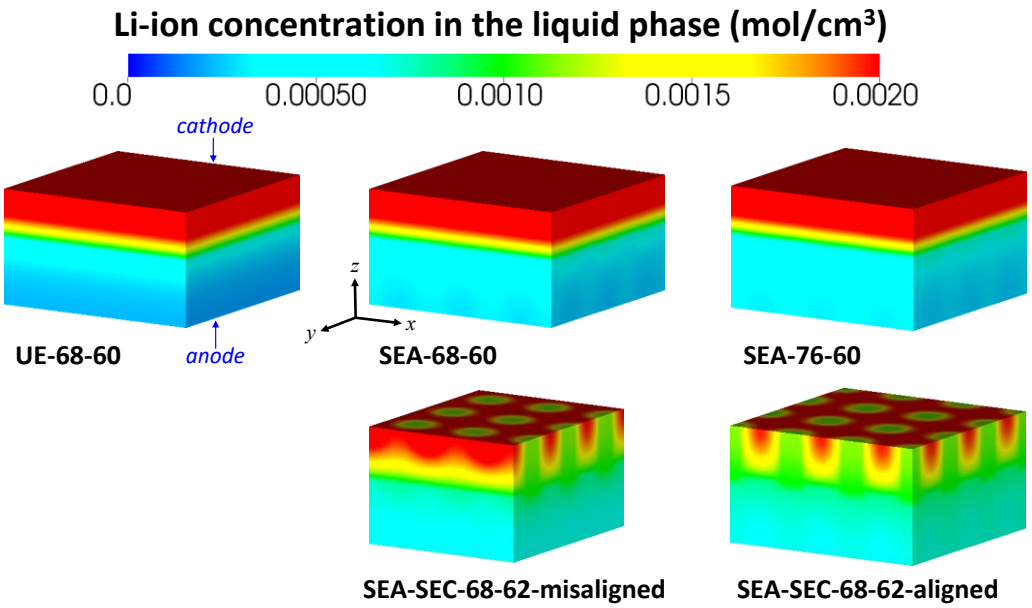

Figure 6.4 Liquid phase Li-ion concentration plots at the end of charge (EOC) for UE-68-60, SEA-68-60, SEA-76-60, SEA-SEC-68-62-misaligned, and SEA-SEC-68-62-aligned. For visualization of the internal structure, the illustration for SEA-SEC-68-62-misaligned is partially sliced, revealing the grid structures in the cathode.

The thickness of plated lithium in the anode at EOC for all models is shown in Figure 6.5. It is important to note that this model assumes a uniform layer of lithium deposition within each finite element in the model mesh, which is larger than the active material particle size. Plated lithium with a maximum thickness of 3.5 nm developed at the top surface of the anode interfacing the separator in UE-68-60. Plated lithium grew into 20 μm of the anode thickness, as shown in red in Figure 6.5 (a). In comparison, SEA-68-60 in Figure 6.5 (b) had a smaller maximum plating thickness of 0.56 nm, and a smaller anode volume that experienced lithium plating. These results generally align with the experimental trends noted by of Chen et al,[21] where more substantial lithium plating was observed in their UE in post-mortem scanning electron microscopy (SEM) analysis, while minimal traces of plated lithium were observed in the SEA. Chen et al.'s SEM analysis was conducted when the graphite anode was fully de-lithiated after 100 cycles of 6C fast charging. The plated lithium found in their SEM imaging was "dead lithium," which is metallic lithium that has become electrochemically inactive. It is important to acknowledge that our model does not differentiate dead lithium from reversible plated lithium nor reflect what occurs after 100 cycles of fast charging; instead, our models highlight the potential locations of lithium plating and the amount of plating that may occur in one galvanostatic charge cycle. Based on this, we make an assumption on regions that are "high risk" for potentially forming dead lithium upon subsequent cycling.

Overall, the SEA-SEC configurations had a larger plating thickness than the other design configurations. This is likely because they held a longer charge time after the onset of lithium plating occurred, as shown in Figure 6.2. If battery cells are charged under constant current (CC) until the cutoff voltage reaches 4.2V, SEA-SEC configurations will generally experience a high amount of lithium deposition. With this in mind, we believe the SEA-76-60 configuration, for the

cases modeled, is the best design option to minimize potential occurrences of dead lithium. However, a common practice in real-world battery testing is to hold the cell at a constant voltage (CV) after a CC cycle until the charge current drops below a predefined value.[167] This relaxes the overpotential caused by Li-ion concentration gradients, and the battery cell is charged either until it reaches its maximum capacity or until a certain amount of time has passed. As shown in Figure 6.2, at the onset of lithium plating for UE-68-60 (4.16 V), SEA-76-60 (4.19 V) and SEA-68-60 (4.20 V), a high overpotential and a low charge capacity between 63 – 75 mAh/g_{active} were observed. If a CC-CV charge protocol were used, the SEAs modeled in this chapter, despite their benefit in reducing lithium plating, may require a long CV charge time while still yielding a low charge capacity at the end of the CV cycle.

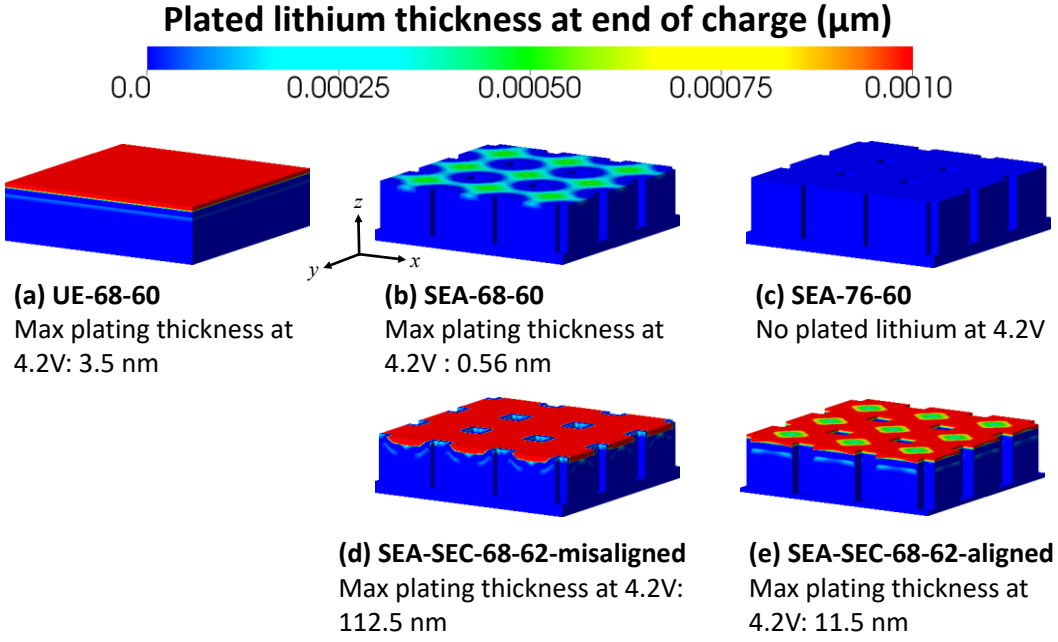

Figure 6.5 Plated lithium thickness in the anode at the end of a 6C charge for (a) UE-68-60, (b) SEA-68-60, (c) SEA-76-60, (d) SEA-SEC-68-62-misaligned, and (e) SEA-SEC-68-62-aligned. The maximum (max) plating thickness at the end of charge are noted below each model contour plot. For comparison purposes, only the anode is shown. All models were charged up to a cut-off voltage of 4.2V. No lithium plating is observed in SEA-76-60, which is reflected by the blue contour plot in (c).

6.3.2 *Lithium Plating at the Anode-Separator Interface*

As shown in Equations 6.15 – 6.17, lithium plating begins when the local liquid-phase potential exceeds the local solid-phase potential in the graphite anode. The electrolyte potential in general will increase as the Li-ion concentration in the liquid phase increases. When this occurs, lithium plating will initiate at the anode-separator interface and form on the anode surface in contact with the separator, where the electrolyte concentration is the highest. Figure 6.6 shows the plating current density in the anode at the onset of lithium plating for each model. For ease of visualizing the plating current density, only the graphite anode structure is displayed.

As shown in Figure 6.6 (a), for UE-68-60, the plating current density was uniform across the anode surface, which is an expected result for a conventional planar cell. In SEA-68-60, a non-uniform current is observed on the anode surface, with higher plating currents observed at the mid-points between the "all-electrolyte" regions. In this configuration, Li-ions transported from the planar cathode were uniform in the *x*-*y* plane at the cathode-separator interface. When these Li-ions reached the anode-separator interface, ions near the "all-electrolyte" regions conducted and diffused more quickly in the *z*-direction than those ions at *x*-*y* locations far away from the "all-electrolyte" regions. Li-ions accumulated at the mid-point regions between the "all-electrolyte" channels. This accumulation created more localized electrolyte concentration and potential gradients, which led to the high plating current density regions shown in red in Figure 6.6 (b).

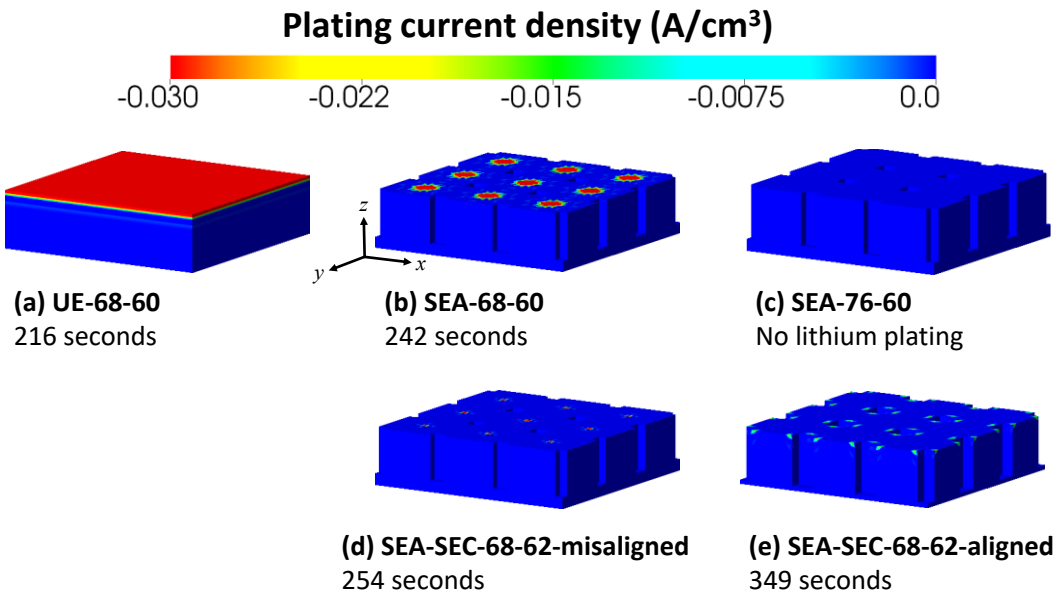

Figure 6.6 Lithium plating current density at the onset of plating for (a) UE-68-60, (b) SEA-68-60, (c) SEA-76-60, (d) SEA-SEC-68-62-misaligned, and (e) SEA-SEC-68-62-aligned. For visualization purposes, the cathode, separator, and "all-electrolyte" regions are not plotted. The onset time of lithium plating is noted for each model. Since no lithium plating is observed in SEA-76-60, the end-of-charge model state is displayed.

The locations of high plating current density in SEA-SEC-68-62-misaligned, as shown in Figure 6.6 (d), are similar to those shown in Figure 6.6 (b) for SEA-68-60. The "all-electrolyte" regions in the SE cathode, which facilitated faster Li-ion transport, were aligned with these *x*-*y* locations that are mid-points between the "all-electrolyte" regions in the SE anode. This led to a faster rate of ion accumulation at the anode surface and a more localized distribution of plating current density in SEA-SEC-68-62-misaligned compared to SEA-68-60. Aligning the "all-electrolyte" regions in the SE anode and SE cathode, as shown in Figure 6.6 (e), shifted the locations of high plating current density to the edges of the "all-electrolyte" regions. Compared to UE-68-60, SEA-68-60, and SEA-SEC-60-62-misaligned, SEA-SEC-60-62-aligned demonstrated a lower plating current density at the onset of lithium plating (indicated in green). This trend

implies that a slower lithium metal deposition rate will occur. The improved performance in SEA-SEC-60-62-aligned is likely due to a more balanced transport rate between the SE anode and the SE cathode. In SEA-SEC-60-62-aligned, there was less local Li-ion accumulation and a lower concentration overpotential overall. By aligning the SE patterns in SEA-SEC, we can potentially delay the onset of plating and slow down the lithium metal deposition rate in a LIB.

6.4 CONCLUSION

In this chapter, a coupled electrochemical-plating model was formulated for the 3D volume average method and implemented in *VIBE-AMPERES* to investigate lithium plating behavior in SEs and UEs. One UE, two SEA, and two SEA-SEC configurations were modeled. Based on the modeling results, it was found that both the N/P ratio and electrode structure play a role in when lithium plating begins and how it forms on the graphite anode. With an N/P ratio of 1.05, the SEA configuration (SEA-68-60) demonstrated a delayed lithium plating onset and a smaller plating thickness at the end of charge compared to a UE with an N/P ratio of 1.17. The SEA configuration with an N/P ratio of 1.18 (SEA-76-60) did not experience lithium plating. The SEA-SEC models, with an N/P ratio of 1.05, experiences delayed lithium plating and an improvement in charge overpotential and capacity. Among all design configurations, the SEA-SEC with perfectly aligned "all-electrolyte" regions yielded the highest charge capacity before lithium plating occurred, demonstrating the most promise for fast charging and lithium plating mitigation based on the limits of the models presented in this chapter.

It was found that SEAs and SEA-SECs can also be designed to alter the locations of lithium plating in a battery cell. Lithium plating was found to concentrate at the mid-points between the "all-electrolyte" regions for the SEA configuration and the SEA-SEC configuration with misaligned "all-electrolyte" regions. Additionally, the SE cathode in SEA-SEC had a larger concentration gradient that reduced lithium plating in the SE anode regions. Aligning the "all-electrolyte" regions in the SEA-SEC changed the spatial distribution of lithium plating to occur near the edges of the "all-electrolyte" regions. Moreover, a lower plating current density was found in the SEA-SEC configuration with aligned "all-electrolyte" regions, indicating a lower rate of lithium deposition compared to the other UE, SEA, and SEA-SEC designs modeled in this study.

Chapter 7. CONCLUSION

7.1 RESEARCH FINDINGS

Addressing Research Question 1a from section 1.3, several key design parameters and performance metrics for 3D LIBs have been identified. Chapter 2 demonstrated that all 3D LIBs, regardless of the material system and electrode architecture, exhibited an electrode thickness dependency that affects rate capability. Although our historical data analysis indicated that 3D LIBs consistently exhibited improved rate capability over conventional planar LIBs, the power and energy density trade-off based on electrode thickness, as discussed in section 1.1.2, remains in 3D LIBs. Like planar LIBs, electrode thickness was confirmed to be a critical design parameter for 3D LIBs.

For IDEs, modeling results from Chapter 3 found that the surface area versus volume ratio (*SA/V*) served as a performance indicator for discharge specific capacity across different IDE architectures. For both LTO|LFP and graphite|NMC-532 material systems, the specific discharge capacity of IDEs with different electrode architectures was positively correlated to the *SA/V* ratio within the same material system. Compared to conventional planar cells with the same active material loading, IDEs had a larger electrode thickness and a higher electrode surface area in contact with the separator. In response to Research Question 1b, concerning how IDEs fundamentally impact cell electrochemistry based on different material systems, results from Chapter 3 found that for material systems constrained by reaction kinetics, such as LTO|LFP, IDE designs demonstrated a 40% – 142% improvement range in discharge capacity over their planar counterpart. Conversely, the graphite|NMC-532 IDEs modeled in Chapter 3 were rate-limited by slow electric transport in the cathode thickness direction. Because of this, some graphite|NMC-532 IDEs, having a larger cathode thickness than their planar counterpart, showed a 18% – 35%

lower discharge capacity. Notably, the graphite|NMC-532 IDE with the largest *SA/V* ratio demonstrated a 10% improvement in discharge capacity, which was still a benefit gained but comparably smaller than what could be achieved in the LTO|LFP material system. Analyses on cell resistances and Li-ion concentration profiles in Chapter 3 revealed that the material system determined the lithiation profile within an IDE. The benefit of IDEs in increasing the *SA/V* ratio was maximized when the lithiation profile aligned with the IDE surface geometry, a condition typically observed in systems limited by reaction kinetics.

A uniformity index, *UI3D*, was also established in Chapter 3 to quantify current density non-uniformity across various cross-sections of IDEs, addressing Research Question 2a. Non-uniformities evaluated on a cross-section sliced in the direction of electrode thickness were found to have the strongest correlation with IDE specific discharge capacity. It was found that the rate of change of *UI3D* on this specific cross-section could be utilized to identify low-performing IDEs early in the discharge cycle. The results indicated that non-uniformities caused by electrode architecture significantly affected material utilization, which should be analyzed in conjunction with the *SA/V* ratio.

Further addressing Research Question 1a, in SEs the electrolyte volume fraction (EVF) was found to be a critical parameter that impact performance in Chapter 4 and Chapter 5. Graphite|NMC-622 SEs modeled in these two chapters demonstrated that both charge and discharge specific capacity of a single-layer cell increased with a higher EVF. In comparison, the charge and discharge energy density of a multi-layer cell stack initially increased with higher EVF values and began to decline beyond a certain EVF threshold, displaying an optimum. SEs demonstrated an up to 45% improvement in discharge energy and up to 33% improvement in charge capacity at the multi-layer stack level. However, a multi-layer pouch cell stack analysis

revealed that graphite|NMC-622 SEs had a lower stack active material loading than conventional planar cells due to the volume occupied by "all-electrolyte" regions, which can lead to negative effects that can exceed the benefits yielded in single-layer cell capacity improvements.

A subsequent analysis done to address Research Question 1c in Chapter 4 revealed that at least one-third of the improvement in graphite|NMC-622 cell capacity achieved by SEs could be attributed to reduced tortuosity, while at least one-half of the performance enhancement was linked to an increased quantity of Li-ions supplied by the additional electrolyte volume in SEs. With a higher EVF, the benefit of increased Li-ion availability outweighed the impact of reduced tortuosity on improving specific capacity. When the EVF was optimally designed, the performance of SEs was minimally impacted by spatial non-uniformities arising from varying the SE geometries and orientations. Based on these findings, it is reasonable to imply that for material systems that have fast ionic transport properties, SE may not offer a significant advantage in material utilization and rate capability. Modeling results in Chapter 5 showed that structuring either the cathode or the anode, as well as structuring both electrodes, resulted in improvements in either or both charge and discharge specific capacity. However, structuring the electrode that was not rate-limiting may increase Li-ion concentration gradients and adversely impact the cell specific capacity.

In Chapter 6, coupled electrochemical-plating models were created for grid pattern SEs based on a graphite|NMC-532 material system to address Research Question 2b. It was found that structuring either the anode or both electrodes led to delayed occurrences of lithium plating while improving charge capacity. Structuring both electrodes and aligning the "all-electrolyte" regions exhibited the highest potential for a higher charge capacity, lower charge time, and reduced risk of lithium plating. At the onset of lithium plating, the SE anodes have a more non-uniform lithium plating profile with fewer areas affected by lithium plating compared to the equivalent planar

electrodes. Moreover, by aligning the "all-electrolyte" regions in the SE cathode and the SE anode, a more balanced transport rate was achieved between the SE cathode and the SE anode. As a result, the locations of lithium plating were shifted to the edges of the "all-electrolyte" regions, and a lower plating current density was observed.

7.2 Future Work

This dissertation studied the effects of 3D IDEs and SEs on altering the transport and kinetic mechanisms within a single-layer battery cell and uncovered their implications on the rate capability of LIBs. Design parameters that serve as performance indicators for designing 3D LIBs were also identified. Further investigation is needed to understand the influence of 3D electrode architecture on cell temperature, internal stress, and material degradation, as these factors significantly impact battery capacity retention over repeated cycles. Implementing physics-based computational models that encompasses both galvanostatic charge and discharge cycles, as well as constant voltage relaxation, will also provide a more comprehensive understanding of how 3D LIBs perform under various electrochemical test conditions before more investments are made into new manufacturing technologies. Furthermore, exploring how electrode structuring and the results of this dissertation can be applied to emerging material chemistries, such as Lithium metal batteries,[171,172] anode-free batteries,[173–175] and solid-state batteries,[23,176,177] may facilitate new opportunities for performance improvements.

APPENDIX A.

*The content in Appendix A has been published in *ACS Energy Letters* as supplemental materials and modified for this dissertation.[2] Reprinted and adapted with permission from Hung, C.-H.; Huynh, P.; Teo, K.; Cobb, C. L. "Are Three-Dimensional Batteries Beneficial? Analyzing Historical Data to Elucidate Performance Advantages." *ACS Energy Lett.* **2022**, 296–305. Copyright 2023 American Chemical Society.

Table A-I. 3D LIBs cases extracted and analyzed from literature. Case numbers used here correspond to the same case number in Chapter 2. Each row corresponds to a unique 3D LIB case, and papers with more than one 3D LIB and capacity-rate data may be referenced multiple times.

Case	Cathode	Anode	Separator	Electrolyte	Cell footprint area [mm^2]	Reference
A:1	$LiFePO_4$	$Li_4Ti_5O_{12}$	Liquid electrolyte	1M $LiClO_4$ in 1v:1v EC:DMC	0.97	Sun et al.[22]
A:2	$LiCoO_2$	$Li_4Ti_5O_{12}$	PMMA gel electrolyte	1M $LiClO_4$ in 1v:1v EC:DEC	0.06	Yoshima et al.[83]
A:3	$LiMn_2O_4$	$Li_4Ti_5O_{12}$	PMMA gel electrolyte	1M $LiClO_4$ in 1v:1v EC:DEC	6.64	Dokko et al.[46]
B1:1	$LiFePO_4$	Lithium Metal	Solid-state electrolyte	0.5M LiTFSI [BMIM] TFSI (ionogel)[90]	8.40	Ashby et al.[23]
B2:1	$LiCoO_2$	Lithium Metal[c]	Polypropylene films (two layers of Celgard 2500)	1.3M $LiPF_6$ in a blend of alkyl carbonates	36.00	Bae et al.[84]
B2:2	$LiCoO_2$	Lithium Metal[c]	Polypropylene films (two layers of Celgard 2500)	1.3M $LiPF_6$ in a blend of alkyl carbonates	36.00	Bae et al.[84]
B2:3	$LiCoO_2$	Lithium Metal[c]	Polypropylene films (two layers of Celgard 2500)	1.3M $LiPF_6$ in a blend of alkyl carbonates	36.00	Bae et al.[84]
B2:4[a]	NMC111[b]	Graphite	Glass fiber film (Type 691, VWR)	1 M $LiPF_6$ in 3:7 EC:EMC (2% VC)	176.71	Habedank et al.[60]
B2:5[a]	NMC111[b]	Graphite	Glass fiber film (Type 691, VWR)	1 M $LiPF_6$ in 3w:7w EC:EMC	154.00	Kraft et al.[65]
B2:6[a]	NMC111[b]	Graphite	Glass fiber film (Type 691, VWR)	1 M $LiPF_6$ in 3w:7w EC:EMC	154.00	Kraft et al.[65]
B2:7[a]	NMC111[b]	Graphite	Glass fiber film (Type 691, VWR)	1 M $LiPF_6$ in 3w:7w EC:EMC	154.00	Kraft et al.[65]
B2:8[a]	NMC111[b]	Graphite	Glass fiber film (Type 691, VWR)	1 M $LiPF_6$ in 3w:7w EC:EMC	154.00	Kraft et al.[65]
B2:9	$LiCoO_2$	Lithium Metal	Polypropylene film (Celgard 2340)	1 M $LiPF_6$ in 1w:1w:1w EC:DMC:EMC	225	Lu et al.[85]

B2:10	$LiCoO_2$	Lithium Metal	Polypropylene film (Celgard 2340)	1 M $LiPF_6$ in 1w:1w:1w EC:DMC:EMC	225	Lu et al.[85]
B2:11	$LiCoO_2$	Lithium Metal[c]	Polypropylene film (two layers of Celgard 305)	1.3 M $LiPF_6$ in EC:DMC	100	Sander et al.[86]
B2:12	$LiCoO_2$	Lithium Metal[c]	Polypropylene film (two layers of Celgard 305)	1.3 M $LiPF_6$ in EC:DMC	100	Sander et al.[86]
B2:13	$LiCoO_2$	Lithium Metal[c]	Polypropylene film (two layers of Celgard 305)	1.3 M $LiPF_6$ in EC:DMC	100	Sander et al.[86]
B2:14	$LiCoO_2$	Lithium Metal[c]	Polypropylene film (two layers of Celgard 305)	1.3 M $LiPF_6$ in EC:DMC	100	Sander et al.[86]
B2:15	$LiCoO_2$	Lithium Metal[c]	Polypropylene film (two layers of Celgard 305)	1.3 M $LiPF_6$ in EC:DMC	100	Sander et al.[86]
B2:16	$LiCoO_2$	Lithium Metal[c]	Polypropylene film (two layers of Celgard 305)	1.3 M $LiPF_6$ in EC:DMC	100	Sander et al.[86]
B3:1	$Li_4Ti_5O_{12}$	Lithium Metal[c]	Polypropylene film (manufacturer not reported)	1 M $LiPF_6$ in 1v:1v EC:EMC	1500.00	Izumi et al.[87]
B3:2	$Li_4Ti_5O_{12}$	Lithium Metal	Film, material not reported	1M $LiPF_6$ in 1v:1v EC:DEC	40.00	Liu et al.[61]
B3:3	$Li_4Ti_5O_{12}$	Lithium Metal	Film, material not reported	1M $LiPF_6$ in 1v:1v EC:DEC	40.00	Liu et al.[61]
B3:4	$Li_4Ti_5O_{12}$	Lithium Metal	Film, material not reported	1M $LiPF_6$ in 1v:1v EC:DEC	40.00	Liu et al.[61]
B4:1	Silver	Lithium Metal[c]	PP/PE/PP film (Celgard)	1M $LiPF_6$ in 1:1:3 EC:PC:EMC	4.84	Saleh et al.[88]
B4:2	Silver	Lithium Metal[c]	PP/PE/PP film (Celgard)	1M $LiPF_6$ in 1:1:3 EC:PC:EMC	4.84	Saleh et al.[88]
B4:3	Silver	Lithium Metal[c]	PP/PE/PP film (Celgard)	1M $LiPF_6$ in 1:1:3 EC:PC:EMC	4.84	Saleh et al.[88]
B4:4	Silver	Lithium Metal[c]	PP/PE/PP film (Celgard)	1M $LiPF_6$ in 1:1:3 EC:PC:EMC	4.84	Saleh et al.[88]
C:1	$LiMnO_2$	NiSn	Liquid electrolyte	1M $LiClO_4$ in 1:1 EC:DMC	4.60	Pikul et al.[89]
C:2	$LiMnO_2$	NiSn	Liquid electrolyte	1M $LiClO_4$ in 1w:1w EC:DMC	3.97	Ning et al.[42]
C:3	$LiMnO_2$	NiSn	Liquid electrolyte	1M $LiClO_4$ in 1:1 EC:DMC	2.00	Pikul et al.[41]
C:4	$LiMnO_2$	NiSn	Liquid electrolyte	1M $LiClO_4$ in 1:1 EC:DMC	1.50	Pikul et al.[41]
C:5	$LiMnO_2$	NiSn	Liquid electrolyte	1M $LiClO_4$ in 1:1 EC:DMC	1.90	Pikul et al.[41]
C:6	$LiMnO_2$	NiSn	Liquid electrolyte	1M $LiClO_4$ in 1:1 EC:DMC	1.70	Pikul et al.[41]

[a] 3D LIBs in Category B with 3D architecture in the anode rather than the cathode.
[b] For brevity, NMC111 is used for $LiNi_{0.33}Mn_{0.33}Co_{0.33}O_2$.
[c] Electrode thickness was not reported.

Table A-II. Upper-bound and units used in the curve-fitting scheme for Q_{max}

Case #	Q_{max} upper-bound	Capacity units	Reference
A:1	170	mAh/g_{active}	Sun et al.[22]
A:2	351	mAh/g_{active}	Yoshima et al.[83]
A:3	320	mAh	Dokko et al.[46]
B1:1	140	mAh/g_{active}	Ashby et al.[23]
B2:1	274	mAh/g_{active}	Nitta et al.[96]
B2:2	274	mAh/g_{active}	Nitta et al.[96]
B2:3	274	mAh/g_{active}	Nitta et al.[96]
B2:4	144	mAh/g_{active}	Habedank et al.[60]
B2:5	3.420	mAh	Kraft et al.[65]
B2:6	3.800	mAh	Kraft et al.[65]
B2:7	4.330	mAh	Kraft et al.[65]
B2:8	5.770	mAh	Kraft et al.[65]
B2:9	274	mAh/g_{active}	Nitta et al.[96]
B2:10	274	mAh/g_{active}	Nitta et al.[96]
B2:11	unbounded	Ah/m^2	Not applicable
B2:12	unbounded	Ah/m^2	Not applicable
B2:13	unbounded	Ah/m^2	Not applicable
B2:14	unbounded	Ah/m^2	Not applicable
B2:15	unbounded	Ah/m^2	Not applicable
B2:16	unbounded	Ah/m^2	Not applicable
B3:1	160	mAh/g_{active}	Izumi et al.[87]
B3:2	175	mAh/g_{active}	Nitta et al.[96]
B3:3	175	mAh/g_{active}	Nitta et al.[96]
B3:4	175	mAh/g_{active}	Nitta et al.[96]
B4:1	290	mAh/g_{active}	Saleh et al.[88]
B4:2	290	mAh/g_{active}	Saleh et al.[88]
B4:3	290	mAh/g_{active}	Saleh et al.[88]
B4:4	290	mAh/g_{active}	Saleh et al.[88]
C:1	0.000500	mAh	Pikul et al.[89]
C:2	0.830	μAh	Ning et al.[42]
C:3	unbounded	Ah/m^2	Not applicable
C:4	unbounded	Ah/m^2	Not applicable
C:5	unbounded	Ah/m^2	Not applicable
C:6	unbounded	Ah/m^2	Not applicable

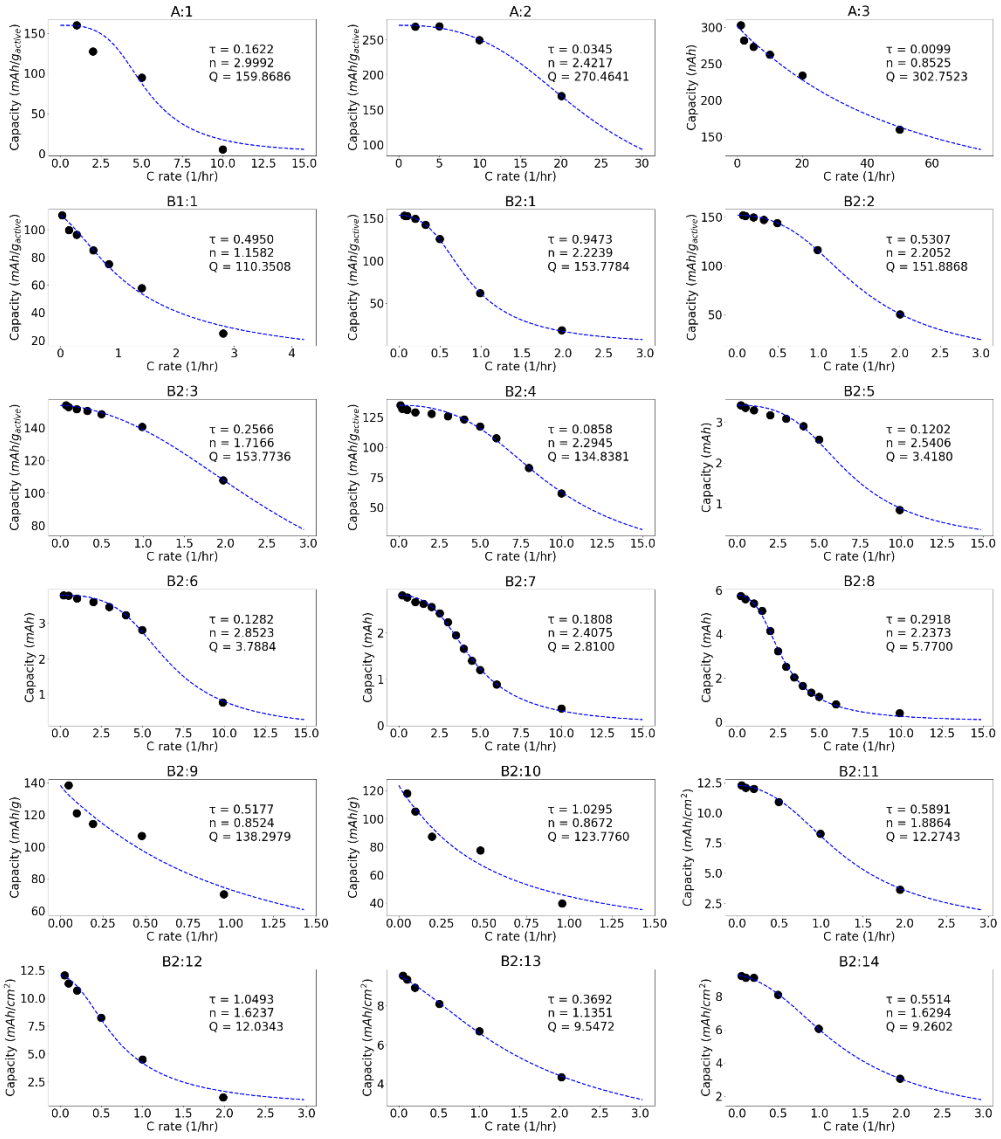

Figure A1. Curve-fitting results of 3D LIBs in Category A, Subcategory B1, and Subcategory B2 (up to case B2:14). Black markers are the data extracted from experimental literature and blue curves are the best-fit curves.

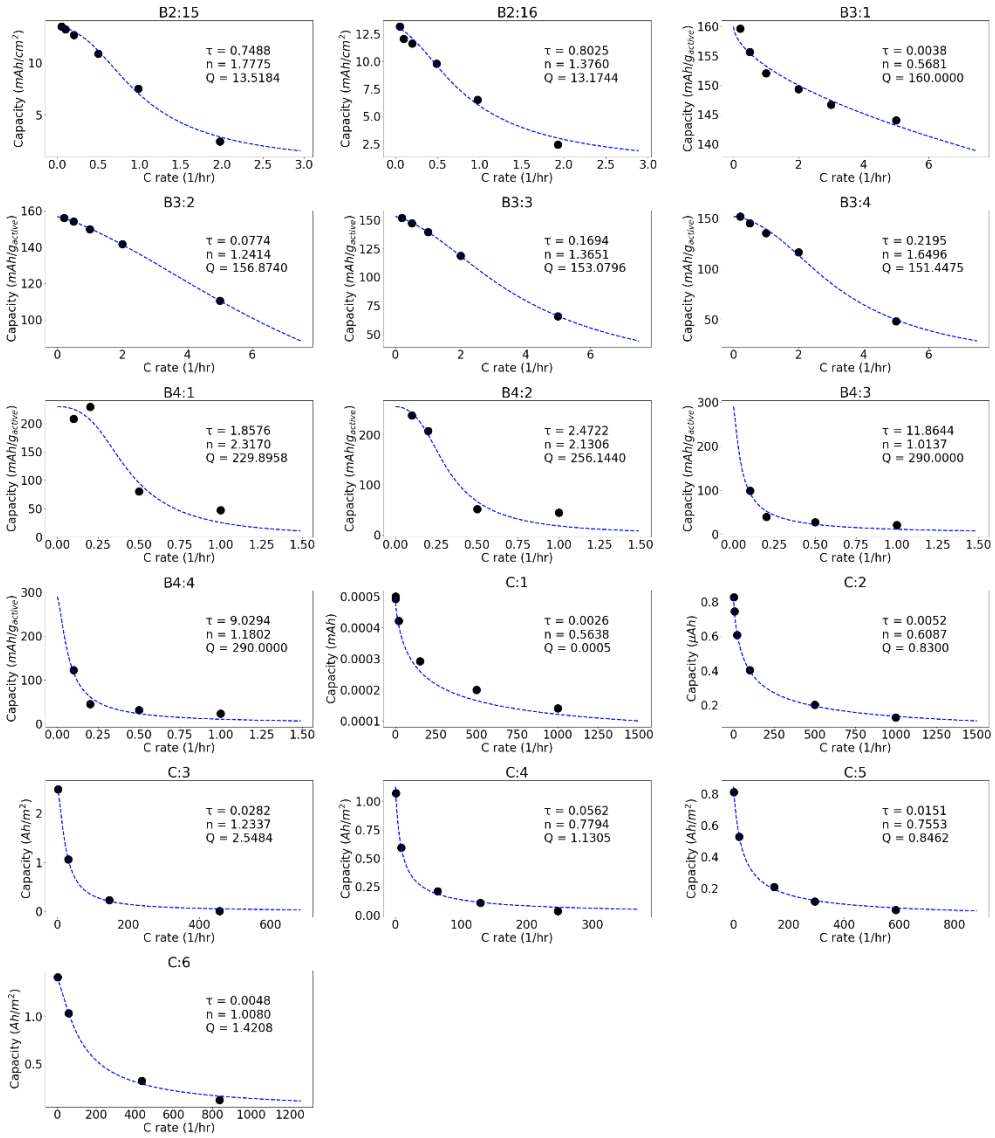

Figure A2. Curve-fitting results of 3D LIBs in Subcategory B2 (starting from case B2:15), Subcategory B3, Subcategory B4, and Category C. Black markers are the data extracted from experimental literature and blue curves are the best-fit curves.

APPENDIX B.

*The content in Appendix B is adapted from the supplemental material of Hung, C.-H.; Allu, S.; Cobb, C. L. "Modeling Current Density Non-Uniformities to Understand High-Rate Limitations in 3D Interdigitated Lithium-Ion Batteries." *J. Electrochem. Soc.* **2021**, *168* (10), 100512. under CC BY 4.0 (https://creativecommons.org/ licenses/by/4.0/).[1]

Pouch cell stack design details and assumptions

The gravimetric and volumetric energy density values were calculated based on the weight and volume of a hypothetical pouch cell stack. Simplified views of the pouch cell stack are shown in Figure B1. The pouch cell stack consists of layers of anodes, cathodes, separators, and current collectors. The stack height ranges from 0.98 – 1.03 cm with an area of 23.49 cm by 19.44 cm. For analysis purposes, our cell designs were modeled after the cell area of the 2017 second generation Nissan Leaf pouch cell and assumed a 10% pouch cell seam.[58] The apparent weight density of a single-layer battery cell is different from that of a multi-layer cell stack because they have different proportions of cell components by volume. As the number of layers (i.e. unit cell sandwiches) increases in a pouch cell stack, the apparent stack weight density (g/cm^3) approaches a stable value. Based on our calculations, the apparent weight density of our pouch cell stacks begins to stabilize within 1% or less at a stack height greater than 0.5 cm. Thus, our pouch cell stacks used stack heights in the range of 0.98 – 1.03 cm to minimize the potential of unfair comparisons due to mismatched weight densities.

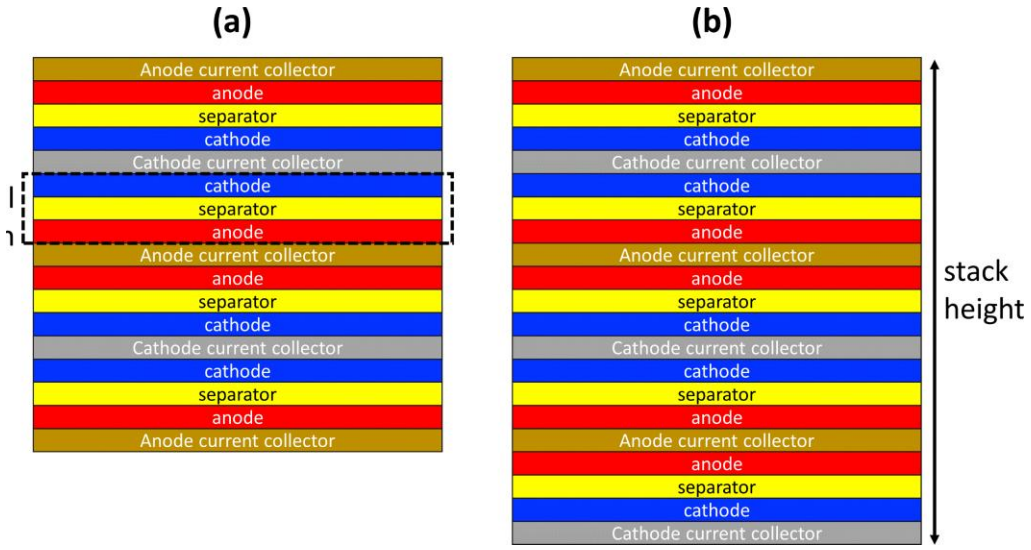

Figure B1. Illustrations of hypothetical pouch cell stacks used in our analysis. Maintaining active material mass loading across all cell designs leads to variations in total stack height ranging from 0.98 – 1.03 cm where an even or odd number of unit cell sandwiches must be used. (a) shows the case of an even number of unit cell sandwiches with four displayed as an example. (b) shows the case of an odd number of unit cell sandwiches with five displayed as an example.

We assumed all electrodes in the pouch cell stack must be electrochemically active. Thus, a cathode was always paired with an anode and a separator in our stack analysis. A cathode, a separator, and an anode form what we call a "unit cell sandwich," as noted in Figure B1. Additionally, we assumed the first and last layers of the pouch cell stack were always current collectors as this arrangement is needed to conduct electrons generated and consumed by electrochemical reactions from the external circuit. Based on these assumptions, there were two possible cell stack scenarios. Figure B1 (a) shows the scenario where there was an even number of unit cell sandwiches. In this case, the first and last layers of the pouch cell stack were both copper current collectors for the anode, resulting in more copper current collectors in the pouch cell stack. In Figure B1 (b), there are an odd number of unit cell sandwiches. In this scenario, the first layer was a copper current collector for the anode, and the last layer was an aluminum current

collector for the cathode. The numbers of copper and aluminum current collectors in this pouch cell stack scenario were the same. Due to variances in cathode and anode thicknesses, the pouch cell stacks analyzed could have an even or an odd number of unit cell to achieve the target stack height range of 0.98 – 1.03 cm.

Computational Setup

Finite element meshes with hexahedral elements were created with a commercial software program, Coreform Cubit.[178] This program enables the definition of geometry and meshes to model electrode cell sandwiches composed of a cathode, an anode, and a separator. Meshes were output to the exodus file format and were imported into VIBE-AMPERES. Boundary conditions were set up such that the cathode-current collector interface has a constant applied discharge current, and the anode-current collector interface has a constant voltage held at 0.1V. Symmetry boundary conditions were imposed for SEs and zero Li-ion flux is assumed across the symmetry boundary.[1] Enforcing symmetry conditions minimizes computational run time and enables efficient 3D modeling of the minimum SE unit cell needed to capture discharge capacity behavior. Meshes ranged from 325 – 6300 hexahedral elements in size and took 5 minutes to 15 hours to run on 4 cores in an AMD EPYC 7702 64-core processor with up to 8 GB RAM.

Uniform electrode (UE) designs

Table B-I Uniform electrodes (UEs) and cell stack design parameters

Design case	Cathode active material loading (mg/cm^2)	Cathode thickness (µm)	Cathode porosity (%)	Anode active material loading (mg/cm^2)	Anode thickness (µm)	Anode porosity (%)
UE-1	30.5	94	20.0	15.5	131	35.1
UE-2	30.8	101	25.0	15.6	132	35.1
UE-3	30.7	108	30.0	15.6	132	35.1
UE-4	30.6	116	35.0	15.5	131	35.1
UE-5	30.7	126	40.0	15.6	132	35.1
UE-6	30.6	137	45.0	15.5	131	35.1
UE-7	30.7	151	50.0	15.5	131	35.1
UE-8	65.0	246	35.0	33.0	279	35.1
UE-9	65.0	320	50.0	32.9	278	35.1

Table B-II. UE pouch cell stack parameters

Design case	Number of unit cell sandwiches	Stack height (cm)	Stack weight (kg)	Stack volume (L)	Stack Capacity (Ah)
UE-1	37	0.992	1.19	0.453	97
UE-2	36	0.993	1.18	0.454	95
UE-3	35	0.991	1.16	0.452	92
UE-4	34	0.986	1.14	0.450	89
UE-5	33	0.993	1.13	0.454	87
UE-6	32	0.995	1.11	0.454	84
UE-7	31	1.01	1.10	0.460	81
UE-8	18	1.02	1.17	0.467	100
UE-9	16	1.03	1.10	0.469	89

Graded electrode (GE) designs

Using VIBE-AMPERES, we manually explored the GE design space to find the appropriate porosity and thickness ranges to analyze and compare against UEs and SEs. Our approach to define the GE design cases for analysis is based on the following three criteria:

(1) The porosity between the first and second layers in a GE must have enough variance to not converge to the behavior of a UE while adhering to practical porosity values of 20% – 50%.

(2) The second layer, which interfaces with the separator, must be more porous than the first layer, which interfaces with the current collector.

(3) Based on the modeling results of UE-1 in Table B-XII, a 20% porous and 94 μm thick UE cathode only achieve a specific discharge capacity of 90 mAh/g_{active} at C/2, which is 48% of the theoretical active material capacity for NMC-622 (187 mAh/g_{active}). Assuming a simple linear relationship between active material utilization and electrode thickness in UEs, we decided that a 20% porous first layer in a GE model should not exceed 50 μm in thickness to avoid unfairly degrading capacity performance at higher rates.

After defining the criteria above, we conducted three different modeling investigations on electrolyte volume fraction (EVF) to understand the impact of EVF on GEs as noted below. Our goal was to understand the modeling limits of GEs before proceeding with a more in-depth analysis and comparison against UEs and SEs at the pouch cell scale.

First model investigation: Fixed electrolyte volume fraction (EVF)

To compare with the 35% porous baseline UE, GE-1 and GE-2 were designed to have a 35% EVF and a total cathode thickness of 116 μm. Both GE-1 and GE-2 have a first layer porosity

of 20% following criterion (1) above. GE-1 has a maximum first layer thickness of 50 μm per criterion (3) above, and GE-2 has half of the first layer thickness.

Second model investigation: Varying EVF

Next, GE-3 to GE-8 were designed to EVFs ranging from 38% to 49% following criteria (1) - (3) above. GE-3, GE-6, and GE-8 have first-layer porosities fixed at the minimum value of 20% and second-layer porosities fixed at the maximum value of 50%. By comparing these three cases, we can see the impact of layer thicknesses in GEs. GE-4, GE-6, and GE-7 have the same first layer thickness with changing first layer porosities. Comparing GE-4 to GE-6 shows the impact of changing second layer porosity, while comparing GE-6 to GE-7 allows us to see the impact of changing first layer porosity.

Third model investigation: EVF limitations

As the third and last investigation to define the GE design case range, a GE was modeled to have 35.0% porous bottom layer and 64.0% porous top layer, resulting in a 55.4% electrolyte volume fraction. This design is case GE-9 in Table B-III, and we intentionally designed a second layer porosity beyond 50% to see if the design trend holds.

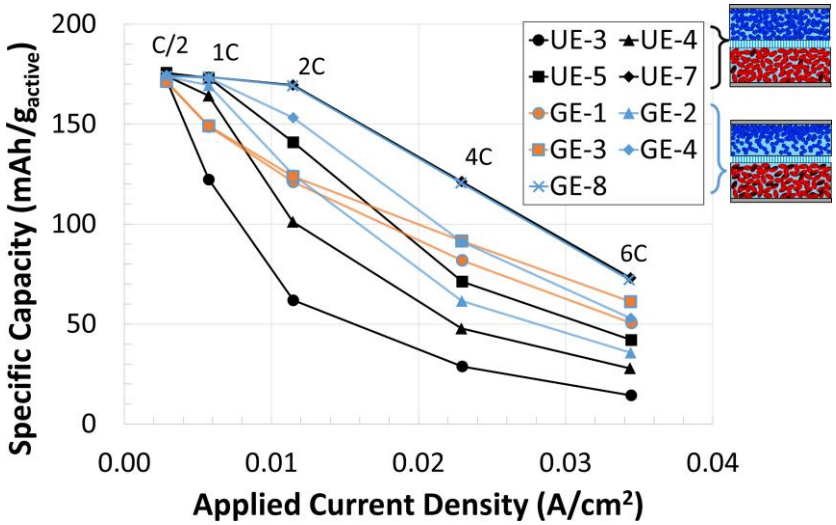

Figure B2. Specific discharge capacity versus applied current density for a subset of uniform electrode (UE) and graded electrode (GE) models. Data points in each line have a current density corresponding to a C/2, 1C, 2C, 4C, and 6C discharge rate.

We examined GE trends as a function of EVF. In **Figure B2**, the specific discharge capacity versus applied current density of UEs and GEs is plotted. GEs can be categorized into three groups based on their rate capability plot: (1) a concave-up curve such as that formed by UE-3, GE-1, and GE-3, (2) a S-shape curve like the one formed by UE-4, UE-5, GE-2, and GE-4, and (3) a concave-down curve such as the one formed by UE-7 and GE-8. In UEs, the plot shape transition from (1) concave-up to (2) S-shape and then to (3) concave-down exhibits a consistent increase in 6C discharge capacity. From (1) to (3), the discharge rate capability increases for UEs. Examining GEs, a different trend is observed, where the GE-1 and GE-3 (orange solid lines) that have a (1) concave-up rate capability curve demonstrates higher 6C discharge capacity than the (2) S-shape curves. We believe this is a characteristic unique to GEs that stemmed from the highly-porous second layer (46% – 50% porous) interfacing the separator. Such high porosity enables better 6C discharge capacity performance. The active material loading in GE-1 and GE-3 was maintained at approximately 31 mg/g_{active} by using a dense and thick first layer (20% porous and 50 μm thick).

Table B-III. Design parameters used for GEs based on parameters defined in Figure 2 in the main text

Design case	Cathode active material loading (mg/cm^2)	Cathode thickness (µm)	First layer thickness (µm)	Second layer thickness (µm)	First layer porosity (%)	Second layer porosity (%)	Electrolyte volume fraction* (%)
GE-1	30.7	116	50	66	20.0	46.0	35
GE-2	30.7	116	25	91	20.0	39.0	35
GE-3	30.7	121	50	71	20.0	50.0	38
GE-4	30.6	126	25	101	20.0	45.0	40
GE-5	30.7	133	50	83	35.0	48.0	43
GE-6	30.7	136	25	111	20.0	50.0	45
GE-7	30.7	143	25	118	35.0	50.0	47
GE-8	30.6	147	6	141	20.0	50.0	49
GE-9	30.6	169	50	119	35.0	64.0	55

*EVF values are rounded to nearest integer

Table B-IV. GE anode parameters and pouch cell stack parameters

Design case	Anode active material loading (mg/cm^2)	Anode thickness (µm)	Anode porosity (%)	Number of unit cell sandwiches
GE-1	15.5	131	35.1	34
GE-2	15.5	131	35.1	34
GE-3	15.5	131	35.1	34
GE-4	15.5	131	35.1	34
GE-5	15.5	131	35.1	33
GE-6	15.5	131	35.1	32
GE-7	15.5	131	35.1	32
GE-8	15.5	131	35.1	31
GE-9	15.5	131	35.1	29
Design case	**Stack height (cm)**	**Stack weight (kg)**	**Stack volume (L)**	**Stack Capacity (Ah)**
GE-1	0.986	1.14	0.450	89
GE-2	0.986	1.14	0.450	89
GE-3	1.01	1.15	0.459	89
GE-4	1.02	1.16	0.467	89
GE-5	1.01	1.14	0.463	87
GE-6	0.995	1.11	0.454	84
GE-7	1.01	1.12	0.463	84
GE-8	0.995	1.09	0.454	81
GE-9	1.03	1.06	0.454	76

Structured electrode (SE) designs

An SE design is fully defined by its cathode thickness, first layer thickness (t_1), electrolyte channel width (w_e), electrolyte channel spacing (w_s), and porosity in the "porous cathode + electrolyte" region (ε) in Figure 2 in the main text. To enable a comparison with the 35.0% porous baseline UE (UE-4), the porosity of the "porous cathode + electrolyte" region is set to 35.0% for all SEs modeled. This means the SE porous cathode + electrolyte region has a porosity of 35.0% but when combined with the additional electrolyte regions, this yields a total effective porosity greater than 35.0%. All electrolyte channels have a width fixed to 40 μm. From there, the first layer t_1 and w_s are varied to meet the 31 mg_{active}/cm^2 cathode active loading requirement. For SEGs, the first layer thickness (t_1) is varied at three different increments of 0 μm, 50 μm, and 75 μm; For SELs, to ensure a connected electrode, the first layer thickness is varied at three different increments of 25 μm, 50 μm, and 75 μm. In general, SEG designs with wider electrolyte channel spacing (w_s) and thicker first layer thickness (t_1) have lower electrolyte volume fraction.

Table B-V. Cathode and electrolyte parameters used for SEGs modeled as parametrized in Figure 2 in the main text

Design case	Cathode active material loading (mg/cm^2)	Cathode thickness (μm)	Electrolyte channel width (μm)	Electrolyte channel spacing (μm)	First layer thickness (μm)	Electrolyte volume fraction* (%)
SEG-1	30.7	118	40	200	75	36
SEG-2	30.7	119	40	200	50	37
SEG-3	30.7	121	40	200	0	38
SEG-4	30.6	126	40	90	75	40
SEG-5	30.8	133	40	90	50	43
SEG-6	30.7	145	40	90	0	48
SEG-7	30.7	149	40	60	75	49
SEG-8	30.7	169	40	60	50	55
SEG-9	30.7	209	40	60	0	64
SEG-10	65.0	307	40	90	0	48

*EVF values are rounded to nearest integer

Table B-VI. SEG anode parameters and pouch cell stack parameters

Design case	Anode active material loading (mg/cm^2)	Anode thickness (µm)	Anode porosity (%)	Number of cathodes/anodes in cell stack
SEG-1	15.5	131	35.1	34
SEG-2	15.5	131	35.1	34
SEG-3	15.5	131	35.1	34
SEG-4	15.5	131	35.1	34
SEG-5	15.5	131	35.1	33
SEG-6	15.5	131	35.1	31
SEG-7	15.5	131	35.1	31
SEG-8	15.5	131	35.1	29
SEG-9	15.5	131	35.1	26
SEG-10	32.9	278	35.1	16
Design case	**Stack height (cm)**	**Stack weight (kg)**	**Stack volume (L)**	**Stack Capacity (Ah)**
SEG-1	0.993	1.14	0.453	89
SEG-2	0.996	1.14	0.455	89
SEG-3	1.00	1.15	0.458	89
SEG-4	1.02	1.16	0.466	89
SEG-5	1.01	1.14	0.463	87
SEG-6	0.989	1.09	0.452	81
SEG-7	1.00	1.09	0.457	81
SEG-8	0.995	1.06	0.454	76
SEG-9	0.996	1.01	0.455	68
SEG-10	1.01	1.09	0.459	89

Table B-VII. Cathode and electrolyte parameters used for SELs modeled as defined in Figure 2 in the main text

Design case	Cathode active material loading (mg/cm^2)	Cathode thickness (µm)	Electrolyte channel width (µm)	Electrolyte channel spacing (µm)	Bottom layer thickness (µm)	Electrolyte volume fraction (%)
SEL-1	30.6	121	40	360	75	38
SEL-2	30.6	124	40	360	50	39
SEL-3	30.6	126	40	200	75	40
SEL-4	30.5	127	40	360	25	41
SEL-5	30.7	133	40	200	50	43
SEL-6	30.5	136	40	120	75	45
SEL-7	30.5	138	40	200	25	46
SEL-8	30.6	149	40	120	50	49
SEL-9	30.6	157	40	80	75	52
SEL-10	30.5	161	40	120	25	53
SEL-11	30.6	182	40	80	50	59
SEL-12	30.6	207	40	80	25	64

*EVF values are rounded to nearest integer

Table B-VIII. SEL anode parameters and pouch cell stack parameters

Design case	Anode active material loading (mg/cm^2)	Anode thickness (µm)	Anode porosity (%)	Number of cathodes/anodes in cell stack
SEL-1	15.5	131	35.1	34
SEL-2	15.5	131	35.1	34
SEL-3	15.5	131	35.1	33
SEL-4	15.5	131	35.1	33
SEL-5	15.5	131	35.1	33
SEL-6	15.5	131	35.1	32
SEL-7	15.5	131	35.1	32
SEL-8	15.5	131	35.1	31
SEL-9	15.5	131	35.1	30
SEL-10	15.5	131	35.1	30
SEL-11	15.5	131	35.1	28
SEL-12	15.5	131	35.1	26
Design case	**Stack height (cm)**	**Stack weight (kg)**	**Stack volume (L)**	**Stack Capacity (Ah)**
SEL-1	1.00	1.15	0.458	89
SEL-2	1.01	1.15	0.463	89
SEL-3	0.993	1.12	0.454	86
SEL-4	0.990	1.12	0.452	86
SEL-5	1.01	1.14	0.463	87
SEL-6	1.00	1.11	0.456	83
SEL-7	0.992	1.11	0.453	83
SEL-8	1.00	1.09	0.457	81
SEL-9	1.01	1.08	0.459	78
SEL-10	0.993	1.07	0.453	78
SEL-11	1.00	1.04	0.455	73
SEL-12	0.991	1.00	0.452	68

SE+GEs model setup and results

To explore if there are benefits that can be realized by combining SEs and GEs designs, three SE+GE design cases were modeled. As shown in Figure B3, SE+GE designs have a "grid" SE pattern and a bi-layer porosity grading for the "porous cathode + electrolyte" regions labeled in Figure B2. With a total of six design parameters, including t_1, $t_{cathode}$, ε_1, ε_2, w_e, and w_s, SE+GEs have a wider design space than individual SEs and GEs to meet a cathode active material loading target of approximately 31 mg_{active}/cm^2. We conducted a control study where all SE+GE designs had a cathode thickness ($t_{cathode}$) of 133 μm, a first layer thickness (t_1) of 50 μm, a first layer porosity of 35.0%, and an EVF of 43%. Benchmarked against UE-4 which has 35% EVF, all SE+GE models have an additional 8% EVF that was added due to either the SE or GE structures. We then individually quantify the contributions of the SE and GE structures by categorizing the additional 8% EVF based on the locations of the electrolyte. For example, any electrolyte volume in the "all electrolyte region" is attributed to the SE, since these electrolyte volumes were introduced by the SE structure. Any electrolyte volume in the "porous cathode + electrolyte" region in addition to the baseline 35.0% porosity is considered a contribution of the GE. Because we fixed the first layer thickness and porosity in all SE+GE models, any additional electrolyte volume in the "porous cathode + electrolyte" region is indeed a result of porosity grading in the second layer. Based on the aforementioned categorization guidelines, the ratio of the electrolyte volume contributed by SE in the additional 8% EVF is referred to as E_{SE}, and the ratio of the electrolyte volume contributed by GE in the additional 8% EVF is referred to as E_{GE}. Note that E_{SE} and E_{GE} sum up to 1. In this way, we quantified the relative percentage contributions of SE and GE in the SE+GE models (see Table B-X).

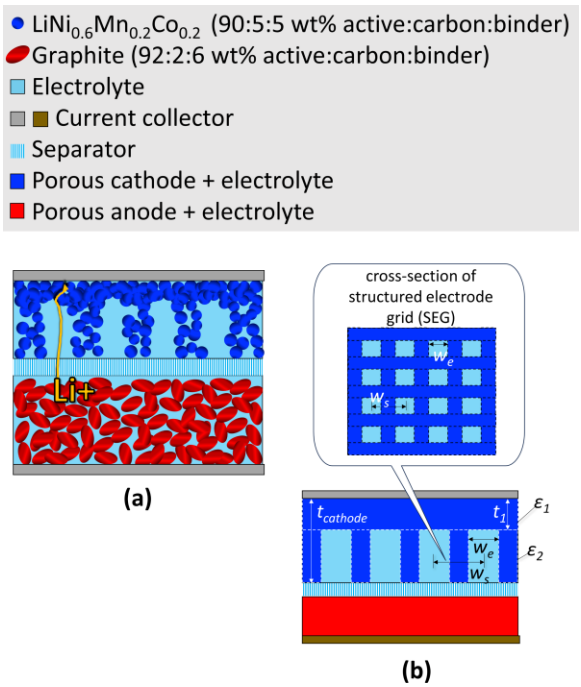

Figure B3. SE+GE design schematic with dimensions labeled.

Table B-IX. Cathode and electrolyte parameters for SE+GEs defined in Figure B3

Design case	Cathode active material loading (mg/cm²)	Cathode thickness (µm)	Electrolyte channel width (µm)	First layer thickness (µm)	First layer porosity (%)	Electrolyte volume fraction* (%)
SE+GE-1	30.7	133	40	50	35	43
SE+GE-2	30.6	133	40	50	35	43
SE+GE-3	30.7	133	40	50	35	43

*EVF values are rounded to nearest integer

Table B-X. Anode and electrolyte parameters for SE+GEs defined in Figure B3

Design case	Anode active material loading (mg/cm²)	Anode thickness (µm)	Anode porosity (%)	Electrolyte channel spacing (µm)	Top layer porosity (%)	E_{SE} (%)	E_{GE} (%)
SE+GE-1	15.5	131	35.1	200	46.0	27	73
SE+GE-2	15.5	131	35.1	145	44.0	48	52
SE+GE-3	15.5	131	35.1	108	40.0	76	24

Table B-XI. SE+GE pouch cell stack parameters

Design case	Number of cathodes/anodes in cell stack	Stack height (cm)	Stack weight (kg)	Stack volume (L)	Stack Capacity (Ah)
SE+GE-1	33	1.01	1.14	0.463	86
SE+GE-2	33	1.01	1.15	0.463	86
SE+GE-3	33	1.01	1.17	0.463	86

In Figure B4, we investigate the potential benefits of concurrently structuring and grading electrodes to understand the degree to which the SE or the GE structure contributes to the overall cell performance based on specific discharge capacity. As summarized in Table B-X, the SE+GE-1 case had a 73% E_{GE} and a 27% E_{SE}. SE+GE-2 had nearly equal contributions from GE and SE in the additional 8% EVF. SE+GE-3 had a 24% E_{GE} and with a higher 76% E_{SE} porosity contribution from the SE structure. SE+GE-1 – SE+GE-3 are plotted as the orange, green, and blue solid lines. Note that all SE+GE models had an EVF value of 43%. SEG-5 (the black dashed line) and GE-5 (the purple dashed line), which also had an EVF value of 43%, are plotted in Figure B4 for comparison purposes.

As seen in Figure B4 (a), SE+GE-3, which had a higher E_{SE} than E_{GE}, demonstrated the best rate capability amongst the SE+GE cases modeled in this study. The SE+GE cases showed modest improved specific discharge capacity values over GE-5, but none of the SE+GEs cases showed improvements over their SEG counterpart that has the same EVF value (SEG-5). In the gravimetric and volumetric Ragone plots in Figure B4 we see that SE+GEs had little to no improvement over GE-5 and SEG-5. These results, while limited in the number of cases examined, indicate that at a fixed EVF, SE+GE designs for their added design complexity yield no significant performance gains over SEs or GEs.

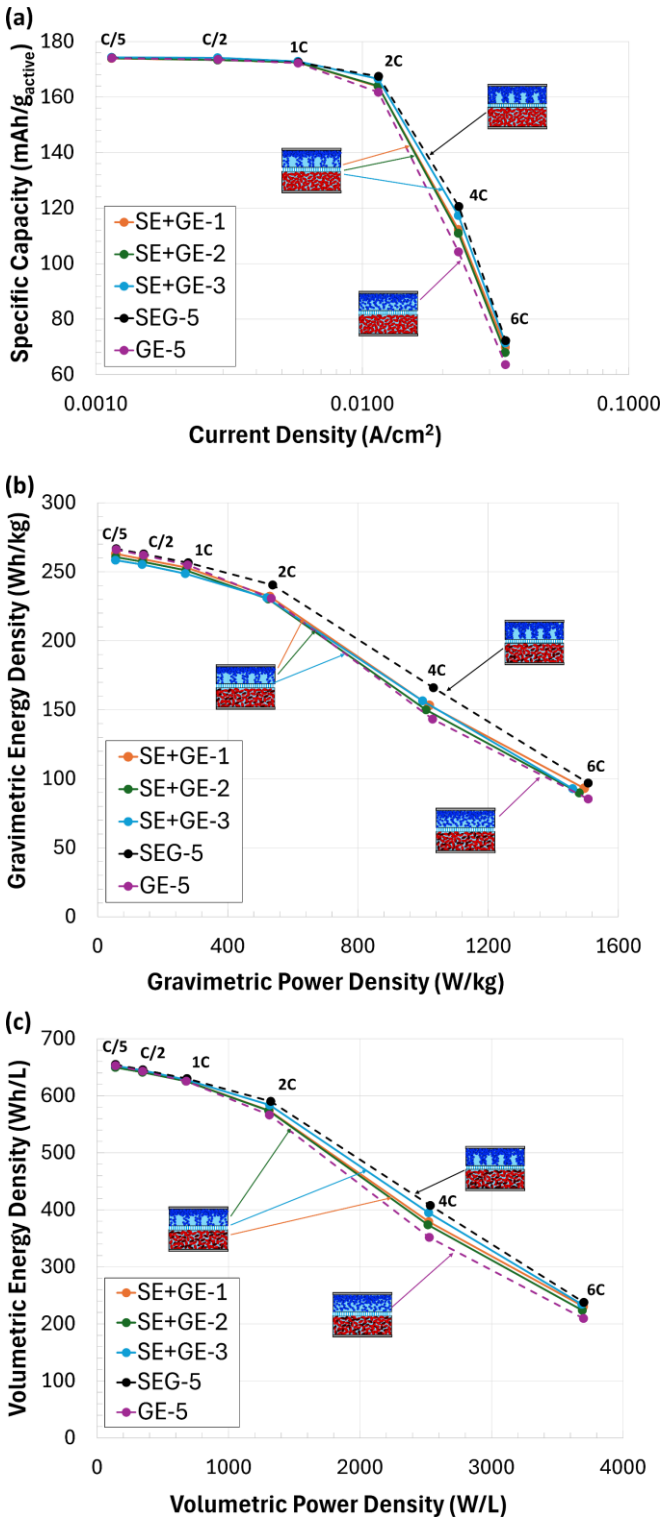

Figure B4. Comparison of SE+GE designs to SE and GE designs with the same electrolyte volume fraction (EVF). Plot (a) shows specific discharge capacity versus current density, plot (b) shows a gravimetric Ragone plot, and plot (c) shows a volumetric Ragone plot. All plots capture data at C/5, C/2, 1C, 2C, 4C, and 6C discharge rates.

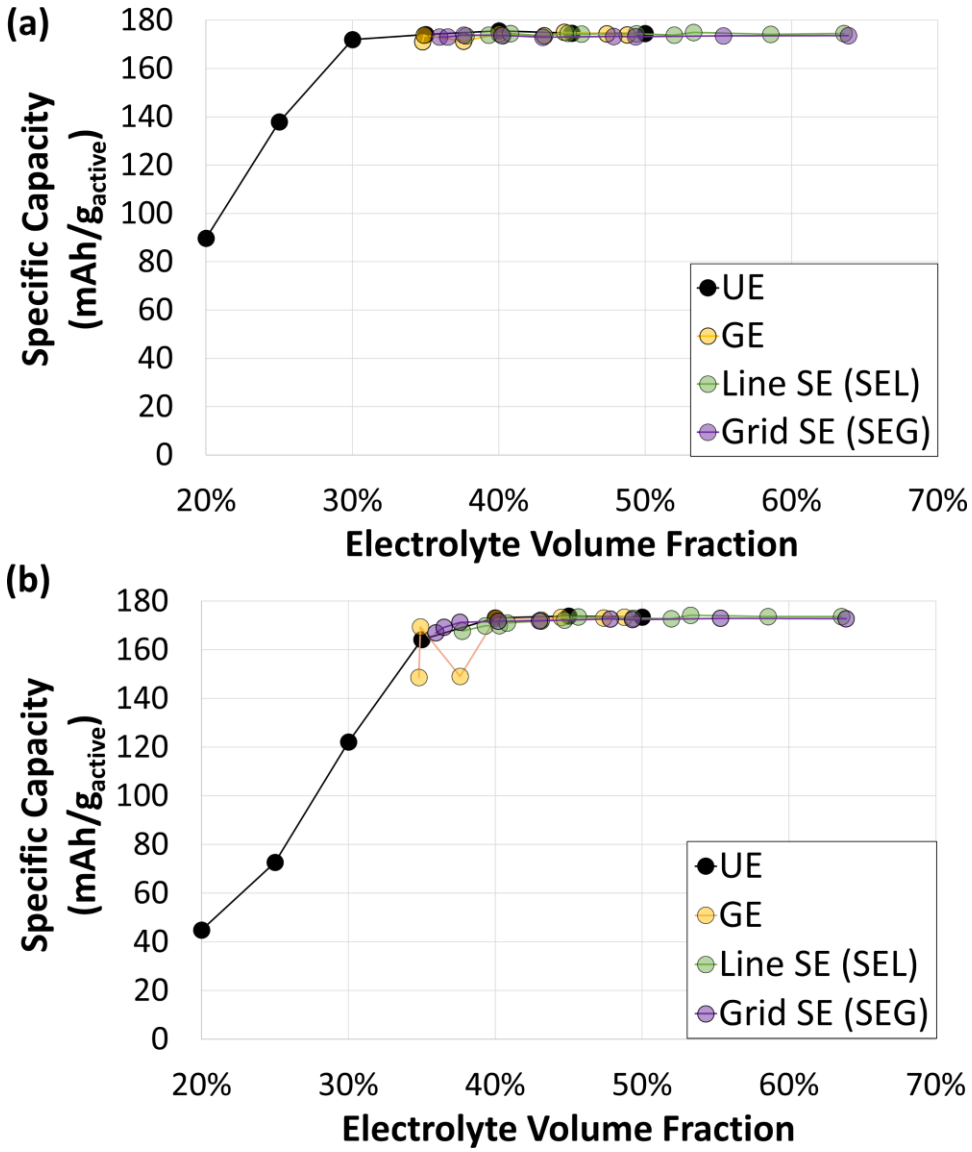

Figure B5. (a) C/2 and (b) 1C specific discharge capacity modeling results for UEs, GE, SELs, and SEGs designed with varying EVFs.

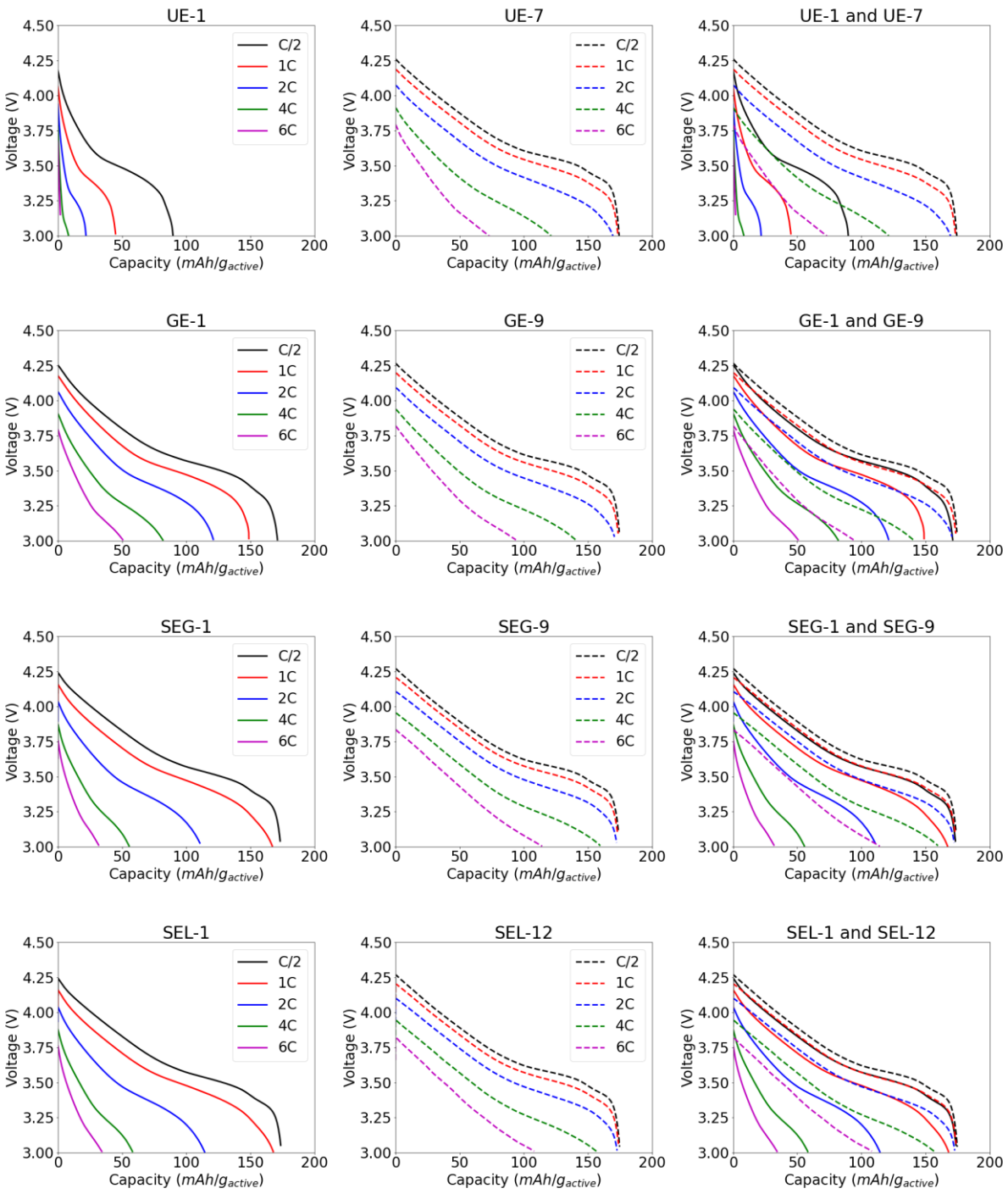

Figure B6. C/2, 1C, 2C, 4C, and 6C discharge curves of representative cases for the UE, GE, SEG, and SEL cases that have a cathode active material loading of approximately 31 mg/cm^2. For comparison purposes, discharge curves in the left and middle columns are overlayed and plotted in the right column.

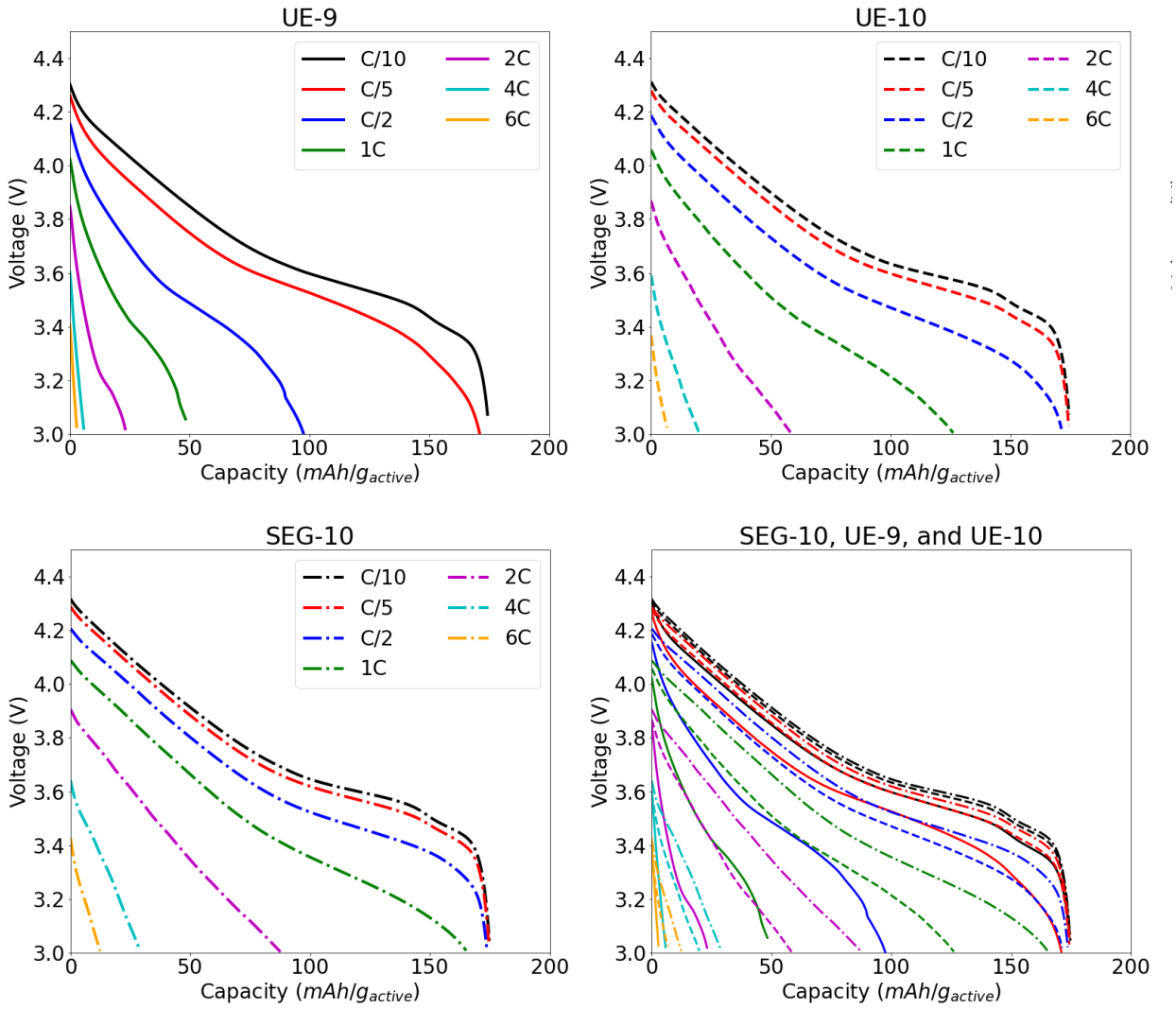

Figure B7. C/10, C/5, C/2, 1C, 2C, 4C, and 6C discharge curves for the UE and SEG cases that have a cathode active material loading of approximately 60 mg/cm^2. For comparison purposes, discharge curves of UE-9, UE-10, and SEG-10 are plotted altogether in the lower-right panel.

Table B-XII. Specific discharge capacity, specific energy, energy density, and power density values for all UE, GE, SE, and SE+GE cases modeled in this study with VIBE-AMPERES. Results include all pouch cell stack volume and weight calculations.

Design case	Discharge C-rate	Specific discharge capacity (mAh/g_{active})	Specific energy (Wh/g_{active})	Volumetric energy density (Wh/L)	Volumetric power density (W/L)	Gravimetric energy density (Wh/kg)	Gravimetric power density (W/kg)
UE-1	C/2	89.7	0.318	362	378	138	144
UE-1	1C	44.9	0.156	177	739	68	281
UE-1	2C	21.9	0.073	83	1424	32	542
UE-1	4C	8.6	0.027	31	2665	12	1015
UE-1	6C	1.9	0.006	7	4024	3	1532
UE-2	C/2	137.9	0.492	549	372	211	143
UE-2	1C	72.7	0.255	284	730	109	281
UE-2	2C	36.5	0.125	139	1426	54	549
UE-2	4C	15.4	0.049	55	2668	21	1026
UE-2	6C	5.9	0.018	21	3903	8	1501
UE-3	C/2	171.9	0.619	671	365	262	143
UE-3	1C	122.2	0.431	468	716	183	280
UE-3	2C	61.9	0.213	231	1399	90	546
UE-3	4C	28.8	0.095	103	2681	40	1047
UE-3	6C	14.3	0.045	49	3843	19	1502
UE-4	C/2	174.1	0.636	672	361	266	143
UE-4	1C	164.2	0.582	615	701	243	277
UE-4	2C	101.1	0.349	369	1366	146	540
UE-4	4C	47.7	0.160	169	2643	67	1045
UE-4	6C	27.9	0.090	95	3833	38	1516
UE-5	C/2	175.6	0.646	659	351	266	141
UE-5	1C	173.1	0.621	633	684	255	276
UE-5	2C	140.9	0.488	497	1321	201	533
UE-5	4C	71.2	0.239	244	2559	98	1032
UE-5	6C	42.0	0.137	140	3736	56	1506
UE-6	C/2	174.7	0.646	635	340	260	139
UE-6	1C	173.9	0.629	619	666	254	273
UE-6	2C	162.3	0.566	557	1283	228	526
UE-6	4C	99.0	0.333	327	2473	134	1013
UE-6	6C	57.7	0.190	187	3635	77	1489
UE-7	C/10	175.1	0.658	621	66	260	28
UE-7	C/5	175.0	0.656	619	132	259	55
UE-7	C/2	174.5	0.647	610	326	256	137
UE-7	1C	173.5	0.631	596	641	250	269
UE-7	2C	169.5	0.595	561	1237	235	518
UE-7	4C	121.2	0.408	385	2373	161	995
UE-7	6C	73.1	0.240	227	3479	95	1458

Table B-XII. Continued (1/5)

Design case	Discharge C-rate	Specific discharge capacity (mAh/g_{active})	Specific energy (Wh/g_{active})	Volumetric energy density (Wh/L)	Volumetric power density (W/L)	Gravimetric energy density (Wh/kg)	Gravimetric power density (W/kg)
UE-8	C/10	174.3	0.643	736	79	294	32
UE-8	C/5	170.9	0.616	705	154	282	62
UE-8	C/2	97.5	0.344	393	377	157	151
UE-8	1C	48.3	0.167	191	740	76	296
UE-8	2C	23.1	0.076	87	1402	35	560
UE-8	4C	5.8	0.018	20	2643	8	1057
UE-8	6C	2.8	0.008	10	3829	4	1531
UE-9	C/10	174.4	0.652	661	71	280	30
UE-9	C/5	174.3	0.644	653	140	277	59
UE-9	C/2	171.3	0.611	620	338	263	143
UE-9	1C	126.1	0.436	441	654	187	278
UE-9	2C	58.4	0.196	199	1272	84	540
UE-9	4C	19.9	0.064	65	2426	27	1029
UE-9	6C	6.6	0.020	20	3385	9	1437
GE-1	C/2	171.0	0.627	664	363	263	144
GE-1	1C	148.7	0.536	568	715	225	283
GE-1	2C	121.0	0.423	448	1386	177	549
GE-1	4C	81.7	0.275	292	2670	115	1057
GE-1	6C	50.5	0.166	176	3905	69	1545
GE-2	C/2	173.8	0.638	675	364	267	144
GE-2	1C	169.5	0.605	640	708	253	280
GE-2	2C	124.7	0.433	458	1376	181	545
GE-2	4C	61.6	0.207	219	2664	87	1054
GE-2	6C	35.7	0.116	123	3880	49	1535
GE-3	C/2	171.3	0.628	651	355	260	142
GE-3	1C	149.1	0.539	558	700	223	279
GE-3	2C	123.8	0.435	451	1360	180	543
GE-3	4C	91.6	0.309	320	2611	128	1042
GE-3	6C	61.2	0.202	209	3824	83	1527
GE-4	C/2	174.4	0.644	656	352	264	142
GE-4	1C	173.1	0.624	636	687	256	277
GE-4	2C	153.2	0.534	544	1327	219	534
GE-4	4C	91.1	0.307	313	2566	126	1033
GE-4	6C	52.8	0.173	176	3735	71	1503
GE-5	C/5	174.1	0.652	653	140	266	57
GE-5	C/2	173.5	0.642	643	347	262	141
GE-5	1C	172.3	0.625	626	680	255	277
GE-5	2C	161.8	0.566	566	1311	231	534
GE-5	4C	104.2	0.351	352	2527	143	1029
GE-5	6C	63.6	0.209	210	3700	85	1508

Table B-XII. Continued (2/5)

Design case	Discharge C-rate	Specific discharge capacity (mAh/g_{active})	Specific energy (Wh/g_{active})	Volumetric energy density (Wh/L)	Volumetric power density (W/L)	Gravimetric energy density (Wh/kg)	Gravimetric power density (W/kg)
GE-6	C/2	175.0	0.647	638	341	261	139
GE-6	1C	173.4	0.628	620	668	254	273
GE-6	2C	163.4	0.572	564	1289	231	527
GE-6	4C	112.3	0.379	373	2485	153	1017
GE-6	6C	69.4	0.229	226	3648	92	1492
GE-7	C/2	174.4	0.646	623	334	258	138
GE-7	1C	173.2	0.630	608	656	252	271
GE-7	2C	168.8	0.592	571	1264	236	523
GE-7	4C	119.0	0.401	387	2431	160	1006
GE-7	6C	71.7	0.237	229	3573	95	1479
GE-8	C/2	173.9	0.645	615	330	256	138
GE-8	1C	173.5	0.632	602	648	251	270
GE-8	2C	169.2	0.594	566	1250	236	521
GE-8	4C	120.6	0.407	388	2403	162	1002
GE-8	6C	72.2	0.239	228	3535	95	1474
GE-9	C/2	174.3	0.648	577	310	249	133
GE-9	1C	173.4	0.634	565	610	243	262
GE-9	2C	170.5	0.604	539	1182	232	509
GE-9	4C	140.4	0.476	425	2263	183	974
GE-9	6C	93.8	0.313	279	3335	120	1435
SEG-1	C/2	173.1	0.635	667	360	265	143
SEG-1	1C	167.0	0.594	625	700	248	278
SEG-1	2C	110.6	0.384	404	1366	160	542
SEG-1	4C	55.5	0.185	195	2629	77	1043
SEG-1	6C	31.7	0.104	109	3851	43	1528
SEG-2	C/2	173.0	0.636	666	360	265	143
SEG-2	1C	169.3	0.604	633	699	252	278
SEG-2	2C	123.2	0.427	447	1357	178	539
SEG-2	4C	59.5	0.200	209	2628	83	1044
SEG-2	6C	33.8	0.110	115	3823	46	1519
SEG-3	C/2	173.8	0.640	665	358	265	143
SEG-3	1C	171.3	0.614	638	697	255	278
SEG-3	2C	135.4	0.469	487	1348	194	538
SEG-3	4C	63.0	0.211	220	2613	88	1042
SEG-3	6C	35.8	0.117	122	3833	49	1529
SEG-4	C/2	173.7	0.642	655	352	263	142
SEG-4	1C	171.8	0.620	633	689	255	277
SEG-4	2C	146.3	0.513	524	1339	211	539
SEG-4	4C	91.7	0.309	315	2570	127	1035
SEG-4	6C	56.1	0.184	188	3766	76	1516

Table B-XII. Continued (3/5)

Design case	Discharge C-rate	Specific discharge capacity (mAh/g_{active})	Specific energy (Wh/g_{active})	Volumetric energy density (Wh/L)	Volumetric power density (W/L)	Gravimetric energy density (Wh/kg)	Gravimetric power density (W/kg)
SEG-5	C/5	174.1	0.653	655	141	267	57
SEG-5	C/2	173.0	0.642	643	348	262	142
SEG-5	1C	171.9	0.626	628	683	256	278
SEG-5	2C	166.9	0.587	588	1318	240	537
SEG-5	4C	120.2	0.405	406	2527	165	1029
SEG-5	6C	72.0	0.236	237	3690	96	1503
SEG-6	C/10	174.1	0.656	631	68	262	28
SEG-6	C/5	174.0	0.653	629	135	261	56
SEG-6	C/2	173.3	0.644	620	334	258	139
SEG-6	1C	172.7	0.632	608	658	253	273
SEG-6	2C	171.0	0.606	584	1276	242	530
SEG-6	4C	140.3	0.475	457	2437	190	1012
SEG-6	6C	88.2	0.293	282	3587	117	1489
SEG-7	C/2	173.2	0.642	609	328	255	137
SEG-7	1C	172.4	0.627	595	644	249	269
SEG-7	2C	157.2	0.558	529	1257	221	525
SEG-7	4C	119.8	0.408	387	2412	162	1008
SEG-7	6C	87.4	0.289	274	3509	114	1467
SEG-8	C/2	173.6	0.646	577	310	248	134
SEG-8	1C	172.9	0.634	567	612	244	263
SEG-8	2C	171.3	0.610	545	1189	235	511
SEG-8	4C	150.8	0.514	459	2275	198	978
SEG-8	6C	107.6	0.358	320	3332	138	1433
SEG-9	C/2	173.6	0.647	518	279	234	126
SEG-9	1C	172.8	0.636	509	550	230	248
SEG-9	2C	172.2	0.617	494	1072	223	484
SEG-9	4C	159.5	0.546	437	2048	197	924
SEG-9	6C	114.2	0.385	308	3026	139	1365
SEG-10	C/10	174.8	0.656	678	73	285	31
SEG-10	C/5	174.5	0.650	672	144	282	61
SEG-10	C/2	173.6	0.631	653	352	274	148
SEG-10	1C	165.1	0.576	596	675	250	284
SEG-10	2C	87.6	0.299	309	1321	130	555
SEG-10	4C	29.1	0.096	99	2550	42	1071
SEG-10	6C	12.4	0.039	40	3667	17	1540
SEL-1	C/2	173.6	0.637	660	356	264	142
SEL-1	1C	167.7	0.598	620	692	248	276
SEL-1	2C	114.3	0.396	411	1345	164	537
SEL-1	4C	58.1	0.195	202	2600	81	1038
SEL-1	6C	34.2	0.111	115	3791	46	1513

Table B-XII. Continued (4/5)

Design case	Discharge C-rate	Specific discharge capacity (mAh/g_{active})	Specific energy (Wh/g_{active})	Volumetric energy density (Wh/L)	Volumetric power density (W/L)	Gravimetric energy density (Wh/kg)	Gravimetric power density (W/kg)
SEL-2	C/2	173.9	0.639	655	352	263	141
SEL-2	1C	169.8	0.607	623	685	250	275
SEL-2	2C	126.8	0.441	452	1332	181	535
SEL-2	4C	65.7	0.220	226	2569	91	1031
SEL-2	6C	37.6	0.123	126	3760	51	1509
SEL-3	C/2	173.6	0.639	651	350	262	141
SEL-3	1C	170.0	0.609	620	682	250	275
SEL-3	2C	128.7	0.447	456	1324	184	534
SEL-3	4C	69.2	0.232	237	2556	95	1031
SEL-3	6C	41.3	0.135	138	3736	56	1507
SEL-4	C/2	174.5	0.642	651	349	263	141
SEL-4	1C	171.1	0.614	623	681	252	275
SEL-4	2C	134.6	0.468	474	1320	192	534
SEL-4	4C	71.9	0.241	244	2547	99	1029
SEL-4	6C	40.2	0.131	133	3723	54	1505
SEL-5	C/2	173.6	0.641	642	346	261	141
SEL-5	1C	171.8	0.620	621	676	253	275
SEL-5	2C	151.5	0.529	529	1308	216	533
SEL-5	4C	86.5	0.290	291	2515	118	1025
SEL-5	6C	48.3	0.159	159	3706	65	1510
SEL-6	C/2	174.6	0.645	635	341	260	139
SEL-6	1C	172.3	0.622	613	666	251	273
SEL-6	2C	148.2	0.519	511	1292	209	529
SEL-6	4C	93.0	0.313	308	2484	126	1017
SEL-6	6C	57.5	0.189	186	3637	76	1489
SEL-7	C/2	174.3	0.645	630	337	259	139
SEL-7	1C	173.6	0.629	614	661	252	271
SEL-7	2C	161.5	0.564	550	1273	226	523
SEL-7	4C	99.9	0.335	327	2449	135	1007
SEL-7	6C	55.9	0.184	180	3604	74	1481
SEL-8	C/2	174.3	0.647	613	329	256	138
SEL-8	1C	173.0	0.631	598	647	250	270
SEL-8	2C	168.5	0.593	562	1248	235	522
SEL-8	4C	124.2	0.419	397	2392	166	1000
SEL-8	6C	75.1	0.247	234	3499	98	1463
SEL-9	C/2	173.8	0.644	596	321	252	135
SEL-9	1C	172.8	0.628	581	629	245	266
SEL-9	2C	157.3	0.556	514	1224	217	517
SEL-9	4C	116.5	0.395	365	2347	154	991
SEL-9	6C	80.2	0.266	246	3441	104	1453

Table B-XII. Continued (5/5)

Design case	Discharge C-rate	Specific discharge capacity (mAh/g_{active})	Specific energy (Wh/g_{active})	Volumetric energy density (Wh/L)	Volumetric power density (W/L)	Gravimetric energy density (Wh/kg)	Gravimetric power density (W/kg)
SEL-10	C/2	175.0	0.650	592	317	252	135
SEL-10	1C	174.2	0.637	581	624	247	265
SEL-10	2C	172.1	0.610	556	1209	236	514
SEL-10	4C	140.7	0.476	434	2309	184	981
SEL-10	6C	88.4	0.294	268	3399	114	1445
SEL-11	C/2	174.1	0.648	557	299	243	131
SEL-11	1C	173.7	0.636	547	589	239	257
SEL-11	2C	171.4	0.610	524	1145	229	500
SEL-11	4C	147.8	0.502	432	2188	189	956
SEL-11	6C	99.7	0.331	285	3208	124	1401
SEL-12	C/2	174.5	0.650	522	280	235	126
SEL-12	1C	173.6	0.638	512	552	231	249
SEL-12	2C	172.6	0.617	496	1075	223	484
SEL-12	4C	156.9	0.535	430	2052	194	924
SEL-12	6C	108.0	0.361	290	3018	131	1359
SE+GE-1	C/5	174.0	0.652	651	140	263	57
SE+GE-1	C/2	173.4	0.642	641	346	259	140
SE+GE-1	1C	172.5	0.627	626	678	253	274
SE+GE-1	2C	163.8	0.575	574	1310	232	529
SE+GE-1	4C	112.3	0.379	379	2523	153	1020
SE+GE-1	6C	69.8	0.231	230	3700	93	1495
SE+GE-2	C/5	174.1	0.651	650	139	261	56
SE+GE-2	C/2	173.4	0.643	641	345	257	139
SE+GE-2	1C	172.6	0.627	626	677	251	272
SE+GE-2	2C	164.0	0.575	574	1307	230	524
SE+GE-2	4C	110.9	0.374	374	2517	150	1010
SE+GE-2	6C	67.9	0.224	224	3690	90	1480
SE+GE-3	C/5	174.3	0.654	653	140	258	56
SE+GE-3	C/2	174.1	0.646	645	347	255	137
SE+GE-3	1C	172.9	0.629	628	680	249	269
SE+GE-3	2C	166.6	0.585	584	1313	231	520
SE+GE-3	4C	117.3	0.396	395	2523	156	999
SE+GE-3	6C	71.4	0.235	234	3687	93	1460

Table B-XIII. Summary of how previous publications have approached modeling graded electrodes (GEs) and structured electrode (SEs).

Studies	**Model dimension**	**Cathode**	**Anode**	**SE geometry**	**Battery Scale for Analysis**	**C-rate**	**Electrolyte volume fraction (EVF)**
Chapter 4	3D	SE, GE, and UE NMC622	UE graphite	Grid and Line	Multi-layer cell stack	C/10 – 6C	Systematically varied to compare to UE and GE
Cobb and Blanco [69]	P2D	SE $LiCoO_2$	Lithium Metal (Half cell)	Line	Single-layer cell sandwich	1C	Unconstrained
Dai and Srinivasan [19]	1D	GE $LiMn_2O_4$	GE graphite	N/A	Single-layer cell sandwich	C/10 – 3C	N/A
Qi et al. [63]	1D	GE $LiCoO_2$	Lithium Metal (Half cell)	N/A	Single-layer cell sandwich	1C	N/A
Cobb and Solberg [10]	P2D	SE NMC111	Lithium Matel (Half Cell)	Line	Multi-layer cell stack (estimated based on half-cell results)	C/2 – 2C	Constrained to 2.2 g/cc and 2.4 g/cc active solid electrode fraction
Habedank et al. [67]	3D	UE NMC111	SE graphite	Grid	Single-layer cell sandwich	C/5 – 10C	N/A
Kraft et al. [65]	1D	UE NMC111	SE graphite	Grid	Single-layer cell sandwich	C/5 – 10C	Constrained to a range of 5% – 10% more electrolyte volume than UE
Chen et al. [21]	3D	UE NMC532	SE graphite	Grid	Single-layer cell sandwich	4C	N/A
Goel et al. [145]	3D	UE NMC532	SE graphite	Grid	Single-layer cell sandwich	4C	Constrained to an electrode volume fraction of 0.895, electrode porosity included
	1D	Lithium Metal (Half Cell)	SE graphite	Grid	Single-layer cell sandwich	6C	

APPENDIX C.

*The content in Appendix C is submitted as the supplemental material to a journal.

Model parameterization

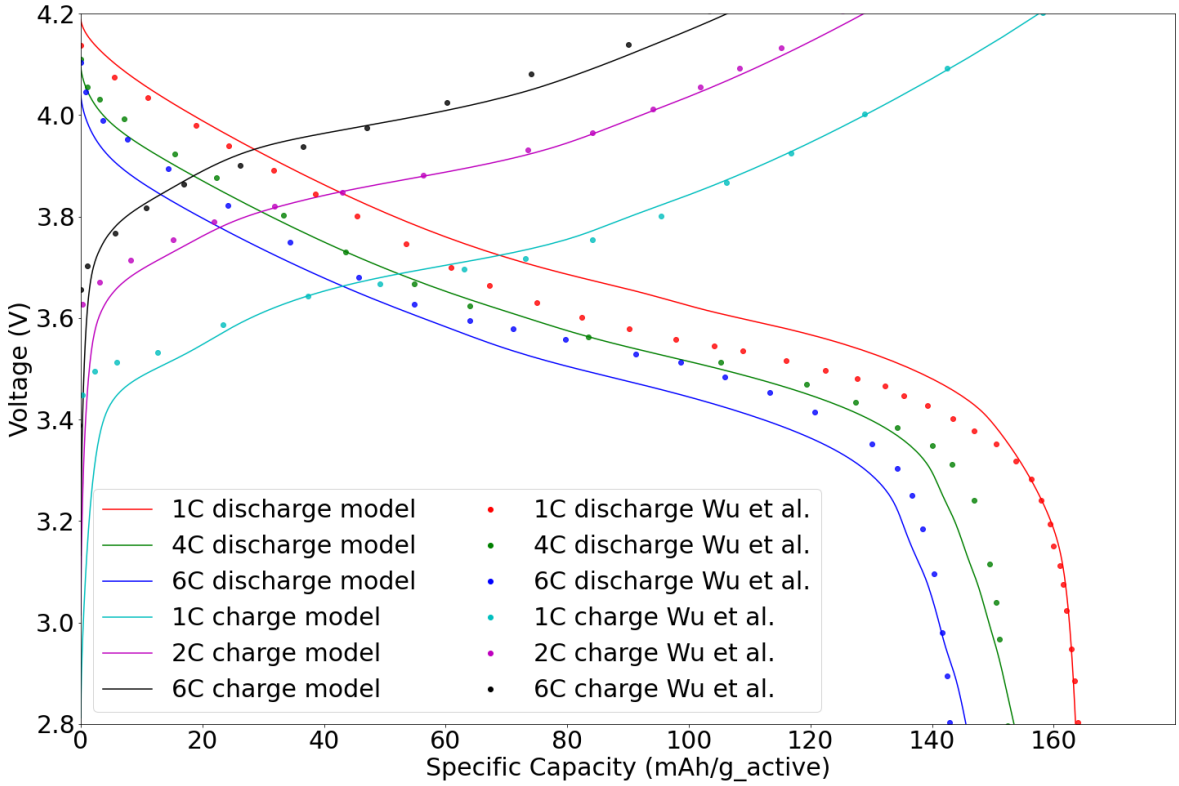

Figure C1. Charge and discharge voltage profiles at 1C, 4C, and 6C for the UE models with a cathode active material loading of 13.1 mg_{active}/cm^2 (UE-13) compared to experimental data from Wu et al.[150] The model data is represented by the solid lines. Experimental data extracted from Wu et al. are plotted in round markers.

Figure C1 compares our UE model (UE-13) to the experimental data reported in Wu et al. [150] The parameters for electrode porosity, thickness, and loading in our models are based on the information and data provided by Wu et al. The experimental data from Wu et al. indicated that the graphite|NMC-622 cell exhibited a relatively stable discharge plateau voltage at 1C, 4C, and 6C rates. With a N/P ratio of approximately 1.14, the voltage of the graphite anode remained

around 0.1V until the end of discharge. This stable plateau voltage suggests that the overpotential resulting from transport limitations did not significantly increase toward the end of the discharge. Instead, the rapid drop in the full-cell voltage likely occurred because the NMC-622 cathode approached full capacity (SOC of 1). The solid-phase diffusivity in our models was found to be several orders of magnitude higher, as detailed in Table 5.1.

The open-circuit potential (OCP) equation for the graphite anode was referenced from a study conducted by Srinivasan and Newman.[4] Our models were unable to achieve an exact fit to the cell capacity and voltage from Wu et al using existing NMC-622 OCP equations from literature shown in Figure C2. To resolve this, we conducted a parameter estimation to define an OCP equation for NMC-622 that aligned better with the 1C charge and discharge results provided by Wu et al. Figure C2 plots our NMC-622 OCP alongside other reported OCP equations from literature. It is assumed that the voltage hysteresis between charge and discharge is negligible; therefore, the same OCP equation was used for both charge and discharge modeling in this work.

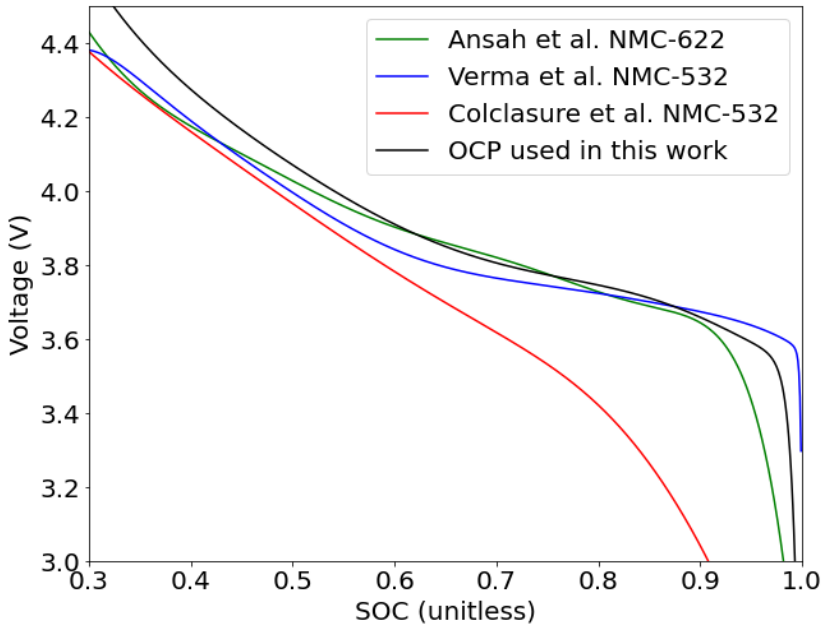

Figure C2. OCP used for the NMC-622 cathode in our models compared OCP equations reported by Ansah et al., Verma et al., and Colclasure et al.[113,127,138]

The reaction rate constants presented in Table 5.1 were adjusted within ranges reported in literature to fit the initial voltage drop observed in the charge and discharge data from Wu et al.[150] Reaction rate values are different for intercalation and de-intercalation reactions corresponding to charge and discharge. Prior modeling work by Doyle et al. observed a larger film resistance in the anode than the cathode.[11] To improve the model fit to experimental data, a film resistance was incorporated in our model for the charge models to account for the potential effects of the solid electrolyte interphase (SEI). In contrast, no film resistance was applied on the cathode side or in the discharge models, operating under the assumption of perfect contact between the electrodes and current collectors.

Finite element meshes consisting of hexahedral elements were generated using the commercial software, *Coreform Cubit* version 17.1.0.[178] This software enables the definition of geometry and meshes to model electrode cells composed of a cathode, an anode, and a separator. The meshes were exported to the Exodus file format and subsequently imported into VIBE-AMPERES. Symmetry boundary conditions were imposed on repeating patterns SE patterns; Implementing symmetry conditions helps to reduce computational run time while enabling effective 3D modeling of the minimum unit cell necessary to accurately capture the discharge behavior of SEAs, SECs, and SEA-SECs. In addition, the lithium-ion flux was assumed to be zero across the symmetry boundaries. The meshes varied in size from 400 to 1292 hexahedral elements. The models took 0.5 to 8 hours to run, utilizing 1 to 4 parallel processes on an Intel® Core™ i5-1135G7 4-core processor with up to 16GB RAM, or on an Intel® Xeon® Silver 4215 8-core processor with up to 64GB RAM.

Summary of UE, SEA, SEC, and SEA-SEC design parameters and modeling results

Table C-I. Design parameters for the UE cells. The 1C applied current density for UE-13 is 2.30 mA/cm^2, and the 1C applied current density for UE-18 is 3.22 mA/cm^2.

Design	Cathode Thickness (μm)	Anode Thickness (μm)	Cathode Active Material Loading (mg_{NMC}/cm^2)	Anode Active Material Loading ($mg_{graphite}/cm^2$)
UE-13	50	52	13.1	7.5
UE-18	70	73	18.4	10.5

Table C-II. Design parameters used for the SEC and SEA models

Design	Cathode Thickness (μm)	Anode Thickness (μm)	Cathode Active Material Loading (mg_{NMC}/cm^2)	Anode Active Material Loading ($mg_{graphite}/cm^2$)	"All-electrolyte" region Line Width	"All-electrolyte" region Line Spacing	EVF
SEC-13-40%	58	52	7.5	13.1	40	159	40%
SEC-13-45%	63	52	7.5	13.1	40	114	45%
SEC-13-50%	70	52	7.5	13.1	40	90	50%
SEC-13-55%	77	52	7.5	13.1	40	77	55%
SEC-13-60%	87	52	7.5	13.1	40	67	60%
SEA-13-35%	56	50	7.5	13.1	40	310	35%
SEA-13-40%	61	50	7.5	13.1	40	165	40%
SEA-13-50%	73	50	7.5	13.1	40	92	50%
SEA-13-60%	91	50	7.5	13.1	40	68	60%
SEC-18-40%	82	73	10.5	18.5	40	194	40%
SEC-18-45%	89	73	10.5	18.4	40	134	45%
SEC-18-50%	99	73	10.5	18.5	40	104	50%
SEC-18-51%	100	73	10.5	18.4	40	100	51%
SEC-18-55%	109	73	10.5	18.4	40	86	55%
SEC-18-60%	123	73	10.5	18.4	40	74	60%
SEA-18-35%	79	70	10.5	18.4	40	380	35%
SEA-18-40%	86	70	10.6	18.4	40	198	40%
SEA-18-50%	103	70	10.5	18.4	40	106	50%
SEA-18-51%	105	70	10.5	18.4	40	100	51%
SEA-18-60%	128	70	10.5	18.4	40	75	60%

Table C-III. Stack properties, specific capacity, and the resulting stack volumetric and gravimetric discharge energy density and charge capacity for all models that have a 13.1 mg_{active}/cm^2 cathode active material loading. "Number of SLCs" represents the number of single-layer cells (SLCs) within the stack.

	Stack Properties			**6C Discharge Model Results**			**6C Charge Model Results**		
Design	Number of SLCs	g_{active}/kg	g_{active}/L	mAh/g_{active}	Wh/kg	Wh/L	mAh/g_{active}	Ah/kg	Ah/L
UE-13	69	377	1005	146	175	467	107	36	97
SEC-13-40%	65	366	946	151	178	461	120	40	102
SEC-13-45%	63	360	916	155	180	458	121	39	100
SEC-13-50%	60	354	883	159	182	454	124	40	99
SEC-13-55%	58	346	847	160	180	440	126	39	96
SEC-13-60%	55	337	800	161	176	418	127	39	92
SEA-13-35%	67	372	978	146	175	458	113	38	100
SEA-13-40%	65	366	946	146	172	444	115	38	98
SEA-13-50%	60	353	878	146	166	414	119	38	94
SEA-13-60%	54	335	791	147	158	374	124	37	88
	Stack Properties			**4C Discharge Model Results**			**4C Charge Model Results**		
Design	Number of SLCs	g_{active}/kg	g_{active}/L	mAh/g_{active}	Wh/kg	Wh/L	mAh/g_{active}	Ah/kg	Ah/L
UE-13	69	377	1005	154	188	500	130	44	118
SEC-13-40%	65	366	946	157	188	485	136	45	116
SEC-13-45%	63	360	916	160	188	478	139	45	115
SEC-13-50%	60	354	883	162	188	470	140	45	112
SEC-13-55%	58	346	847	163	185	453	141	44	108
SEC-13-60%	55	337	800	163	134	317	142	43	103
SEA-13-35%	67	372	978	154	186	489	136	46	120
SEA-13-40%	65	366	946	154	184	474	135	45	115
SEA-13-50%	60	353	878	154	177	441	140	45	111
SEA-13-60%	54	335	791	154	168	398	139	42	99

Table C-IV. Stack properties, specific capacity, and the resulting stack volumetric and gravimetric discharge energy density and charge capacity for all models that have an 18.4 – 18.5 mg_{active}/cm^2 cathode active material loading. "Number of SLCs" represents the number of single-layer cells (SLCs) within the stack.

	Stack Properties			**6C Discharge Model Results**			**6C Charge Model Results**		
Design	Number of SLCs	g_{active}/kg	g_{active}/L	mAh/g_{active}	Wh/kg	Wh/L	mAh/g_{active}	Ah/kg	Ah/L
UE-18	53	414	1096	126	162	430	78	29	77
SEC-18-40%	50	402	1033	138	174	448	85	31	79
SEC-18-45%	48	394	993	146	182	458	92	33	83
SEC-18-50%	46	387	955	152	186	459	98	34	84
SEC-18-51%	46	384	943	153	186	457	100	35	85
SEC-18-55%	44	376	905	156	186	447	103	35	84
SEC-18-60%	41	365	853	158	183	427	105	35	81
SEA-18-35%	52	407	1062	123	157	411	80	29	77
SEA-18-40%	50	400	1024	123	156	399	86	31	79
SEA-18-50%	46	384	943	124	150	369	95	33	81
SEA-18-51%	45	383	935	124	150	366	95	33	80
SEA-18-60%	41	363	845	124	143	332	99	33	76
SEA-SEC-18-51%-parallel-aligned	40	357	822	156	178	409	120	38	88
SEA-SEC-18-51%-parallel-misaligned	40	357	822	156	178	409	118	38	88
SEA-SEC-18-51%-perpendicular	40	357	822	156	179	411	119	39	89
	Stack Properties			**4C Discharge Model Results**			**4C Charge Model Results**		
Design	Number of SLCs	g_{active}/kg	g_{active}/L	mAh/g_{active}	Wh/kg	Wh/L	mAh/g_{active}	Ah/kg	Ah/L
UE-18	53	414	1096	138	183	484	110	41	109
SEC-18-40%	50	402	1033	149	192	493	117	43	109
SEC-18-45%	48	394	993	155	196	494	124	44	111
SEC-18-50%	46	387	955	159	199	490	127	44	109
SEC-18-51%	46	384	943	160	198	486	126	44	108
SEC-18-55%	44	376	905	161	195	470	128	43	104
SEC-18-60%	41	365	853	161	191	446	130	43	100
SEA-18-35%	52	407	1062	140	183	476	114	42	110
SEA-18-40%	50	400	1024	141	180	461	118	43	109
SEA-18-50%	46	384	943	141	174	427	122	42	104
SEA-18-51%	45	383	935	141	173	423	122	42	103
SEA-18-60%	41	363	845	141	165	383	126	42	97
SEA-SEC-18-51%-parallel-aligned	40	357	822	160	187	429	137	44	102
SEA-SEC-18-51%-parallel-misaligned	40	357	822	160	186	428	136	44	101
SEA-SEC-18-51%-perpendicular	40	357	822	160	186	429	137	44	101

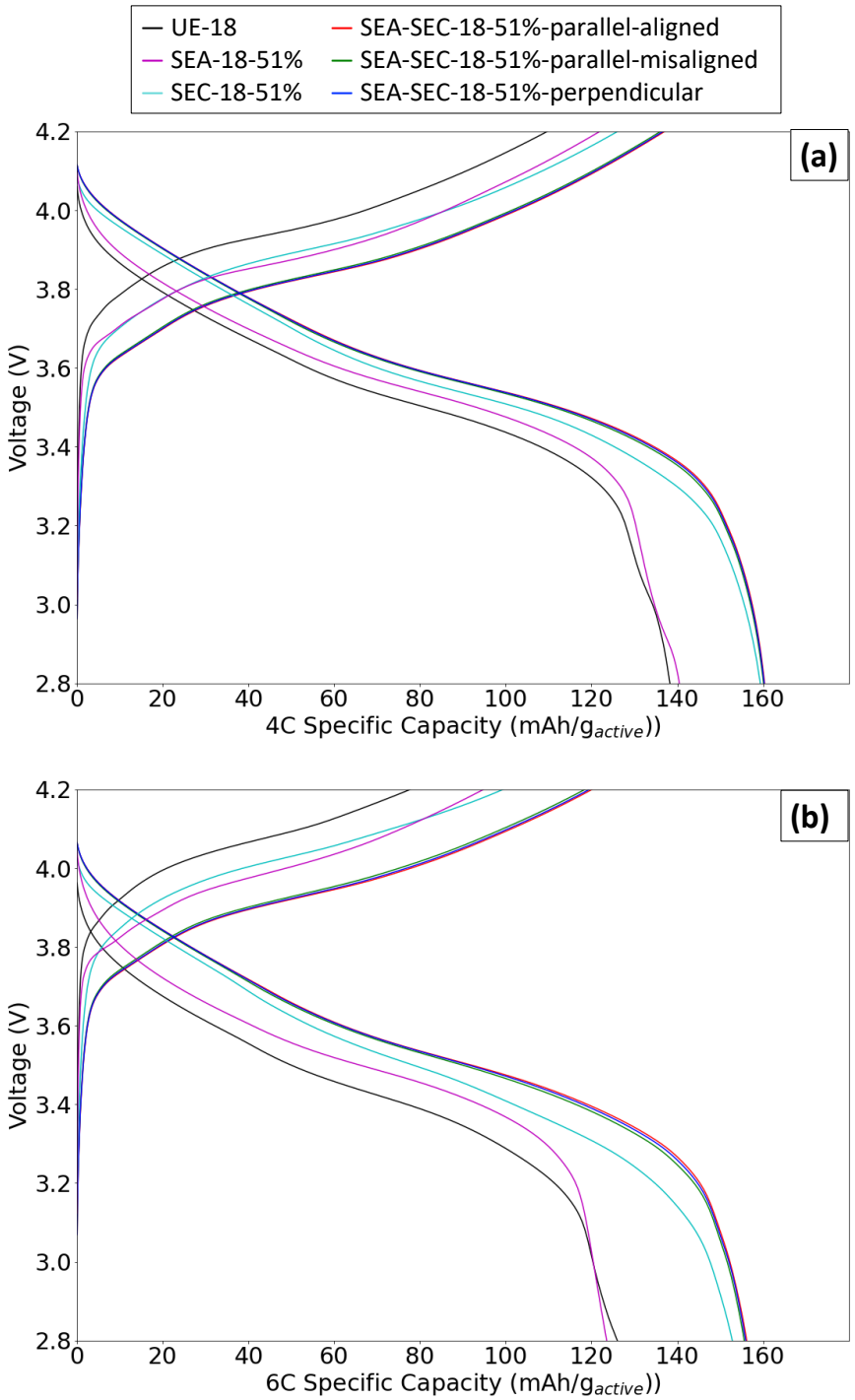

Figure C3. Charge and discharge voltage profiles at (a) 4C and (b) 6C for UE-18, SEA-18-51%, SEC-18-51% are shown. In addition, modeling results for the three SEA-SEC configurations are shown: SEA-SEC-18-51%-parallel-aligned, SEA-SEC-18-51%-parallel-misaligned, and SEA-SEC-18-51%-perpendicular. All cases have a cathode active material loading of 18.4 mg_{active}/cm^2.

Data interpolation for SEA-SEC cases

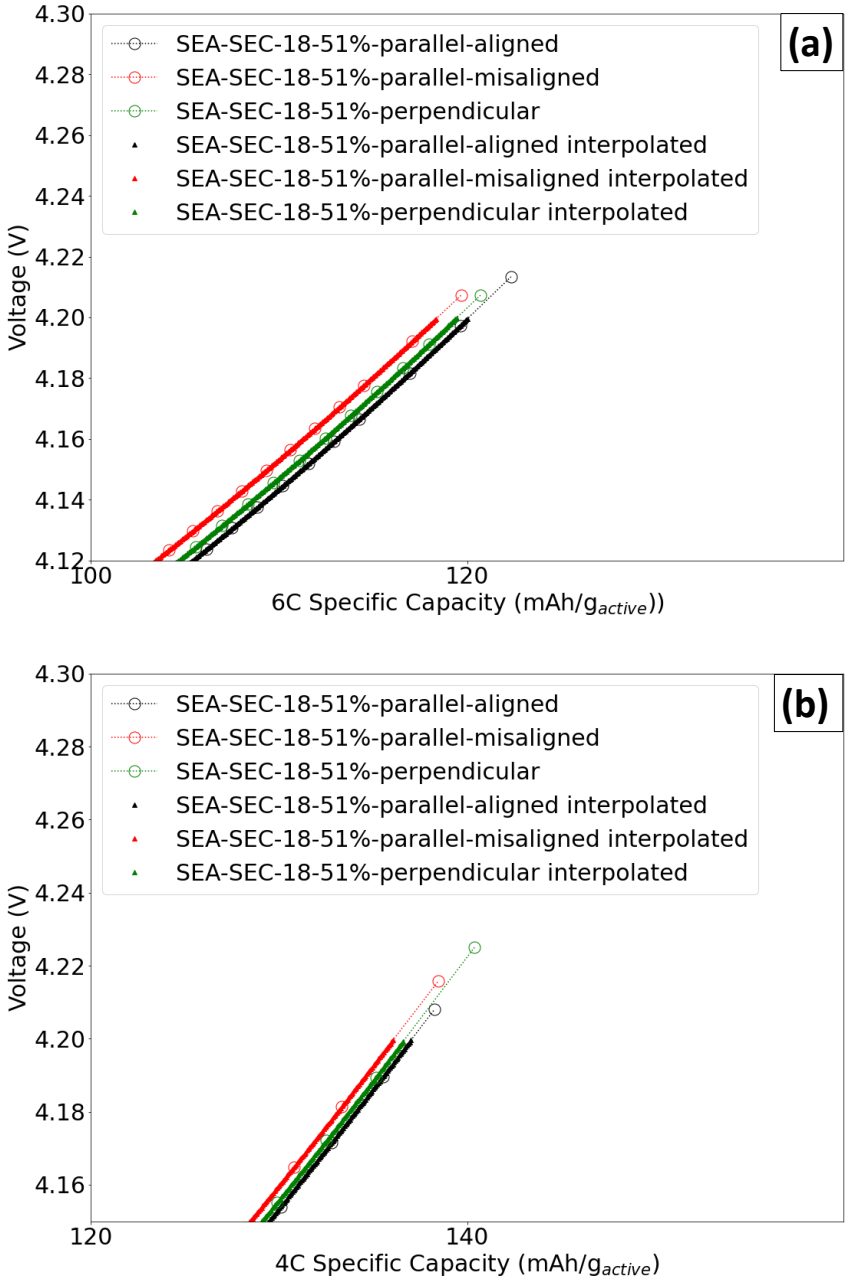

Figure C4. Close-up of the charge voltage profiles at (a) 4C and (b) 6C at the end of charge for SEC-18-51 SEA-SEC-18-51%-parallel-aligned, SEA-SEC-18-51%-parallel-misaligned, and SEA-SEC-18-51%-perpendicular. The empty circle markers are modeling results from *VIBE-AMPERES*. The solid triangle markers are the high-resolution voltage versus capacity data interpolated based on the *VIBE-AMPERES* modeling results and cut off at 4.2V. The interpolated capacity data at 4.2V was used as the charge capacity of SEA-SECs.

BIBLIOGRAPHY

(1) Hung, C.-H.; Allu, S.; Cobb, C. L. Modeling Current Density Non-Uniformities to Understand High-Rate Limitations in 3D Interdigitated Lithium-Ion Batteries. *J. Electrochem. Soc.* **2021**, *168* (10), 100512. https://doi.org/10.1149/1945-7111/ac2ac5.

(2) Hung, C.-H.; Huynh, P.; Teo, K.; Cobb, C. L. Are Three-Dimensional Batteries Beneficial? Analyzing Historical Data to Elucidate Performance Advantages. *ACS Energy Lett.* **2023**, *8* (1), 296–305. https://doi.org/10.1021/acsenergylett.2c02208.

(3) Li, J.; Du, Z.; Ruther, R. E.; AN, S. J.; David, L. A.; Hays, K.; Wood, M.; Phillip, N. D.; Sheng, Y.; Mao, C.; Kalnaus, S.; Daniel, C.; Wood, D. L. Toward Low-Cost, High-Energy Density, and High-Power Density Lithium-Ion Batteries. *JOM* **2017**, *69* (9), 1484–1496. https://doi.org/10.1007/s11837-017-2404-9.

(4) Lyubimov, I. A.; Kurmaev, R. K. The Choice of a Performance Criterion for a High-Voltage Battery of a Vehicle. *IOP Conf. Ser. Mater. Sci. Eng.* **2020**, *819*, 012015. https://doi.org/10.1088/1757-899X/819/1/012015.

(5) Iclodean, C.; Varga, B.; Burnete, N.; Cimerdean, D.; Jurchiş, B. Comparison of Different Battery Types for Electric Vehicles. *IOP Conf. Ser. Mater. Sci. Eng.* **2017**, *252*, 012058. https://doi.org/10.1088/1757-899X/252/1/012058.

(6) Liu, J.; Bao, Z.; Cui, Y.; Dufek, E. J.; Goodenough, J. B.; Khalifah, P.; Li, Q.; Liaw, B. Y.; Liu, P.; Manthiram, A.; Meng, Y. S.; Subramanian, V. R.; Toney, M. F.; Viswanathan, V. V.; Whittingham, M. S.; Xiao, J.; Xu, W.; Yang, J.; Yang, X.-Q.; Zhang, J.-G. Pathways for Practical High-Energy Long-Cycling Lithium Metal Batteries. *Nat. Energy* **2019**, *4* (3), 180–186. https://doi.org/10.1038/s41560-019-0338-x.

(7) Bonnassieux, Y.; Brabec, C. J.; Cao, Y.; Carmichael, T. B.; Chabinyc, M. L.; Cheng, K.-T.; Cho, G.; Chung, A.; Cobb, C. L.; Distler, A.; Egelhaaf, H.-J.; Grau, G.; Guo, X.; Haghiashtiani, G.; Huang, T.-C.; Hussain, M. M.; Iniguez, B.; Lee, T.-M.; Li, L.; Ma, Y.; Ma, D.; McAlpine, M. C.; Ng, T. N.; Österbacka, R.; Patel, S. N.; Peng, J.; Peng, H.; Rivnay, J.; Shao, L.; Steingart, D.; Street, R. A.; Subramanian, V.; Torsi, L.; Wu, Y. The 2021 Flexible and Printed Electronics Roadmap. *Flex. Print. Electron.* **2021**, *6* (2), 023001. https://doi.org/10.1088/2058-8585/abf986.

(8) Chukewad, Y. M.; James, J.; Singh, A.; Fuller, S. RoboFly: An Insect-Sized Robot with Simplified Fabrication That Is Capable of Flight, Ground, and Water Surface Locomotion. *ArXiv200102320 Cs Eess* **2020**.

(9) Wood, D. L.; Li, J.; Daniel, C. Prospects for Reducing the Processing Cost of Lithium Ion Batteries. *J. Power Sources* **2015**, *275*, 234–242. https://doi.org/10.1016/j.jpowsour.2014.11.019.

(10) Cobb, C. L.; Solberg, S. E. Communication—Analysis of Thick Co-Extruded Cathodes for Higher-Energy-and-Power Lithium-Ion Batteries. *J. Electrochem. Soc.* **2017**, *164* (7), A1339–A1341. https://doi.org/10.1149/2.0101707jes.

(11) Doyle, M.; Newman, J.; Gozdz, A. S.; Schmutz, C. N.; Tarascon, J.-M. Comparison of Modeling Predictions with Experimental Data from Plastic Lithium Ion Cells. *J. Electrochem. Soc.* **1996**, *143* (6), 1890–1903. https://doi.org/10.1149/1.1836921.

(12) Christensen, J.; Newman, J. Effect of Anode Film Resistance on the Charge/Discharge Capacity of a Lithium-Ion Battery. *J. Electrochem. Soc.* **2003**, *150* (11), A1416. https://doi.org/10.1149/1.1612501.

(13) Tjaden, B.; Cooper, S. J.; Brett, D. J.; Kramer, D.; Shearing, P. R. On the Origin and Application of the Bruggeman Correlation for Analysing Transport Phenomena in Electrochemical Systems. *Curr. Opin. Chem. Eng.* **2016**, *12*, 44–51. https://doi.org/10.1016/j.coche.2016.02.006.
(14) Rayleigh, Lord. LVI. On the Influence of Obstacles Arranged in Rectangular Order upon the Properties of a Medium. *Lond. Edinb. Dublin Philos. Mag. J. Sci.* **1892**, *34* (211), 481–502. https://doi.org/10.1080/14786449208620364.
(15) Wood, M.; Li, J.; Du, Z.; Daniel, C.; Dunlop, A. R.; Polzin, B. J.; Jansen, A. N.; Krumdick, G. K.; Wood, D. L. Impact of Secondary Particle Size and Two-Layer Architectures on the High-Rate Performance of Thick Electrodes in Lithium-Ion Battery Pouch Cells. *J. Power Sources* **2021**, *515*, 230429. https://doi.org/10.1016/j.jpowsour.2021.230429.
(16) Newman, J. Optimization of Porosity and Thickness of a Battery Electrode by Means of a Reaction-Zone Model. *J. Electrochem. Soc.* **1995**, *142* (1), 97. https://doi.org/10.1149/1.2043956.
(17) Wu, B.; Han, S.; Shin, K. G.; Lu, W. Application of Artificial Neural Networks in Design of Lithium-Ion Batteries. *J. Power Sources* **2018**, *395*, 128–136. https://doi.org/10.1016/j.jpowsour.2018.05.040.
(18) Malifarge, S.; Delobel, B.; Delacourt, C. Experimental and Modeling Analysis of Graphite Electrodes with Various Thicknesses and Porosities for High-Energy-Density Li-Ion Batteries. *J. Electrochem. Soc.* **2018**, *165* (7), A1275. https://doi.org/10.1149/2.0301807jes.
(19) Dai, Y.; Srinivasan, V. On Graded Electrode Porosity as a Design Tool for Improving the Energy Density of Batteries. *J. Electrochem. Soc.* **2015**, *163* (3), A406. https://doi.org/10.1149/2.0301603jes.
(20) Dargaville, S.; Farrell, T. W. Predicting Active Material Utilization in LiFePO4 Electrodes Using a Multiscale Mathematical Model. *J. Electrochem. Soc.* **2010**, *157* (7), A830–A840. https://doi.org/10.1149/1.3425620.
(21) Chen, K.-H.; Namkoong, M. J.; Goel, V.; Yang, C.; Kazemiabnavi, S.; Mortuza, S. M.; Kazyak, E.; Mazumder, J.; Thornton, K.; Sakamoto, J.; Dasgupta, N. P. Efficient Fast-Charging of Lithium-Ion Batteries Enabled by Laser-Patterned Three-Dimensional Graphite Anode Architectures. *J. Power Sources* **2020**, *471*, 228475. https://doi.org/10.1016/j.jpowsour.2020.228475.
(22) Sun, K.; Wei, T.-S.; Ahn, B. Y.; Seo, J. Y.; Dillon, S. J.; Lewis, J. A. 3D Printing of Interdigitated Li-Ion Microbattery Architectures. *Adv. Mater.* **2013**, *25* (33), 4539–4543. https://doi.org/10.1002/adma.201301036.
(23) Ashby, D. S.; Choi, C. S.; Edwards, M. A.; Talin, A. A.; White, H. S.; Dunn, B. S. High-Performance Solid-State Lithium-Ion Battery with Mixed 2D and 3D Electrodes. *ACS Appl. Energy Mater.* **2020**, *3* (9), 8402–8409. https://doi.org/10.1021/acsaem.0c01029.
(24) Parker, J. F.; Chervin, C. N.; Pala, I. R.; Machler, M.; Burz, M. F.; Long, J. W.; Rolison, D. R. Rechargeable Nickel–3D Zinc Batteries: An Energy-Dense, Safer Alternative to Lithium-Ion. *Science* **2017**, *356* (6336), 415–418. https://doi.org/10.1126/science.aak9991.
(25) O'Hanlon, S.; McNulty, D.; Tian, R.; Coleman, J.; O'Dwyer, C. High Charge and Discharge Rate Limitations in Ordered Macroporous Li-Ion Battery Materials. *J. Electrochem. Soc.* **2020**, *167* (14), 140532. https://doi.org/10.1149/1945-7111/abc6cb.

(26) Nyström, G.; Marais, A.; Karabulut, E.; Wågberg, L.; Cui, Y.; Hamedi, M. M. Self-Assembled Three-Dimensional and Compressible Interdigitated Thin-Film Supercapacitors and Batteries. *Nat. Commun.* **2015**, *6* (1), 7259. https://doi.org/10.1038/ncomms8259.
(27) Wang, W.; Tian, M.; Abdulagatov, A.; George, S. M.; Lee, Y.-C.; Yang, R. Three-Dimensional Ni/TiO2 Nanowire Network for High Areal Capacity Lithium Ion Microbattery Applications. *Nano Lett.* **2012**, *12* (2), 655–660. https://doi.org/10.1021/nl203434g.
(28) Zeng, W.; Zheng, F.; Li, R.; Zhan, Y.; Li, Y.; Liu, J. Template Synthesis of SnO2/α-Fe2O3 Nanotube Array for 3D Lithium Ion Battery Anode with Large Areal Capacity. *Nanoscale* **2012**, *4* (8), 2760–2765. https://doi.org/10.1039/C2NR30089C.
(29) Tian, M.; Wang, W.; Wei, Y.; Yang, R. Stable High Areal Capacity Lithium-Ion Battery Anodes Based on Three-Dimensional Ni–Sn Nanowire Networks. *J. Power Sources* **2012**, *211*, 46–51. https://doi.org/10.1016/j.jpowsour.2012.03.084.
(30) Xie, K.; Lu, Z.; Huang, H.; Lu, W.; Lai, Y.; Li, J.; Zhou, L.; Liu, Y. Iron Supported C@Fe3O4 Nanotube Array: A New Type of 3D Anode with Low-Cost for High Performance Lithium-Ion Batteries. *J. Mater. Chem.* **2012**, *22* (12), 5560–5567. https://doi.org/10.1039/C2JM15955D.
(31) Zhu, Y.; Ju, Z.; Zhang, X.; Lutz, D. M.; Housel, L. M.; Zhou, Y.; Takeuchi, K. J.; Takeuchi, E. S.; Marschilok, A. C.; Yu, G. Evaporation-Induced Vertical Alignment Enabling Directional Ion Transport in a 2D-Nanosheet-Based Battery Electrode. *Adv. Mater.* **2020**, *32* (10), 1907941. https://doi.org/10.1002/adma.201907941.
(32) Sun, H.; Mei, L.; Liang, J.; Zhao, Z.; Lee, C.; Fei, H.; Ding, M.; Lau, J.; Li, M.; Wang, C.; Xu, X.; Hao, G.; Papandrea, B.; Shakir, I.; Dunn, B.; Huang, Y.; Duan, X. Three-Dimensional Holey-Graphene/Niobia Composite Architectures for Ultrahigh-Rate Energy Storage. *Science* **2017**, *356* (6338), 599–604. https://doi.org/10.1126/science.aam5852.
(33) Liu, Z.; Yuan, X.; Zhang, S.; Wang, J.; Huang, Q.; Yu, N.; Zhu, Y.; Fu, L.; Wang, F.; Chen, Y.; Wu, Y. Three-Dimensional Ordered Porous Electrode Materials for Electrochemical Energy Storage. *NPG Asia Mater.* **2019**, *11* (1), 1–21. https://doi.org/10.1038/s41427-019-0112-3.
(34) Vu, A.; Qian, Y.; Stein, A. Porous Electrode Materials for Lithium-Ion Batteries – How to Prepare Them and What Makes Them Special. *Adv. Energy Mater.* **2012**, *2* (9), 1056–1085. https://doi.org/10.1002/aenm.201200320.
(35) Zhang, H.; Braun, P. V. Three-Dimensional Metal Scaffold Supported Bicontinuous Silicon Battery Anodes. *Nano Lett.* **2012**, *12* (6), 2778–2783. https://doi.org/10.1021/nl204551m.
(36) Zhang, H.; Yu, X.; Braun, P. V. Three-Dimensional Bicontinuous Ultrafast-Charge and -Discharge Bulk Battery Electrodes. *Nat. Nanotechnol.* **2011**, *6* (5), 277–281. https://doi.org/10.1038/nnano.2011.38.
(37) Kuang, Y.; Chen, C.; Kirsch, D.; Hu, L. Thick Electrode Batteries: Principles, Opportunities, and Challenges. *Adv. Energy Mater.* **2019**, *9* (33), 1901457. https://doi.org/10.1002/aenm.201901457.
(38) Zhang, X.; Ju, Z.; Zhu, Y.; Takeuchi, K. J.; Takeuchi, E. S.; Marschilok, A. C.; Yu, G. Multiscale Understanding and Architecture Design of High Energy/Power Lithium-Ion Battery Electrodes. *Adv. Energy Mater.* **2021**, *11* (2), 2000808. https://doi.org/10.1002/aenm.202000808.

(39) Li, W.; Fang, R.; Xia, Y.; Zhang, W.; Wang, X.; Xia, X.; Tu, J. Multiscale Porous Carbon Nanomaterials for Applications in Advanced Rechargeable Batteries. *Batter. Supercaps* **2019**, *2* (1), 9–36. https://doi.org/10.1002/batt.201800067.
(40) Priimägi, P.; Asfaw, H. D.; Srivastav, S.; Kasemägi, H.; Aabloo, A.; Brandell, D.; Zadin, V. Modeling 3D-Microbatteries Based on Carbon Foams. *Electrochimica Acta* **2018**, *281*, 665–675. https://doi.org/10.1016/j.electacta.2018.05.179.
(41) Pikul, J. H.; Braun, P. V.; King, W. P. Performance Modeling and Design of Ultra-High Power Microbatteries. *J. Electrochem. Soc.* **2017**, *164* (11), E3122. https://doi.org/10.1149/2.0151711jes.
(42) Ning, H.; Pikul, J. H.; Zhang, R.; Li, X.; Xu, S.; Wang, J.; Rogers, J. A.; King, W. P.; Braun, P. V. Holographic Patterning of High-Performance on-Chip 3D Lithium-Ion Microbatteries. *Proc. Natl. Acad. Sci.* **2015**, *112* (21), 6573–6578. https://doi.org/10.1073/pnas.1423889112.
(43) Nathan, M.; Golodnitsky, D.; Yufit, V.; Strauss, E.; Ripenbein, T.; Shechtman, I.; Menkin, S.; Peled, E. Three-Dimensional Thin-Film Li-Ion Microbatteries for Autonomous MEMS. *J. Microelectromechanical Syst.* **2005**, *14* (5), 879–885. https://doi.org/10.1109/JMEMS.2005.851860.
(44) Pearse, A.; Schmitt, T.; Sahadeo, E.; Stewart, D. M.; Kozen, A.; Gerasopoulos, K.; Talin, A. A.; Lee, S. B.; Rubloff, G. W.; Gregorczyk, K. E. Three-Dimensional Solid-State Lithium-Ion Batteries Fabricated by Conformal Vapor-Phase Chemistry. *ACS Nano* **2018**, *12* (5), 4286–4294. https://doi.org/10.1021/acsnano.7b08751.
(45) Chamran, F.; Yeh, Y.; Min, H.-S.; Dunn, B.; Kim, C.-J. Fabrication of High-Aspect-Ratio Electrode Arrays for Three-Dimensional Microbatteries. *J. Microelectromechanical Syst.* **2007**, *16* (4), 844–852. https://doi.org/10.1109/JMEMS.2007.901638.
(46) Dokko, K.; Sugaya, J.; Nakano, H.; Yasukawa, T.; Matsue, T.; Kanamura, K. Sol–Gel Fabrication of Lithium-Ion Microarray Battery. *Electrochem. Commun.* **2007**, *9* (5), 857–862. https://doi.org/10.1016/j.elecom.2006.11.025.
(47) Teixidor, G. T.; Zaouk, R. B.; Park, B. Y.; Madou, M. J. Fabrication and Characterization of Three-Dimensional Carbon Electrodes for Lithium-Ion Batteries. *J. Power Sources* **2008**, *183* (2), 730–740. https://doi.org/10.1016/j.jpowsour.2008.05.065.
(48) Talin, A. A.; Ruzmetov, D.; Kolmakov, A.; McKelvey, K.; Ware, N.; El Gabaly, F.; Dunn, B.; White, H. S. Fabrication, Testing, and Simulation of All-Solid-State Three-Dimensional Li-Ion Batteries. *ACS Appl. Mater. Interfaces* **2016**, *8* (47), 32385–32391. https://doi.org/10.1021/acsami.6b12244.
(49) McKelvey, K.; Talin, A. A.; Dunn, B.; White, H. S. Microscale 2.5D Batteries. *J. Electrochem. Soc.* **2017**, *164* (12), A2500–A2503. https://doi.org/10.1149/2.0771712jes.
(50) Priimägi, P.; Brandell, D.; Srivastav, S.; Aabloo, A.; Kasemägi, H.; Zadin, V. Optimizing the Design of 3D-Pillar Microbatteries Using Finite Element Modelling. *Electrochimica Acta* **2016**, *209*, 138–148. https://doi.org/10.1016/j.electacta.2016.05.047.
(51) Xie, J.; Oudenhoven, J. F. M.; Li, D.; Chen, C.; Eichel, R.-A.; Notten, P. H. L. High Power and High Capacity 3D-Structured TiO2 Electrodes for Lithium-Ion Microbatteries. *J. Electrochem. Soc.* **2016**, *163* (10), A2385. https://doi.org/10.1149/2.1141610jes.
(52) Mazor, H.; Golodnitsky, D.; Burstein, L.; Gladkich, A.; Peled, E. Electrophoretic Deposition of Lithium Iron Phosphate Cathode for Thin-Film 3D-Microbatteries. *J. Power Sources* **2012**, *198*, 264–272. https://doi.org/10.1016/j.jpowsour.2011.09.108.

(53) Zadin, V.; Brandell, D. Modelling Polymer Electrolytes for 3D-Microbatteries Using Finite Element Analysis. *Electrochimica Acta* **2011**, *57*, 237–243. https://doi.org/10.1016/j.electacta.2011.03.026.
(54) Zadin, V.; Kasemägi, H.; Aabloo, A.; Brandell, D. Modelling Electrode Material Utilization in the Trench Model 3D-Microbattery by Finite Element Analysis. *J. Power Sources* **2010**, *195* (18), 6218–6224. https://doi.org/10.1016/j.jpowsour.2010.02.056.
(55) Zadin, V.; Brandell, D.; Kasemägi, H.; Lellep, J.; Aabloo, A. Designing the 3D-Microbattery Geometry Using the Level-Set Method. *J. Power Sources* **2013**, *244*, 417–428. https://doi.org/10.1016/j.jpowsour.2012.12.004.
(56) Grazioli, D.; Verners, O.; Zadin, V.; Brandell, D.; Simone, A. Electrochemical-Mechanical Modeling of Solid Polymer Electrolytes: Impact of Mechanical Stresses on Li-Ion Battery Performance. *Electrochimica Acta* **2019**, *296*, 1122–1141. https://doi.org/10.1016/j.electacta.2018.07.234.
(57) Zadin, V.; Brandell, D.; Kasemägi, H.; Aabloo, A.; Thomas, J. O. Finite Element Modelling of Ion Transport in the Electrolyte of a 3D-Microbattery. *Solid State Ion.* **2011**, *192* (1), 279–283. https://doi.org/10.1016/j.ssi.2010.02.007.
(58) Cirigliano, N.; Sun, G.; Membreno, D.; Malati, P.; Kim, C. J.; Dunn, B. 3D Architectured Anodes for Lithium-Ion Microbatteries with Large Areal Capacity. *Energy Technol.* **2014**, *2* (4), 362–369. https://doi.org/10.1002/ente.201402018.
(59) Dunlap, N.; Sulas-Kern, D. B.; Weddle, P. J.; Usseglio-Viretta, F.; Walker, P.; Todd, P.; Boone, D.; Colclasure, A. M.; Smith, K.; Tremolet de Villers, B. J.; Finegan, D. P. Laser Ablation for Structuring Li-Ion Electrodes for Fast Charging and Its Impact on Material Properties, Rate Capability, Li Plating, and Wetting. *J. Power Sources* **2022**, *537*, 231464. https://doi.org/10.1016/j.jpowsour.2022.231464.
(60) Habedank, J. B.; Kriegler, J.; Zaeh, M. F. Enhanced Fast Charging and Reduced Lithium-Plating by Laser-Structured Anodes for Lithium-Ion Batteries. *J. Electrochem. Soc.* **2019**, *166* (16), A3940. https://doi.org/10.1149/2.1241915jes.
(61) Liu, C.; Xu, F.; Liu, Y.; Ma, J.; Liu, P.; Wang, D.; Lao, C.; Chen, Z. High Mass Loading Ultrathick Porous Li4Ti5O12 Electrodes with Improved Areal Capacity Fabricated via Low Temperature Direct Writing. *Electrochimica Acta* **2019**, *314*, 81–88. https://doi.org/10.1016/j.electacta.2019.05.082.
(62) Zhang, Y.; Shahriar, M.; Hu, S. Structuring Electrodes via Acoustic-Field-Assisted Particle Patterning for Enhanced Performance of Lithium-Ion Batteries. *J. Mater. Chem. A* **2023**, *11* (22), 11849–11858. https://doi.org/10.1039/D3TA01180A.
(63) Qi, Y.; Jang, T.; Ramadesigan, V.; Schwartz, D. T.; Subramanian, V. R. Is There a Benefit in Employing Graded Electrodes for Lithium-Ion Batteries? *J. Electrochem. Soc.* **2017**, *164* (13), A3196. https://doi.org/10.1149/2.1051713jes.
(64) Chowdhury, R.; Zhao, Y.; Xia, Y.; Ouyang, M.; Brandon, N.; Banerjee, A. Revisiting the Promise of Bi-Layer Graded Cathodes for Improved Li-Ion Battery Performance. *Sustain. Energy Fuels* **2021**, *5* (20), 5193–5204. https://doi.org/10.1039/D1SE01077H.
(65) Kraft, L.; Habedank, J. B.; Frank, A.; Rheinfeld, A.; Jossen, A. Modeling and Simulation of Pore Morphology Modifications Using Laser-Structured Graphite Anodes in Lithium-Ion Batteries. *J. Electrochem. Soc.* **2019**, *167* (1), 013506. https://doi.org/10.1149/2.0062001JES.
(66) Habedank, J. B.; Günter, F. J.; Billot, N.; Gilles, R.; Neuwirth, T.; Reinhart, G.; Zaeh, M. F. Rapid Electrolyte Wetting of Lithium-Ion Batteries Containing Laser Structured

Electrodes: In Situ Visualization by Neutron Radiography. *Int. J. Adv. Manuf. Technol.* **2019**, *102* (9), 2769–2778. https://doi.org/10.1007/s00170-019-03347-4.
(67) Habedank, J. B.; Kraft, L.; Rheinfeld, A.; Krezdorn, C.; Jossen, A.; Zaeh, M. F. Increasing the Discharge Rate Capability of Lithium-Ion Cells with Laser-Structured Graphite Anodes: Modeling and Simulation. *J. Electrochem. Soc.* **2018**, *165* (7), A1563. https://doi.org/10.1149/2.1181807jes.
(68) Mukherjee, P. P.; Pannala, S.; Turner, J. A. Modeling and Simulation of Battery Systems. In *Handbook of Battery Materials*; John Wiley & Sons, Ltd, 2011; pp 841–875. https://doi.org/10.1002/9783527637188.ch25.
(69) Cobb, C. L.; Blanco, M. Modeling Mass and Density Distribution Effects on the Performance of Co-Extruded Electrodes for High Energy Density Lithium-Ion Batteries. *J. Power Sources* **2014**, *249*, 357–366. https://doi.org/10.1016/j.jpowsour.2013.10.084.
(70) Allu, S.; Kalnaus, S.; Simunovic, S.; Nanda, J.; Turner, J. A.; Pannala, S. A Three-Dimensional Meso-Macroscopic Model for Li-Ion Intercalation Batteries. *J. Power Sources* **2016**, *325*, 42–50. https://doi.org/10.1016/j.jpowsour.2016.06.001.
(71) Trembacki, B. L.; Vadakkepatt, A.; Roberts, S. A.; Murthy, J. Y. Volume-Averaged Electrochemical Performance Modeling of 3D Interpenetrating Battery Electrode Architectures. *J. Electrochem. Soc.* **2020**, *167* (1), 013507. https://doi.org/10.1149/2.0072001JES.
(72) Trembacki, B.; Duoss, E.; Oxberry, G.; Stadermann, M.; Murthy, J. Mesoscale Electrochemical Performance Simulation of 3D Interpenetrating Lithium-Ion Battery Electrodes. *J. Electrochem. Soc.* **2019**, *166* (6), A923. https://doi.org/10.1149/2.0031906jes.
(73) Hutzenlaub, T.; Thiele, S.; Paust, N.; Spotnitz, R.; Zengerle, R.; Walchshofer, C. Three-Dimensional Electrochemical Li-Ion Battery Modelling Featuring a Focused Ion-Beam/Scanning Electron Microscopy Based Three-Phase Reconstruction of a LiCoO2 Cathode. *Electrochimica Acta* **2014**, *115*, 131–139. https://doi.org/10.1016/j.electacta.2013.10.103.
(74) Goldin, G. M.; Colclasure, A. M.; Wiedemann, A. H.; Kee, R. J. Three-Dimensional Particle-Resolved Models of Li-Ion Batteries to Assist the Evaluation of Empirical Parameters in One-Dimensional Models. *Electrochimica Acta* **2012**, *64*, 118–129. https://doi.org/10.1016/j.electacta.2011.12.119.
(75) Wiedemann, A. H.; Goldin, G. M.; Barnett, S. A.; Zhu, H.; Kee, R. J. Effects of Three-Dimensional Cathode Microstructure on the Performance of Lithium-Ion Battery Cathodes. *Electrochimica Acta* **2013**, *88*, 580–588. https://doi.org/10.1016/j.electacta.2012.10.104.
(76) Less, G. B.; Seo, J. H.; Han, S.; Sastry, A. M.; Zausch, J.; Latz, A.; Schmidt, S.; Wieser, C.; Kehrwald, D.; Fell, S. Micro-Scale Modeling of Li-Ion Batteries: Parameterization and Validation. *J. Electrochem. Soc.* **2012**, *159* (6), A697. https://doi.org/10.1149/2.096205jes.
(77) Newman, J. S.; Tobias, C. W. Theoretical Analysis of Current Distribution in Porous Electrodes. *J. Electrochem. Soc.* **1962**, *109* (12), 1183. https://doi.org/10.1149/1.2425269.
(78) Newman, J.; Tiedemann, W. Porous-Electrode Theory with Battery Applications. *AIChE J.* **1975**, *21* (1), 25–41. https://doi.org/10.1002/aic.690210103.
(79) Vidts, P. D.; White, R. E. Governing Equations for Transport in Porous Electrodes. *J. Electrochem. Soc.* **1997**, *144* (4), 1343. https://doi.org/10.1149/1.1837595.
(80) Trainham, I. I. I. FLOW-THROUGH POROUS ELECTRODES. **1979**.

(81) Allu, S.; Kalnaus, S.; Elwasif, W.; Simunovic, S.; Turner, J. A.; Pannala, S. A New Open Computational Framework for Highly-Resolved Coupled Three-Dimensional Multiphysics Simulations of Li-Ion Cells. *J. Power Sources* **2014**, *246*, 876–886. https://doi.org/10.1016/j.jpowsour.2013.08.040.
(82) Tian, R.; Park, S.-H.; King, P. J.; Cunningham, G.; Coelho, J.; Nicolosi, V.; Coleman, J. N. Quantifying the Factors Limiting Rate Performance in Battery Electrodes. *Nat. Commun.* **2019**, *10* (1), 1–11. https://doi.org/10.1038/s41467-019-09792-9.
(83) Yoshima, K.; Munakata, H.; Kanamura, K. Fabrication of Micro Lithium-Ion Battery with 3D Anode and 3D Cathode by Using Polymer Wall. *J. Power Sources* **2012**, *208*, 404–408. https://doi.org/10.1016/j.jpowsour.2012.02.045.
(84) Bae, C.-J.; Erdonmez, C. K.; Halloran, J. W.; Chiang, Y.-M. Design of Battery Electrodes with Dual-Scale Porosity to Minimize Tortuosity and Maximize Performance. *Adv. Mater.* **2013**, *25* (9), 1254–1258. https://doi.org/10.1002/adma.201204055.
(85) Lu, L.-L.; Lu, Y.-Y.; Xiao, Z.-J.; Zhang, T.-W.; Zhou, F.; Ma, T.; Ni, Y.; Yao, H.-B.; Yu, S.-H.; Cui, Y. Wood-Inspired High-Performance Ultrathick Bulk Battery Electrodes. *Adv. Mater.* **2018**, *30* (20), 1706745. https://doi.org/10.1002/adma.201706745.
(86) Sander, J. S.; Erb, R. M.; Li, L.; Gurijala, A.; Chiang, Y.-M. High-Performance Battery Electrodes via Magnetic Templating. *Nat. Energy* **2016**, *1* (8), 1–7. https://doi.org/10.1038/nenergy.2016.99.
(87) Izumi, A.; Sanada, M.; Furuichi, K.; Teraki, K.; Matsuda, T.; Hiramatsu, K.; Munakata, H.; Kanamura, K. Development of High Capacity Lithium-Ion Battery Applying Three-Dimensionally Patterned Electrode. *Electrochimica Acta* **2012**, *79*, 218–222. https://doi.org/10.1016/j.electacta.2012.07.001.
(88) Saleh, M. S.; Li, J.; Park, J.; Panat, R. 3D Printed Hierarchically-Porous Microlattice Electrode Materials for Exceptionally High Specific Capacity and Areal Capacity Lithium Ion Batteries. *Addit. Manuf.* **2018**, *23*, 70–78. https://doi.org/10.1016/j.addma.2018.07.006.
(89) Pikul, J. H.; Gang Zhang, H.; Cho, J.; Braun, P. V.; King, W. P. High-Power Lithium Ion Microbatteries from Interdigitated Three-Dimensional Bicontinuous Nanoporous Electrodes. *Nat. Commun.* **2013**, *4* (1), 1732. https://doi.org/10.1038/ncomms2747.
(90) Ashby, D. S.; DeBlock, R. H.; Lai, C.-H.; Choi, C. S.; Dunn, B. S. Patternable, Solution-Processed Ionogels for Thin-Film Lithium-Ion Electrolytes. *Joule* **2017**, *1* (2), 344–358. https://doi.org/10.1016/j.joule.2017.08.012.
(91) Eftekhari, A. Lithium-Ion Batteries with High Rate Capabilities. *ACS Sustain. Chem. Eng.* **2017**, *5* (4), 2799–2816. https://doi.org/10.1021/acssuschemeng.7b00046.
(92) Rohatgi, A. WebPlotDigitizer, 2021. https://automeris.io/WebPlotDigitizer.
(93) Higgins, T. M.; Coleman, J. N. Avoiding Resistance Limitations in High-Performance Transparent Supercapacitor Electrodes Based on Large-Area, High-Conductivity PEDOT:PSS Films. *ACS Appl. Mater. Interfaces* **2015**, *7* (30), 16495–16506. https://doi.org/10.1021/acsami.5b03882.
(94) Horváth, D. V.; Coelho, J.; Tian, R.; Nicolosi, V.; Coleman, J. N. Quantifying the Dependence of Battery Rate Performance on Electrode Thickness. *ACS Appl. Energy Mater.* **2020**, *3* (10), 10154–10163. https://doi.org/10.1021/acsaem.0c01865.
(95) Virtanen, P.; Gommers, R.; Oliphant, T. E.; Haberland, M.; Reddy, T.; Cournapeau, D.; Burovski, E.; Peterson, P.; Weckesser, W.; Bright, J.; van der Walt, S. J.; Brett, M.; Wilson, J.; Millman, K. J.; Mayorov, N.; Nelson, A. R. J.; Jones, E.; Kern, R.; Larson, E.;

Carey, C. J.; Polat, İ.; Feng, Y.; Moore, E. W.; VanderPlas, J.; Laxalde, D.; Perktold, J.; Cimrman, R.; Henriksen, I.; Quintero, E. A.; Harris, C. R.; Archibald, A. M.; Ribeiro, A. H.; Pedregosa, F.; van Mulbregt, P. SciPy 1.0: Fundamental Algorithms for Scientific Computing in Python. *Nat. Methods* **2020**, *17* (3), 261–272. https://doi.org/10.1038/s41592-019-0686-2.

(96) Nitta, N.; Wu, F.; Lee, J. T.; Yushin, G. Li-Ion Battery Materials: Present and Future. *Mater. Today* **2015**, *18* (5), 252–264. https://doi.org/10.1016/j.mattod.2014.10.040.

(97) Long, J. W.; Dunn, B.; Rolison, D. R.; White, H. S. Three-Dimensional Battery Architectures. *Chem. Rev.* **2004**, *104* (10), 4463–4492. https://doi.org/10.1021/cr020740l.

(98) Zheng, H.; Li, J.; Song, X.; Liu, G.; Battaglia, V. S. A Comprehensive Understanding of Electrode Thickness Effects on the Electrochemical Performances of Li-Ion Battery Cathodes. *Electrochimica Acta* **2012**, *71*, 258–265. https://doi.org/10.1016/j.electacta.2012.03.161.

(99) Yu, D. Y. W.; Donoue, K.; Inoue, T.; Fujimoto, M.; Fujitani, S. Effect of Electrode Parameters on LiFePO4 Cathodes. *J. Electrochem. Soc.* **2006**, *153* (5), A835. https://doi.org/10.1149/1.2179199.

(100) Gallagher, K.; Trask, S.; Bauer, C.; Woehrle, T.; Lux, S.; Tschech, M.; Lamp, P.; Polzin, B.; Ha, S.; Long, B.; Wu, Q.; Lu, W.; Dees, D.; Jansen, A. Optimizing Areal Capacities through Understanding the Limitations of Lithium-Ion Electrodes. *J. Electrochem. Soc.* **2016**, *163*, A138–A149. https://doi.org/10.1149/2.0321602jes.

(101) Myung, S.-T.; Maglia, F.; Park, K.-J.; Yoon, C. S.; Lamp, P.; Kim, S.-J.; Sun, Y.-K. Nickel-Rich Layered Cathode Materials for Automotive Lithium-Ion Batteries: Achievements and Perspectives. *ACS Energy Lett.* **2017**, *2* (1), 196–223. https://doi.org/10.1021/acsenergylett.6b00594.

(102) Cobb, C. L.; Ho, C. C. Additive Manufacturing: Rethinking Battery Design. *Electrochem. Soc. Interface* **2016**, *25* (1), 75. https://doi.org/10.1149/2.F08161if.

(103) Strauss, F.; Bartsch, T.; de Biasi, L.; Kim, A.-Y.; Janek, J.; Hartmann, P.; Brezesinski, T. Impact of Cathode Material Particle Size on the Capacity of Bulk-Type All-Solid-State Batteries. *ACS Energy Lett.* **2018**, *3* (4), 992–996. https://doi.org/10.1021/acsenergylett.8b00275.

(104) Hart, R.; White, H.; Dunn, B.; Rolison, D. 3-D Microbatteries. *Electrochem. Commun.* **2003**, *5*, 120–123. https://doi.org/10.1016/S1388-2481(02)00556-8.

(105) Hur, J. I.; Smith, L. C.; Dunn, B. High Areal Energy Density 3D Lithium-Ion Microbatteries. *Joule* **2018**, *2* (6), 1187–1201. https://doi.org/10.1016/j.joule.2018.04.002.

(106) Fu, K.; Wang, Y.; Yan, C.; Yao, Y.; Chen, Y.; Dai, J.; Lacey, S.; Wang, Y.; Wan, J.; Li, T.; Wang, Z.; Xu, Y.; Hu, L. Graphene Oxide-Based Electrode Inks for 3D-Printed Lithium-Ion Batteries. *Adv. Mater.* **2016**, *28* (13), 2587–2594. https://doi.org/10.1002/adma.201505391.

(107) Kotobuki, M.; Suzuki, Y.; Munakata, H.; Kanamura, K.; Sato, Y.; Yamamoto, K.; Yoshida, T. Fabrication of Three-Dimensional Battery Using Ceramic Electrolyte with Honeycomb Structure by Sol–Gel Process. *J. Electrochem. Soc.* **2010**, *157* (4), A493–A498. https://doi.org/10.1149/1.3308459.

(108) Long, B. R.; Rinaldo, S. G.; Gallagher, K. G.; Dees, D. W.; Trask, S. E.; Polzin, B. J.; Jansen, A. N.; Abraham, D. P.; Bloom, I.; Bareño, J.; Croy, J. R. Enabling High-Energy, High-Voltage Lithium-Ion Cells: Standardization of Coin-Cell Assembly, Electrochemical

Testing, and Evaluation of Full Cells. *J. Electrochem. Soc.* **2016**, *163* (14), A2999. https://doi.org/10.1149/2.0691614jes.
(109) Srinivasan, V.; Newman, J. Design and Optimization of a Natural Graphite/Iron Phosphate Lithium-Ion Cell. *J. Electrochem. Soc.* **2004**, *151* (10), A1530–A1538. https://doi.org/10.1149/1.1785013.
(110) Rashid, M.; Sahoo, A.; Gupta, A.; Sharma, Y. Numerical Modelling of Transport Limitations in Lithium Titanate Anodes. *Electrochimica Acta* **2018**, *283*, 313–326. https://doi.org/10.1016/j.electacta.2018.06.147.
(111) Harlow, J. E.; Ma, X.; Li, J.; Logan, E.; Liu, Y.; Zhang, N.; Ma, L.; Glazier, S. L.; Cormier, M. M. E.; Genovese, M.; Buteau, S.; Cameron, A.; Stark, J. E.; Dahn, J. R. A Wide Range of Testing Results on an Excellent Lithium-Ion Cell Chemistry to Be Used as Benchmarks for New Battery Technologies. *J. Electrochem. Soc.* **2019**, *166* (13), A3031. https://doi.org/10.1149/2.0981913jes.
(112) Usseglio-Viretta, F. L. E.; Colclasure, A.; Mistry, A. N.; Claver, K. P. Y.; Pouraghajan, F.; Finegan, D. P.; Heenan, T. M. M.; Abraham, D.; Mukherjee, P. P.; Wheeler, D.; Shearing, P.; Cooper, S. J.; Smith, K. Resolving the Discrepancy in Tortuosity Factor Estimation for Li-Ion Battery Electrodes through Micro-Macro Modeling and Experiment. *J. Electrochem. Soc.* **2018**, *165* (14), A3403. https://doi.org/10.1149/2.0731814jes.
(113) Colclasure, A. M.; Dunlop, A. R.; Trask, S. E.; Polzin, B. J.; Jansen, A. N.; Smith, K. Requirements for Enabling Extreme Fast Charging of High Energy Density Li-Ion Cells While Avoiding Lithium Plating. *J. Electrochem. Soc.* **2019**, *166* (8), A1412. https://doi.org/10.1149/2.0451908jes.
(114) Gilbert, J. A.; Bareño, J.; Spila, T.; Trask, S. E.; Miller, D. J.; Polzin, B. J.; Jansen, A. N.; Abraham, D. P. Cycling Behavior of NCM523/Graphite Lithium-Ion Cells in the 3–4.4 V Range: Diagnostic Studies of Full Cells and Harvested Electrodes. *J. Electrochem. Soc.* **2016**, *164* (1), A6054. https://doi.org/10.1149/2.0081701jes.
(115) Jaiswal, A.; Horne, C. R.; Chang, O.; Zhang, W.; Kong, W.; Wang, E.; Chern, T.; Doeff, M. M. Nanoscale LiFePO4 and Li4Ti5O12 for High Rate Li-Ion Batteries. *J. Electrochem. Soc.* **2009**, *156* (12), A1041–A1046. https://doi.org/10.1149/1.3223987.
(116) Cho, T.-H.; Tanaka, M.; Ohnishi, H.; Kondo, Y.; Yoshikazu, M.; Nakamura, T.; Sakai, T. Composite Nonwoven Separator for Lithium-Ion Battery: Development and Characterization. *J. Power Sources* **2010**, *195* (13), 4272–4277. https://doi.org/10.1016/j.jpowsour.2010.01.018.
(117) Chen, W.; Liu, Y.; Ma, Y.; Liu, J.; Liu, X. Improved Performance of PVdF-HFP/PI Nanofiber Membrane for Lithium Ion Battery Separator Prepared by a Bicomponent Cross-Electrospinning Method. *Mater. Lett.* **2014**, *133*, 67–70. https://doi.org/10.1016/j.matlet.2014.06.163.
(118) Katz, M. E. R.; Cobb, C. L. High-Viscosity Phase Inversion Separators for Freestanding and Direct-on-Electrode Manufacturing in Lithium-Ion Batteries. *ACS Appl. Mater. Interfaces* **2024**, *16* (34), 44863–44878. https://doi.org/10.1021/acsami.4c09342.
(119) Thorat, I. V. Understanding Performance-Limiting Mechanisms in Lithium-Ion Batteries for High-Rate Applications. Ph.D., Brigham Young University, United States -- Utah, 2009.
(120) Dees, D.; Gunen, E.; Abraham, D.; Jansen, A.; Prakash, J. Electrochemical Modeling of Lithium-Ion Positive Electrodes during Hybrid Pulse Power Characterization Tests. *J. Electrochem. Soc.* **2008**, *155* (8), A603. https://doi.org/10.1149/1.2939211.

(121) Mao, C.; Ruther, R. E.; Li, J.; Du, Z.; Belharouak, I. Identifying the Limiting Electrode in Lithium Ion Batteries for Extreme Fast Charging. *Electrochem. Commun.* **2018**, *97*, 37–41. https://doi.org/10.1016/j.elecom.2018.10.007.
(122) Stewart, S.; Albertus, P.; Srinivasan, V.; Plitz, I.; Pereira, N.; Amatucci, G.; Newman, J. Optimizing the Performance of Lithium Titanate Spinel Paired with Activated Carbon or Iron Phosphate. *J. Electrochem. Soc.* **2008**, *155* (3), A253–A261. https://doi.org/10.1149/1.2830552.
(123) Kashkooli, A. G.; Amirfazli, A.; Farhad, S.; Lee, D. U.; Felicelli, S.; Park, H. W.; Feng, K.; De Andrade, V.; Chen, Z. Representative Volume Element Model of Lithium-Ion Battery Electrodes Based on X-Ray Nano-Tomography. *J. Appl. Electrochem.* **2017**, *47* (3), 281–293. https://doi.org/10.1007/s10800-016-1037-y.
(124) Valøen, L. O.; Reimers, J. N. Transport Properties of LiPF6-Based Li-Ion Battery Electrolytes. *J. Electrochem. Soc.* **2005**, *152* (5), A882–A891. https://doi.org/10.1149/1.1872737.
(125) Tatara, R.; Yu, Y.; Karayaylali, P.; Chan, A. K.; Zhang, Y.; Jung, R.; Maglia, F.; Giordano, L.; Shao-Horn, Y. Enhanced Cycling Performance of Ni-Rich Positive Electrodes (NMC) in Li-Ion Batteries by Reducing Electrolyte Free-Solvent Activity. *ACS Appl. Mater. Interfaces* **2019**, *11* (38), 34973–34988. https://doi.org/10.1021/acsami.9b11942.
(126) Logan, E. R.; Tonita, E. M.; Gering, K. L.; Ma, L.; Bauer, M. K. G.; Li, J.; Beaulieu, L. Y.; Dahn, J. R. A Study of the Transport Properties of Ethylene Carbonate-Free Li Electrolytes. *J. Electrochem. Soc.* **2018**, *165* (3), A705. https://doi.org/10.1149/2.0981803jes.
(127) Verma, A.; Smith, K.; Santhanagopalan, S.; Abraham, D.; Yao, K. P.; Mukherjee, P. P. Galvanostatic Intermittent Titration and Performance Based Analysis of $LiNi_{0.5}Co_{0.2}Mn_{0.3}O_2$ Cathode. *J. Electrochem. Soc.* **2017**, *164* (13), A3380–A3392. https://doi.org/10.1149/2.1701713jes.
(128) Chen, Y.-H.; Wang, C.-W.; Liu, G.; Song, X.-Y.; Battaglia, V. S.; Sastry, A. M. Selection of Conductive Additives in Li-Ion Battery Cathodes: A Numerical Study. *J. Electrochem. Soc.* **2007**, *154* (10), A978. https://doi.org/10.1149/1.2767839.
(129) Plett, G. L. *Battery Management Systems*; Artech House, 2015.
(130) Forman, J. C.; Moura, S. J.; Stein, J. L.; Fathy, H. K. Genetic Identification and Fisher Identifiability Analysis of the Doyle–Fuller–Newman Model from Experimental Cycling of a LiFePO4 Cell. *J. Power Sources* **2012**, *210*, 263–275. https://doi.org/10.1016/j.jpowsour.2012.03.009.
(131) Thorat, I. V.; Stephenson, D. E.; Zacharias, N. A.; Zaghib, K.; Harb, J. N.; Wheeler, D. R. Quantifying Tortuosity in Porous Li-Ion Battery Materials. *J. Power Sources* **2009**, *188* (2), 592–600. https://doi.org/10.1016/j.jpowsour.2008.12.032.
(132) Hung, C.-H.; Allu, S.; Cobb, C. L. Modeling Structured Electrodes and Graded Porosity for Improving Discharge Rate Capability in Ultra-Thick Graphite|LiNi0.6Mn0.2Co0.2O2 Batteries. *J. Electrochem. Soc.* **2025**, *172* (1), 010513. https://doi.org/10.1149/1945-7111/ada4e0.
(133) Tian, R.; Alcala, N.; O'Neill, S. J. K.; Horvath, D. V.; Coelho, J.; Griffin, A. J.; Zhang, Y.; Nicolosi, V.; O'Dwyer, C.; Coleman, J. N. Quantifying the Effect of Electronic Conductivity on the Rate Performance of Nanocomposite Battery Electrodes. *ACS Appl. Energy Mater.* **2020**, *3* (3), 2966–2974. https://doi.org/10.1021/acsaem.0c00034.

(134) Shante, V. K. S.; Kirkpatrick, S. An Introduction to Percolation Theory. *Adv. Phys.* **1971**, *20* (85), 325–357. https://doi.org/10.1080/00018737100101261.
(135) Heubner, C.; Nickol, A.; Seeba, J.; Reuber, S.; Junker, N.; Wolter, M.; Schneider, M.; Michaelis, A. Understanding Thickness and Porosity Effects on the Electrochemical Performance of LiNi0.6Co0.2Mn0.2O2-Based Cathodes for High Energy Li-Ion Batteries. *J. Power Sources* **2019**, *419*, 119–126. https://doi.org/10.1016/j.jpowsour.2019.02.060.
(136) Parikh, D.; Christensen, T.; Li, J. Correlating the Influence of Porosity, Tortuosity, and Mass Loading on the Energy Density of LiNi0.6Mn0.2Co0.2O2 Cathodes under Extreme Fast Charging (XFC) Conditions. *J. Power Sources* **2020**, *474*, 228601. https://doi.org/10.1016/j.jpowsour.2020.228601.
(137) Appiah, W. A.; Park, J.; Song, S.; Byun, S.; Ryou, M.-H.; Lee, Y. M. Design Optimization of LiNi0.6Co0.2Mn0.2O2/Graphite Lithium-Ion Cells Based on Simulation and Experimental Data. *J. Power Sources* **2016**, *319*, 147–158. https://doi.org/10.1016/j.jpowsour.2016.04.052.
(138) Ansah, S.; Hyun, H.; Shin, N.; Lee, J.-S.; Lim, J.; Cho, H.-H. A Modeling Approach to Study the Performance of Ni-Rich Layered Oxide Cathode for Lithium-Ion Battery. *Comput. Mater. Sci.* **2021**, *196*, 110559. https://doi.org/10.1016/j.commatsci.2021.110559.
(139) Huang, S.; Wu, X.; Cavalheiro, G. M.; Du, X.; Liu, B.; Du, Z.; Zhang, G. In Situ Measurement of Lithium-Ion Cell Internal Temperatures during Extreme Fast Charging. *J. Electrochem. Soc.* **2019**, *166* (14), A3254. https://doi.org/10.1149/2.0441914jes.
(140) Singh, M.; Kaiser, J.; Hahn, H. Thick Electrodes for High Energy Lithium Ion Batteries. *J. Electrochem. Soc.* **2015**, *162* (7), A1196. https://doi.org/10.1149/2.0401507jes.
(141) Günter, F. J.; Wassiliadis, N. State of the Art of Lithium-Ion Pouch Cells in Automotive Applications: Cell Teardown and Characterization. *J. Electrochem. Soc.* **2022**, *169* (3), 030515. https://doi.org/10.1149/1945-7111/ac4e11.
(142) Azami-Ghadkolai, M.; Yousefi, M.; Allu, S.; Creager, S.; Bordia, R. Effect of Isotropic and Anisotropic Porous Microstructure on Electrochemical Performance of Li Ion Battery Cathodes: An Experimental and Computational Study. *J. Power Sources* **2020**, *474*, 228490. https://doi.org/10.1016/j.jpowsour.2020.228490.
(143) *USABC – USCAR*. https://uscar.org/usabc/ (accessed 2024-08-21).
(144) Fordham, A.; Milojevic, Z.; Giles, E.; Du, W.; Owen, R. E.; Michalik, S.; Chater, P. A.; Das, P. K.; Attidekou, P. S.; Lambert, S. M.; Allan, P. K.; Slater, P. R.; Anderson, P. A.; Jervis, R.; Shearing, P. R.; Brett, D. J. L. Correlative Non-Destructive Techniques to Investigate Aging and Orientation Effects in Automotive Li-Ion Pouch Cells. *Joule* **2023**, *7* (11), 2622–2652. https://doi.org/10.1016/j.joule.2023.10.011.
(145) Goel, V.; Chen, K.-H.; Dasgupta, N. P.; Thornton, K. Optimization of Laser-Patterned Electrode Architectures for Fast Charging of Li-Ion Batteries Using Simulations Parameterized by Machine Learning. *Energy Storage Mater.* **2023**, *57*, 44–58. https://doi.org/10.1016/j.ensm.2023.01.050.
(146) Schmuch, R.; Wagner, R.; Hörpel, G.; Placke, T.; Winter, M. Performance and Cost of Materials for Lithium-Based Rechargeable Automotive Batteries. *Nat. Energy* **2018**, *3* (4), 267–278. https://doi.org/10.1038/s41560-018-0107-2.
(147) Kumberg, J.; Müller, M.; Diehm, R.; Spiegel, S.; Wachsmann, C.; Bauer, W.; Scharfer, P.; Schabel, W. Drying of Lithium-Ion Battery Anodes for Use in High-Energy Cells: Influence of Electrode Thickness on Drying Time, Adhesion, and Crack Formation. *Energy Technol.* **2019**, *7* (11), 1900722. https://doi.org/10.1002/ente.201900722.

(148) Hille, L.; Xu, L.; Keilhofer, J.; Stock, S.; Kriegler, J.; Zaeh, M. F. Laser Structuring of Graphite Anodes and NMC Cathodes – Proportionate Influence on Electrode Characteristics and Cell Performance. *Electrochimica Acta* **2021**, *392*, 139002. https://doi.org/10.1016/j.electacta.2021.139002.
(149) Nemani, V. P.; Harris, S. J.; Smith, K. C. Design of Bi-Tortuous, Anisotropic Graphite Anodes for Fast Ion-Transport in Li-Ion Batteries. *J. Electrochem. Soc.* **2015**, *162* (8), A1415–A1423. https://doi.org/10.1149/2.0151508jes.
(150) Wu, X.; Bai, Y.; Li, Z.; Liu, J.; Zhao, K.; Du, Z. Effects of Charging Rates on LiNi0.6Mn0.2Co0.2O2 (NMC622)/Graphite Li-Ion Cells. *J. Energy Chem.* **2021**, *56*, 121–126. https://doi.org/10.1016/j.jechem.2020.08.008.
(151) Park, J. H.; Yoon, H.; Cho, Y.; Yoo, C.-Y. Investigation of Lithium Ion Diffusion of Graphite Anode by the Galvanostatic Intermittent Titration Technique. *Materials* **2021**, *14* (16), 4683. https://doi.org/10.3390/ma14164683.
(152) Lakhdar, Y.; Chen, Y.; Geary, H.; Houck, M. E.; Groombridge, A. S.; Slater, P. R.; Kendrick, E. Toward Higher-Power Li-Ion Batteries: Unravelling Kinetics and Thermodynamics of MoNb12O33 *vs.* NMC622. *J. Power Sources* **2023**, *588*, 233710. https://doi.org/10.1016/j.jpowsour.2023.233710.
(153) Chaouachi, O.; Réty, J.-M.; Génies, S.; Chandesris, M.; Bultel, Y. Experimental and Theoretical Investigation of Li-Ion Battery Active Materials Properties: Application to a Graphite/Ni0.6Mn0.2Co0.2O2 System. *Electrochimica Acta* **2021**, *366*, 137428. https://doi.org/10.1016/j.electacta.2020.137428.
(154) Lin, X.; Khosravinia, K.; Hu, X.; Li, J.; Lu, W. Lithium Plating Mechanism, Detection, and Mitigation in Lithium-Ion Batteries. *Prog. Energy Combust. Sci.* **2021**, *87*, 100953. https://doi.org/10.1016/j.pecs.2021.100953.
(155) Liu, Q.; Du, C.; Shen, B.; Zuo, P.; Cheng, X.; Ma, Y.; Yin, G.; Gao, Y. Understanding Undesirable Anode Lithium Plating Issues in Lithium-Ion Batteries. *RSC Adv* **2016**, *6*, 88683–88700. https://doi.org/10.1039/C6RA19482F.
(156) Sun, S.; Wang, J.; Chen, X.; Ma, Q.; Wang, Y.; Yang, K.; Yao, X.; Yang, Z.; Liu, J.; Xu, H.; Cai, Q.; Zhao, Y.; Yan, W. Thermally Stable and Dendrite-Resistant Separators toward Highly Robust Lithium Metal Batteries. *Adv. Energy Mater.* **2022**, *12* (41), 2202206. https://doi.org/10.1002/aenm.202202206.
(157) Jana, A.; Ely, D. R.; García, R. E. Dendrite-Separator Interactions in Lithium-Based Batteries. *J. Power Sources* **2015**, *275*, 912–921. https://doi.org/10.1016/j.jpowsour.2014.11.056.
(158) Rangarajan, S. P.; Barsukov, Y.; Mukherjee, P. P. In Operando Signature and Quantification of Lithium Plating. *J. Mater. Chem. A* **2019**, *7* (36), 20683–20695. https://doi.org/10.1039/C9TA07314K.
(159) Konz, Z. M.; McShane, E. J.; McCloskey, B. D. Detecting the Onset of Lithium Plating and Monitoring Fast Charging Performance with Voltage Relaxation. *ACS Energy Lett.* **2020**, *5* (6), 1750–1757. https://doi.org/10.1021/acsenergylett.0c00831.
(160) Janakiraman, U.; Garrick, T. R.; Fortier, M. E. Review—Lithium Plating Detection Methods in Li-Ion Batteries. *J. Electrochem. Soc.* **2020**, *167* (16), 160552. https://doi.org/10.1149/1945-7111/abd3b8.
(161) Arora, P.; Doyle, M.; White, R. E. Mathematical Modeling of the Lithium Deposition Overcharge Reaction in Lithium-Ion Batteries Using Carbon-Based Negative Electrodes. *J. Electrochem. Soc.* **1999**, *146* (10), 3543. https://doi.org/10.1149/1.1392512.

(162) Ge, H.; Aoki, T.; Ikeda, N.; Suga, S.; Isobe, T.; Li, Z.; Tabuchi, Y.; Zhang, J. Investigating Lithium Plating in Lithium-Ion Batteries at Low Temperatures Using Electrochemical Model with NMR Assisted Parameterization. *J. Electrochem. Soc.* **2017**, *164* (6), A1050. https://doi.org/10.1149/2.0461706jes.
(163) Carelli, S.; Bessler, W. G. Prediction of Reversible Lithium Plating with a Pseudo-3D Lithium-Ion Battery Model. *J. Electrochem. Soc.* **2020**, *167* (10), 100515. https://doi.org/10.1149/1945-7111/ab95c8.
(164) Vishnugopi, B. S.; Verma, A.; Mukherjee, P. P. Fast Charging of Lithium-Ion Batteries via Electrode Engineering. *J. Electrochem. Soc.* **2020**, *167* (9), 090508. https://doi.org/10.1149/1945-7111/ab7fb9.
(165) Cai, W.; Yan, C.; Yao, Y.-X.; Xu, L.; Chen, X.-R.; Huang, J.-Q.; Zhang, Q. The Boundary of Lithium Plating in Graphite Electrode for Safe Lithium-Ion Batteries. *Angew. Chem. Int. Ed.* **2021**, *60* (23), 13007–13012. https://doi.org/10.1002/anie.202102593.
(166) Kim, C.-S.; Jeong, K. M.; Kim, K.; Yi, C.-W. Effects of Capacity Ratios between Anode and Cathode on Electrochemical Properties for Lithium Polymer Batteries. *Electrochimica Acta* **2015**, *155*, 431–436. https://doi.org/10.1016/j.electacta.2014.12.005.
(167) Keil, P.; Jossen, A. Charging Protocols for Lithium-Ion Batteries and Their Impact on Cycle Life—An Experimental Study with Different 18650 High-Power Cells. *J. Energy Storage* **2016**, *6*, 125–141. https://doi.org/10.1016/j.est.2016.02.005.
(168) Huang, W.; Ye, Y.; Chen, H.; Vilá, R. A.; Xiang, A.; Wang, H.; Liu, F.; Yu, Z.; Xu, J.; Zhang, Z.; Xu, R.; Wu, Y.; Chou, L.-Y.; Wang, H.; Xu, J.; Boyle, D. T.; Li, Y.; Cui, Y. Onboard Early Detection and Mitigation of Lithium Plating in Fast-Charging Batteries. *Nat. Commun.* **2022**, *13* (1), 7091. https://doi.org/10.1038/s41467-022-33486-4.
(169) Koleti, U. R.; Bui, T. N. M.; Dinh, T. Q.; Marco, J. The Development of Optimal Charging Protocols for Lithium-Ion Batteries to Reduce Lithium Plating. *J. Energy Storage* **2021**, *39*, 102573. https://doi.org/10.1016/j.est.2021.102573.
(170) Mai, W.; Colclasure, A. M.; Smith, K. Model-Instructed Design of Novel Charging Protocols for the Extreme Fast Charging of Lithium-Ion Batteries Without Lithium Plating. *J. Electrochem. Soc.* **2020**, *167* (8), 080517. https://doi.org/10.1149/1945-7111/ab8c84.
(171) Liu, J.; Bao, Z.; Cui, Y.; Dufek, E. J.; Goodenough, J. B.; Khalifah, P.; Li, Q.; Liaw, B. Y.; Liu, P.; Manthiram, A.; Meng, Y. S.; Subramanian, V. R.; Toney, M. F.; Viswanathan, V. V.; Whittingham, M. S.; Xiao, J.; Xu, W.; Yang, J.; Yang, X.-Q.; Zhang, J.-G. Pathways for Practical High-Energy Long-Cycling Lithium Metal Batteries. *Nat. Energy* **2019**, *4* (3), 180–186. https://doi.org/10.1038/s41560-019-0338-x.
(172) Park, J.; Jeong, J.; Lee, Y.; Oh, M.; Ryou, M.-H.; Lee, Y. M. Micro-Patterned Lithium Metal Anodes with Suppressed Dendrite Formation for Post Lithium-Ion Batteries. *Adv. Mater. Interfaces* **2016**, *3* (11), 1600140. https://doi.org/10.1002/admi.201600140.
(173) Nanda, S.; Gupta, A.; Manthiram, A. Anode-Free Full Cells: A Pathway to High-Energy Density Lithium-Metal Batteries. *Adv. Energy Mater.* **2021**, *11* (2), 2000804. https://doi.org/10.1002/aenm.202000804.
(174) Qian, J.; Adams, B. D.; Zheng, J.; Xu, W.; Henderson, W. A.; Wang, J.; Bowden, M. E.; Xu, S.; Hu, J.; Zhang, J.-G. Anode-Free Rechargeable Lithium Metal Batteries. *Adv. Funct. Mater.* **2016**, *26* (39), 7094–7102. https://doi.org/10.1002/adfm.201602353.

(175) Qiao, Y.; Yang, H.; Chang, Z.; Deng, H.; Li, X.; Zhou, H. A High-Energy-Density and Long-Life Initial-Anode-Free Lithium Battery Enabled by a Li2O Sacrificial Agent. *Nat. Energy* **2021**, *6* (6), 653–662. https://doi.org/10.1038/s41560-021-00839-0.
(176) Schnell, J.; Günther, T.; Knoche, T.; Vieider, C.; Köhler, L.; Just, A.; Keller, M.; Passerini, S.; Reinhart, G. All-Solid-State Lithium-Ion and Lithium Metal Batteries – Paving the Way to Large-Scale Production. *J. Power Sources* **2018**, *382*, 160–175. https://doi.org/10.1016/j.jpowsour.2018.02.062.
(177) Kazyak, E.; Wang, M. J.; Lee, K.; Yadavalli, S.; Sanchez, A. J.; Thouless, M. D.; Sakamoto, J.; Dasgupta, N. P. Understanding the Electro-Chemo-Mechanics of Li Plating in Anode-Free Solid-State Batteries with Operando 3D Microscopy. *Matter* **2022**, *5* (11), 3912–3934. https://doi.org/10.1016/j.matt.2022.07.020.
(178) Coreform Cubit. http://coreform.com.